Contents

Chapter 1

Introduction

1.1 Overview

In 1964 Penzias and Wilson [120] discovered the Cosmic Microwave Background (CMB) radiation as an excess instrument noise with temperature $\sim$ 3K, coming from all directions in the sky. Dicke and Peebles *et al.* (1965) [49] interpreted this as the relic radiation from the Big Bang. The discovery of this relic radiation in conjunction with Hubble's observation of the cosmic expansion in 1927 [83], the synthesis of the light elements, the evolution of radio source counts etc, provided strong support to the hot Big Bang model.

Recently the FIRAS instrument on the COBE satellite has confirmed that this radiation has a Planck spectrum with [111]:

$$T_0 = 2.726 \pm 0.010\text{K (95\% confidence)}. \tag{1.1}$$

In the standard Big Bang model thermalization of the CMB occurs at a redshift $z \sim 10^6$ at $T \geq 10^7$K, via double Compton scattering ($e + \gamma \rightarrow e + 2\gamma$) and bremsstrahlung ($e + p \rightarrow e + p + \gamma$) processes, resulting in a Planckian spectrum kept along its subsequent evolution. So, the observed black body spectrum of the CMB radiation suggests its origin in the early universe; this is further supported by its high degree of isotropy. The CMB photons were last scattered at a redshift $z \sim 1100$, when the expanding universe had cooled to temperatures $T \sim 3000$K, sufficient for protons to capture the free electrons producing neutral atoms. After this period of recombination the CMB photons free stream towards us from this 'last scattering surface', providing direct information about this early epoch 300,000 years after the initial singularity. Initial theoretical predictions suggested that structure formation in the universe like galaxies, clusters of galaxies, etc., implied fluctuations in the CMB, due to the presence of primordial seed structures at the time when the CMB radiation decouples from the matter distribution. Consequently observations of CMB radiation anisotropies provide a means of testing stucture formation theories. On large angular scales the CMB fluctuations may probe the inflationary power spectrum and therefore the physics of the first 10^{-35}s. The original detection paper by Penzias and Wilson 1965 [120], set an upper limit of $< 10\%$ on any anisotropy. The initial predictions indicated that galaxy formation would produce fluctuations in the CMB of the order of 1 part in 10^2 [129], or 10^3 [139, 140].

Since then work on the CMB anisotropy question has shown improvements in experimental sensitivity and in theoretical calculations with increasingly sophisticated estimations of the temperature fluctuations of the CMB. For universes containing predominantly baryonic matter, a prediction of $\Delta T/T \sim 10^{-4}$ was obtained by several authors [118, 52, 164]. By 1980, the hypothesis of non-baryonic dark matter universes [18, 53] was encouraged by the claims of the existence of a electron neutrino mass of $\sim$ 30eV [106]. Although the neutrino as a candidate of dark matter failed to explain the structure formation [85, 166, 167], it still is an acceptable dark matter candidate [147]. At the same time inflationary scenarios paid particular attention to cold dark matter dominated universes [17, 119, 61], where cold means that the candidate particles have small thermal velocities (the free streaming length of such particles is much smaller than the size of any galaxy or cluster of stars). Following improvements in the upper limits on smaller scales of $\Delta T/T \sim 10^{-4}$ [157, 158, 159], new theoretical calculations predicted that for models with a cold dark matter component, the amplitude of the temperature fluctuations of the CMB could be reduced by an order of magnitude.

The first detection of large angular scale primordial CMB anisotropy came in 1992, reported by Smoot *et al.* [144] using the COBE DMR experiment [143]. This initial result consisted of statistical evidence for CMB anisotropy; the CMB maps were not sensitive enough to pin down actual CMB features on the sky. In 1993 the MIT experiment [112, 62] reported results at high frequency which confirmed the COBE detection. Given the frequency range and the sky coverage between these two experiments this confirmed that the detected signal was indeed CMB anisotropy. This was followed by low frequency confirmation in 1994, from the Tenerife experiment [75], which enabled the association of the detected statistical anisotropy with actual CMB features on the sky. (The Tenerife results are revised and corrected in Chapter 5 of this thesis, followed by a combined analysis of data from the Tenerife and COBE experiments, with improved constraints on the normalization and spectral index of an initial power-law power spectrum of the fluctuations.) Since the COBE detection, several other experiments have reported detections on intermediate angular scales (for a review see Chapter 3), although given their sky coverage and frequency range spanned, the possibility of foreground contamination is in some of the cases still under consideration. The systematic effects affecting some of these observations are another cause of concern. Recently new interesting detections have been reported by the Saskatoon [114] and the CAT [137] experiments, which with the other observations cover angular scales ranging from $10°$ to $0.25°$. Meanwhile questions such as the process of structure formation, the origin of the seed perturbations, the nature and quantity of the matter content of the universe, the values of the density parameter Ω, of the Hubble constant H_0 , and of other cosmological parameters remain still to be answered conclusively.

All these new exciting results and more sophisticated theoretical calculations motivated the work carried out in this thesis in search of satisfactory answers to such questions, bearing in mind the limitations imposed by the status of the data.

1.2 Outline

The thesis covers several techniques of intercomparison of CMB anisotropy experiments and models of structure formation. It presents the constraints on several cosmological parameters using current CMB observations. The essential concepts and mathematical tools used in later chapters are introduced in Chapter 2. Chapter 3 describes several existing experiments and the potential foreground contaminants of CMB observations. Chapter 4 deals with the 'rms temperature fluctuation' framework for comparison of theory and observations, followed by a description of the Monte Carlo simulations pursued in order to calculate the theoretical uncertainties affecting the predictions. The Tenerife experiment and the statistical techniques used to investigate the structure present in its scans are described in Chapter 5 and a correction to the level of CMB detection previously reported is presented. This is followed by a comparison of Tenerife CMB features with those in the 2-year COBE data. Here a Bayesian analysis of the data is undertaken and briefly compared with the previous frequentist approach. It also gives evidence for a successful method of reconstruction of the intrinsic CMB sky via a 'maximum entropy based method'. Chapters 6 and 7 deal with the 'flat bandpower' framework for intercomparison procedures. An analytic approximate expression to describe some of the models of structure formation is used in Chapter 6, while Chapter 7 uses the exact form of the 'angular power spectrum' as predicted by the considered models. The conclusions are presented in Chapter 8.

The results confirm the existence of the main Doppler peak in the angular power spectrum, a feature predicted by several models, strongly constraining the reionization history of the universe. This intercomparison further rules out low-Ω universes, favours low values of H_0 (assuming that the Saskatoon calibration is correct), prefers a low-Λ model, show consistency of the data with models in which the fluctuations originate from cosmic strings, pins the fluctuation spectral index down to the range $0.85 \leq n \leq 1.18$ consistent with inflationary predictions, and states that the existence of a gravity wave background is unlikely.

Chapter 2

Essential concepts and mathematical tools

2.1 Introduction

This Chapter describes the mathematical tools and essential concepts relevant to the work developed in the following chapters. Section 2.2 gives a brief account of the standard cosmological model, of both the inflationary and topological defect scenarios and describes some of the most popular models of structure formation. In Section 2.3 an account is given of the statistical description of the CMB anisotropy, in particular we mention the two-point angular correlation function which fully characterizes fluctuations with a Gaussian distribution. In Section 2.4 we give expressions for the rms temperature fluctuations for several observational strategies. This observable is the representation used for the inter-comparison of experiments and models presented in Chapter 4. The details of each observation are given in terms of its window function, which is described in Section 2.5. Section 2.6 focuses on the cosmic and sample variances; these theoretical uncertainties constitute a limitation to the accuracy of the estimation of the cosmological parameters. The angular power spectrum is a powerful means of characterizing a given model and has been more recently used in the comparison of models and experiments; this is the representation used in Chapter 6 and Chapter 7. In Section 2.7 we describe the shape and normalization of the angular power spectrum, and discuss the various sources of anisotropy and their dependence on cosmological parameters. In Section 2.7.3 an account of the theoretical calculation of this angular power spectrum is given, in particular we discuss the technique we used for small angular scales, previous to the availability of CMB codes. Section 2.8 describes a statistical data analysis technique very much in use in CMB community: the 'likelihood function', which we apply to the Tenerife experiment as described in Chapter 5. We were also interested in the information included in the error bars of this Bayesian analysis which we compare with frequentist techniques; this is addressed in Chapter 4. Finally Section 2.9 gives an account of an hypothetical sky model used by observers to compare their results with other experiments: the Gaussian auto-correlation function.

2.2 Structure formation in the universe

2.2.1 The Big Bang model

The standard cosmological model the so-called Big Bang model, is characterized by a homogeneous and isotropic universe which began from a singularity (the primeval fireball) with subsequent cosmological expansion. The spacetime metric describing the universe is the Friedman-Robertson-Walker (FRW) metric:

$$ds^2 = dt^2 - a(t)^2 \left(\frac{dr^2}{1-kr^2} + r^2 \left(d\theta^2 + \sin^2\theta d\phi^2 \right) \right), \tag{2.1}$$

where t is the physical time, $a(t)$ is the scale factor, (r, θ, ϕ) are spherical coordinates and k is the curvature constant. The FRW metric follows directly from the cosmological principle wich states that the universe is spatialy homogeneous and isotropic on large scales. This principle is supported by the observed high degree of isotropy of the CMB radiation and by the measured distribution of galaxies and faint radio sources. The cosmological expansion is expressed in terms of the scale factor $a(t)$, whose evolution is governed by the Friedmann equations which are obtained from General Relativity:

$$\left(\frac{\dot{a}}{a}\right)^2 = \frac{8\pi G}{3}\rho - \frac{k}{a^2} + \frac{\Lambda}{3}, \tag{2.2}$$

$$\frac{\ddot{a}}{a} = -\frac{4\pi G(\rho + 3p)}{3} + \frac{\Lambda}{3}. \tag{2.3}$$

The main components of this universe may be described as radiation and matter fluids. This model assumes that the radiation is of cosmological origin and this is why it is called 'hot'. This model provides a tractable framework within which one can try to understand how the structure we see today, like galaxies and clusters of galaxies, orginated from small density fluctuations in the early universe. The density necessary for the universe to be flat, the critical density, is given by:

$$\rho_c = \frac{3H^2 - \Lambda}{8\pi G}, \tag{2.4}$$

where

$$H = \frac{\dot{a}}{a}, \tag{2.5}$$

is the Hubble parameter. Ignoring Λ, since it never dominates the dynamics of the universe and is negligible at early times, ρ_c can be written as $\rho_c = 3H^2/8\pi G$. The cosmological parameters characterizing this model are the Hubble parameter as defined above, the deceleration parameter

$$q = -\frac{\ddot{a}a}{\dot{a}^2}, \tag{2.6}$$

the density parameter

$$\Omega = \frac{\rho}{\rho_c} = \frac{8\pi G\rho}{3H^2}, \tag{2.7}$$

where ρ is the energy density and usually Ω_0 is the density parameter today. The universe is flat, open or closed depending on whether Ω is equal to one, less than one, or greater than one. Neglecting the curvature term and the cosmological constant term and solving the Friedmann equations one obtains the following evolution laws for the scale factor :

$$a \propto t^{1/2},\ \rho = \frac{3}{32\pi G t^2}\ \text{(radiation era)} \tag{2.8}$$

$$a \propto t^{2/3},\ \rho = \frac{1}{6\pi G t^2}\ \text{(matter era)} \tag{2.9}$$

A concept of particular importance is the Hubble radius which by definition is the sphere such that its radius at time t is given by $L_H = c/H$, i.e., it contains all objects that are receding from us with a velocity less than c the speed of light. Some authors use the term 'Hubble radius' to denote the distance ct rather than the terminology 'particle horizon' (see below); they are not strictly the same, although they will agree to within factors of 2 or 3. There are three main epochs in the evolution of the universe of particular interest: the point a_{enter} at which the fluctuations enter the horizon, i.e., the physical size of the fluctuation is equal to the horizon; a_{eq} the time of matter-radiation equality, which occurs when the radiation and matter densities are equal, and a_{rec} the time of recombination, when protons capture free electrons producing neutral atoms and radiation is last scattered. Among the effects that follow from the FRW metric one has:

The cosmological redshift,

$$(1+z) = \frac{a(t_0)}{a(t_i)} \tag{2.10}$$

where t_i is the time of emission of a photon from an object at redshift z and t_0 is the time at which the photon is seen by the observer.

The Hubble expansion law,

$$z \sim \frac{v}{c} = \dot{d} = Hd, \tag{2.11}$$

where d is the proper distance between two objects, v is the recessional velocity, c is the speed of light and H is the Hubble parameter.

The proper distance that light can travel since the beginning of the universe, the particle horizon is given by;

$$d_H \sim 2ct\ \text{(radiation era)} \tag{2.12}$$

$$d_H \sim 3ct\ \text{(matter era)} \tag{2.13}$$

where c is the speed of light.

The angle-size relation,

$$\theta = \frac{L}{a(t_0) r_0 (1+z)^{-1}} \tag{2.14}$$

where θ is the angle subtended by an object with proper length L at a distance $r = r_0$ and r is the radial coordinate of the FRW metric. At redshifts $z \gg 1$, a comoving length, d, subtends an angle θ given by:

$$\theta \sim \frac{d}{2c} \Omega_0 H_0 \text{ (radians)}, \tag{2.15}$$

in particular the Hubble radius at $z \gg 1$ subtends an angle θ_H

$$\theta_H = \left(\frac{\Omega_0}{z}\right)^{1/2} \text{ (radians)} \tag{2.16}$$

and $\theta_H \sim 1 - 2°$, for $z \sim z_{rec} \sim 1000$, where z_{rec} is the redshift at recombination.

We now list some successes and problems with the Big Bang model.

Successes of the Big Bang model

The successes of this model amount to:

The observed primordial light element abundances are predicted by primordial nucleosynthesis.

Recent results suggest $0.009 \leq \Omega_b h^2 \leq 0.02$ [35], where $\Omega_b = \rho_b/\rho_c$ and ρ_b is the baryon density.

The observed expansion of the universe (Hubble expansion law).

The existence of the Cosmic Microwave Background radiation with a black body spectrum.

The evolution of radio source counts.

Problems of the Big Bang model

Among the shortcomings of this model one has:

The horizon problem: the microwave background radiation we receive today on scales separated by more than $\sim 1°$ comes from regions which were not in causal contact at the time of the last scattering, so in order to explain its high degree of isotropy, initial conditions must be imposed in the standard model.

The flatness problem: $\Omega = 1$ is an unstable equilibrium point in the standard model, hence is hard to understand why Ω is close to unity today.

The cosmological constant problem: there is empirical evidence that the cosmological constant Λ, is much smaller than expected on dimensional grounds.

The monopole problem: in the early universe it is expected that phase transitions produce exotic particles, small black holes and topological defects. In particular grand unified theories (GUT) predict large quantities of monopoles. This is not supported by observations.

The structure formation problem: this model has no mechanism to generate the density perturbations that gave rise to the structure on small scales like galaxies, clusters of galaxies, etc. The seed structure need to be imposed as initial conditions rather than produced dynamically.

The dark matter problem: there is observational evidence that most of the matter in our universe is in the form of non-luminous matter [165]. Some possibilities for this dark matter are non-luminous baryonic matter (e.g. jupiters, brown dwarfs [29]), MACHO's (Massive Compact Halo Objects) formed from an early population of black holes or neutron stars or white dwarfs [3]. The nucleosynthesis constraints on the abundances of baryonic matter [35] imply the existence of non-baryonic dark matter. Possibilities for this dark matter are, e.g., in the form of weakly interacting massive particles (WIMPS) [155] which can be classsified as Cold Dark Matter (CDM) or Hot Dark Matter (HDM) according to their thermal velocities. A candidate proposed for the HDM has been the neutrinos with non-zero mass while for CDM the most popular is the axion; however there is not yet evidence for the existence of WIMPS.

In order to solve these limitations concepts like Inflation [104, 72] and Topological defect models [36] arose from the combined areas of particle physics and cosmology.

2.2.2 Inflation

The flatness and horizon problems are solved by the inflationary scenario. This consists of a phase of rapid expansion where the scale factor grows faster than the horizon. If there is a moment at which the universe goes through a phase-transition (e.g., associated with symmetry breaking of the grand unified field) then a false-vacuum is generated with the vacuum density energy acting like a cosmological repulsion (equivalent to non-zero cosmological constant Λ). As a consequence there is an exponential expansion of the scale factor inflating the universe by a factor $\sim 10^{28}$, the end of which the vacuum energy density is transformed into matter and radiation. The evolution of the scale factor is given by:

$$a(t) \propto e^{Ht}, \tag{2.17}$$

with

$$H^2 = \frac{8\pi G}{3}\rho_v, \tag{2.18}$$

where ρ_v is the false vacuum energy density. In particular Inflation provides a mechanism to generate the seed fluctuations via amplification of quantum irregularities. This scenario predicts a scale-invariant or Harrison Zel'dovich form for the fluctuations power spectrum (see Section 2.2.5) and produces fluctuations distributed according to Gaussian statistics.

2.2.3 Topological defects

Topological defects arise as a natural outcome of phase-transitions in the early universe. It provides an alternative mechanism of generation of seed fluctuations. In standard theories spontaneous symmetry breaking at a critical temperature T_c, at $t < 10^{-35}$s (energies $\gtrsim 10^{16}$ GeV) at the time where the electromagnetic, weak and strong forces are unified, results in a phase expected to contain topological defects. These defects are called monopoles, cosmic strings [25], domain walls or textures [156] for 0,1,2, and 3 dimensions respectively. These defects act as seeds for structure formation via their gravitational efects. The generation and evolution of these defects is a non-linear process and therefore the fluctuations they generate are not Gaussian distributed.

2.2.4 Type of fluctuations

The initial fluctuations may be either adiabatic or isocurvature fluctuations.

Adiabatic fluctuations

These fluctuations are perturbations in the density field, $\delta\rho \neq 0$, and are predicted by inflation.

$$\delta = \frac{\delta n_b}{n_b} = \frac{\delta n_x}{n_x} = \frac{\delta s}{s}, \tag{2.19}$$

where b refers to baryons, x to any other species and s is the entropy density. These fluctuations conserve the photon entropy per species x, ie conserve the number per comoving volume of species x:

$$\delta\left(\frac{n_x}{s}\right) = \left(\frac{\delta n_x}{n_x} - \frac{\delta s}{s}\right)\frac{n_x}{s} = 0, \tag{2.20}$$

and therefore

$$\frac{\delta\rho_x}{\rho_x} = \frac{3}{4}\frac{\delta\rho_\gamma}{\rho_\gamma}. \tag{2.21}$$

where ρ_γ is the radiation energy density [56]. Fluctuations in the temperature of the CMB relates with fluctuations in the matter density by:

$$\frac{\delta T}{T} \sim \frac{1}{3}\frac{\delta\rho}{\rho}. \tag{2.22}$$

Isocurvature fluctuations

These fluctuations are characterized by $\delta\rho = 0$, and correspond to fluctuations in the form of the local equation of state, ie perturbation in the entropy per particle of species x:

$$\delta\left(\frac{n_x}{s}\right) \neq 0. \tag{2.23}$$

Here perturbations in matter and radiation densities are of opposite sign. It can be shown that an isocurvature mode transforms into an energy density fluctuation once it enters within the horizon, due to pressure gradients. Therefore, isocurvature fluctuations generate perturbations in the matter component when they enter the horizon and therefore produce gravitational potential fluctuations. As, after matter domination, initial entropy perturbations are transferred to the perturbations of the radiation, a significant radiation density fluctuation is then generated.

2.2.5 Power spectrum and evolution of seed perturbations

An initial power-law spectrum of the density fluctuations, as expected from inflationary scenarios is often assumed, and is in particular predicted by slow-roll inflation [101]. The form assumed is:

$$P(k) = Ak^n, \tag{2.24}$$

where A is the amplitude and n is the spectral index, both to be determined from observations. A spectral index $n = 1$ describes scale-invariant fluctuations, the so-called Harrison-Zel'dovich spectrum [177, 76]. This spectrum is scale-invariant because, for $n = 1$, the variance of the density fuctuations at horizon crossing, i.e. when the physical size of the fluctuation is equal to the Hubble radius ($\lambda_H = ct$), is independent of scale. To see that this is the case [23], consider the variance of the density fluctuations on a scale size $\simeq x$:

$$\langle(\delta\rho/\rho)^2\rangle_x \propto \frac{V}{2\pi^3}\int_0^{k\simeq 1/x} P(k)d^3k \propto t^2 x^{-(n+3)}, \tag{2.25}$$

where t^2 comes from the growth factor of the density fluctuations (here considered during the radiation dominated epoch with $(\delta\rho/\rho) \propto t$ for scales larger than the horizon size and $a(t) = t^{1/2}$). The physical size, λ, of the patch is equal to the Hubble radius when $\lambda = a(t)x = ct$, where $a(t)$ is the scale factor (one scales spatial dimensions, as t changes, by multiplying the comoving coordinates by $a(t)$). Thus the horizon crossing happens when $t \simeq x^2$, this being so one has:

$$\langle(\delta\rho/\rho)^2\rangle_{\lambda=ct} = k^{n-1} = \text{constant if } n = 1 \tag{2.26}$$

The most natural outcome of an inflationary phase at early times is Gaussian, adiabatic fluctuations, with a scale invariant spectrum [95] though it is not the only possibility. In linear perturbation theory each Fourier mode of the perturbations evolves independently of the others. This permits one to relate the fluctuations at the present epoch, t_0, with the perturbations when they were generated at time, t_i, via a linear transfer function, $T(k)$:

$$\delta(k, t_0) \propto T(k)\delta(k, t_i), \tag{2.27}$$

or in terms of the power spectrum:

$$P(k, t_0) = (g(t_0)/g(t_i))^2\, T^2(k)P(k, t_i), \tag{2.28}$$

where $g(t)$ is the linear growth law for perturbations above the Jeans length [34]. The processing of the power spectrum depends on cosmological parameters like total density of the universe, Ω_0, the Hubble constant, H_0 , and the nature of the non-baryonic dark matter. An important quantity to be mentioned is the dispersion, $\sigma(R)$, of the density field smoothed in a comoving scale, R:

$$\sigma^2(R) = \int_0^\infty W^2(kR)P(k, t_0)\frac{dk}{k}, \tag{2.29}$$

where $W(kR)$ is the window function used in the smoothing.

For a given formula, given the origin and power spectrum of the fluctuations, the quantity and nature of the dark matter and the type of perturbations, one can evolve these fluctuations in an expanding universe. During the growth of a fluctuation there are three main epochs to consider: the point a_{enter} at which the fluctuations enter the horizon, i.e., the physical size of the fluctuation is equal to the Hubble radius, a_{eq} the epoch of matter-radiation equality, and a_{rec} the epoch of recombination.

2.2.6 Models of structure formation

Baryonic models

During the radiation dominated era ($a < a_{eq}$), perturbations on scales larger than the horizon size grow according to $\delta \propto t$ and therefore to $\delta \propto a^2$, while during the matter dominated epoch they grow according to $\delta \propto t^{2/3}$, and therefore $\delta \propto a$. Matter fluctuations on scales smaller than the horizon size interact with the radiation such that those on scales greater than the Jeans length ($\lambda > \lambda_J$), where pressure gradients can be ignored, collapse under self gravity, whereas those with $\lambda < \lambda_J$, where gravity can be ignored, undergo acoustic oscillations. The Jeans length is defined by:

$$\lambda_J = 2\pi \left(\frac{v_s^2}{4\pi G\rho} \right), \tag{2.30}$$

where v_s is the adiabatic sound speed, with corresponding Jeans mass. Before recombination the radiation and matter are tightly coupled by Thomson scattering, with Thomson cross-section $\sigma_T = (8\pi e^4)/(3m_e^2) = 0.6652 \times 10^{-24}$ cm^2. Matter and radiation act like a single fluid with $M_J \sim 9 \times 10^{16} (\Omega h^2)^{-2} M_\odot$, where $M_\odot$ is the solar mass. After recombination the adiabatic speed is that of a monoatomic gas, since the photons are no longer coupled to the matter. Then $M_J \sim 1.3 \times 10^6 (\Omega h^2)^{-1/2} M_\odot$, a mass close to the mass of globular star clusters. Hence, before matter and radiation decouple, adiabatic perturbations on scales smaller than supercluster scales oscillate like sound waves whereas after recombination the Jeans mass decreases by more than a factor $\sim 10^{10}$ to globular cluster masses. Fluctuations inside the horizon oscillate acoustically and therefore their amplitude is damped with respect to fluctuations outside the horizon producing a turnover in the fluctuation power spectrum. Imperfect coupling of matter and radiation lead to a damping of adiabatic fluctuations on smaller scales usually called 'Silk damping' [140], in which the photons may move from and into overdensities or underdensities of scale $\lambda \lesssim \lambda_D$, carrying matter with them. This damping is characterised by a length scale and mass given by:

$$\lambda_D = c(At)^{1/2}, \ A \sim \frac{4\pi^2}{6} \frac{1}{\sigma_T n_e c}, \tag{2.31}$$

$$M_D = 9 \times 10^{10} \left(\Omega h^2\right)^{-5/4} M_0, \ (\text{for } z \sim 1000), \tag{2.32}$$

where n_e is the electron number density, c is the speed of light and σ_T is the Thomson cross-section. Recombination does not occur instantaneously at $z \sim 1000$, and so it should be expected that expression 2.32 is an understimate. The effect of the scattering on a perturbation $\delta T(z)$ is given by:

$$\int_0^z \frac{\delta T(z)}{T} e^{-\tau(z)} \frac{d\tau}{dz} dz, \tag{2.33}$$

where τ is the optical depth to Thomson scatterings . The function $e^{-\tau(z)}\frac{d\tau}{dz}$ is well approximated by a Gaussian with mean $z_{rec} \sim 1100$ independent of Ω and h (150,165) and $\Delta z = 80$, but in the context of standard theory of recombination, it can go up to $\Delta z \sim 400$ which corresponds to a proper distance $\Delta L \sim 40h^{-1}$Mpc and to an angular scale $\sim 20'$. The finite thickness of the last scattering surface can erase fluctuations on scales smaller than its width.

The main problems of this model are:

As the density fluctuations only grow after decoupling, the amplitude $\delta\rho/\rho$ predicted to fit the structure we see today is greater than the upper limit set up by the CMB fluctuations.

Models with $\Omega h^2 \leq 0.1$ give rise to fluctuations in the mass distribution on scales $\sim (10-20)h^{-1}$ Mpc, larger than those observed in the distribution of galaxies, assuming that $n \leq 2$ [56]. In this case an initial scale invariant spectrum is inconsistent with the low amplitude of the galaxy correlation function observed on large angular scales.

The desire of satisfying simultaneously the requirements of the inflationary scenario ($\Omega = 1$) and the nucleosynthesis constraints.

CDM models

The gowth of the fluctuations in the baryonic component remains unchanged until the recombination epoch. Adiabatic CDM fluctuations which enter the horizon at $a < a_{eq}$, grow according to $\delta \propto \ln a$, suffering a smaller growth as compared with fluctuations outside the horizon. This fact gives rise to a characteristic turnover in the fluctuation power spectrum, such that initially scale-invariant perturbations evolve to produce a power spectrum with the asymptotic behaviour: $P(k) \propto k$ for $k \to 0$ and $P(k) \propto k^{-3}$ for $k \to \infty$. The scale corresponding to the transition between these two regimes is the size of the horizon at the time of matter-radiation equality (point of deflection), $\lambda = ct_{eq}\,(a_0/a_{eq}) \simeq 10(\Omega h^2)^{-1}$ Mpc. Fluctuations that enter the horizon at $a > a_{eq}$ grow according to $\delta \propto a$, since they are not coupled to the photons. Since fluctuations in the CDM component begin to grow just as the universe becomes matter dominated, by the end of the recombination the amplitude of the CDM fluctuations are larger than the baryonic fluctuations by a factor

$$\frac{a_{rec}}{a_{eq}} \sim 21\Omega h^2. \tag{2.34}$$

The baryons after decoupling from the radiation, at the end of the recombination fall into the potential wells created by CDM fluctuations. This provides a process of amplifying the baryonic fluctuations after recombination. After recombination both baryons and CDM grow according to $\delta \propto a$. In these CDM components there is also a damping of the fluctuations due to the free-streaming of matter particles out the fluctuations. The free-streaming scale is $\lambda_D \sim 1$ Mpc. Fluctuations on scales smaller than 1 Mpc are wiped out, this results in a 'bottom-up' scenario with higher structures forming due to tidal forces and by merging of smaller structures.

The linear transfer function in adiabatic CDM models has the form [56]:

$$t(k) = [1 + (ak + (bk)^{3/2} + (ck)^2)^\nu]^{-1/\nu} \tag{2.35}$$

where $a = 6.4(\Omega h^2)^{-1}$ Mpc, $b = 3.0(\Omega h^2)^{-1}$ Mpc, $c = 1.7(\Omega h^2)^{-1}$ Mpc and $\nu = 1.13$.

The two major problems of this model are:

Assuming that light traces mass, simulations show that the correlation function for these models, when compared to the observed correlation implies a $\Omega h \sim 0.2$ (against $\Omega = 1$).

The predicted correlation function at large scales is less by a factor of 3 than the observed correlation. Also simulations do not produce giant voids as observed.

Some of these problems are thought to be solved by considering 'biased CDM models', although consistency with recent CMB observations seem to require anti-biased CDM models (see Chapter 7).

HDM models

The growth of the fluctuations for adiabatic HDM models is similar to that for CDM models as described above. Fluctuations on scales smaller than

$$\lambda_D \sim 40 \left(\frac{m_\nu}{30 \text{ eV}}\right)^{-1} \text{ Mpc} \tag{2.36}$$

are erased due to the neutrino free-streaming. The free-streaming scale is the distance travelled by a neutrino by the present epoch:

$$\lambda_D \sim 5ct_{rn}\frac{a(t_0)}{a(t_{rn})}, \tag{2.37}$$

where t_{rn} is the time separating the relativistic/non-relativistic regimes of the neutrino, which happens when $3kT_\nu \sim m_\nu c^2$. This damping scale corresponds to scales of superclusters ($\sim 10^{15}\ M_0$) and galaxies are formed from fragmentation of large pancake-like structures, in a 'top-down' scenario.

The problems of this model are:

This process of structure formation seems to suggest that galaxies are outside clusters in contradiction with observations. This could be solved by incorporating topological defect models as seeds of the structure; as they are not affected by the neutrino free streaming, galaxies could be seeded at $t > t_{rn}$.

The observed galaxy-galaxy correlation function requires a pancake formation at $z \sim 1$, contradicting the existence of galaxies with $z > 1$ and quasars with $z > 3$. On the other hand in order to produce galaxies and quasars at high redshifts this model should produce a high level of clustering today and this is not observed.

It does not explain the dark halos of galaxies because they cannot cluster at these scales.

Among possible solutions to these problems are: neutrinos with $\Omega_\nu h^2 \sim 2$ implying $\lambda_D \sim 5h^{-1}$ Mpc; to assume that clusters trace better the density distribution, diminishing the existing discrepancies with observations; existence of additional seeds of structure like topological defects or primordial black holes.

MDM models

Since adiabatic HDM models fail to explain the observed small-scale structure in the universe, whereas CDM does not seem to reproduce the large-scale structure present in large-scale structure surveys [161, 130, 108], a mixture of both hot and cold dark matter in conjunction with the baryonic matter seem to be a possible means of balancing the contributions from both components in order to reproduce the observed power spectrum.

2.3 Statistical description of the CMB field

It is standard procedure to express the temperature fluctuations of the CMB on the celestial sphere using an expansion in spherical harmonics:

$$\Delta T/T(\alpha,\phi) = \sum_{l=2}^{\infty} \sum_{m=-l}^{l} a_{lm} Y_{lm}(\alpha,\phi) \tag{2.38}$$

where (α,ϕ) are the polar coordinates of a point in the spherical surface. We have ignored the dipole ($l = 1$) which is largely dominated by the Doppler effect due to the motion of our Galaxy with respect to the last scattering surface. Inflationary models predict that the initial CMB perturbations follow a Gaussian distribution, and as the observed CMB field conserves the original distribution we can consider it as a 2-dimensional Gaussian random field on the sky. In this case the multipole moments a_{lm} are stochastic variables with random phase, zero mean and variance given by $C_l = \langle |a_{lm}|^2 \rangle$ which defines a power-spectrum.

The properties of a Gaussian field are fully specified by the two-point angular auto-correlation function (ACF), the expected average of the product of the temperature fluctuations in two directions in the sky separated by an angle θ :

$$C(\theta) = \left\langle \frac{\Delta T}{T}(\vec{n_1}) \frac{\Delta T}{T}(\vec{n_2}) \right\rangle \tag{2.39}$$

where $\vec{n_1} \cdot \vec{n_2} = \cos\theta$ and the angle brackets refer to an average over the whole sky. Using Equation (2.38) the expression of the ACF becomes:

$$C_{ran}(\theta) = \sum_{l,m} \sum_{l',m'} \langle a_{lm} a^*_{l'm'} \rangle Y_{lm}(\alpha,\phi) Y^*_{l'm'}(\alpha',\phi') \tag{2.40}$$

For a temperature pattern that is statistically isotropic, the rotational symmetry implies:

$$\langle a^*_{lm} a_{l'm'} \rangle = \delta_{ll'} \delta_{mm'} C_l. \tag{2.41}$$

Using the relation (2.41) and the addition theorem for spherical harmonics, one can express the random variable $C(\theta)$, as an expansion in Legendre polynomials [133]:

$$C_{ran}(\theta) = \frac{1}{4\pi}\sum_{l\geq 2} Q_l^2(x)P_l(\cos\theta), \tag{2.42}$$

where

$$Q_l^2(x) = \sum_{m=-l}^{l} |a_{lm}|^2, \tag{2.43}$$

with a χ^2_{2l+1} distribution and

$$\langle Q_l^2(x)\rangle = (2l+1)C_l, \tag{2.44}$$

and variance

$$\mathrm{var}(Q_l^2) = 2\langle Q_l^2\rangle^2/(2l+1). \tag{2.45}$$

The relationship between the angular scale θ and the multipole l is given by $l \simeq 2/\theta$, with θ in radians. The coefficients C_l constitute the angular power spectrum of the temperature fluctuations and, as we will see, play an important role in the comparison of CMB experiments with theoretical models of structure formation. As shown in Equation (2.45) the uncertainty scales as $(l+1/2)^{-1/2}$ which explains the fact that smaller angular scale experiments have smaller cosmic variances (see also Section 2.6), since they probe larger multipoles l. For large scale experiments this is an unavoidable uncertainty and in particular it limits the accuracy of the normalization of the power spectrum. The expectation value of the temperature correlation function, i.e., the ensemble average, is given by:

$$C(\theta) = \frac{1}{4\pi}\sum_{l}(2l+1)C_lP_l(\cos\theta). \tag{2.46}$$

In this statistical description of the CMB fluctuations, our universe is considered as a realization of the theoretical field, and therefore the observed ACF represents an estimation of the ACF of the field from a finite sample. The uncertainty of these estimations constitutes an intrinsic limitation imposed by the statistical nature of the theory and is independent of the instrumental sensitivity.

2.4 $(\Delta T/T)_{rms}$

One of the observables in CMB experiments is the rms of temperature fluctuations, This quantity may then be compared with the expected temperature fluctuation for a given experiment and model. For a rigorous comparison the theoretical uncertainty must also be considered (see Section 1.5). The expected temperature fluctuation, $(\Delta T/T)_{rms}$, may be computed directly from the two-point angular correlation function, $C(\theta)$, or from the angular power spectrum, C_l. The former may be used if the theory provides an analytical expression for the angular correlation function (e.g., a fitted parameterized expression) or, e.g., a parameterized expression for the transfer function of the temperature fluctuations (for transfer function see Section 1.6).

The expression of $(\Delta T/T)_{rms}$ depends on the experimental configuration, e.g., beam size, switching pattern, etc. Most CMB experiments use beam-switching techniques, using e.g. single, double differences etc., i.e., double or triple beams respectively. A two-beam experiment measures the temperature difference between beams separated by an angle β on the sky

$$\Delta T/T = (T_1 - T_2)/T, \tag{2.47}$$

and its expected variance is written in terms of the temperature autocorrelation function :

$$\left(\frac{\Delta T}{T}\right)^2_{rms} = \left\langle \left(\frac{T_1 - T_2}{T}\right)^2 \right\rangle = 2(C(0) - C(\beta)). \tag{2.48}$$

A three-beam experiment measures the difference between a field point, T_f, and the mean value of the temperature in two directions which are separated from the field point by an angle β

$$\Delta T/T = T_f - \tfrac{1}{2}(T_1 + T_2), \tag{2.49}$$

and its expected variance is given by:

$$\left(\frac{\Delta T}{T}\right)^2_{rms} = \left\langle \left(\frac{T_f - \frac{1}{2}(T_1 + T_2)}{T}\right)^2 \right\rangle = \tfrac{3}{2}C(0) - 2C(\beta) + \tfrac{1}{2}C(2\beta) \tag{2.50}$$

A four-beam experiment measures e.g.:

$$\Delta T_j/T = -\tfrac{1}{4}T_j + \tfrac{3}{4}T_{j+1} - \tfrac{3}{4}T_{j+2} + \tfrac{1}{4}T_{j+3}. \tag{2.51}$$

Where $\angle(T_j, T_{j+1}) = \beta$, the beamthrow, and its expected variance is expressed by:

$$\left(\frac{\Delta T}{T}\right)^2_{rms} = \tfrac{5}{4}C(0) - \tfrac{15}{8}C(\beta) + \tfrac{3}{4}C(2\beta) - \tfrac{1}{8}C(3\beta). \tag{2.52}$$

All these expressions are true for an ideal experiment with an infinitely narrow beam; for a real observation it is necessary to consider the beam smearing due to the finite resolution of the antenna. This is usually taken into account by convolving the radiation intensity with a beam approximated by a Gaussian $G(\theta)$:

$$G(\theta) = \frac{1}{2\pi\sigma^2} \exp\left(-\frac{\theta^2}{2\sigma^2}\right), \tag{2.53}$$

where σ is the dispersion of the Gaussian. The correlation function of the convolved radiation field is given by [23]:

$$C(\theta,\sigma) \simeq \frac{1}{2\sigma^2}\int_0^\infty C(\theta')e^{-\frac{\theta^2+\theta'^2}{4\sigma^2}} I_0\left(\frac{\theta\theta'}{2\sigma^2}\right)\theta' d\theta', \tag{2.54}$$

where I_0 is the modified Bessel function. So for a single difference one has:

$$\left(\frac{\Delta T}{T}\right)^2_{rms} = 2(C(0,\sigma) - C(\beta,\sigma)) \tag{2.55}$$

and for a double difference:

$$\left(\frac{\Delta T}{T}\right)^2_{rms} = \tfrac{3}{2}C(0,\sigma) - 2C(\beta,\sigma) + \tfrac{1}{2}C(2\beta,\sigma), \tag{2.56}$$

where β is the beamthrow. For a four-beam experiment:

$$\left(\frac{\Delta T}{T}\right)^2_{rms} = \tfrac{5}{4}C(0,\sigma) - \tfrac{15}{8}C(\beta,\sigma) + \tfrac{3}{4}C(2\beta,\sigma) - \tfrac{1}{8}C(3\beta,\sigma) \tag{2.57}$$

One is able to compute $(\frac{\Delta T}{T})^2_{rms}$ using Equations (2.54) and (2.55), (2.56) or (2.57) according to the experimental configuration.

The use of the angular power spectrum has in the last few years become the most successful representation and methodology for treatment of CMB anisotropies. The use of this approach is possible because the proponents of several models of structure formation are now making predictions of the power spectrum of the fluctuations. This approach uses the expression of $C(\theta)$ as in Equation (2.46), which considers ensemble-averaged values. As an example of this approach consider the particular case of a single Gaussian beam (the general case is addressed in Section 2.5), for comparison with the description given previously. In this case the smearing effect due to finite resolution of the antenna is taken into account in terms of a function $\mathcal{W}_l$ which affects the spherical harmonic expansion of the temperature fluctuations:

$$\frac{\Delta T}{T}(\alpha,\phi,\sigma_b) = \sum_{l,m} a_{lm} Y_{lm}(\alpha,\phi)\mathcal{W}_l(\sigma_b). \tag{2.58}$$

This is translated in terms of a window function W_l acting on the C_l expansion of the correlation function:

$$C(\theta,\sigma) = \frac{1}{4\pi}\sum_l (2l+1) C_l P_l(\cos\theta) W_l(\sigma), \tag{2.59}$$

where [133]

$$\mathcal{W}_l(\sigma) = e^{-(2l+1)^2\sigma^2/8} \tag{2.60}$$

and

$$W_l(\sigma) = e^{-(2l+1)^2\sigma^2/4} \tag{2.61}$$

which is usually approximated by

$$W_l = \exp(-l(l+1)\sigma^2), \tag{2.62}$$

where $\sigma = \mathrm{FWHM}/2\sqrt{2\ln 2}$, with FWHM standing for full width at half maximum of the beam. Equation 2.59 is a particular case, for a singlr Gaussian beam, of a more general expression which is given in Section 2.5. Once given the C_l's one can compute the correlation using Equation (2.46) or (2.59) and $\Delta T/T$ from Equations (2.55), (2.56) or (2.57), for the 2, 3 and 4-beam experiments respectively. Some experiments using switching techniques do not use a square wave chop; however, it may be used as an approximation. If one wants to be more precise one should use the appropriate beam on the sky. It is standard procedure to describe the details of the observation in terms of the window function, W_l, which is then used in the C_l expansion of $(\Delta T/T)_{rms}$ in order to compute directly the expected temperature fluctuations: this is addressed in the following Section (Section 2.5).

2.5 Window functions

A real CMB experiment is only sensitive to a given range in angular scales with a response to each multipole that can be characterized by the window function, W_l. For example, the beam smearing due to finite resolution results in the convolution of the radiation intensity with a beam approximated by a Gaussian. In the multipole space this will correspond to a multiplication of the coefficients of the Legendre polynomials by the corresponding window function as given by Equation (2.59) and (2.61). As already mentioned the intrinsic auto-correlations function C_{int} is transformed by convolution with the autocorrelated beam pattern of the telescope and is given by:

$$C_{conv}(\theta) = C_{int}(\theta) \star C_{beam}(\theta), \tag{2.63}$$

where C_{conv} is the autocorrelation function of the convolved radiation intensity, incorporating all the effects of the observational strategy e.g. the finite resolution of the antena, the switching pattern etc., C_{beam} is the instrumental ACF defined by the configuration of the telescope and $\star$ refers to convolution. The beam pattern of the telescope depends on the experimental strategy and for example is given by a triple beam pattern for double differences experiments. For a real observation Equation (2.46) becomes

$$C_{conv}(\theta) = \frac{1}{4\pi} \sum_l (2l+1) C_l P_l(\cos\theta) W_l. \tag{2.64}$$

From now on $C(\theta)$ will represent the autocorrelation function of the intrinsic radiation intensity. The expression for the rms temperature fluctuations becomes

$$\left(\frac{\Delta T}{T}\right)^2_{rms} = \frac{1}{4\pi} \sum_l (2l+1) C_l W_l, \tag{2.65}$$

where we are considering ensemble average values. For a Gaussian beam pattern the window function describing the finite beam resolution is given by Equation (2.62) [133] The multipole, l_s, corresponding to the dispersion of the beam, σ, is given by $l_s + 1/2 = 1/(2\sin(\sigma/2))$ [19]. This function determines the maximum resolution or the minimum angular scale to which the instrument is sensitive. It corresponds to a high l cut off which is controlled by the beamwidth of the experiment.
The window function is given by, for a 2-beam experiment:

$$W_l = \exp(-l(l+1)\sigma^2)\, [2(1 - P_l(\cos(\beta)))]\,. \tag{2.66}$$

for a 3-beam experiment:

$$W_l = \exp(-l(l+1)\sigma^2) \left[\tfrac{1}{2}(3 - 4P_l(\cos(\beta)) + P_l(\cos(2\beta)))\right]. \tag{2.67}$$

and for a 4-beam experiment:

$$W_l = \exp(-l(l+1)\sigma^2) \left[\tfrac{5}{4} - \tfrac{15}{8} P_l(\cos(\beta)) + \tfrac{3}{4} P_l(\cos(2\beta)) - \tfrac{1}{8} P_l(\cos(3\beta))\right] \tag{2.68}$$

where β is the beamthrow. These expressions may be easily derived from Equations (2.65), (2.55), (2.56), and (2.57). The differencing techniques introduce a low l cutoff which is determined by the beamthrow. As mentioned above there are experiments that do not use a 'square wave chop', in which case the window function needs to be derived separately, but in most of these cases the observing strategy may still be approximated as a single or double difference switching. For example, the experiments at the South-Pole (SP91 [63, 134] , SP94 [69]), MAX [33, 46, 152] and Saskatoon [174] use a sine wave chop with a weighting of $\pm$ 1 for the South-Pole, and the first and second harmonic of the chop frequency for MAX and Saskatoon respectively [170, 169, 168].

All these cases may be incorporated in a generic expression of the window function, according to White and Srednicki [168]. Following their approach, the temperature observed by an experiment for a given point, $\vec{n}$, in the sky, which for simplicity is denoted by T_{obs} is given by:

$$T_{obs} = \int d\Omega_{\vec{n}'} M(\vec{n},\vec{n}')T(\vec{n}'), \tag{2.69}$$

where $\vec{n}'$ is in the vicinity of $\vec{n}$, $T(\vec{n}')$ is the intrinsic temperature, $\vec{n}$ is a unit vector expressed in terms of the polar and azimuthal angles and $M(\vec{n},\vec{n}')$ is the mapping function which contains information about the detailed experimental strategy. The mapping function contains in particular the beam profile function, $B(\vec{n},\vec{n}')$, which for a Gaussian beam is expressed by Equation (2.53). For the COBE experiment [144] this is the only effect to take into account, with $M(\vec{n},\vec{n}') = B(\vec{n},\vec{n}')$, being completely specified by the beam profile function. For experiments using a chopping stategy, sometimes in conjunction with a smooth scan, one needs to specify the following quantities: the beam position function, $\vec{n}(t) = (\theta(t),\phi(t))$, which gives the position of the center of the beam at time t; the weighting or lock-in function, $L(t)$, which expresses the weight given to each point of the beam trajectory contributing for a given point of the scan, for the calculation of temperature, and the overall normalization, N. For a time interval $t_i - \frac{1}{2}\delta_i$,$t_i + \frac{1}{2}\delta_i$, one computes the temperature at an average position of the beam for this interval of time, $\vec{n}_i$, $T_{obs}(\vec{n}_i)$, which is given by:

$$T_{obs}(\vec{n}_i) = \frac{N}{\delta_i}\int_{t_i-\delta_i/2}^{t_i+\delta_i/2} dt L(t)\left(\int d\Omega_{\vec{n}'} B(\vec{n}(t),\vec{n}')T(\vec{n}')\right). \tag{2.70}$$

The window function $W_l(\vec{n}_1,\vec{n}_2)$ is given by:

$$W_l(\vec{n}_1,\vec{n}_2) = \int d\Omega_{\vec{n}'_1}\int d\Omega_{\vec{n}'_2} M(\vec{n}_1,\vec{n}'_1)M(\vec{n}_2,\vec{n}'_2)P_l(\vec{n}'_1\cdot\vec{n}'_2). \tag{2.71}$$

For the zero lag case, $W_l(\vec{n},\vec{n})$, is to a good approximation independent of the choice of $\vec{n}$, being mentioned uniquely by W_l. For the particular case of a single Gaussian beam, the finite beam resolution is given in terms of the beam profile function $B(\vec{n},\vec{n}')$. A beam profile, $B(\vec{n},\vec{n}')$, only dependent on $\vec{n}\cdot\vec{n}'$ may be expanded in Legendre polynomials. In this case $W_l(\vec{n},\vec{n}') = B_l^2 P_l(\vec{n}\cdot\vec{n}')$. For zero lag, $W_l = B_l^2$, where B_l^2 is given in Equation (2.61) or (2.62) . One can proceed to some simplifications in the case of observations with one of the coordinates kept constant (e.g. observations at constant θ) as is the case for e.g. experiments performing constant elevation scans. In this case the window function only depends on $|\phi-\phi'|$. There are two types of scans stepped and smooth, for a stepped scan the beam is centered at a point $\vec{n}=(\theta_0,\phi_0)$ and chopped back and forth in the ϕ direction. In this case $\vec{n}(t)$ is given by:

$$\vec{n}(t) = (\theta(t), \phi(t))$$
$$\theta = \theta_0$$
$$\phi(t) = \phi_0 + \alpha_0 \sin(\omega_c t),$$

where, $\omega_c/2\pi$ is the chop frequency, α_0 is half of the peak-to-peak chop angle. For a smooth scan the beam is chopped while moved smoothly at an angular velocity, ω_s. In this case $\vec{n}(t)$ is given by:

$$\theta(t) = \theta_0$$
$$\phi(t) = \phi_0 + \alpha_0 \sin(\omega_c(t)) + \omega_s t$$

The data is then binned in bins the size of which is usually a multiple of the period of the chop. Assuming this and that the period of the lock-in function is the same as of the chopping function and $\omega_s \ll \omega_c$, it can be shown that the expression of the window function is given by [168]:

$$W_l(\phi) = N^2 B_l^2(\sigma)\frac{4\pi}{2l+1}\sum_{m=-l}^{l}|Y_{lm}(\theta,0)|^2 L_m^2(\alpha_0)S_m^2(\Delta\phi)\cos(m\phi), \tag{2.72}$$

where

$$L_m(\alpha_0) = \frac{\omega_c}{2\pi}\int_{-\pi/\omega_c}^{\pi/\omega_c} dt L(t)\exp(im\alpha_0\sin(\omega_c t)), \tag{2.73}$$

and for a smooth scan:

$$S_m(\Delta\phi) = j_0\left(\frac{m\Delta\phi}{2}\right) = \frac{\sin(m\Delta\phi/2)}{(m\Delta\phi/2)}, \tag{2.74}$$

where $\Delta\phi = \omega_s\delta$ is the size of the bin in ϕ. For a stepped scan $S_m = 1$. Assuming that the line is a portion of a great circle, i.e., neglecting curvature, one can assume that $\theta = \pi/2$ and ϕ is the actual angle in the sky, the expression of the window function then becomes:

$$W_l(\phi) = N^2 B_l^2(\sigma)\sum_{r=0}^{l}\frac{(2l-r)!(2r)!}{(2^l r!(l-r)!)^2}L_{l-2r}^2(\alpha_0)S_{l-2r}^2(\Delta\phi)\cos((l-2r)\phi) \tag{2.75}$$

where ϕ, $\Delta\phi$ and α_0 are angles on the sky. For the already mentioned 2, 3, 4-beam experiments, $L(t)$ is the lock-in function corresponding to a square wave chop, consisting in a linear combination of Dirac δ functions, $\frac{\omega_c}{2\pi}L(t)$ is given by:

$$\frac{\omega_c}{2\pi}L(t) = \begin{cases} \delta(t+t_c) - \delta(t-t_c) & (2-\mathrm{beam}) \\ -\frac{1}{2}\delta(t+t_c) + \delta(t) - \frac{1}{2}\delta(t-t_c) & (3-\mathrm{beam}) \\ \frac{1}{4}\delta(t+t_c) - \frac{3}{4}\delta(t+\xi t_c) + \frac{3}{4}\delta(t-\xi t_c) - \frac{1}{4}\delta(t-t_c) & (4-\mathrm{beam}) \end{cases}$$

where $\xi = \frac{2}{\pi}\sin^{-1}(\frac{1}{3})$ and $t_c = \frac{\pi}{2\omega_c}$, the time to chop from ϕ_0 to $\phi_0 + \alpha_0$. The mapping function is a weighted sum of beam profile functions and $L_m(\alpha_0)$ is given by:

$$L_m(\alpha_0) = \begin{cases} 2\sin(m\alpha_0) & (2-\mathrm{beam}) \\ 2\sin^2(m\alpha_0/2) & (3-\mathrm{beam}) \\ \frac{1}{2}(\sin(m\alpha_0) - 3\sin(m\alpha_0/3)) & (4-\mathrm{beam}) \end{cases}$$

For a check, substituting the above expressions for $L_m(\alpha_0)$ into Equation (2.72) with $\phi = 0$ we reobtain the form of the window functions as given by Equations (2.66), (2.67) and (2.68). The Tenerife experiment [75], MSAM3 [31] and OVRO [113, 123] are examples of a 3-beam experiment, MSAM2 [30] is an example of a 2-beam experiment while PYTHON [54, 128] is an example of a 4-beam experiment. Other small angle experiments use different lock-in functions, e.g. South-Pole (SP91) [134, 63] and ARGO [44] experiments use a 'square-wave lock-in' with:

$$L(t) = k\mathrm{sign}(\alpha_0 \sin(\omega_c t))$$

$$L_m(\alpha_0) = kH_0(m\alpha_0) \tag{2.76}$$

where $k = 2$ for SP91 and $k = 1$ for the ARGO experiment and $H_0(x)$ is the Struve function:

$$H_0(x) = \frac{2}{\sqrt{\pi}\Gamma(1/2)} \int_0^1 dt(1-t^2)^{-1/2} \sin xt.$$

For the South-Pole experiment (SP91) the window function is given by:

$$W_l = 4N^2 \frac{4\pi}{2l+1} B_l^2(\sigma) \sum_{m=-l}^{l} |Y_{lm}(\theta,\phi)|^2 H_0^2(m\alpha). \tag{2.77}$$

The MAX experiment [33, 46, 152] uses a 'sine wave lock-in', where:

$$L(t) = \pi \sin(\omega_c t)$$

$$L_m(\alpha_0) = \pi J_1(m\alpha_0) \tag{2.78}$$

where J_1 is the Bessel function. The window function for this case becomes:

$$W_l = \pi^2 N^2 \frac{4\pi}{2l+1} B_l^2(\sigma) \sum_{m=-l}^{l} |Y_{lm}(\theta,\phi)|^2 J_1^2(|m\alpha_0|), \tag{2.79}$$

and the Saskatoon experiment [174] uses a double angle "cosine lock-in", where:

$$L(t) = \pi \cos(2\omega_c t)$$

$$L_m(\alpha_0) = \pi J_2(m\alpha_0). \tag{2.80}$$

In this case the window function is given by:

$$W_l = \pi^2 N^2 \frac{4\pi}{2l+1} B_l^2 \sum_{m=-l}^{l} |Y_{lm}(\theta,\phi)|^2 J_2^2(m\alpha_0). \tag{2.81}$$

The numerical factors in $L(t)$ are chosen such that:

$$\frac{\omega_c}{2\pi}\int_{-\pi/\omega_c}^{\pi/\omega_c}|L(t)|dt = 2.$$

The calculation of the normalization factor, N, is obtained as follows: for South-Pole (SP91) and MAX experiments one considers a sharp boundary between two regions at temperature T_1 and T_2 and N is such that, the temperature in the boundary obtained by chopping perpendicular to the boundary, is equal to $T_1 - T_2$. When $\sigma = 0$ one has that $N = 1$ and in this case the $L_m(\alpha_0)$ given by Equations (2.76), (2.78) and (2.80) is already normalized such that $N = 1$. So for the South-Pole experiment one has:

$$L_m(\alpha_0) = 2H_0(m\alpha_0) \tag{2.82}$$

and the window function is given by:

$$W_l = 4\frac{4\pi}{2l+1}B_l^2(\sigma)\sum_{m=-l}^{l}|Y_{lm}(\theta,\phi)|^2 H_0^2(m\alpha) \tag{2.83}$$

For the MAX experiment, considering $\alpha_0 = 0.65°$ and $\sigma = 0.425\times 0.5°$, one has that $N^2 = 1.13$. In order to have $L_m(\alpha_0)$ normalized, the numerical factor π should be replaced by $k = \sqrt{1.13}\times\pi = 3.34$, such that:

$$L_m(\alpha_0) = kJ_1(m\alpha_0) \tag{2.84}$$

and

$$W_l = k^2\frac{4\pi}{2l+1}B_l^2(\sigma)\sum_{m=-l}^{l}|Y_{lm}(\theta,\phi)|^2 J_1^2(|m\alpha_0|). \tag{2.85}$$

For Saskatoon with $\alpha_0 = 2.45°$ and $\sigma = 0.425\times 1.44°$ one has $N^2 = 1.74$, so as in the previous case in order to have $L_m(\alpha_0)$ normalized to $N = 1$ the numerical factor π should be substituted by $k = \sqrt{1.74}\times\pi = 4.14$, such that:

$$L_m(\alpha_0) = kJ_2(m\alpha_0) \tag{2.86}$$

and

$$W_l = k^2\frac{4\pi}{2l+1}B_l^2\sum_{m=-l}^{l}|Y_{lm}(\theta,\phi)|^2 J_2^2(m\alpha_0). \tag{2.87}$$

Other experiments use interferometry techniques (e.g., CAT [137]), where the window function is the UV-sampling convolved with the Fourier Transform of the primary beam and is usually given by the observers (see also Chapter 6). An easy way to parameterise the window functions is by using three numbers which represent the multipole at which the instrument achieves its maximum sensitivity, and the multipoles at which the sensitivity decreases by a factor 2 from the peak, these are given in Chapter 4 and Chapter 6. According to White and Srednicki [168, 50], the approximation of the South-Pole experiment by a 2-beam, gives a difference with respect to the exact window function of the order 20%; while for MAX it is of the order of 10%.

2.6 Statistical uncertainties

The theories predict only the statistics of the temperature fluctuations and ensemble average values, but not their value in our universe. The $C(\theta, \sigma)$ is a random variable with ensemble average value given by Equation (2.59). It may be expressed as:

$$C_{ran}(\theta, \sigma) = \frac{1}{4\pi} \sum_{l \geq 2} Q_l^2(x) P_l(\cos\theta) W_l(\sigma), \tag{2.88}$$

where all the quantities are as defined in Section 2.3 and 2.5. The cosmic variance, σ^2_{cos}, is defined in terms of $\mathrm{var}(Q_l^2)$ and represents an intrinsic limitation of the statistical description of the CMB fluctuations. As already mentioned in Section 2.3 this intrinsic cosmic variance is different for the different angular scales depending on the number of independent samples in the sky on those angular scales. The variance is therefore larger for large angular scales. Several authors have considered how this uncertainty affects the estimation of the ACF. Cayón et al. (1991) [28] obtained a semi-analytic expression for the probability density function, pdf, of the temperature autocorrelation, ACF:

$$f_z(t) = \frac{1}{2\pi} \int_{-\infty}^{+\infty} dx (\prod_{l=2} (1 - 2ix\bar{\sigma}_l)^{-(2l+1)/2}) \exp(-itx), \tag{2.89}$$

where Z is $C(\theta, \sigma)$, $\bar{\sigma}_l = (\sigma_l^2/4\pi) P_l(\cos\theta) \exp(-(l+1/2)^2\sigma^2)$ with $\sigma_l^2 = (4A)/(\pi l(l+1))$, where A is the amplitude of the initial power spectrum of the density fluctuations (see Section 2.7), here assumed to be of the form $P(k) = Ak$. This expression applies to a single beam experiment; for beam-switching experiments new variables Z_2, Z_3 are defined. The distribution function is defined using the same expression with the new $\bar{\sigma}_l$ defined according to the switching pattern. Scaramela & Vittorio (1990) [132] used the multipole expansion of the ACF and computed their distribution by Monte Carlo simulations. Alternatively Bond & Efstathiou (1987) [23, 56] derived an analytic expression to compute σ^2_{cos}, which is expressed in terms of the C_l:

$$\mathrm{var}(C(\theta)) = \frac{1}{2\pi^2} \sum_{l \geq 2} (2l+1) C_l^2 P_l^2 \tag{2.90}$$

Or in terms of the window function, W_l, of a given experiment:

$$\mathrm{var}(C_{conv}(0)) = \frac{1}{2\pi^2} \sum_{l \geq 2} (2l+1) C_l^2 W_l^2. \tag{2.91}$$

Small angular scale experiments have negligible cosmic variance, since in this case, ergodicity applies and ensemble average is well represented by the angular average over the sky. The problem is that if the observations sample only part of the sky, the number of independent samples in the sky at these angular scales will be reduced, this translates into an enhancement of the cosmic variance, called sample variance. Scott et al (1994) [135] derived an approximate relation between the sample variance (σ^2_{sam}) and the cosmic variance:

$$\sigma^2_{sam} \simeq \left(\frac{4\pi}{A}\right) \sigma^2_{cos} \tag{2.92}$$

where A is the solid angle covered by the experiment. The above methods are applied to experiments considering, e.g., their scan strategy, appropriate solid angle, etc. The sample variance may be obtained by computing the cosmic variance via Equations (2.89) or (2.91), or Monte Carlo simulations and then using the approximate relation given in Equation (2.92). We used a different approach, producing Monte Carlo simulations of the temperature fluctuations according to the specific characteristics of each experiment, such as the beamwidth, the sky coverage, the switching pattern, the beamthrow, etc. Proceeding in this way one computes directly the overall theoretical uncertainty for a given experiment. This method was of particular interest to us because we were concerned with the confrontation of frequentist with Bayesian techniques of data analysis (see Chapter 4). These simulations follow different strategies according to angular scale and experimental configuration. This is described in more detail in Chapter 4.

2.7 Angular power spectrum

Having discussed the effects of particular experimental arrangements we now discuss the form of the power spectrum itself. The description of the CMB anisotropy in terms of the angular power spectrum, C_l, has proved to be an invaluable method and has become a standard procedure for treatment of the temperature fluctuations of the CMB radiation. The competing models for the origin and evolution of structure, for example [23, 81] predict the shape and amplitude of the CMB power spectrum and its Fourier equivalent, the autocorrelation function $C(\theta)$.

2.7.1 Power spectrum normalization

The galaxy clustering normalization: σ_8

The quantity, σ_8 , is the dispersion of the density field in a sphere of radius $8h^{-1}$Mpc, (see Section 2.2.5). The observed quantity is the variance of counts of galaxies in spheres of the size $8h^{-1}$Mpc, $\sigma_8(galaxies)$ which is related with the corresponding variance but in terms of mass, $\sigma_8(mass)$ via the bias parameter, b:

$$b^2 = \frac{\sigma_8^2(galaxies)}{\sigma_8^2(mass)}. \tag{2.93}$$

It is an observational result that $\sigma_8(galaxies) \simeq 1$ [80], this being so, one has:

$$b \simeq 1/\sigma_8(mass). \tag{2.94}$$

Previous to the COBE detection the most common normalization of models used was based on the value of σ_8 , derived from galaxy clustering assuming a bias $b = 1$ *i.e.* that light traces mass [86, 40]. If in fact galaxies are more highly clustered than matter [40, 11], the amplitude of the initial matter perturbations (and hence $\Delta T_{rms}/T$) necessary to produce the observed clustering is reduced by the factor b. The power on large scales depends on this normalization and therefore depends on the Hubble constant, h, ($h = \mathrm{H}_0/100\,\mathrm{km\,s^{-1}\,Mpc^{-1}}$). It also depends on $\Omega_0 h^2$, the quantity determining the deflection point of the power spectrum, where Ω_0 is the ratio of the total density of the universe to the critical density, for simplicty hereafter referred as to the total density of the universe. The relevant quantity related with this normalization is the amplitude of baryonic fluctuations necessary at recombination in order to obtain the fluctuations we see today. This amplitude lowers if the growth factor increases consequently lowering the normalization of the temperature fluctuations. This effect may be obtained, e.g., varying the value of the total density of the universe, Ω_0 or, e.g., considering non-baryonic dark matter. For example the lower the value of Ω_0 the lower the fluctuation growth therefore the larger the normalization of $\Delta T/T$. The non-baryonic dark matter increases the growth of fluctuations, for instance in cold dark matter (CDM) models the CDM perturbations have an extra growth between the epoch of matter-radiation equality and the end of recombination $\propto \Omega_0 h^2$ as compared to the baryonic perturbations. When baryons decouple at the end of recombination they fall into the potential wells of the non-baryonic dark matter and increase their amplitude to match the CDM perturbations. A flat model with non-zero cosmological constant, Λ, has a reduced growth factor when compared with a flat model with zero Λ. On the other hand for the same Ω_0 and same Ω_b increasing the Λ component increments the growth of perturbations. There is also a dependence on the geometry of the universe via the angle-distance relation which affects the value of $\Delta T/T$ observed. This normalization is not ideal since it depends on the processing of the power spectrum of fluctuations and on the relationship between the structure we observe and the underlying density field.

COBE-normalization

Since the detections of CMB anisotropy other normalizations have been adopted. On scales $\gtrsim$ few degrees, CMB observations probe scales of 1000's of Mpc, inaccessible to other means of measuring large-scale structure such as redshift surveys or galaxy counts. At these large angles, the structures form part of an intrinsic spectrum of fluctuations generated through topological defects or inflation. In this linear growth regime, observations of the scalar CMB fluctuations provide a clean measure of the normalisation of the intrinsic fluctuation power spectrum. This normalisation has been established by a number of independent CMB observations [144, 62, 75]. Since the COBE detection [144] it became common procedure to consider the models COBE-normalised. This normalization is usually given in terms of the quadrupole term, C_2 or equivalently quoted in terms of the Q_{rms-ps} where:

$$Q_{rms-ps} = T\sqrt{\frac{5C_2}{4\pi}}, \tag{2.95}$$

where $T = 2.736°\mathrm{K}$. This quantity is obtained by fitting a given model to the COBE data, according to several techniques [65, 66, 153, 21, 26, 14, 175], etc. The relationship between this and the previous normalization is given by:

$$C_2 \simeq \frac{\pi}{3}\left(\frac{\mathrm{H}_0 R}{c}\right)^4 \left(\frac{\delta M}{M}\right)^2_R, \tag{2.96}$$

(Coles, 1995 [34]), where $\delta M/M = \sigma_M$ is the mass fluctuation observed at the present epoch on a scale R, and is σ_8 when $R = 8h^{-1}$Mpc .

2.7.2 The shape of the power spectrum

Doppler peaks

Contemporary cosmological models with adiabatic fluctuations predict a sequence of peaks on the power spectrum which are generated by acoustic oscillations of the photon-baryon fluid at recombination. Photon pressure resists compression of the fluid by gravitational infall and sets up acoustic oscillations. The fluctuations as a function of k go as $\cos(kc_s\eta_*)$ at last scattering, where k is the wavenumber of the fluctuation, c_s is the sound speed and η_* is the conformal time at recombination. This will produce a harmonic series of temperature fluctuation peaks, as shown in Fig. 2.1 and 2.2, with the mth peak corresponding to $k_m = m\pi/c_s\eta_*$. The critical scale is essentially the sound horizon $c_s\eta_*$ at last scattering [150, 81, 82]. Of particular interest is the height and position of the main acoustic peak — the so called Doppler peak. The height depends on quantities like the baryonic content of the universe, Ω_b, and Hubble constant, H_0, whilst the position depends on the total density of the universe, Ω_0 and is expected to occur on an angular scale $\sim 1°$. The precise form of the Doppler peak depends on the nature of the dark matter, and the values of Ω_0, Ω_b and H_0. The scale l_p of the main peak reflects the size of the horizon at last scattering of the CMB photons and thus depends almost entirely [81, 87] on the total density of the universe according to $l_p \propto 1/\sqrt{\Omega}$. This relation comes from the conversion of a spatial fluctuation on a distant surface to an anisotropy on the sky. This conversion involves the spectrum of spatial fluctuations, the distance to the surface of their generation and the curvature (or lensing in light propagation to the observer). The most important effect is due to the background curvature of the universe, e.g. for an open universe a given scale subtends a smaller angle on the sky than in the flat universe, due to the fact that photons curve in their geodesics. In a ΛCDM universe (CDM model with $\Lambda \neq 0$) this main peak is located at around $l \sim 220$, approximately at the same scale as in a flat CDM model, with a small dependence on Ω_0 and h [102]. In conventional inflationary theory [72], one expects the universe to be flat with $\Omega = 1.0$, which can be achieved if the total mass density is equivalent to the critical density or if there is a contribution from a cosmological constant Λ in the right amount. The height of the peak provides additional cosmological information since it is directly proportional to the fractional mass in baryons Ω_b and also varies according to the expansion rate of the universe as specified by the Hubble constant H_0; in general [81] for baryon fractions $\Omega_b \lesssim 0.05$, increasing H_0 reduces the peak height whilst the converse is true at higher baryon densities.

In the case of topological defect models there is also a sequence of peaks on the power spectrum for the texture model, while for the cosmic strings model only the main Doppler peak is present with no existence of the secondary peaks [109], as shown on the right hand side of Fig. 2.2; although the situation is not entirely clear yet.

Damped tail

At higher l a damping of the fluctuations occurs due to imperfect coupling of photons and baryons. The photons possess a mean free path in the baryons, λ_c, due to Compton scattering. Assuming a standard recombination history, the damping length approximately scales as $\lambda_D(\eta_*) \propto \eta^{\frac{1}{2}}(\Omega_b h^2)^{-\frac{1}{4}}$.

Sachs-Wolfe effect

The low l region of the power spectrum is mainly contributed by the potential fluctuations in the last scattering surface, the so called Sachs-Wolfe effect [129] . This efect corresponds to red shifting of the photon as it climbs out of the potential well on the surface of the last scattering, but also to a time dilation effect which makes as to see them at a different time to unperturbed photons [34, 56]. Its expression is given by:

$$\left(\frac{\Delta T}{T}\right)_{sw} = \frac{1}{3}\frac{\delta\phi}{c^2} \tag{2.97}$$

where $\delta\phi$ is the perturbations to the graviational potential and c is the speed of light. For flat ($\Omega = 1$) scale invariant ($n = 1$) models with no contribution from a cosmological constant this effect gives rise to a flat power spectrum, i.e., $l(l+1)C_l$ =constant, where the quantity $l(l+1)C_l$ is the power of the fluctuations per logarithmic interval in l. Its shape is altered if one assumes a tilted initial power spectrum with a power law, $P(k) = Ak^n$ or if one incorporates a cosmological constant, or assumes other than flat models. In the last two cases another source of anisotropy appears, the so-called integrated Sachs-Wolfe effect and is due to the fact that potential fluctuations are no longer time independent.

An ilustration of the CMB anisotropy spectrum is given in Fig. 2.1. The angular power spectrum for several models is plotted in Fig. 2.2; on the left hand side for inflationary models: a standard CDM model, an open model and a Λ model, and on the right hand side the same standard CDM model is compared with topological defect models: a cosmic string model and a texture model.

2.7.3 Calculation of the C_l's

Theoretical calculation of the CMB anisotropies are based on linear theory of cosmological perturbations. Most of these calculations solve the Boltzmann equation using Legendre expansion of the photon distribution function. This method expands each Fourier mode of temperature anisotropy in Legendre series up to some l_{max}. This system of equations is then numerically evolved in time from the radiation dominated epoch until today. These theoretical calculations were first developed by

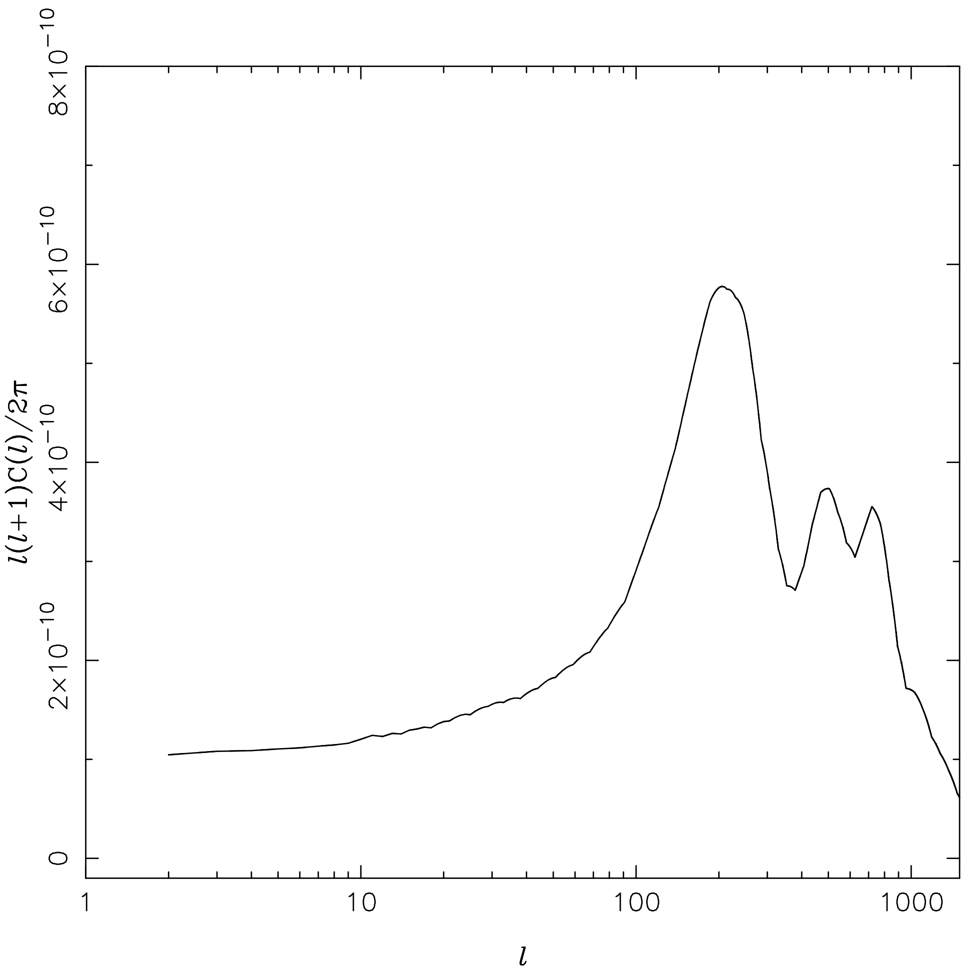

Figure 2.1: The angular power spectrum for a standard CDM model with $\Omega = 1$, $\Omega_b = 0.05$, $\mathrm{H}_0 = 50\,\mathrm{km\,s^{-1}\,Mpc^{-1}}$ and $n = 1$. The high l region of the power spectrum exhibits the sequence of peaks generated by acoustic oscillations of the photon-baryon fluid at recombination while the plateau in the low l region is mainly due to the Sachs-Wolfe effect. At higher l we observe a damping of the fluctuations due to imperfect coupling of photons and baryons.

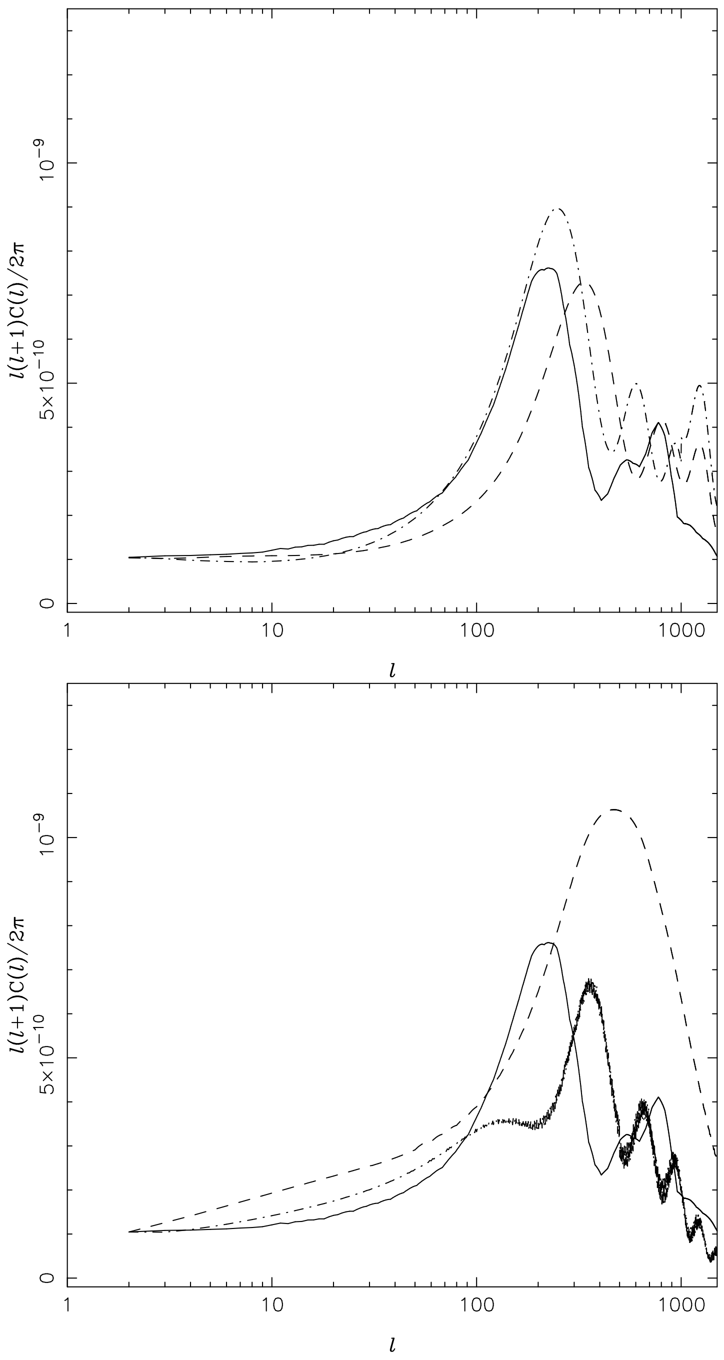

Figure 2.2: The angular power spectrum for several models. Top: for an $\Omega = 1$, $\Omega_b = 0.10$, $\mathrm{H}_0 = 50\,\mathrm{km\,s^{-1}\,Mpc^{-1}}$ standard CDM model (bold line), an $\Omega = 0.5$, $\Omega_b = 0.06$, $\mathrm{H}_0 = 50\,\mathrm{km\,s^{-1}\,Mpc^{-1}}$ open model (dashed line), a flat $\Omega = 0.3$, $\Omega_\Lambda = 0.7$, $\Omega_b = 0.05$, $\mathrm{H}_0 = 50\,\mathrm{km\,s^{-1}\,Mpc^{-1}}$ model (dot-dash line). Bottom: the same standard CDM model of top plot, compared with an example cosmic string model (dashed line) and an $\Omega = 1$, $\Omega_b = 0.05$, $\mathrm{H}_0 = 50\,\mathrm{km\,s^{-1}\,Mpc^{-1}}$ texture model (dot-dash line).

Lifshitz (1946) [103], while Peebles and Yu (1970) [118] applied these calculations to the CMB anisotropies, considering only photons and baryons. Later other authors included e.g. dark matter (Bond & Efstathiou 1984 [22], 1987 [23], Vittorio & Silk 1984 [160]), curvature (Wilson& Silk 1981 [173], Sugiyama & Gouda 1992 [151], White& Scott 1995 [171]), tensor modes or gravitational waves (Crittenden *et al.* 1993 [38]) and massive neutrinos (Bond & Szalay 1983 [24], Ma & Bertschinger 1995 [107], Dodelson, Gates & Stebbins 1995 [51]). Other calculations have been done e.g. by Holtzman 1989 [80], Sugiyama 1995 [150], Wayne & Sugiyama 1995 [81] which used an analytic approach, Stompor 1994 [148], Seljac & Zaldarriaga 1996 [138] which method is based on integration over sources along the photon past light cone).

The multipole coefficients C_l's may be obtained, for example, using the solutions to the equations describing temperature fluctuations evolution by [23, 56]:

$$C_l = \frac{V_x}{8\pi}\int_0^\infty k^2 dk|\Delta_{Tl}(k,\tau_0)|^2, \tag{2.98}$$

where $\Delta_{Tl}(k,\tau_0)$ are the coefficients of the Legendre polynomials expansion of, $\Delta_T(k,\tau_0)$, the radiation intensity fluctuations, τ is the conformal time $\int dt/a(t)$ where $a(t)$ is the cosmological factor, and k is the wavenumber of the Fourier mode. In particular in the case of large angular scales for $\Omega = 1$ and an initial power-law form of the density fluctuations power spectrum $P(k) \propto k^n$, an expression for the $C_l(n)$ may be used:

$$C_l = C_2\frac{\Gamma(l+(n-1)/2)\Gamma((9-n)/2)}{\Gamma(l+(5-n)/2)\Gamma((3+n)/2)} \tag{2.99}$$

with $n < 3$, $l \geq 2$, $l < 40$ [23, 56, 131]. This expression is only adequate for experiments probing angular scales larger than the horizon size at recombination ($\geq 1°$) where only Sachs-Wolfe or isocurvature effects are dominant.

For small angular scales, with $l >> k\tau_{rec}$, $k\tau_0 >> 1$ and $l >> 1$, a useful approximation to C_l is [23, 56]:

$$C_l \sim \frac{V_x}{8\pi}\int_{l/\tau_0}^\infty \frac{k^2 dk}{2k\tau_0\left[(k\tau_0^2 - l^2)\right]^{1/2}} W_T^2(0,k), \tag{2.100}$$

and for $k\tau_{rec} >> 1$ the contribution from a 3D plane wave in the sky is sigificant when seen in a direction perpendicular to the wave vector, in this case one has

$$l^2 C_l \sim \frac{V_x}{16\pi}k^3 W_T^2(0,k), \quad k = l/\tau_0, \tag{2.101}$$

where τ_{rec} is the conformal time at recombination and W_T is

$$W_T^2(\theta,k) = \sum_{l\geq 2}(2l+1)|\Delta_{Tl}(k,\tau_0|^2 P_l(\cos\theta),$$

C_l is in this way describable in terms of a transfer function $\propto W_T$.

In order to get the C_l's for smaller angular scales we made use of an alternative method; this consists of using the expression of the expected temperature autocorrelation function and the orthogonality property of the Legendre polynomials, which generates C_l for all angular scales:

$$C_l = 2\pi \int_0^\pi C(\theta) P_l(\cos\theta) \sin\theta d\theta. \tag{2.102}$$

We have applied this method to the models proposed by Bond & Efstathiou, 1987 (BE87) [23] models using the fitting parameter expression of the $C(\theta)$:

$$C(\theta) = \frac{A\exp(-(\theta/\theta_1)^2)}{(1+(\theta/\theta_2)^2+(\theta/\theta_3)^4)^\chi} + \frac{3a_2^2}{\pi}\left(\tfrac{1}{2}\ln(1+4/\theta_4^2) - \tfrac{1}{2} - \tfrac{1}{8}\ln(1+(\bar{\omega}/\theta_4)^8) - \tfrac{3}{4}\cos\theta\right), \tag{2.103}$$

where $\bar{\omega} = 2\sin(\theta/2)$ and A, a_2, θ_1, θ_2, θ_3, θ_4, χ are tabulated for each model in Bond & Efstathiou, 1987 [23]). Inserting 2.103 in 2.102 and computing the integral one obtains the C_l. We found good agreement with the C_l obtained by numerical integration of the equations representing the temperature fluctuation evolution and plotted in BE87 [23]. This method was also checked by calculation of $(\Delta T/T)_{rms}$ using both (2.54) and the C_l technique. As an illustration in Fig. 2.3 it is plotted the angular correlation function and the angular power spectrum obtained using Equation 2.102; it shows the agreement with the plots in BE87 [23].

In the last couple of years various groups have been producing their own CMB codes to generate the C_l's according to different approaches (G. Efstathiou, N. Sugiyama, U. Seljac and M. Zaldarriaga, M. White etc...) which are now publicly available.

2.8 Likelihood analysis

A most commonly used statistical technique to analyse the data is the Bayesian 'likelihood function' analysis [15, 75, 97], which we will describe in this section. This analysis permits one to use the correlation information existing in the data and to deconvolve the switching correlations allowing one to test directly a given sky temperature fluctuation model. In order to apply this analysis one assumes a given structure formation model and considers its predicted power spectrum which defines the intrinsic angular correlation function:

$$C_{int}(\theta) = \left\langle \frac{\Delta T}{T}(\vec{n_1})\frac{\Delta T}{T}(\vec{n_2})\right\rangle, \tag{2.104}$$

where $\vec{n_1}$, $\vec{n_2}$ are two directions on the sky such that: $\vec{n_1}.\vec{n_2}$=cos(θ). This relates with the autocorrelation function of the observations by:

$$C_{obs}(\theta) = \left\langle \frac{\Delta T^{obs}}{T}(\vec{n_1})\frac{\Delta T^{obs}}{T}(\vec{n_2})\right\rangle, \tag{2.105}$$

which is equal to $C_{int}(\theta)\star C_{beam}(\theta)$ where $\star$ refers to convolution and $C_{beam}(\theta)$ is the autocorrelation function of the beam of the telescope. (see also Section 2.5). For example for the Tenerife experiment the measured quantities are second differences in temperature. The ACF measured between two points on the sky i and j with coordinates (α, δ) and (α', δ') (in RA and dec), M_{ij}, is defined by:

$$M_{ij} = \left\langle \left(\frac{\Delta T}{T}\right)_i^{obs} \left(\frac{\Delta T}{T}\right)_j^{obs} \right\rangle . \tag{2.106}$$

These are components of a matrix (M_{ij}) called the covariance matrix which in particular contains information about the beam switching as follows:

$$\begin{aligned} M_{ij} \;=\; & \left\langle \left(\frac{\Delta T^g}{T}(\alpha,\delta) - \tfrac{1}{2}\left(\frac{\Delta T^g}{T}(\alpha_e,\delta_e) + \frac{\Delta T^g}{T}(\alpha_w,\delta_w) \right)\right) \right. \\ & \left. \left(\frac{\Delta T^g}{T}(\alpha',\delta') - \tfrac{1}{2}\left(\frac{\Delta T^g}{T}(\alpha'_e,\delta'_e) + \frac{\Delta T^g}{T}(\alpha'_w,\delta'_w) \right)\right) \right\rangle , \end{aligned} \tag{2.107}$$

where α_e, δ_e and α_w,δ_w are the right ascension RA and declination of the East and West beamthrow positions, and $\frac{\Delta T^g}{T}$ is the temperature fluctuation after convolution in the Gaussian beam pattern from a single antenna. For a small beamthrow θ_b, $\delta_e \simeq \delta \simeq \delta_w$, such that

$$\alpha_e = \alpha + \left(\frac{\theta_b}{\cos\delta}\right) \text{ and } \alpha_{\mathrm{w}} = \alpha - \left(\frac{\theta_{\mathrm{b}}}{\cos\delta}\right). \tag{2.108}$$

M_{ij} can be expressed in terms of the ACF of the intrinsic fluctuations after convolution in a single Gaussian beam (see also Section 2.9) i.e.

$$\left\langle \frac{\Delta T^g}{T}(\alpha,\delta), \frac{\Delta T^g}{T}(\alpha',\delta') \right\rangle = C_g(\theta), \tag{2.109}$$

where θ is the angle between the coordinates (α, δ) and (α', δ') which is given by:

$$\theta = \cos^{-1}\left(\sin\delta\sin\delta' + \cos\delta\cos\delta'\cos(\alpha-\alpha')\right). \tag{2.110}$$

For a given model of the intrinsic ACF, C_{int}, one can obtain the C_g (e.g. Section 2.9) and fully define the covariance matrix M_{ij}. For observations at the same declination, M_{ij}, can be expressed in terms of C_g as defined by Equation 2.109, by:

$$M_{ij} = \tfrac{3}{2}\, C_g(\theta) - C_g(\theta+\theta_b) - C_g(\theta-\theta_b) + \tfrac{1}{4}\, C_g(\theta+2\theta_b) + \tfrac{1}{4}\, C_g(\theta-2\theta_b), \tag{2.111}$$

where θ is the angle on the sky between points i and j; θ_b is the switch angle between horns. Adding to (M_{ij}) the covariance matrix for the errors (E_{ij}) one obtains the total covariance matrix V_{ij}=M_{ij}+E_{ij}. For Gaussian-distributed fluctuations the likelihood function for the total covariance matrix V_{ij}, is

$$L(\Delta\, T|C_{int}(\theta)) = \frac{1}{(2\pi)^{\frac{N}{2}}\sqrt{|V|}} \exp(-\frac{1}{2}\Delta\, T^T V^{-1} \Delta\, T). \tag{2.112}$$

which expresses the probability of obtaining the data set $\Delta T = (\Delta T_1, \ldots, \Delta T_n)$ given some intrinsic autocorrelation function C_{int}. The analysis proceeds calculating different values of $C_{int}(\theta)$ by varying the parameters of the model and evaluating the respective likelihood. Searching for the maximum value of the likelihood function the most probable parameters of the model are obtained. Considering e.g. the variation of the amplitude parameter of the sky fluctuation model, two things can happen: the point of maximum can be different or equal to zero. In the first case one has a detection of fluctuations, in the second a monotonically decreasing function is obtained and there is not a detection of fluctuations in the data. The next step consists in evaluating the likelihood ratio L_{max}/L_0 where L_0 is the likelihood evaluated at zero. This ratio gives an idea of how representative the maximum value of the likelihood function is. The upper and lower limits on the amplitude $\sqrt{C(0)}$ of the fluctuations are obtained invoking Bayes theorem:

$$P(\sqrt{C(0)}|\Delta T) \propto L(\Delta\, T|\sqrt{C(0)})P(\sqrt{C(0)}), \tag{2.113}$$

where $P(\sqrt{C(0)}|\Delta T)$ is the posterior probability (of obtaining the intrinsic sky fluctuations given the observed data set); $L(\Delta T|\sqrt{C(0)})$ is the likelihood (of obtaining the data set given the intrinsic sky fluctuations) and $P(\sqrt{C(0)})$ is the prior probability. Once the form to give to the prior probability is known we are able to know the probability of obtaining the amplitude of the intrinsic sky fluctuations given the observed data set. Some Bayesians use the Jeffreys prior, uniform in $\log(A)$ space i.e.

$$Pr(A) = \frac{1}{(A)}. \tag{2.114}$$

This is based on the idea that when there is no prior information available, invariance arguments imply that the prior probability density of a scale factor parameter, A, (which C_0 is) should be uniform in $1/A$. This poses a problem because when $A \to 0$ the $Pr(A) \to \infty$ and the posterior probability cannot be normalized. The solution could consist in considering a cutoff at low A. Instead we have just assumed a uniform prior such that: P($\sqrt{C(0)}$)=1 for $\sqrt{C(0)} \geq 0$ and P($\sqrt{C(0)}$)=0 for $\sqrt{C(0)} < 0$. In this way, the area under the likelihood curve between 0 and $\sqrt{C(0)}$ gives the probability of obtaining $\sqrt{C(0)}$. So looking for the value of $\sqrt{C(0)}$ such that this area is 95% of the total area one obtains a 95% upper limit. In a similar way one calculates the 95% lower limit to the intrinsic sky fluctuations. In a similar way, the 68% upper and lower limits to the detected fluctuation amplitude are obtained by integrating down from the peak of the likelihood curve at plateaus of equal likelihood, until the area under the curve delimited by the upper and lower values is equal to 68 % of the total area under the likelihood curve.

2.9 The Gaussian auto-correlation function

At an earlier point in CMB work, the Gaussian auto-correlation function (GACF) was the tool most frequently used to describe an hypothetical sky model, and originally was intended to be used for small scales [162, 170]. This representation is not physically realistic but is useful for comparison of the results from different experiments. In the GACF model we assume that the intrinsic autocorrelation function is a Gaussian of amplitude C_0 and dispersion θ_c:

$$C(\theta) = C_0 \exp\left(-\frac{\theta^2}{2\theta_c^2}\right), \tag{2.115}$$

even for more general autocorrelation functions is useful to define, θ_c, by:

$$\theta_c = \left(-\frac{C(0)}{C''(0)}\right)^{1/2} \tag{2.116}$$

$\sqrt{C_0}$ then gives an indication of the *rms* amplitude of the intrinsic fluctuation on some coherence scale defined by θ_c. In the angular power spectrum language, this corresponds to considering C_l to be expressed by [170]:

$$C_l = 2\pi C_0 \theta_c^2 \exp(-\frac{1}{2} l(l+1)\theta_c^2) \tag{2.117}$$

The form of the autocorrelation function after convolution with the beam from a single instrument horn, assumed to be a Gaussian, is given by the convolution of the intrinsic autocorrelation function, C_{int}, with the beam autocorrelation function, C_{beam}:

$$C(\theta, \sigma) = C_{int}(\theta) \star C_{beam}(\theta), \tag{2.118}$$

where C_{int} is given by Equation (2.115) and C_{beam}, in this case, is given by:

$$C_{beam}(\theta) = B(\theta) \star B(\theta) = \frac{1}{4\pi\sigma^2} \exp\left(-\frac{\theta^2}{4\sigma^2}\right). \tag{2.119}$$

where $B(\theta)$ is the beamshape for a single antenna. Equation (2.118) then becomes:

$$C(\theta, \sigma) = \frac{C_0 \theta_c^2}{2\sigma^2 + \theta_c^2} \exp\left(\frac{-\theta^2}{2(2\sigma^2 + \theta_c^2)}\right). \tag{2.120}$$

Experiments observing the same intrinsic sky fluctuation do not, in general, measure the same rms signal level because this signal depends on the observational strategy. This rms signal can only be interpreted if accompanied by information about the window function of the observation. In a GACF analysis we assume a power spectrum with a Gaussian shape and take into account the peak and area of the window function. This model is a good approximation for an experiment where the power spectrum is smooth and the window function can be considered to be a Gaussian, because the two convolved spectra are very similar, in which case the quoted C_0 gives a measure of the intrinsic sky fluctuation. The sensitivity of an experiment to fluctuations on various scales is commonly described by a plot of C_0 vs θ_c, assuming that the sky correlation function is a GACF. The experiment is most sensitive to a GACF which peaks at the maximum of its window function, and the amplitude of fluctuations to which the experiment is sensitive is parameterized by the minimum value of C_0.

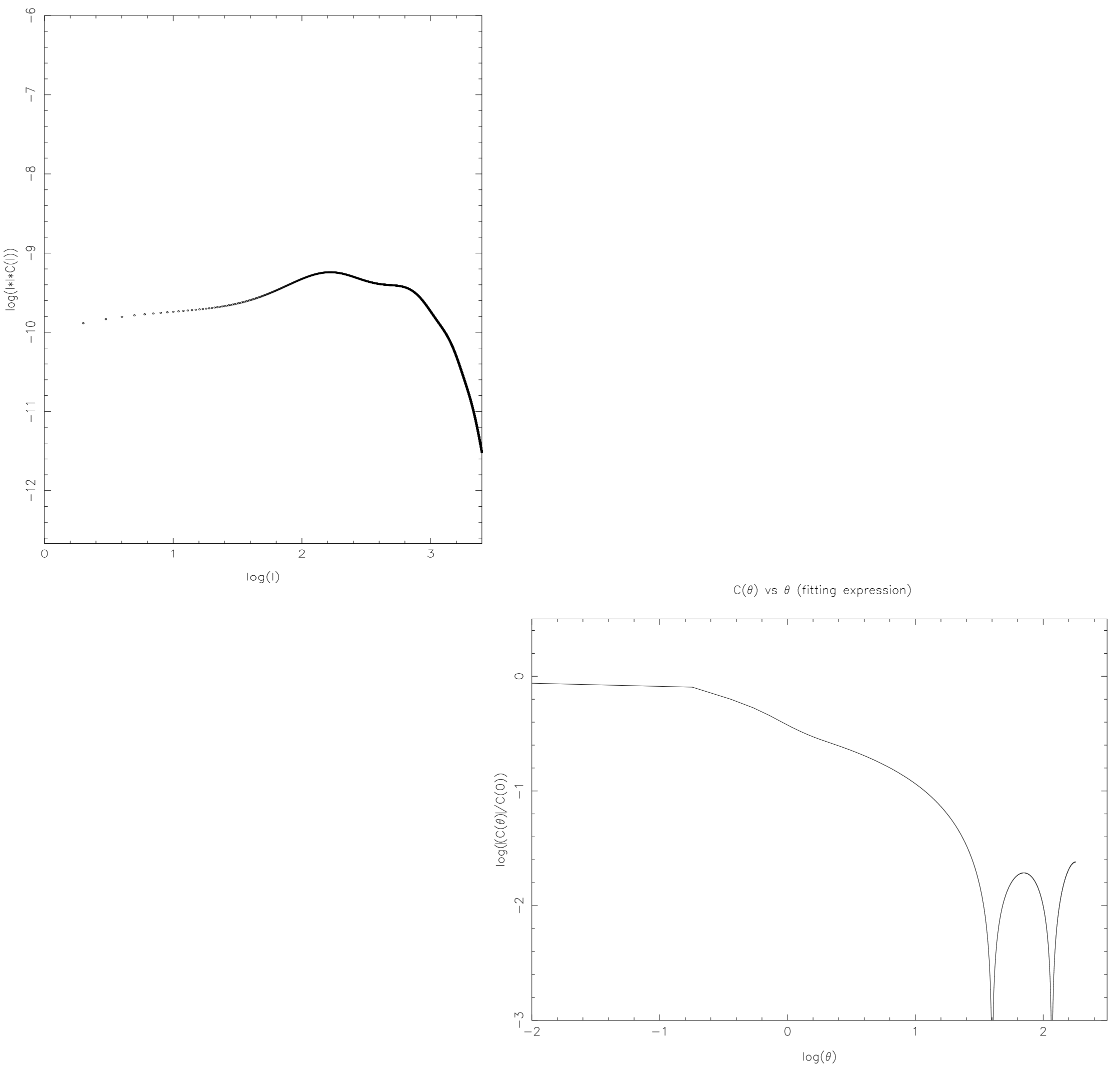

Figure 2.3: The angular power spectrum for a CDM model, with $H_0 = 75\,\mathrm{km\,s^{-1}\,Mpc^{-1}}$ and $\Omega_b = 0.03$, as obtained using Equation (2.102) (left). On the right hand side is plotted the corresponding angular correlation function.

2.10 Conclusions

In later chapters we test the concepts here defined using the mathematical tools described; we intended to find possible solutions to the problem of origin of structure in our Universe using the current CMB data.

Chapter 3

The experiments

3.1 Introduction

This Chapter gives an account of the current experimental status, describing the various observational strategies and giving the results of several experiments. Usually the experiments are classified according to the angular scales they probe. The usual classification considers large angular scales as being angles larger than the horizon size at recombination i.e. $\theta \gtrsim 2^\circ$; medium scales comprehends the range $10' \lesssim \theta \lesssim 2^\circ$ and covers the region of the Doppler peaks; small scales lie in the range $1' \lesssim \theta \lesssim 10'$ and very small scales for $\theta \lesssim 1'$. However in Chapter 4 we refer to all experiments that observe on scales $\theta < 2^\circ$ as small angular scales experiments, in order to describe the different techniques used in their simulations. When analysing the data from CMB anisotropy experiments one must take into account contaminants like free-free and synchroton radiation from the Galaxy which are dominant at low frequencies ($\simeq$ 10-50 GHz) and dust at higher frequencies ($\geq$ 100 GHz) [98]. These are plotted in Fig 3.1. Another source of contamination is the possibility of discrete source contamination [98]. The main parameters of several recent experiments are displayed in Table 3.1. Some of the text of this Chapter is based upon previously published reviews by Lasenby and Hancock but has been updated and enlarged for recent experiments and new information.

3.2 Foreground emission

3.2.1 Diffuse Galactic emission

A detailed study of the diffuse Galactic emission has been done at low frequencies ($38 \lesssim \nu \lesssim 1420$ MHz), using radio telescopes [100] and at the higher frequencies of 60μm and $100\mu m$ using the IRAS satellite. The FIRAS and DMR instruments on board of the COBE satellite provided further information on the Galactic emission on 7° scales. In the microwave regime the emission from our Galaxy is composed of

Figure 3.1: Estimates of the amplitudes of the anisotropic component of foreground emission (Anthony Lasenby private communication). As a reference, a typical 10 μK CMB signal is shown.

synchroton emission from cosmic ray electrons, free-free (bremsstrahlung) radiation from thermal electrons and thermal emission from dust. Fig. 3.1 shows estimates (Lasenby priv. comm.) of the relative antenna temperature contributions expected from each of these diffuse Galactic foregrounds, as a function of observing frequency ν. It represents the anisotropic component of the emission at high Galactic latitude ($|b| \geq 40°$). The CMB radiation has a Planckian spectral form:

$$\Delta T_A = f(\nu)\Delta T = \frac{\Delta T x^2 e^x}{(e^x - 1)^2}, \tag{3.1}$$

where $x = h\nu/kT$ and ΔT_A is the antenna temperature contribution from a black-body temperature ΔT. The spectra of the foreground emission can be given by the relation $T_A = \nu^{-\beta}$, where β is the temperature spectral index. The different frequency spectral signatures of these components allow their discrimination via observations at several frequency ranges.

The synchroton radiation is the dominant Galactic component at $\nu \lesssim 30$ GHz, which results from relativistic electrons spiralling in the magnetic field of the Galaxy. Assuming that the number density of the electrons is of the form $N(E) \propto E^{-\gamma}$, $\beta = (\gamma + 3)/2$, the intensity of synchroton radiation, $I(\nu)$, is given by:

$$I(\nu) \propto B^{\beta - 1} \nu^{2-\beta}, \tag{3.2}$$

where B is the magnetic flux density, and β is the temperature spectral index. The spectrum steepens from $\beta \simeq 2.75$ at 1 GHz to $\beta \simeq 2.9$ at 15 GHz, due to increased loss of energy by electrons at higher energies. A spatial variation of β is expected as a consequence of the spatial variation of the magnetic field [5]. So the modeling of this foreground involves the steepening of the spectrum with frequency and the spatial dependence of the frequency spectral index β. The low frequency surveys can be used to extrapolate (see also Banday and Wolfendale 1991 [7]) the synchroton component to other frequencies. There are low frequency surveys conducted at 408 MHz [77], 820 MHz [16], and 1420 MHz [124]. The 408 MHz is an all-sky survey while the 1420 MHz covers only the declination range $-19° < \delta < 90°$. Given the frequency range probed by these surveys it is difficult to estimate the spectral steepening at higher frequencies. Bennet *et al.* [12] made an attempt to account for the steepening by assuming that the spectrum of the local electrons reflects that of the electrons producing the observed synchroton emission.

The free-free emission is also a problem at $\nu < 50$ GHz and possibly higher as well. Free-free emission (bremsstrahlung) results from the acceleration of electrons (when they interact with the warm ionized component of the Galaxy) in the electric field of the ions. Its spectral index is a weak function of frequency [12] and is given by:

$$\beta_{ff} = 2 + \frac{1}{10.48 + 1.5 \ln(T_e/8000\mathrm{K}) - \ln \nu(\mathrm{GHz})}, \tag{3.3}$$

where T_e is the electron temperature and $\beta \simeq 2.1$ at the Tenerife experiment frequencies. This component of emission is large within the Galactic plane, but at $\nu \lesssim 15$ GHz and at high Galactic latitude it is expected to be much lower than the synchroton emission. It is thought that the free-free emission reaches $\simeq$ the same level of the synchroton at frequencies $\simeq$ 20-30 GHz, and to be larger for higher frequencies, although the accurate amplitude of this Galactic foreground is not yet well understood.

At higher frequencies, larger than $\simeq$ 100 GHz, the contribution to foreground emission comes from the Galactic dust emission. The modeling of this foreground is difficult because it requires the knowledge of the temperatures, emissivities and spatial distributions of the dust grains in the Galaxy. Before the publication of COBE data, Banday and Wolfendale 1991 [6] concluded that IRAS observations provided useful information at high frequencies but its extrapolation for frequencies where the CMB is observable is difficult given the uncertainties in the dust model. Bennet *et al.* 1992 [12], using empirical fits to the COBE FIRAS data estimated the dust contribution to the COBE observing frequencies and found that the *rms* dust signal was less than 8 μK at 90 GHz.

Dust emission increases with increasing frequency with a spectral index $\beta \simeq -1.5$.

3.2.2 Discrete source emission

Another source of contamination of CMB observations is the discrete source emission. Most of these sources have a flat or falling spectra such that their flux decreases with increasing frequency. The identification of the brightest sources at low frequencies is made using the existing catalogues, but in some cases it is necessary to use separate high resolution surveys. The antenna temperature contribution for a source of flux, S, in a single beam is given by:

$$T_A = \frac{A_{eff} S}{2k}, \tag{3.4}$$

where

$$A_{eff} = \pi \left(\frac{c}{2\nu\theta_{\rm FWHM}} \right)^2, \tag{3.5}$$

is the effective area of a single beam. Even for a flat spectrum i.e. $S \propto \nu^0$, T_A decreases with frequency as ν^2, and is inversely proportional to the square of the beamwidth. On scales $\theta < 0.5^\circ$ at $\nu < 20$ GHz, the foreground radio sources are important contaminants of CMB observations. Franceschini *et al.* [59] concluded that for $\theta < 1^\circ$ and 20 GHz$\leq \nu \leq$200 GHz the contribution to $\Delta T/T$ is just below 10^{-5}. The Kuhr *et al.* catalogue [90] of radio sources provides information about surveys ranging in frequency from 26 to 90 GHz.

3.2.3 Atmospheric emission

Atmospheric emission causes serious problems to CMB observations. Water vapour emission lines dominate at 22 and 182 GHz, while oxygen line emission is significant at 60 and 118 GHz. These emission lines define the range of frequencies of the atmospheric windows through which CMB observations can be made. Experiences with

Experiment	Institution	Type	Beamwidth/ Beamthrow (°)	ν (GHz)
DMR-COBE	NASA	Satellite	7	31, 53, 90
Tenerife	NRAL/MRAO/IAC	Ground	5/8	10, 15, 33
MIT/FIRS	GSFC/Chicago/...	Balloon	3.8	180 +3 higher
ACME/HEMT	UCSB	Ground	1.5/2.1	30/40
MAX	Berkeley/UCSB	Balloon	0.5/1.0	110, 180, 270, 360
MSAM	GSFC/Chicago/...	Balloon	0.5/0.6	180 + 3 higher
White dish	CARA	Ground	0.18/0.47	90
Python	CARA	Ground	0.75/2.75	90
Saskatoon	Princeton	Ground	1.5/2.45	26 − 36
ARGO	Rome/Berkeley	Balloon	0.9/1.8	150 + 3 higher
CAT	Cambridge	Interferometer	0.25	13.5, 15.5, 16.5

Table 3.1: Some recent CMB anisotropy measurements.

differential observing techniques are only affected by the anisotropic component of the atmospheric emission. Fig. 3.1 shows an estimate of this anisotropic component at a good ground-based observatory. The atmospheric emission increases with frequency and is a serious obstacle to CMB observations with increasing frequencies.

3.3 Large angular scales

The large scale CMB anisotropy is mainly due to the so-called Sachs-Wolfe effect (see Chapter 2). Fluctuations in scales larger then the horizon size at recombination retain their primordial characteristics since they have not been changed by any causal processes inside the horizon before recombination. So the CMB power spectrum mirrors that of the initial seed perturbations and therefore reflects the primordial unprocessed power spectrum. Observations at these scales allow us to determine the normalization and slope of the primordial power spectrum. They may also be used to distinguish between the adiabatic and isocurvature fluctuations (see Chapter 2). These tasks can be complicated by the existence of a gravity wave background (see Chapter 2). At these scales it is not expected to obtain information about the Gaussianity of the fluctuations since the beam will average over the number of defects and the central limit theorem states that the result will be Gaussian. There are three main experiments operating on these scales: COBE, Tenerife, MIT/FIRS. In Chapter 5 we give a detailed description of the Tenerife experiment, so it will not be addressed here.

3.3.1 The COBE Experiment

The Cosmic Background Explorer satellite (COBE) was launched on 18th November 1989. The measurements of the Primordial anisotropy are made using the DMR experiment, which consists of six differential microwave radiometers, two at each of 31.5 GHz, 53.0 GHz and 90.0 GHz. These frequencies were chosen to cover the region of minimum Galactic foreground emission. Each radiometer pair has two independent receiver channels (denoted A and B) and measures the difference between the sky signal separated by 60° on the sky as observed in the 7° FWHM beam. The orbit of the satellite is such that one has full sky coverage every six months. Using the first year of data from the DMR experiment Smoot *et al.* [144] made the first detection of primordial anisotropy in the CMB. The results were given in terms of an excess *rms* noise and a cross-correlation function. After correction for the kinematic dipole and removal of the Galactic plane ($|b| \leq 20°$), the sum and difference of the A and B channel maps was made at each frequency. The maps resulting from the sum contain the signal plus the instrument noise, while the maps obtained from the difference consist in instrumental noise. Subtracting the *rms* of the sum and difference maps and smoothing to 10° Smoot *et al.* found an *rms* sky signal of 30 ± 5 μK. Bennet *et al.*, 1992 [12] concluded that a Galactic origin was unlikely and by combining the maps from each frequency so as to minimise the Galactic foreground contribution, produced a 'Reduced Galactic Map'. This experiment has low sensitivity to point sources due to the large beamwidth of the instruments combined with the high frequencies. So discrete radio source emission did not seem to be a reasonable explanation for the detected sky signal. Systematic effects were accounted for to very low tolerance levels [91]. The first-year COBE observations provided in this way a convincing statistical evidence for the existence of CMB fluctuations. It was not possible at the time to distinguish individual features in the maps, since the signal to noise was less than one, with a noise level per beam of $\simeq 45$ μK for the combined maps. Some of these problems are expected to be solved by more integration time, e.g reduction of the noise level per beam, increase of the signal to noise ratio and reduction of systematic effects. The results of the analysis of all four years of DMR data have now become available [9, 10, 67, 92, 93, 94, 78, 79, 176] and a summary of the key results is given in Bennett *et al.* 1996 [14]. Bennett *et al.* quote for $n = 1$ (the Harrison-Zel'dovich value) a Q_{rms-ps} $=18 \pm 1.6$ μK. The joint best fit values of n and Q_{rms-ps} are $n = 1.2 \pm 0.3$ and Q_{rms-ps} $=15.3^{+3.8}_{-2.8}$ μK. Note that this Q_{rms-ps} value, obtained by a fit of the full power spectrum power-law to the data, need not be the same as the actual measured quadrupole component. In fact the observed quadrupole amplitude has a lower value than the value of Q_{rms-ps} . It is not known if this is related with the statistical nature of the theory via the cosmic variance or if it reflects the cosmology of the universe. These results are obtained with inclusion of the quadrupole term, its exclusion gives consistent results with increased uncertainties. These values are consistent with both previous 1-year and 2-year results (an account of these is given in Chapter 5). In Chapter 4 we give the all sky maps at each frequency taken from Bennett *et al.* . Given the improved signal to noise ratio of $\simeq 2$ per 10° patch for the frequency averaged maps, it is expected that some of the features in these maps, away from the Galactic plane, correspond to real CMB fluctuations. The mean signal to noise in each of the 10° smoothed maps are $\simeq 0.5$, 1.5 and 1 for 31, 53 and 90 GHz, respectively. A visual inspection of these maps show that some features are common at different frequencies. These maps also allow for an improvement on the Galactic modeling. With respect to the Gaussianity of the signal Bennett *et al.* concludes non-Gaussian toy models are 5 times less likely to describe the true statistical distribution in the maps, than the Gaussian power law models.

3.3.2 The MIT/FIRS Experiment

This experiment is a balloon-bourne instrument with a 3.8° FWHM beam. It uses bolometric receivers and observes in four frequency bands centred at 170, 270, 475 and 680 GHz. The most sucessful flight of this experiment occurred on 6th October 1989 with a duration of $\simeq$10 hours. This observation mapped out a heart shaped sky area lying within $45°\lesssim l\lesssim 200°$, $+60°\lesssim b\lesssim -80°$. Meyer *et al.* [112] analyzed the 170 GHz data after removal of the Galactic plane ($|b| \leq 15°$), considering a Gaussian autocorrelation function (GACF) and using Monte Carlo techniques. They concluded that the data was consistent with a 95% upper limit of $\Delta T/T \leq 1.6 \times 10^{-5}$ to CMB fluctuations for a coherence scale of 13°. The map presented structure at a level $\Delta T/T = 1 - 2 \times 10^{-5}$ on scales $\geq 4°$. The origin of this structure could not be disentangled with only this observation since at these high frequencies both atmospheric emission and Galactic dust emission contribute at the level of CMB amplitude. Ganga *et al.* [62] proceeded with a cross-correlation of the MIT data with the COBE Reduced Galaxy Map. The cross-correlation function provided good statistical evidence for the common origin of the structures seen by both the COBE and MIT experiments. This result gave good support to the COBE detection in particular due to the fact that these experiments probe quite different frequencies.

3.4 Medium angular scale observations

At these angular scales models predict larger amplitudes of the CMB fluctuations arising from the Doppler peaks (see Chapter 2). These oscillatory features are very sensitive to the details and are model dependent, therefore their observation should allow good constraints to be established on model parameters. Comparing these experiments to those on larger angular scales one may separate the scalar fluctuations from any possible gravity wave background. At these scales the effect of the cosmic variance is small but a new source of uncertainty arises due to the small size of the sky areas probed by these experiments, the sample variance. According to Coulson *et al.* [36], at these scales, it should be possible to detect non-Gaussianity induced by defect models. Reionization of the Universe at some epoch can smear out these fluctuations to scales depending on the epoch of reionization. If it happened early enough it could erase perturbations up to scales of less than few degrees. There are several experiments operating on these scales SP/ACME-HEMT, Saskatoon, ARGO, Python, MAX, MSAM, etc.

3.4.1 The SP/ACME-HEMT Experiment

The ACME-HEMT (Advanced Cosmic Microwave Explorer) is one of the various experiments working at the South-Pole but is usually known as the South Pole (SP) experiment. It consists of a ground-based off-axis Gregorian telescope and a HEMT receiver and observes four equal bands between 25 and 35 GHz. The beam has 1.5° FWHM and is sinusoidally switched on the sky to give a peak to peak throw of the beam of 3°. This instrumental disposition results in maximum sensitivity to sky temperature differences separated by 2.1°. Gaier *et al.* [63] analysed a 9 point scan, considering a GACF and using the highest frequency channel a 95% upper limit of $\Delta T/T < 1.4\times 10^{-5}$ was set to the CMB fluctuations with a coherence angle of 2.1°. On the other hand they found that the signals at the lower frequency channels decrease with increasing frequencies, as expected for Galactic free-free or synchroton emission. Schuster *et al.* (SP91) [134] analysed an independent 13 point scan (DEC=$-63°$, centered at RA=2h), who found the existence of structure the spectrum of which is 2σ away from a Planck spectrum. Assuming that the signal in the data is CMB and using a GACF an amplitude of $\Delta T/T = 8.6 \times 10^{-6}$ and a 95% upper limit of $\Delta T/T < 1.6 \times 10^{-5}$ is obtained for fluctuations with $\theta_c = 1.5°$. This signal is identified with two scan points that may be contaminated by Galactic emission or source contamination. None of these authors mention the possibility of discrete source emission contamination. These results set upper limits that are inconsistent with other reported detections if the fluctuations are described by Gaussian statistics. Meanwhile Gundersen *et al.* (SP94) [69] analysed the most recent data set which partially overlaps the SP91 data set, taken during the 1993-1994 austral summer. The data set consist in a $20° \times 1°$ strip on the sky. For these obervations a new receiver operating in 3 bands between 38 and 45 GHz (Q-band) with a FWHM varying from $1°$ to $1.15°$ was added. This provides an improved frequency coverage which allows a better discriminatory power of the origin of the signal in the data. A detection inconsistent with Galactic emission at 5σ level and with dust was reported. However, there is still the possibility of flat or inverted spectrum point sources contamination. The amplitude of the combined data taken with both instruments is $\Delta T_{rms} = 42.0^{+15.8}_{-6.8}$ μK. A band power estimate of the CMB power spectrum, C_l, gives $\langle \frac{C_l l(l+1)}{2\pi} \rangle_B = 1.77^{+1.58}_{-0.54} \times 10^{-10}$.

3.4.2 The Saskatoon Experiment

This experiment is a ground-based telescope located in Saskatoon, Canada, equiped with a cooled HEMT receiver with six equally spaced channels and observes a frequency range of 26 to 36 GHz. For the observational strategy described in Wollack *et al.* [174], the beam $1.5°$ FWHM is swept in azimuth sinusoidally to measure the sky. It uses a sine wave chop with a weighting corresponding to the second harmonic of the chop frequency. This chopping strategy resembles a three-beam chop with a beamthrow of $2.45°$ (see Chapter 2 and 4). Wollack *et al.* analysed data of a 24 hour RA strip at declination $+85.1°$. The likelihood analysis of the data using a GACF, gives a detection with amplitude $\sqrt{C(0)} = 41^{+16}_{-13}$ μK, on a coherence scale of $1.2°$. The best fit spectrum $\beta = -0.3^{+0.7}_{-1.2}$ which is consistent with that expected from CMB, although free-free emission is excluded with only 90% confidence. The contribution from discrete source emission is very small compared with the detected signal. Netterfield *et al.* [114] presented recent interesting results wich show not just a detection but also evidence for the form of the angular power spectrum on the scales probed. This was achieved by using a set of synthesized beams and the corresponding window functions are given in Chapter 6. The beam is swept in azimuth on the sky over many beam widths with a large flat chopping mirror, then the effective antenae are synthesized in software by choice of the weighting vector. The frequency spectral index of the fluctuations was found to be consistent with that of the CMB but inconsistent with Galactic free-free emission or dust. The contamination by unresolved point sources was estimated to be small but an improved discrimination from point sources is still required if e.g. one extends the coverage to smaller angular scales. The CMB anisotopy was measured in 23 different multipole bands from $l = 54$ ($\simeq 3°$) to $l = 404$ ($\simeq 0.45°$). Fig. 3.2 shows the results for the angular power spectrum. The angular power spectrum was presented in three different ways, in Table 3.2, we display the results for the angular power spectrum in 5 bins, which were obtained by combining all of the data sensitive to a given range of angular scales using the full correlation matrix. The

l_e	$\delta T_l(\mu\mathrm{K})$
87^{+39}_{-29}	49^{+8}_{-5}
166^{+30}_{-43}	69^{+7}_{-6}
237^{+29}_{-41}	85^{+10}_{-8}
286^{+24}_{-38}	86^{+12}_{-10}
349^{+44}_{-41}	69^{+19}_{-28}

Table 3.2: The Saskatoon results in terms of the angular power spectrum in 5 bins.

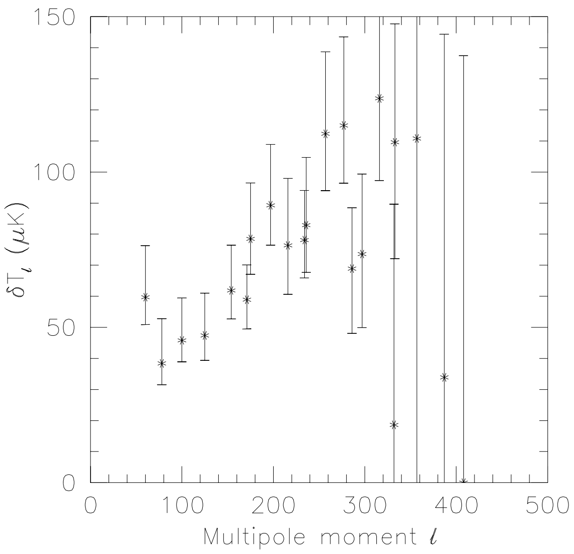

Figure 3.2: Latest Saskatoon results as a function of spherical harmonic coefficient ℓ, taken from Netterfield *et al.* .

plot shows a clear rise of the angular power spectrum from $\delta T_l = \sqrt{\frac{l(2l+1)C_l}{4\pi}} = 49^{+8}_{-5}$ μK, at $l = 87$ to $\delta T_l = 85^{+10}_{-8}$ μK at $l = 237$, for a flat band power spectrum. These results do not take into account the overall $\pm 14\%$ (1σ) calibration uncertainty. Netterfield *et al.* repeated and confirmed the observations of MSAM1-92 [30] (see below). These results in conjunction with remaining experiments and in particular with CAT (see below) are used in Chapter 6 to provide good evidence, for the first time, for the existence of the main Doppler peak with implications for the reionization history of the universe.

3.4.3 The ARGO Experiment

This experiment is a balloon-bourne experiment and uses a 1.2 m on-axis Cassegrain telescope and observes four bands centered at 150, 250, 375 and 600 GHz. The 52' FWHM beam is sinusoidally switched on the sky through 1.8° peak to peak. De Bernardis *et al.* [44] analysed data recorded in the August 1993 flight. He found correlation between the signals in the two highest frequency channels with emission in the IRAS 100μm data this is related to cirrus dust emission. In the lower channels there exists structure with an amplitude $1.4 \times 10^{-5} < \Delta T/T < 3.0 \times 10^{-5}$ (95% confidence) for a GACF on a coherence scale of 30'. Although the spectral index of the signal is consistent with a CMB spectrum, there is the possibility that the signals are due to a cold dust component, and errors due to ground spillover cannot be ruled out.

3.4.4 The PYTHON Experiment

This instrument consists of a 0.75 m diameter off-axis parabolic telescope and a 2×2 array of bolometric detectors with $0.75°$ FWHM beam. The combination of a fast three-beam chop and slower beam switching results in a four-beam response on the sky with a beamthrow of $2.75°$. This instrument has performed two sets of observations, the first observations were made between 1 and 15 of January 1993, the second ones between 12 and 23 of December 1993. The second season spent part of its time repeating the first season observations and found good agreement between them. The first season observations [54] gave a statistical sky signal with an amplitude $\Delta T/T \simeq 3.5 \times 10^{-5}$ for a GACF with coherence angle of $1°$. Ruhl *et al.* [128] analysed the second set of observations, using a GACF analysis. They conclude that the data yelds a CMB anisotropy detection with amplitude $\Delta T/T = 2.8^{+1.1}_{-0.7} \times 10^{-5}$ with coherence angle of $1°$.

3.4.5 The MAX Experiment

The Millimetre-wave Anisotropy eXperiment (MAX) is a balloon-bourne instrument with a $0.5°$ FWHM beam and a $1.3°$ peak-to-peak sinusoidal chop. It uses a sine wave chop with a weighting corresponding to the first harmonic of the chop frequency. The first three flights observed three frequency bands centered at 180, 270 and 360 GHz while the fourth and fifth flights added to those a 105 GHz channel. The 270 and 360 GHz channels are used to obtain information about the dust emission. Observation have been taken in six regions of the sky centred near the stars Gamma Ursa Minoris (GUM), Mu Pegasi, Sigma Hercules, Iota Draconis, Phi Herculis and HR5127. The sky coverage is around $6° \times 0.6°$ and for the last two regions $8° \times 0.6°$. The sky areas were selected acording to minimum foreground emission. The GUM region was observed on the 2nd [4], 3rd [68] and 4th [47] flights. In each case it was detected corrrelated structure inconsistent with dust but consistent with CMB, at similar levels (see Table 3.3). Comparable results were obtained for the Sigma Hercules, Iota Draconis [33] and Phi Herculis [152] scans and are also tabulated in Table 3.3. The Mu Pegasi scan [48, 33] and the HR5127 [152] provide detections much lower than the detections in the other regions observed. One explanation could be that these sky scans are particularly quiet areas of the CMB sky. This hypothesis is just about consistent with Gaussian fluctuations. Another explanation for the case of the scan Mu Pegasi is that the subtraction of a dust component as considered by Devlin *et al.* [48] could have lowered the expected CMB signal. The dust contamination is negligible in the other MAX scans. The difference between the Phi Herculis and the HR5127 results are comparable to the difference between the GUM and the Mu Pegasis results. The complete Phi Herculis data set is spectrally inconsistent with all four astrophysical processes, free-free, synchroton, dust and CMB emission. However the data at the two lower frequencies are spectrally consistent with free-free, dust, and CMB emission but spectrally inconsistent with synchroton emission. The HR5127 data set is spectrally consistent with free-free, synchroton and CMB emission. The dust contributes only a few μK in the higher frequency data and is negligible at lower frequencies for both these scans. The low level of HR5127 result is still under consideration, although a reanalysis of MAX4 limits in the CMB

Flight	Region	GACF $\Delta T/T$	δT_l
2nd	GUM	$4.5^{+5.7}_{-2.6} \times 10^{-5}$	
3rd	Mu pegasi	$1.5^{+1.1}_{-0.7} \times 10^{-5}$	
3rd	GUM	$4.2^{+1.7}_{-1.1} \times 10^{-5}$	
4th	GUM	$3.7^{+1.9}_{-1.1} \times 10^{-5}$	
4th	Iota Draconis	$3.3^{+1.1}_{-1.1} \times 10^{-5}$	
4th	Sigma Hercules	$3.1^{+1.7}_{-1.3} \times 10^{-5}$	
5th	GUM	$3.1^{+1.2}_{-0.8} \times 10^{-5}$	$2.0^{+0.6}_{-0.4} \times 10^{-5}$
5th	Iota Draconis	$2.6^{+1.3}_{-0.8} \times 10^{-5}$	$1.7^{+0.8}_{-0.5} \times 10^{-5}$
5th	Sigma Hercules	$2.8^{+1.2}_{-0.9} \times 10^{-5}$	$1.8^{+0.8}_{-0.6} \times 10^{-5}$
5th	HR5127	$1.8^{+0.6}_{-0.5} \times 10^{-5}$	$1.2^{+0.4}_{-0.3} \times 10^{-5}$
5th	Phi Herculis	$2.9^{+1.0}_{-0.7} \times 10^{-5}$	$1.9^{+0.7}_{-0.4} \times 10^{-5}$

Table 3.3: Summary of MAX $\Delta T/T$ measurements assuming a GACF with $\theta_c = 25'$, and for a flat band power spectrum. Confidence intervals are 95%, except for the 5th flight which are 68%.

anisotropy for GUM, Iota Draconis and Sigma Herculis, conducted by Tanaka *et al.* [152] gives GACF limits $\simeq$ 20% lower than previously published. These revised values are closer to the results obtained for the Phi Herculis, HR5127 and Mu Pegasi scans. The results are displayed in Table 3.3, where $\delta T_l = \langle \frac{l(l+1)C_l}{2\pi} \rangle^{1/2}$, assuming a flat band power spectrum.

3.4.6 The MSAM Experiment

The MSAM (Medium-Scale Anisotropy Measurement) uses the 4 channel radiometer previosly used in the MIT experiment. It consists of a 1.5 m Cassegrain telescope with a 0.5° FWHM beam. The telescope is mounted in a gondola and flown in a balloon at high altitude to allow observations at high frequencies to be made. This instrument chops the beam in a three-position pattern with a beamthrow of $\pm 40'$ and simultaneouly measures single- and double-differenced signals depending on the summing of the chop periods considered. It observes in four frequency channels centered at $\simeq$ 180, 270, 495, 675 GHz, allowing for the separation of CMB anisotropies and dust emission. The fist flight (MSAM1-92) covered RA $14^h.44 - 16^h.89$ and $17^h.18 - 20^h.33$ at declination $+82.0°$. Cheng *et al.* [30] analysed this data using for both the two and three-beam data, a two component fit, CMB and dust spectra, to extract the CMB signal. He found the presence of two cadidate unresolved sources at the same position in the sky for both CMB components. They do not conform to Gaussian statistics if they are CMB features and it is not ruled out the possibility of these being Galactic bremsstrahlung sources. After removal of the regions contaminated by these sources, a GACF analysis of the remaining data indicates a detection of anisotropy of $0.6 \times 10^{-5} < \Delta T/T < 2.2 \times 10^{-5}$ (90% confidence) at a correlation angle 0.5° using the single-difference demodulation; and $1.1 \times 10^{-5} < \Delta T/T < 3.1 \times 10^{-5}$ (90% confidence) at a correlation angle 0.3°, for the double-difference demodulation. However the grounds for eliminating the two unresolved sources from the analysis are questionable given that observations with high resolution (1.7') at $4.7 cm^{-1}$ by Church *et al.* (1995) [32] using the CSO give no evidence for the existence of such point sources. The second

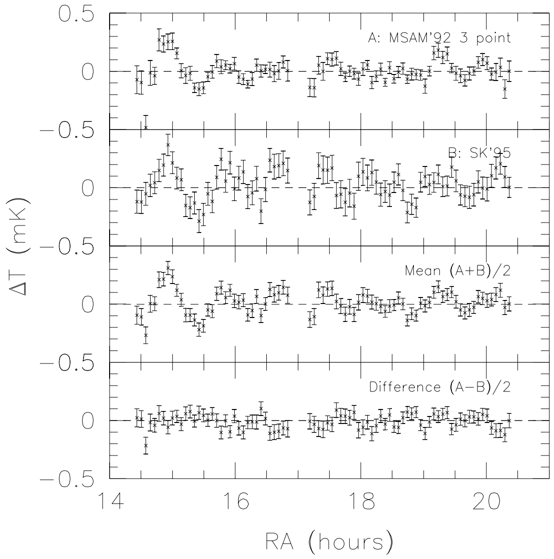

Figure 3.3: Saskatoon results versus MSAM in overlap region

flight (MSAM1-94) observed the same field as the first flight to check previous results. Cheng *et al.* [31] analysed this new data to confirm the earlier measurement of the CMB anisotropy. They found that the CMBR observations in the double-difference channel correlate well with the earlier observations but the same is not true for the single-difference channel which presents some discrepancies and is not ruled out that threr is a possibility of contamination. This data indicates a detection of fluctuations spectrally consistent with CMB of $\Delta T/T = 1.9^{+1.3}_{-0.7}\times 10^{-5}$ (90% confidence with calibration uncertainty included) for a GACF with correlation angle 0.3°, based on the double-difference demodulation. There is another experiment covering the same region of the sky as this one, the Saskatoon experiment. This enables a consistency check between the two very diferent sets of data, providing a wide frequency range between them. Netterfield *et al.* [114] multiplied their data by a weighting vector which synthesised the MSAM three-beam and obtained a high degree of overlap of the window functions. Fig. 3.3 shows the comparison of the Saskatoon and MSAM scans. The results are fully consistent and a determination of the spectral index β, ($T \propto \nu^{\beta}$), from the combination of Saskatoon data (SK95) and MSAM1-92, yields $\beta = -0.1 \pm 0.2$. This corresponds to saying that using the frequency range from 36 GHz to 240 GHz the signal has the frequency spectrum of the CMB, and over this large range no other known source has this spectrum. This confirms previous considerations and rules out the possibility of foreground contamination.

3.4.7 The CAT Experiment

The CAT (Cosmic Anisotropy Telescope) is a three element, ground based interferometer telescope, the description of which is given in Robson *et al.* [125]. Horn-reflector antennas mounted on a rotating turntable, track the sky, providing maps at four (non-simultaneous) frequencies of 13.5, 14.5, 15.5 and 16.5 GHz. The interferometric technique ensures high sensitivity to CMB fluctuations on scales of 0.5°, (baselines $\simeq$ 1 m). It also provides a good level of rejection to atmospheric fluctuations. This instrument is located at a relatively

Figure 3.4: The CAT Telescope at Cambridge

poor observing site in Cambridge, however the data is receiver noise limited for $\simeq 60\%$ of the time, proving the effectiveness of the interferometer strategy. Fig. 3.4 is a picture of the CAT telescope. The first observations were concentrated on a blank field called the CAT1 field. This region was selected from the Green Bank 5 GHz surveys satisfying the requisites of minimum discrete source contamination and low Galactic foreground. This field is centred on RA $08^h20^m00^s$, dec $+68°59'54''$. Accurate information about the point source contribution to the CAT1 field is obtained surveying the fields with the Ryle Telescope at Cambridge. The multi-frequency CAT data can be used to discriminate the remaining CMB and Galactic components. O'Sullivan *et al.* [115] presented the first map obtained at 13.5 GHz and maps at the remaining frequencies were given in Scott *et al.* [137]. These maps are shown in Fig. 3.5 in conjunction with a map obtained from the combination of the others weighted so as to put in evidence the CMB component. A visual impression from this final map is of clear structure and is thought to be real CMB, on scales of $\simeq 0.25°$. For an interferometer the results may be used to constrain directly the CMB angular power spectrum, since there is a direct relation between visibility space and the multipole l space. The results are given in terms of two independent bins in l shown in Fig. 3.6 taken from Scott *et al.* [137]. The solid circles and associated one-sigma error bars show the results for the CMB after marginalizing over any Galactic contribution. This is obtained assuming that the Galactic spectral index lies somewhere between -2.1 (free-free) and -3.0 (synchroton) (with $T \propto \nu^{\beta}$) and using the frequency information of the three maps. The open circles show the results but now the CMB contribution is marginalized over instead, and the squares represent averages over the two bins in l. These results are compared to a theoretical curve for a standard CDM model; the CAT result is fully consistent with this. Currently another field is being observed, CAT2, and new results are expected in the near future.

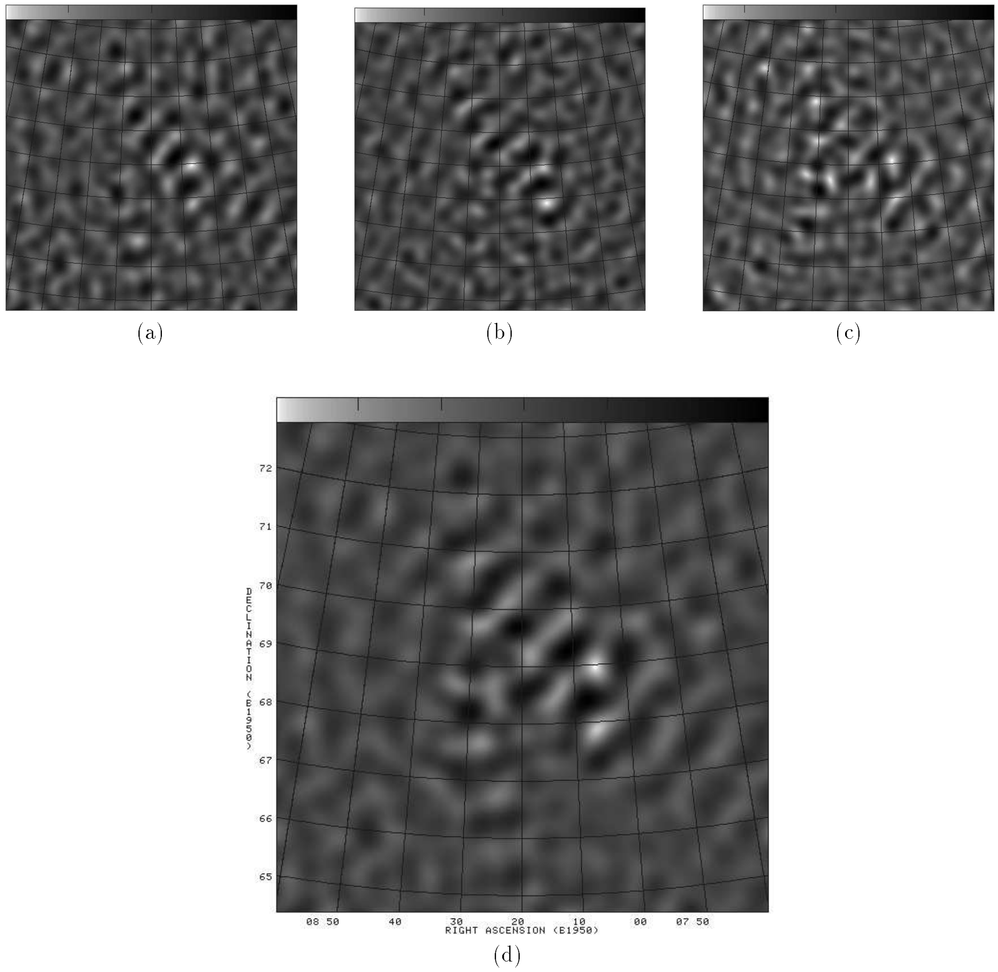

Figure 3.5: Maps of the CAT1 field: (a) 13.5 GHz; (b) 15.5 GHz; (c) 16.5 GHz; (d) weighted combination.

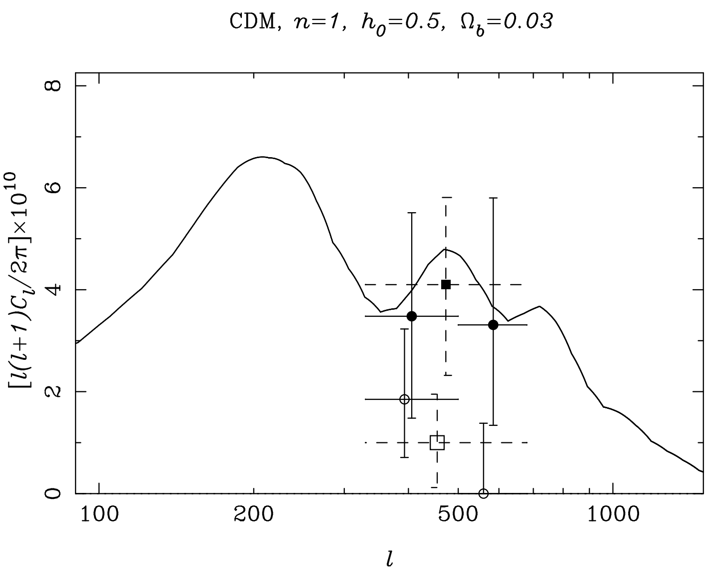

Figure 3.6: The CAT1 field results for the power spectrum

3.5 Small and very small angular scales

At these angular scales the amplitudes of the fluctuations are expected to be reduced due to damping effects such as the Silk damping and damping due to the finite thickness of the last scattering surface (see Chapter 2). They may be further reduced by secondary scattering processes and damping mechanisms, although if there has been reionization the generation of CMB fluctuations at small scales is expected (Ostriker-Vishniac effect). These experiments are sensitive to imprints on the CMB from the seeds of galaxies and clusters of galaxies. Observations at these scales give information about the non-linear physics of galaxy formation and about the thermal history of the universe. They may be compared with other experiments in order to constrain the angular power spectrum of a given model.

3.5.1 The OVRO Experiment

The OVRO experiment consists in a 40 m altazimuth telescope and observes at 20 GHz. It uses double switching to produce a triple beam pattern with 1.8' beamwidth and 7.15' beamthrow. There are uncertainties produced by the tracking of sources on the sky due to the variation of atmospheric contribution with variation of zenith angle and also due to differential spillover. The former was reduced by observing near the North Celestial Pole (NCP). From 1984 to 1987 eight consecutive fields were observed, but some of them were found to be contaminated by discrete sources emission. In order to correct for point sources it is necessary to use separate high resolution surveys. The use of an interferometer presents the advantage of measuring their flux this is particularly useful if the sources are variable. Readhead *et al.* [123] excluded contaminated fields from the analysis instead of proceding to their source correction. The likelihood analysis of the data using a GACF produced 95% upper limits of $\Delta T/T < 1.9 \times 10^{-5}$ to CMB anisotropy with a coherence angle of 2.6'; and upper limits of $\Delta T/T < 9.4 \times 10^{-5}$ for $\theta_c = 12''$ and $\Delta T/T < 3.0 \times 10^{-4}$ for $\theta_c = 25'$. For uncorrelated patches of sky that are uniform on a 2' scale these observations gave an upper limit to the CMB anisotropy of $\Delta T/T < 1.7\times10^{-5}$ (95% confidence). Readhead *et al.* used these results to place constraints on models of galaxy formation, in particular models with adiabatic and isocurvature fluctuations in baryonic matter with, if any, reionization ocurring at redshift z<40, were considered. It was concluded that models with adiabatic fluctuations are ruled out with greater than 95% confidence while isocurvature models with $\Omega < 0.8$ present inconsistency with the reported limits. Further observations were conducted by Myers *et al.* [113] using a ring configuration of 96 interlocked fields at declination $88°10'42''$. The results obtained from statistical analysis of the data are inconsistent at the 95% level with the previous results of Readhead *et al.* , Myers *et al.* concluded that a reasonable explanation for the detections obtained was discrete source contamination of a number of fields.

3.5.2 The VLA Results

Using the Very Large Array (VLA) limits have been placed on fluctuations at very small scales. Fomalont *et al.* [58] observed two $7' \times 7'$ fields to set up upper limits of $\Delta T/T < 3.0 \times 10^{-5}$ with $22'' < \theta_c < 60''$ to Gaussian fluctuations. Their best limits were for fluctuations with a coherence angle of $80''$ of $\Delta T/T < 1.9 \times 10^{-5}$.

3.6 Future Experiments

In the near future it is expected that new instruments will be built with better accuracy and a broader range of frequency coverage, providing improved quality CMB data. For balloon experiments one can improve the quality of the data through the use of long-duration balloon flights, e.g. launched in Antartica, and circling the Pole, and pixels sampled, and the use of arrays of detectors in order to extend the frequency range observed. Examples of these are Boomerang, Maxima, and TOPHAT. On the ground a great improvement is expected from interferometers, one example is the Very Small Array (VSA), to be built by Cambridge and Jodrell Bank in the U.K., and to be sited in Tenerife, which is expected to be operational by the year 2000. Fig. 3.7 shows an artist's impression of the completed VSA array. The CAT is a prototype for this more advanced instrument. The VSA is expected to give detailed maps of the CMB anisotropy with a sensitivity $\simeq 5$ μK and comprehending a range of angular scales from $10'$ to $2°$, and covering a frequency range of 28 and 38 GHz. This instrument uses an interchangeable T-shaped configuration of 10-15 horn elements and simulations have shown that such a configuration is able of attaining a good sensitivity over the range of angular scales planned to be used. It is also expected to measure the values of Ω and H_0 with an accuracy of better than 10% due to the good accuracy expected over the region of the first and secondary Doppler peaks. Simulations have shown that this instrument will be quite sensitive to non-Gaussian features on these angular scales. For future satellite experiments one has the Microwave Anisotropy Probe (MAP) and COBRAS/SAMBA satellite. MAP has been selected by NASA as a Midex mission and is expected to be launched between 1999 and 2001 while COBRAS/SAMBA has been selected by ESA as an M3 mission and will be launched probably around 2005. A very important characteristic of satellite experiments is that they are not affected by the problems caused by the atmosphere. Consequently a satellite is capable of full-sky coverage and has the potential to map features on large angular scales ($>\sim 10°$). On the other hand it has more problems in reaching resolution

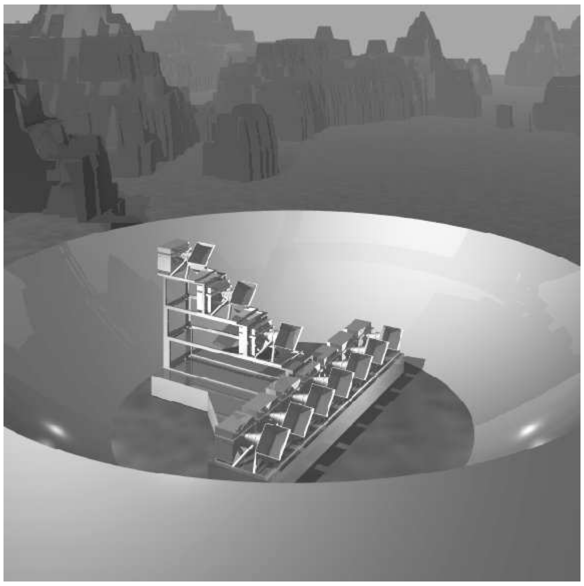

Figure 3.7: Artist's impression of the completed VSA array.

on smaller angular scales due to the limitations imposed on the dish size. The MAP median resolution of its channels is around 30 arcmin while the best angular resolution is 18 arcmin, in its frequency channel at 90 GHz. Consequently it may have problems in determining the shape of the first and almost certainly of the secondary Doppler peaks of the angular power spectrum. COBRAS/SAMBA is expected to attain a resolution around 4 arcmin, with a median resolution of its 6 channels of about 10 arcmin. Consequently it will be possible to determine the angular power spectrum with good accuracy including the secondary peaks, and therefore the determination of the cosmological parameters with good accuracy. With the good angular resolution of COBRAS/SAMBA it is expected to obtain a joint determination of Ω and H_0 to 1% accuracy. All these, balloon, ground-based and satellites experiments to come constitute a good improvement of CMB data and represents an important step towards understanding the characteristics of our Universe.

Chapter 4

Generating maps

4.1 Introduction

In this Chapter we give an inter-comparison of models and experiments using the value of $(\Delta T/T)_{rms}$ to express the comparison. This is a somewhat oldfashioned representation and has been superseded by the 'flat bandpower' framework of which we have also made use and which is introduced in Chapter 6. We use $(\Delta T/T)_{rms}$ here because it was the way the work was initially carried out and also because the conversion from one to another is a simple operation (as explained in Chapter 6). Also some of the concepts and calculations are common to both frameworks, so it represents a very useful step in the understanding of the contents of some of the following Chapters. This Chapter is also of importance by itself because it describes the procedures followed in the simulations of CMB maps for several experiments. For a given model we compute the ensemble average value of $(\Delta T/T)_{rms}$ as described in Section 4.2, and compute the theoretical confidence intervals via Monte Carlo simulations as described in Section 4.3. For the experimental data we extract the observed value of $(\Delta T/T)_{rms}$ from the measurements of the particular experiment. It has been common practice for experimentalists to consider a hypothetical sky model described by a Gaussian auto-correlation function (GACF), and to quote their results in terms of the amplitude of this GACF for a chosen coherence angle, as obtained from a likelihood analysis of the data (see Chapter 2). These results are therefore a measure of the intrinsic anisotropy. In order to compare properly with our theoretical predictions we therefore had to compute the corresponding amplitude after taking account of the beam convolution and the effect of switching techniques, as described in Section 4.2.

Generating CMB maps involves producing Monte Carlo simulations of the temperature fluctuations according to the specific characteristics of each experiment, such as the beamwidth, the sky coverage, the switching pattern, the beamthrow, etc. Simulated skies may be compared with the observed sky and used to test, for example, the underlying model, or the efficiency of the method used to reconstruct the intrinsic sky given the data contamination by our own Galaxy or by experimental noise. In particular we tested the maximum entropy method (MEM) of reconstruction of the CMB sky for the Tenerife experiment, as described in Chapter 5. These simulations are also useful in the estimation of specific quantities prior to the observations, e.g., the smearing due to a given beam, which allows a prediction of the amplitude of the temperature fluctuations to which a given experiment is sensitive. We were also particularly interested in analysing the simulated data calculating the correlation at zero lag, its probability distribution, variance and confidence intervals. In this way one computes the overall theoretical uncertainty for a given experiment. One of our goals was to confront this frequentist approach with Bayesian methods of data analysis, in particular, to investigate the information contained in the error bars of the experimental results obtained via likelihood analysis of the data.

The calculation of the predictions and the simulations follow different strategies according to angular scale and experimental configuration. For large angular scale experiments such as COBE and Tenerife, we used the C_l analytical expression for the Sachs-Wolfe effect as given by Equation (2.99) of Chapter 2. A comparable analytic expression does not exist for small angular scales and we generated the C_l using Equation (2.102) of Chapter 2 for some models proposed by Bond and Efstathiou (BE hereafter), making use of the fitting parameter expression of the autocorrelation function, $C(\theta)$ given by Equation (2.103) (BE, 1987)[23], of Chapter 2. These C_l were used to simulate results from the South-Pole, MAX and Saskatoon experiments. Later we had access to the angular power spectrum for several CDM models kindly provided by G. Efstathiou, which we used to check previous results. We found that the proper C_l are well described by the previous methods as shown in Fig. 2.3 of Chapter 2. In particular, for the Tenerife experiment, we tested the deviation from the simple Sachs-Wolfe effect in order to quantify the contribution from the first Doppler peak to the anisotropy observed. Considering, e.g., a standard CDM model, the l-range probed by this experiment is situated in the beginning of the slope rising up to the first Doppler peak, so one should expect some contribution arising from other than the Sachs-Wolfe effect. In fact the contribution is not particularly significant, and is of the order of a few percent (see Chapter 5).

In the calculations presented here we considered the models proposed by Bond and Efstathiou (BE), [23, 55, 24]. In these models one assumes that the present universe is dominated by cold dark matter, CDM, that the initial conditions are scale invariant (Harrison-Zeldovich spectrum; P(k)$\propto k^n$ with $n = 1$), and Gaussian fluctuations on a flat universe ($\Omega = 1$ Friedmann background) as expected in inflationary scenarios. We have considered three models with adiabatic fluctuations for different values of the baryon density (Ω_b) and of the Hubble constant ($h_0 = H_0/100$ km s^{-1} Mpc^{-1}) and one isocurvature model.

4.2 Predictions and observations

In Chapter 2 we gave a detailed account of how to compute, for a given model and a given experiment, both the ensemble average value of the temperature fluctuations, $\langle(\Delta T/T)_{rms}\rangle_{ens}$, and the cosmic variance, σ^2_{cos}. For the sample variance, σ^2_{sam}, we gave an approximate relation between this quantity and the cosmic variance. The calculation of $(\Delta T/T)_{rms}$ and σ^2_{cos} involves two quantities: the angular power spectrum of a given model, C_l, and the window function of the experiment, W_l, as expressed via Equations (2.65) and (2.91) of Chapter 2. The window functions were obtained numerically using Equations (2.62), (2.66), (2.67), (2.68) and (2.83), (2.85) and (2.87) and are represented in Fig. (4.1). The parameters of the window functions are tabulated in Table 4.1 for the approximate window functions and in Table 4.2 for the exact windows for COBE, South-Pole, Saskatoon, ARGO and MAX. For the COBE experiment the only effect to be considered is the finite beam resolution, and the window function is given by Equa-

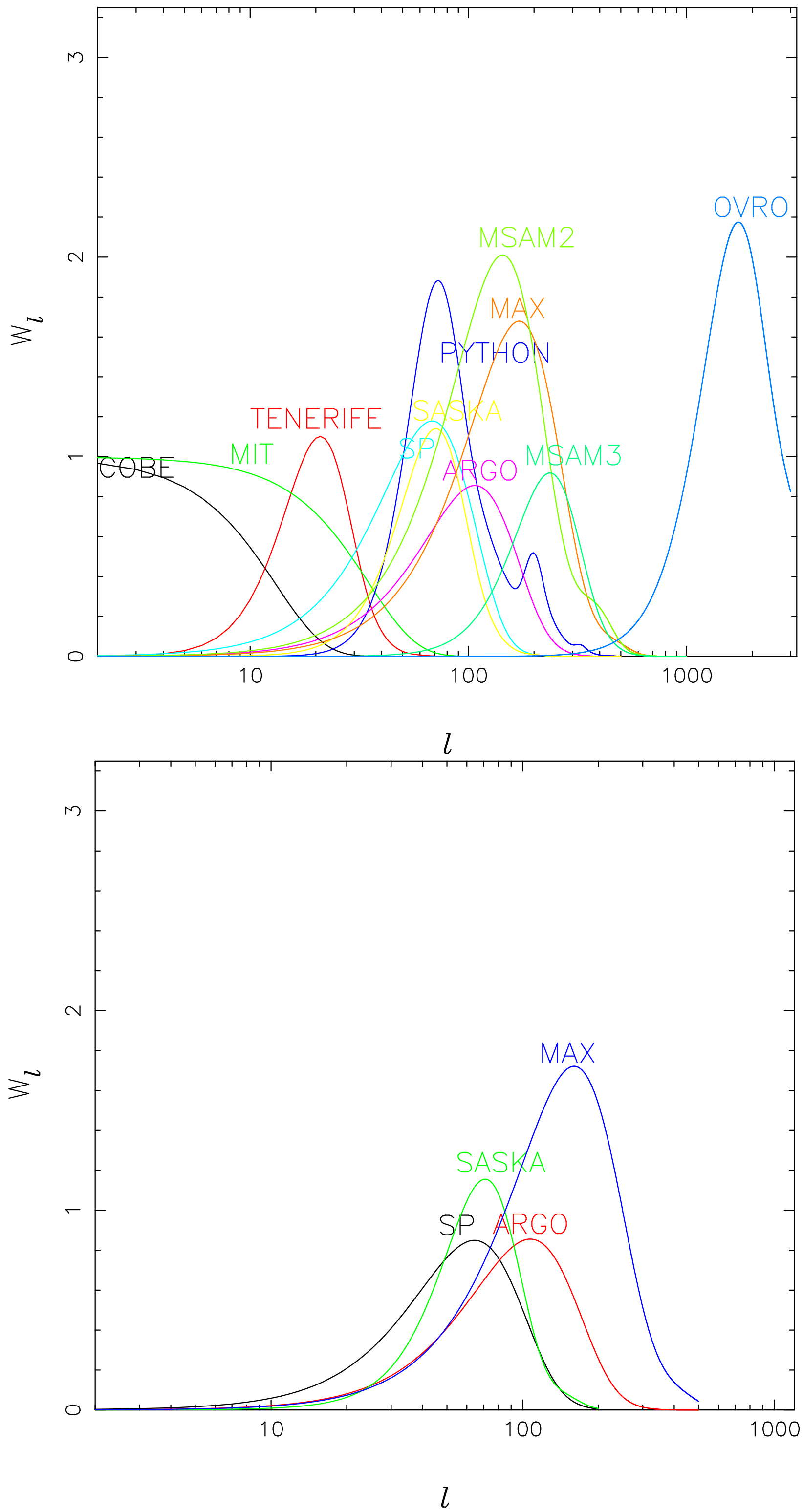

Figure 4.1: The window functions for some experiments. Top: the approximate window functions. Bottom: the exact window functions for the South-Pole, Saskatoon, ARGO and MAX experiments.

Experiment	l_{max}	l_l	l_u	W_{max}
COBE	2	2	12	0.97
Tenerife	21	13	31	1.10
MIT	2	2	27	0.99
PYTHON	73	50	107	1.88
South-Pole	68	33	112	1.18
ARGO	107	52	176	0.86
Saskatoon	71	44	103	1.14
MAX	171	83	279	1.68
MSAM2	144	70	234	2.01
MSAM3	237	147	342	0.92
OVRO	1728	1069	2661	2.17

Table 4.1: Parameters of the approximate window functions for some experiments. The l_{max} represents the multipole corresponding to the peak value of the window function, W_{max}, l_l and l_u represent the lower and upper points at which the window function reaches half of its peak value.

Experiment	l_{max}	l_l	l_u	W_{max}
South-Pole	64	31	106	0.85
ARGO	107	52	176	0.86
Saskatoon	71	44	102	1.16
MAX	160	78	263	1.72

Table 4.2: Parameters of the exact window functions for some experiments. The parameters l_{max}, W_{max}, l_l and l_u are as in Table 4.1.

tion (2.62) of Chapter 2 with FWHM = 10°; we also considered the exact window function as provided by COBE team. The Tenerife experiment consists of a 3-beam experiment with FWHM = 5.1°, beamthrow $\beta = 8.1°$, and the window function is given by Equation (2.67) of Chapter 2. For the South-Pole and MAX experiments we considered both the approximation by a 2-beam experiment with the window function given by Equation (2.66), and the exact W_l as given by Equations (2.83) and (2.85) respectively, of Chapter 2. For the Saskatoon experiment we used both the approximation by a 3-beam experiment as in the case of Tenerife and the correct window function given by Equation (2.87) of Chapter 2. The MSAM2 and MSAM3 experiments are described by a 2 and 3-beam experiment, respectively, and the OVRO experiment by a 3-beam experiment.

The predictions for $\Delta T/T$ using BE models are displayed in Table 4.3 for the 2nd year COBE normalization, where we used for the normalization the value of $Q_{rms-ps} = 20.3\mu$K [153]. The results for the exact window functions for the South-Pole, MAX and Saskatoon experiments, are displayed in Table 4.4 for 2nd year COBE normalization. The factor, f, displayed in these tables is the scaling factor from the value of C_2 for each model as tabulated in BE87 [23, 56], to the value of the COBE quadrupole. The COBE C_2 was obtained from the value of Q_{rms-ps} using the relation $C_2 = (4\pi/5)Q^2_{rms-ps}$. For a cold dark matter dominated universe with $\Omega = 1$ and scale invariant adiabatic perturbations, one has:

$$C_2^{1/2} = 4.5 \times 10^{-6} h^{-1}/b \tag{4.1}$$

where the amplitude of the spectrum is normalized to the second moment of the galaxy autocorrelation function $J_3(10h^{-1}\text{Mpc})$. This normalization prescription gives similar answers to the σ_8 normalization (see Chapter 2). The constant b in Equation (4.1) is the biasing parameter of galaxy clustering introduced in Chapter 2, $b \simeq 1/\sigma_8(mass)$ and h is the Hubble constant ($h = H_0/100\,\text{km}\,\text{s}^{-1}\,\text{Mpc}^{-1}$). So the factor f corresponds to the scaling factor from the σ_8 to the 2nd year COBE normalization and Equation (4.1) states that f is related to the bias of galaxy clustering via , $f \simeq 1/b$, for the particular set of models mentioned above. As described in Chapter 2, we computed the angular power spectrum for small angular scales using Equation (2.102) of Chapter 2. In order to show that this method gives a reasonable agreement with the proper angular power spectrum obtained from some CMB codes, we considered two of the models provided by G. Efstathiou. The predictions for both cases are displayed in Table 4.4 in the second and third column, and they illustrate the close correspondance of the results. In Chapter 2 we have already commented that this method gives good agreement with the proper angular power spectrum as obtained from, e.g., numerical integration of the Boltzmann equations for the evolution of the temperature fluctuations of the CMB, as is shown in Fig. 2.3 of Chapter 2. In order to have an idea of how the approximation of the window function assuming a square wave chop differs from the exact window functions we must compare Tables 4.3 and 4.4. We conclude that while the Saskatoon experiment seems to be only mildly affected by the use of the approximation as a 3-beam experiment, the same is not true for MAX, where the differences are up to 10%, nor for the South-Pole, where the deviation may be up to 15%. The observational results are displayed in Table 4.5. (Some of these observational results have been updated by more recent ones and these are used in the comparison described in Chapter 6.) In Fig. 4.2 we plot the observational results displayed in the last column of Table 4.5 and the predictions tabulated in Table 4.3. The uncertainty in the normalization of the theoretical power spectrum is determined by the uncertainty of the COBE detection. The four plots represent four CDM models for several

experiment	*model*				
	$h_0 = 0.75$ $\Omega_b = 0.03$ ad f=2.09	$h_0 = 0.5$ $\Omega_b = 0.03$ ad f=1.36	$h_0 = 0.5$ $\Omega_b = 0.1$ ad f=1.2	$h_0 = 1$ $\Omega_b = 0.03$ ad f=2.67	$h_0 = 0.75$ $\Omega_b = 0.03$ iso f=0.18
	$\Delta T/T (\times 10^5)$				
COBE, FWHM=10°	1.51	1.49	1.5	1.52	1.45
Tenerife, FWHM=5.1°, $\beta = 8.1°$, triple beam	1.23	1.17	1.2	1.36	1.12
MIT, FWHM=3.8°	1.92	1.90	1.92	2.0	1.80
South-Pole, FWHM=1.5° $\beta = 2.1°$, double beam	1.92	1.77	2.04	2.14	1.11
Saskatoon, FWHM=1.5° $\beta = 2.45°$, triple beam	1.65	1.49	1.70	1.82	0.85
MAX, FWHM=0.5° $\beta = 1.0°$, double beam	2.76	2.86	3.36	2.99	0.99
MSAM, FWHM=0.5°					
double beam β=1.3°	3.01	3.13	3.65	3.28	1.15
triple beam β=0.7°	1.73	1.9	2.28	1.9	0.5
OVRO, FWHM=1.6′ β=7.15′, triple beam	1.11	1.16	1.48	1.15	0.12

Table 4.3: Predictions in terms of $(\Delta T/T)_{rms}$ for BE models where ad stands for adiabatic, iso for isocurvature, β for beamthrow. COBE normalization ($Q_{rms-ps} = 20.3\mu$K) is used. The factor, f, is the scaling factor from the σ_8 to 2nd year COBE normalization.

experiment	*model*							
	$h_0 = 0.75$ $\Omega_b = 0.03$ ad f=2.09	$h_0 = 0.5$ $\Omega_b = 0.03$ ad f=1.36		$h_0 = 0.5$ $\Omega_b = 0.1$ ad f=1.2		$h_0 = 1$ $\Omega_b = 0.03$ ad f=2.67	$h_0 = 0.75$ $\Omega_b = 0.03$ iso f=0.18
	$\Delta T/T(\times 10^5)$						
South-Pole	1.60	1.50	1.60	1.70	1.80	1.80	0.97
Saskatoon	1.65	1.50	1.60	1.73	1.80	1.84	0.86
MAX	2.72	2.89	3.00	3.48	3.60	3.04	1.03

Table 4.4: Predictions in terms of $(\Delta T/T)_{rms}$ for BE models where ad stands for adiabatic, iso for isocurvature, β for beamthrow (COBE normalization ($Q_{rms-ps} = 20.3\mu K$)), using the exact window functions. These W_l are given by Equations (2.83), (2.85) and (2.87) of Chapter 2 for the South-Pole, MAX and Saskatoon experiments respectively. In the second and third column there are two sub-columns: the first displays the results obtained using the C_l from Equation (2.102) of Chapter 2, and the second using the proper C_l provided by G. Efstathiou. The factor, f, is the scaling factor from the σ_8 to 2nd year COBE normalization.

values of Ω_b and H_0 . The three first plots correspond to adiabatic fluctuations while the fourth plot refers to an isocurvature model. The observational values were obtained by conversion of the published results to $(\Delta T/T)_{rms}$. Some of these detections are given in terms of a measure of the intrinsic anisotropy from a likelihood analysis of the data. This analysis is often applied assuming a Gaussian autocorrelation function GACF in which case the results are given in terms of $\sqrt{C(0)}$, or a power law spectrum (PLS) in which case the results are given in terms of Q_{rms-ps} . Some of the experiments quote their results using other spectra; this is the case for, e.g., the South-Pole experiment which considers a scale invariant flat radiation power spectrum [69], and we use the published value of $(\Delta T/T)_{rms}$. For both the Saskatoon [174] and the OVRO [123] we quote the published value of $(\Delta T/T)_{rms}$. For the OVRO experiment we used the result obtained for uncorrelated patches of sky that are uniform on a $2'$ scale. For the COBE experiment we use the value of $Q_{rms-ps} = 20.3 \pm 1.5\,\mu$K as found by Tegmark and Bunn (1995) [153] for the 2nd year data, converted to $(\Delta T/T)_{rms}$. The conversion of $\sqrt{C(0)}$ to $(\Delta T/T)_{rms}$ is obtained considering the effects of convolution with the beam and switching. The factor of conversion, g, from $\sqrt{C(0)}$ to $(\Delta T/T)_{rms}$ is displayed in Table 4.6, for some experiments. For the OVRO experiment the published value (p) is tabulated which is obtained according to the approximate relation $(\frac{\Delta T}{T})^2_{rms} \sim 1.5C(0)$ when $\theta_c \ll \beta$ and $\theta_c \gg \sigma$ with coherence angle, θ_c, beam-switching angle β and dispersion of the beam σ [123]. For a 2-beam experiment the expression for g is derived using the Equation (2.55) for a GACF as in Equations (2.115) and (2.120) of Chapter 2, and is given by:

$$g^2 = \frac{2\theta_c^2}{2\sigma^2 + \theta_c^2}\left(1 - \exp(-\frac{\beta^2}{2\,(2\sigma^2 + \theta_c^2)}\right). \tag{4.2}$$

experiment	*experimental results*				
	Excess rms noise	L.A. GACF $\sqrt{C(0)}$	L.A. PLS Q_{rms-ps}	L.A. Other	$(\Delta T/T)_{rms}$
			$(\times 10^5)$		
COBE, FWHM=10°	1.11		0.75		1.5 (IPLS)
	(0.92,1.3)		(0.69,0.81)		(1.39,1.61)
Tenerife, FWHM=5.1°,	1.44	1.8	0.82	1.4 (IGCS)	1.3 (IPLS)
$\beta = 8.1°$, triple beam	(1.14,1.74)	(1.2,2.6)	(0.59,1.19)	(0.94,2.03)	(0.9,1.9)
South-Pole, FWHM=1.5°			0.6	1.77 (Clb)	1.56 (LPLSp)
$\beta = 2.1°$, double beam			(0.5,0.8)	(1.24,3.35)	(1.3,2.2)
Saskatoon, FWHM=1.5°		1.52		1.2 (IGCS)	1.2 (Lp)
$\beta = 2.45°$, triple beam		(1.04,2.1)		(0.82,1.66)	(0.89,1.59)
MAX, FWHM=0.5°					
$\beta = 1.0°$, double beam					
MAX4GUM		3.7			
		(2.6,5.6)			
MAX4ID		3.3			
		(2.2,4.4)			
MAX4SH		3.1			
		(1.8,4.8)			
MAX3μPeg		1.5			
		(0.8,2.6)			
MSAM, FWHM=0.5°					
double beam		(0.6,2.2)			(0.7,2.6) (IGCS)
β=1.3°					
triple beam		(1.1,3.1)			(0.7,2.0) (IGCS)
β=0.7°					
OVRO, FWHM=1.6′				1.7 (ul)	2.1(ul)
β=7.15′, triple beam				(LUPp)	(LUPp)

Table 4.5: Experimental results: L.A. stands for Likelihood Analysis. When this L.A. is applied to a Gaussian Autocorrelation Function (GACF) the result is given in terms of $\sqrt{C(0)}$, when it is applied to a Power Law Spectrum (PLS) the result is given in terms of Q_{rms-ps}. The L.A. is in some cases applied to other spectrums or form of the autocorrelation function considered by the experimentalists in order to quote their results (see corresponding literature). The column with L.A. Other displays: for IGCS, the results obtained by convolving the intrinsic anisotropy (as obtained using L.A.) with the beam and switching techniques; for Clb: the broad band spectrum estimation obtained directly from a L.A.; for LUPp: results from L.A. assuming uncorrelated patches of sky as published (p) and ul stands for upper limit. The last column displays the values used in Fig. 4.2, where IPLS stands for calculation of this rms using Q_{rms-ps} and an angular power spectrum and LPLSp this rms obtained from L.A. for a power law spectrum as published and Lp this rms from a L.A. as published.

experiment	g
Tenerife	0.78
Saskatoon	0.79
MAX	1.05
MSAM 2	1.16
MSAM3	0.63
OVRO	1.23 p

Table 4.6: Factor used to convert from $\sqrt{C(0)}$ to $(\Delta T/T)_{rms}$ taking account of beam convolution and switching, g, defined by $(\Delta T/T)_{rms} = g \times \sqrt{C(0)}$. MSAM2 and MSAM3 stand for double and triple-beam experiments respectively and the OVRO factor is as published (p).

For a 3-beam experiment, using Equation (2.56), it becomes:

$$g^2 = \frac{1}{2\sigma^2 + \theta_c^2} \left(\frac{3}{2} - 2\exp(-\frac{\beta^2}{2\,(2\sigma^2 + \theta_c^2)}) + \frac{1}{2}\exp(-\frac{(2\beta)^2}{2\,(2\sigma^2 + \theta_c^2)}) \right) . \qquad (4.3)$$

The conversion from Q_{rms-ps} to $(\Delta T/T)_{rms}$ is made by computing the $(\Delta T/T)_{rms}$ for a given model normalized to the quadrupole corresponding to the value of Q_{rms-ps} . For large angular scales, as is the case for the COBE and Tenerife experiments, we may approximate the calculations by assuming that the anisotropy is mainly due to the Sachs-Wolfe effect. The error bars represent 68% confidence intervals (c.i.) for all experiments except for MAX, with 95% c.i., and MSAM, with 90% c.i. The OVRO value represents a 95% upper limit. From these plots we can draw some qualitative conclusions, for instance the models showing better consistency with the data are the ones with $\Omega_b = 0.03$ and $h_0 = 0.5$ and $h_0 = 0.75$, with most of the predicted values laying inside the error bars of the detections except for the case of the MSAM3 (triple beam) experiment and the case of the μ Pegasii scan of MAX experiment. Comparing the several scans of MAX experiment we notice that the μ Pegasii scan detection level is much lower than the other MAX detections. It is believed that this scan is contaminated by dust emission [57] (see also Chapter 6) and we exclude it for the purposes of this comparison. The model in worst circumstances seems to be the isocurvature model with most of the predicted values laying outside the detections error bars. Here we have considered the COBE normalization and therefore isocurvature models underestimates the amplitude of the fluctuations on smaller scales. One should underline the fact that this comparison has been made between the experimental results obtained following a likelihood analysis of the data and the ensemble average value expected from a given model. This comparison assumes that the Bayesian error bars includes information about the theoretical uncertainties. As we will see in the following Section, this seems to be the appropriate procedure to follow.

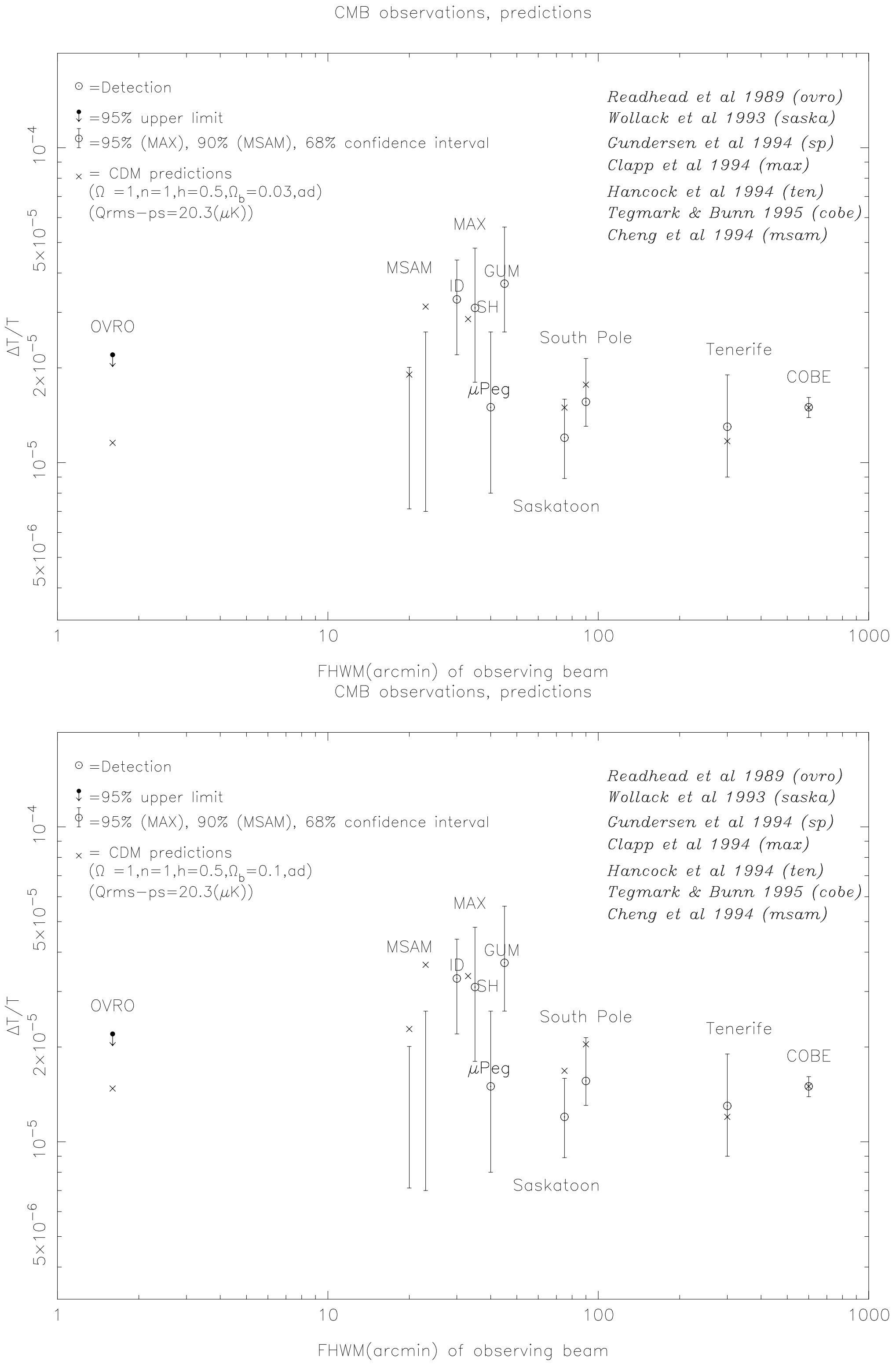

Figure 4.2: Plots of the predicted $\Delta T/T$ vs the FWHM of the observing beam from Table 4.3, 2nd year COBE normalized (crosses), and of the observations displayed in the last column of Table 4.5 (circles). The error bars represent 95% c.i. for MAX, 90% for MSAM and 68% for the other experiments, while the OVRO data point represents a 95% upper limit. The model parameters are given at the top left of each panel. The uncertainty in the normalization of the theoretical power spectrum is determined by the uncertainty of the COBE detection.

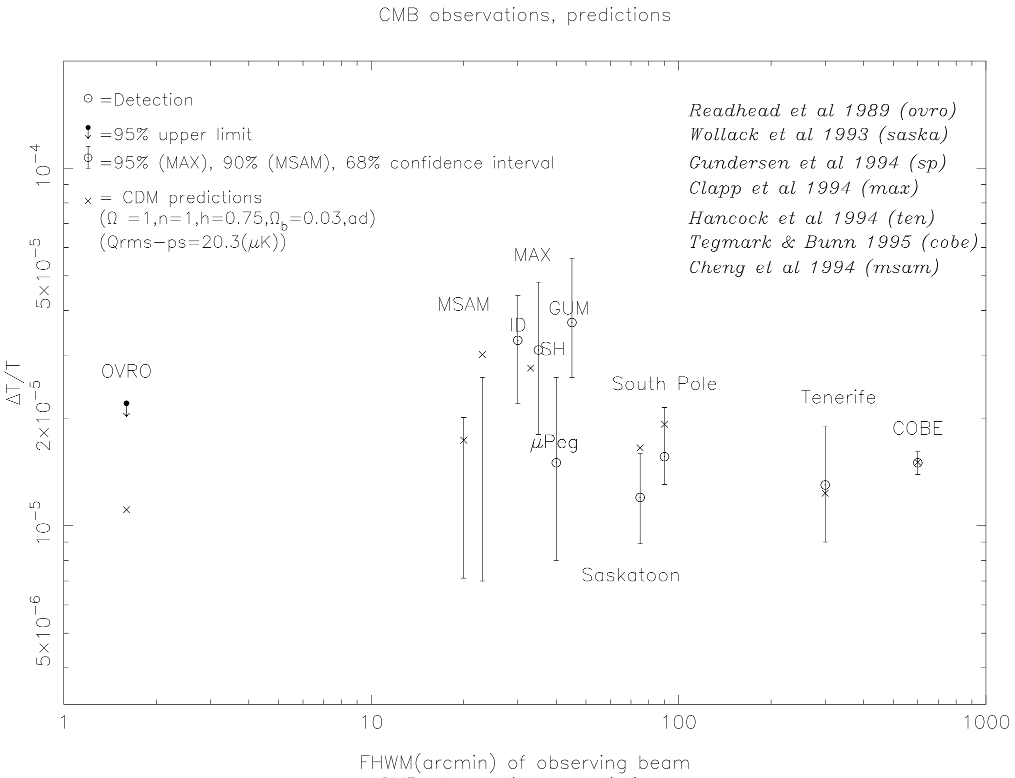

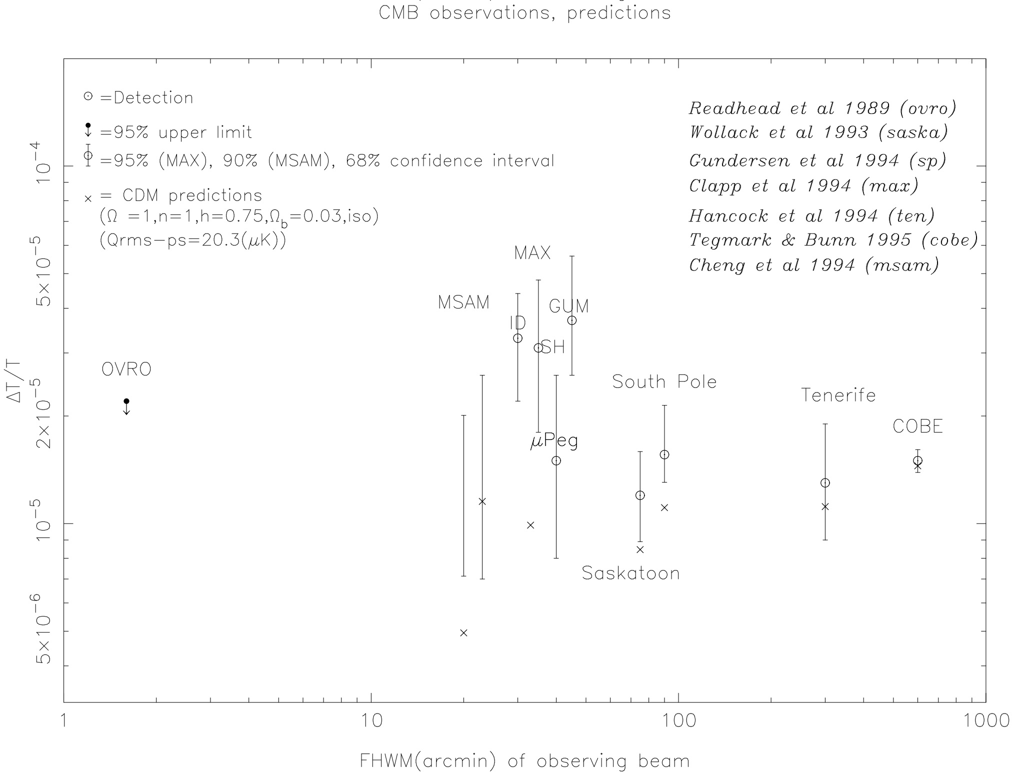

Figure 4.2: continued

4.3 Monte Carlo simulations

In this Section we describe the procedures followed to simulate the experiments of COBE, Tenerife, South-Pole, MAX and Saskatoon. For large angular scales one uses the standard spherical harmonics expansion of $\Delta T/T$, as given by Equations (2.38) and (2.58) of Chapter 2, considering the coefficients as stochastic variables with a Gaussian distribution, zero mean, and variance C_l. These scales are contributed to by low order multipoles only. The relationship between the angular scale θ and the multipole l is given by $l \simeq 2/\theta$, with θ in radians. For small angular scales one considers the CMB radiation pattern as a Gaussian field in a flat 2D space (BE, 1987) [23] with $\Delta T/T$ given by a Fourier expansion as follows:

$$\Delta T/T = \sum_{n_x,n_y} D(\vec{n}) \exp(i\frac{2\pi}{L}\vec{n}\cdot\vec{\theta}) \tag{4.4}$$

where L is the size of the small patch of the sky, $\vec{n} = (n_x, n_y)$ is the spatial frequency, $D(\vec{n})$ is a variable with a Gaussian distribution with zero mean and variance $\langle|D(\vec{n})|^2\rangle = C_l$ with $l \sim \frac{2\pi}{L}n$ and with a random phase in the interval $(0,2\pi)$. $\Delta T/T$ is obtained by evaluating a Fast Fourier Transform (FFT) of $D(\vec{n})$. For each experiment one must consider the sky coverage and use the selected points to do statistics according to the experimental configuration.

4.3.1 Large angular scales

The temperature fluctuations are usually expressed in terms of a spherical harmonics expansion which, considering the smearing due to finite resolution of the beam, may be expressed as:

$$\frac{\Delta T}{T}(\theta,\phi,\sigma_b) = \sum_{l,m} a_{lm} Y_{lm}(\theta,\phi)\mathcal{W}_l(\sigma_b) \tag{4.5}$$

where $\mathcal{W}_l(\sigma_b)$ takes into account the convolution with the beam, and is given by $\mathcal{W}_l(\sigma_b) = e^{-(2l+1)^2\sigma_b^2/8}$ ([133], see also Chapter 2), where $\sigma_b = \mathrm{FWHM}/2\sqrt{2\ln 2}$, and from now on σ_b will be referred to as σ. For Gaussian initial conditions the a_{lm} are stochastic variables with random phase, zero mean and as variance the angular power spectrum C_l. Equation (4.5) may be expressed in the following form:

$$\frac{\Delta T}{T}(\theta,\phi) = \sum_l (\alpha_{l0} f_{l0}(\theta) + \sum_{m=1}^{l} \sqrt{2}(\alpha_{lm}\cos m\phi - \beta_{lm}\sin m\phi) f_{lm}(\theta)) \tag{4.6}$$

where

$$f_{lm}(\theta) = \sqrt{\left(\frac{2l+1}{4\pi}\right)\left(\frac{(l-m)!}{(l+m)!}\right)} P_l^m(\cos\theta)\exp(-l(l+1)\sigma^2/2) \tag{4.7}$$

where $\exp(-l(l+1)\sigma^2/2)$ is an approximation to $\mathcal{W}_l$. The coefficients α_{lm} and β_{lm} are stochastic variables with a Gaussian distribution, zero mean and variance C_l.

COBE

For the COBE experiment [144] one uses FWHM=10° and l is considered to lie in the range 2-40. We proceeded with the computation of the mean value of the correlation at zero lag, its variance and confidence intervals and the rms of temperature fluctuations given by

$$\left(\frac{\Delta T}{T}\right)^2_{rms}(\sigma) = \langle C(0,\sigma)\rangle \tag{4.8}$$

where angle brackets stand for averaging over simulations. The sky coverage of this experiment, taking into account the galactic plane cut $|b| > 20°$, may be approximated by $A \simeq 8.306$ sterad. Fig. 4.3 shows the actual CMB sky plus noise as observed with the 10° beam of the COBE satellite [14]. The typical signal-to-noise ratio is $\simeq 2$ in the frequency-averaged map. Fig. 4.4 shows an all sky simulation of the temperature fluctuations due to the Sachs-Wolfe effect, the dominant source of anisotropy for the angular scales probed by COBE which has not been convolved with the 10° COBE beam. For these simulations we considered the Sachs-Wolfe analytic Expression 2.99 given in Chapter 2, for the multipole range, $l = 2 - 40$, for which this formula is valid. The simulated CMB map exhibits much more detail and higher angular resolution when compared with Fig. 4.3 and shows the great amount of information left in the sky on smaller scales than those accessible to COBE.

Tenerife

The Tenerife experiment [75] is a triple beam experiment with FWHM=5.1° and beam-throw $\beta = 8.1°$. One uses Equation (4.6) with l =2 to 60 for the temperature fluctuation $\Delta T/T$ and then compute double differences i.e.:

$$\left(\frac{\Delta T}{T}\right)_d(\theta,\phi) = \frac{\Delta T}{T}(\theta,\phi) - \frac{1}{2}\left(\frac{\Delta T}{T}(\theta_1,\phi_1) + \frac{\Delta T}{T}(\theta_2,\phi_2)\right) \tag{4.9}$$

where $\angle((\theta,\phi)(\theta_1,\phi_1)) = \beta$ and $\angle((\theta,\phi)(\theta_2,\phi_2)) = -\beta$. We consider one declination, $\delta = 40°$ and scan the sky in R.A. so the expression becomes:

$$\left(\frac{\Delta T}{T}\right)_d(\phi) = \frac{\Delta T}{T}(\phi) - \frac{1}{2}\left(\frac{\Delta T}{T}(\phi + \beta_{eff})) + \frac{\Delta T}{T}(\phi - \beta_{eff})\right) \tag{4.10}$$

where β_{eff} is β in R.A. i.e. $\beta_{eff} \sim \beta/\cos\delta$. We compute $(\Delta T/T)_d$ for 70 points separated by 1° in RA for the RA range 161° − 230°. We then compute the correlation at zero lag of $(\Delta T/T)_d$,

$$C_d(0,\sigma) = \left\langle\left(\frac{\Delta T}{T})^2_d\right)\right\rangle \tag{4.11}$$

where angle brackets refer to sky average, and its statistics. The rms temperature fluctuations are given by:

$$\left(\frac{\Delta T}{T}\right)^2_{rms}(\beta,\sigma) = \langle C_d(0,\sigma)\rangle \tag{4.12}$$

where angle brackets refer to an average over the simulations. The sky coverage of an experiment with a single line scan may be approximated by $A \simeq \alpha \times \theta_c$ where α is the angular length of the scan pattern and θ_c is the coherence angle of the observation. For the Tenerife experiment this may be approximated by $A \simeq 0.085$ sterad.

We also produced 2-dim simulated skies of the intrinsic CMB anisotropy for $\delta = 20°$ to 60° and R.A.= 130° to 180° with l =2 to 200, for a CDM model with $\Omega_b = 0.1$ and $\mathrm{H}_0 = 50\,\mathrm{km\,s^{-1}\,Mpc^{-1}}$. This was then convolved with the beams of the old 8.4° (FWHM) Tenerife experiment and is represented in Fig. 4.5 for $\delta = 35°$ to 45° and the same range in

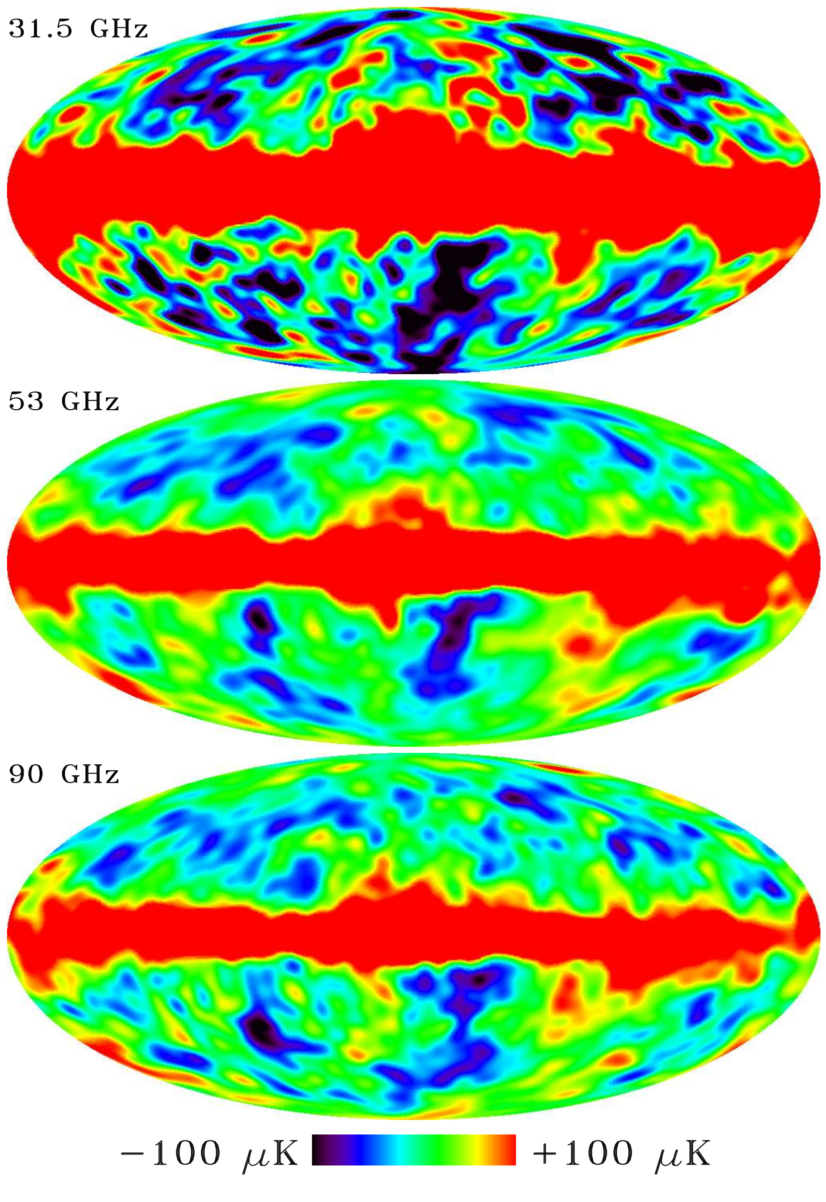

Figure 4.3: All sky map of the CMB anisotropies as observed by COBE experiment. These are Mollweide projections of the 31, 53 and 90 GHz 4-year maps, after the mean offset and the dipole are removed. The central band of the map is dominated by the emission from the Galaxy.[14]

Figure 4.4: An all sky simulation of the CMB anisotropy due to the Sachs-Wolfe effect, using spherical harmonics with $l = 2 - 40$.

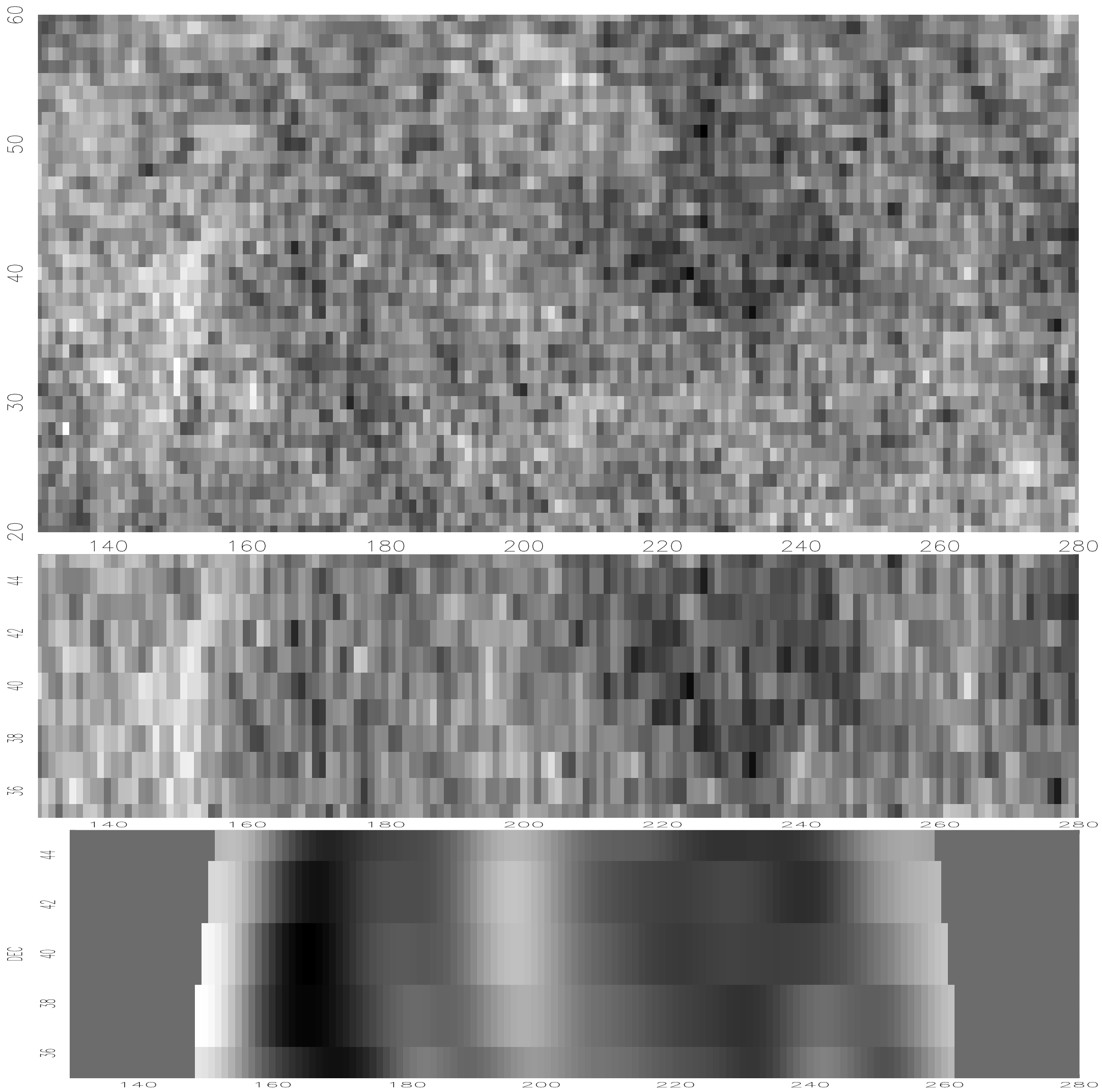

Figure 4.5: Top: a 2-dim simulation of intrinsic anisotropy using spherical harmonics for $\delta = 20°$ to $60°$ and R.A.$= 130°$ to $280°$ and l =2 to 200, for a CDM model with $\Omega_b = 0.1$ and $\mathrm{H}_0 = 50\,\mathrm{km\,s^{-1}\,Mpc^{-1}}$. Middle: a section of this simulation for $\delta = 35°$ to $45°$ and same range of R.A. Bottom: the same area of sky as the middle map convolved with a beam $8.4°$ FWHM.

R.A. These simulations were used to test the efficiency of the MEM method as described in Chapter 5.

For the comparison of the Tenerife results with the COBE experiment we used the linear scan simulations to obtain the ratio between the amplitudes of the temperature fluctuations after convolution with the Tenerife beam and after the convolution with the Tenerife and COBE beams, considering the fluctuations due to the Sachs-Wolfe effect. This was required because we wanted to compare the fluctuations obtained from applying the Tenerife scan strategy to a COBE map with the actual Tenerife data (see Chapter 5). In Fig. 4.6 we plot both one simulated scan after Tenerife beam convolution (T) and after both Tenerife and COBE beams convolution (TC) for the switching strategy of the Tenerife experiment, normalized to $Q_{rms-ps} = 26\mu$K, [75]. We produced 500 simulations of the temperature fluctuations T and TC binned in 4° bins for RA= 145° to 245°, then we sampled the temperature fluctuations in bins of amplitude $10\mu K$ and computed the average of the ratios between T and TC over these simulations. This binning was made in two ways; one considers T as the quantity to bin and the other considers TC. For both cases we calculated the corresponding ratio T/TC. In Table 4.7 the ratio between these is given by the factor T/TC, averaged for 500 simulations: the first column displays the amplitude of the binned temperature fluctuations, T, in bins of $10\mu K$ for the range $-200\mu K, 200\mu K$; the second column gives the corresponding ratio T/TC, the third column gives the amplitude of the binned temperature fluctuations after convolution with both the COBE and Tenerife beams, TC, and the fourth column displays the corresponding ratios, T/TC. These results were obtained considering the Tenerife beam with FWHM= 5.6° and FWHM= 7° for the COBE experiment as an approximation.

4.4 Small angular scales

South-Pole

The South-Pole experiment, SP91 [134]; SP94 [69], may be considered as a double beam experiment with FWHM=1.5° and beamthrow $\beta = 2.1°$. In this case we have considered 2 methods:

1. Assume the approximation by a double beam experiment.

2. Simulate accurately the observational stratregy using FFT techniques reproducing the corresponding window function.

1. One computes $\Delta T/T$ using expression (4.6) with l =2 to 200 and then computes single differences:

$$(\frac{\Delta T}{T})_s(\theta,\phi) = \frac{\Delta T}{T}(\theta,\phi) - \frac{\Delta T}{T}(\theta_1,\phi_1) \tag{4.13}$$

where $\angle((\theta,\phi)(\theta_1,\phi_1)) = \beta$, and we consider a fixed value of the declination and scan the sky in R.A. This could also be phrased as constant elevation with scans along ϕ, then the above expression becomes:

$$(\frac{\Delta T}{T})_s(\phi) = \frac{\Delta T}{T}(\phi) - \frac{\Delta T}{T}(\phi+\beta_{eff}). \tag{4.14}$$

We computed the temperature fluctuations for the data points with coordinates as given by Schuster *et al.* [134] (SP91) and also for convenience we considered this experiment as

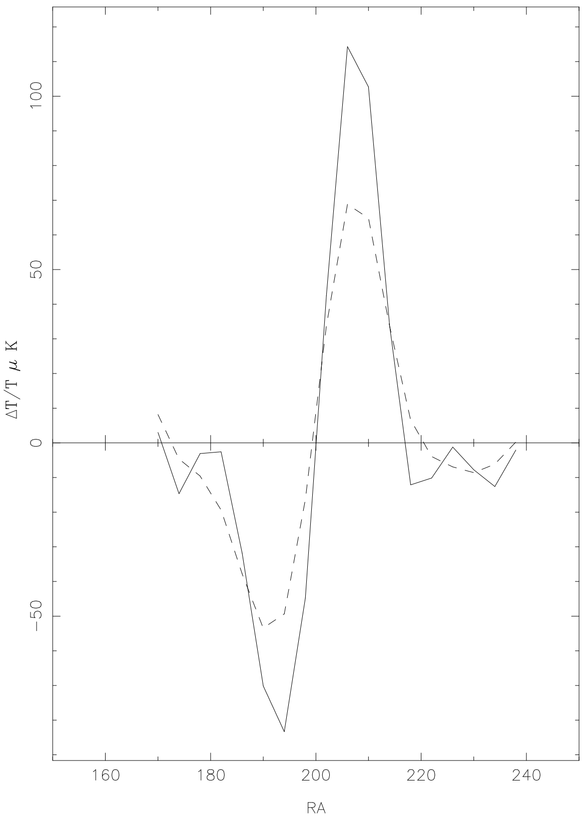

Figure 4.6: A simulation for the Tenerife scan strategy as applied to an intrinsic CMB map (bold line) and as applied to a map obtained from the convolution of the intrinsic one with the COBE beam (dotted line), for a flat scale invariant model with fluctuations arising from the Sachs-Wolfe effect normalized to $Q_{rms-ps} = 26\mu$K.

TBIN(T) (μK)	T/TC	TBIN(TC) (μK)	T/TC
-143	1.64	-95	1.37
-133	1.48	-85	1.48
-123	1.68	-75	1.51
-113	1.55	-65	1.49
-103	1.62	-55	1.50
-93	1.66	-45	1.51
-83	1.71	-35	1.48
-73	1.73	-25	1.47
-63	1.77	-15	1.44
-53	1.72	-5	-1.06
-43	1.88	5	1.49
-33	1.80	15	1.49
-23	0.17	25	1.51
-13	0.86	35	1.46
-3	3.36	45	1.45
7	1.30	55	1.49
17	-5.36	65	1.52
27	2.03	75	1.65
37	1.93		
47	1.73		
57	1.74		
67	1.71		
77	1.64		
87	1.60		
97	1.63		
107	1.67		
117	1.73		
127	1.71		

Table 4.7: Table with the values of T/TC, the ratio of the temperature fluctuations convolved with Tenerife beam only (T) to the temperature fluctuations convolved with both Tenerife and COBE beams (TC). This ratio is given for the binned temperatures, T and TC, as an average for 500 Monte Carlo simulations.

performed at $\delta = 0°$. As for the latter case angles in the sky correspond to angles in RA we have sampled 13 points and compute

$$\Delta_i = \frac{\Delta T}{T}(\phi_i) - \frac{\Delta T}{T}(\phi_i + \beta_{eff}) \tag{4.15}$$

with $\phi_i = (i-1) \times 2.1°$.

2. In this case the temperature difference at (θ_0, ϕ_0) is measured by chopping the beam at fixed $\theta = \theta_0$ through $\phi(t) = \phi_0 + \alpha \sin(2\pi\nu t)$ and sampling $\Delta T/T(\theta, \phi)$ with weight $\mathrm{sign}(\phi(\mathrm{t}) - \phi_0)$, where the temperature difference is twice the weighted average. This can be expressed by transforming $Y_l^m(\theta, \phi)$ into [169]:

$$2\nu \int_0^{1/\nu} dt \mathrm{sign}(\phi(t) - \phi_0) Y_l^m(\theta_0, \phi(t)) = 2iH_0(m\alpha) Y_l^m(\theta_0, \phi_0) \tag{4.16}$$

where $\alpha \sin(\theta_0) = 1.5°$ with θ_0 the co-declination of the points observed. This can be reproduced considering the expression (2.70) of Chapter 2 with a Lock-in function given by $L(t) = 2\mathrm{sign}(\alpha \sin(\omega_c t))$, where $\omega_c = 2\pi\nu_c$, is the chopping frequency.

This is an experiment in smaller angular scales so one may approximate the multipole expansion by a Fourier expansion using FFT techniques. We have considered patches of the sky of size L^2 and simulate for a grid of N^2 points, $\Delta T/T$, according to Equation (4.4), taking into account the convolution with the beam. We then pick up 13 points according to Equation (4.16). To simulate this for a given (ϕ_0) (θ is fixed) one considers m points around ϕ_0 as follows: $\phi_i^+ = \phi_0 + \alpha \sin x_i$ and $\phi_i^- = \phi_0 - \alpha \sin x_i$ where $x_i = (\pi/2)(i/(m-1))$ and $i = 1, m-1$; and one obtains the temperature fluctuation in the point ϕ_0 according to the following expression:

$$\frac{\Delta T}{T}(\phi_0) = \frac{1}{m-1} \left(\sum_{i=1}^{m-1} \frac{\Delta T}{T}(\phi_i^+) - \frac{\Delta T}{T}(\phi_i^-) \right). \tag{4.17}$$

The sky coverage of SP91 may be approximated by $A \simeq 13 \times 2.1° \times 1° \simeq 0.0088$ sterad.

MAX

The MAX experiment [33, 46] may also be considered as a double beam experiment with FWHM=0.5° and beamthrow $\beta = 1°$. As for the South-Pole experiment one may consider the same two methods.

1. $\Delta T/T$ is computed using expression (4.6) with l =2 to 500. Then we compute single differences for 21 pixels separated by $17'$ in the sky. The expression for $\Delta T/T$ becomes:

$$\frac{\Delta T}{T}(\phi) = \frac{\Delta T}{T}(\phi) - \frac{\Delta T}{T}(\phi - \beta_{eff}) \tag{4.18}$$

2. In this case one replaces $\mathrm{sign}(\phi(\mathrm{t}) - \phi(0))$ in Equation (4.16) by $(\phi(t) - \phi(0))/\alpha$, which has the effect of extracting the frequency component of the sky signal which matches the chop frequency, ν, and transforms $Y_l^m(\theta, \phi)$ into [169]:

$$2\nu \int_0^{1/\nu} dt \frac{\phi(t) - \phi_0}{\alpha} Y_l^m(\theta_0, \phi(t)) = \pi i J_1(|m\alpha|) Y_l^m(\theta_0, \phi_0) \tag{4.19}$$

with $\alpha = 0.65°$ for $\theta_0 = 90°$ (as it is for the μ -Pegasii scan). This can be reproduced considering the expression (2.70) of Chapter 2 with a Lock-in function given by $L(t) =$

$k \sin(\omega_c t)$, where the chopping frequency $\omega_c = 2\pi\nu$, and $k = \pi$ for σ=0 (as is the case in Equation (4.19)) and $k = 3.34$ for the MAX value of σ [145].

The temperature fluctuations were obtained following the same procedure as in the South-Pole experiment, with the difference that here we sample 21 points separated by $17'$ in the sky, according to Equation (4.19). This is obtained by expressing the temperature fluctuation at ϕ_0 as:

$$\frac{\Delta T}{T}(\phi_0) = \frac{k}{2 \times (m-1)} \left(\sum_{i=1}^{m-1} \sin x_i \left(\frac{\Delta T}{T}(\phi_i^+) - \frac{\Delta T}{T}(\phi_i^-) \right) \right) \tag{4.20}$$

with x_i , ϕ_i^+ and ϕ_i^- defined as in South-Pole experiment with $i = 1, m-1$

Once the temperature fluctuations are obtained one computes the correlation at zero lag

$$C_s(0,\sigma) = \left\langle \left(\frac{\Delta T}{T} \right)_s^2 \right\rangle$$

and its statistics. The rms temperature fluctuations are given by:

$$\left(\frac{\Delta T}{T} \right)_{rms}^2 (\beta, \sigma) = \langle C_s(0,\sigma) \rangle \tag{4.21}$$

where angle brackets refer to an average over the simulations. The sky coverage of this experiment may be approximated by: $A \simeq 6^\circ \times 0.5^\circ \simeq 9 \times 10^{-4}$sterad, assuming a single line scan as in the μ Pegasii scan.

Saskatoon

The Saskatoon experiment [174] may be considered as a triple beam experiment with FWHM= 1.5° and beamthrow $\beta = 2.45^\circ$. As in the last two cases we considered the same two methods:

1. Assumes the approximation by a triple beam using the spherical harmonics formalism. We compute $\Delta T/T$ using expression (4.6) with l =2 to 200 then compute double differences for 24 points separated by 1.25° in the sky, according to expression (4.9). We then proceeded computing $C_d(0,\sigma)$ and $(\Delta T/T)_{rms}^2$.

2. In this case the temperature difference at a given point (θ,ϕ) is measured by chopping the beam at fixed θ through $\phi_i = \phi_0 + \alpha \cos(2\pi\nu t_i)$ with $\alpha = 2.45^\circ$ and sampling $\Delta T/T(\theta,\phi)$ with weight $\cos(4\pi\nu t)$. This transforms $Y_l^m(\theta,\phi)$ into:

$$2\nu \int_0^{1/\nu} dt \cos(4\pi\nu t) Y_l^m(\theta_0, \phi(t)) = -\pi J_2(m\alpha) Y_l^m(\theta_0,\phi_0) \tag{4.22}$$

This can be reproduced considering the expression (2.70) of Chapter 2 with a Lock-in function given by $L(t) = k\cos(2\omega_c t)$, where $k = \pi$ for σ=0 (as is the case in Equation (4.22)) and $k = 4.14$ for the Saskatoon value of σ [168].

We have computed $\Delta T/T$ for a grid of N^2 points on a box of size L^2. We considered 24 points separated by 1.25°. For each point, ϕ_0, we considered m points around it such that $\phi_i^+ = \phi_0 + \alpha \cos x_i$ and $\phi_i^- = \phi_0 - \alpha \cos x_i$ where $x_i = (\pi/2)(i/(m-1))$ and $i = 1, m-1$, and obtained the temperature fluctuation in the point ϕ_0 according to the following expression

$$\frac{\Delta T}{T}(\phi_0) = -\frac{k}{2 \times (m-1)} \left(\sum_{i=1}^{m-1} \cos(2x_i) \left(\frac{\Delta T}{T}(\phi_i^+) + \frac{\Delta T}{T}(\phi_i^-) \right) \right) \tag{4.23}$$

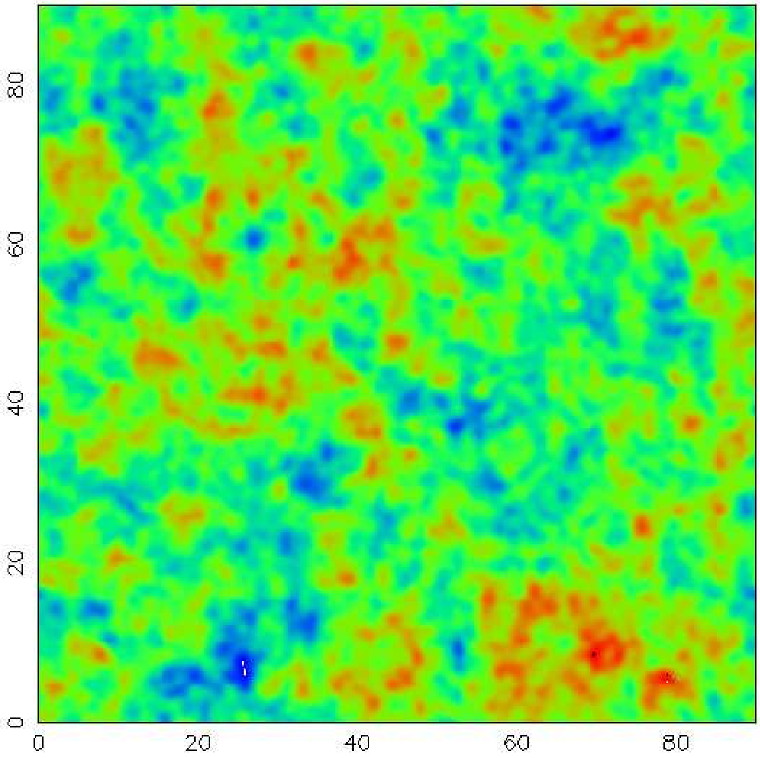

Figure 4.7: A simulation for small angular scales obtained using FFT techniques, for a standard CDM model with $\Omega_b = 0.1$ and $\mathrm{H}_0 = 50\,\mathrm{km\,s^{-1}\,Mpc^{-1}}$. The temperature fluctuations are smoothed to $1.5°$ for a box size of $L = 90°$.

where α is given above. Once the temperature fluctuations, t.f., are obtained one computes the rms of the t.f., the correlation at zero lag and its statistics. The sky coverage of this experiment may be approximated by $A \simeq 30° \times 1.5° \simeq 0.01361$ sterad.

As an illustration we plot in Fig. 4.7 a simulation of CMB radiation anisotropy for small angular scales for a standard CDM model, with $\Omega_b = 0.1$ and $\mathrm{H}_0 = 50\,\mathrm{km\,s^{-1}\,Mpc^{-1}}$. The simulation was done using FFT techniques with the fluctuation smoothed to $1.5°$. On small angular scales the anisotropies are mainly due to the Doppler peaks as mentioned in Chapter 2.

For each of the simulated experiments we have computed the mean and variance of the correlation function and its confidence intervals. As we simulate the experiments taking into account the sky coverage we obtain directly the overall uncertainty: cosmic and sample variance. The results are displayed in Tables 4.8, 4.9, 4.10, 4.11 and in Figs. 4.8, 4.9 and 4.10. Table 4.8 displays the 68% confidence interval (c.i.) of $(\Delta T/T)_{rms}$ obtained from

experiment	*model*			
	$h_0 = 0.75$ $\Omega_b = 0.03$ ad f=2.09	$h_0 = 0.5$ $\Omega_b = 0.03$ ad f=1.36	$h_0 = 0.5$ $\Omega_b = 0.1$ ad f=1.2	$h_0 = 0.75$ $\Omega_b = 0.03$ iso f=0.18
	68% conf. interval ($\times 10^5$)			
COBE, FWHM=10°	(1.32,1.63)	(1.31,1.62)	(1.31,1.61)	(1.28,1.58)
Tenerife, FWHM=5.1°, $\beta = 8.1°$, triple beam	(0.89,1.53)	(0.84,1.44)	(0.88,1.51)	(0.81,1.38)
South-Pole, FWHM=1.5° $\beta = 2.1°$, double beam	(1.46,2.26)	(1.35,2.07)	(1.52,2.36)	(0.84,1.29)
Saskatoon, FWHM=1.5° $\beta = 2.45°$, triple beam	(1.25,1.76)	(1.06,1.59)	(1.22,1.82)	(0.59,0.91)
MAX, FWHM=0.5° $\beta = 1.0°$, double beam	(2.03,3.51)	(2.11,3.65)	(2.47,4.31)	(0.69,1.26)

Table 4.8: Theoretical uncertainties (cosmic and sample variances) in terms of 68% confidence intervals for BE models where ad stands for adiabatic, iso for isocurvature (COBE normalization).

simulations using the spherical harmonics expansion of the temperature fluctuations and the approximation of the experiments by a 2 and 3-beam when applicable. These results were obtained using 500 simulations for the COBE experiment and 1000 simulations of the other experiments. Table 4.9 displays the 68% c.i. of $(\Delta T/T)_{rms}$ as obtained for the small angle experiments using FFT techniques with the proper C_l as provided by G. Efstathiou and the accurate observational strategy for 500 simulations. From the comparison of these two tables we encounter for South-Pole and MAX the differences pointed out in Section 4.2. This was expected to be so since the method applied to get the results tabulated in Table 4.9 reproduce the exact window function while the one used to get the results in Table 4.8 reproduce the window function in terms of the 2 and 3-beam approximation. For the Saskatoon experiment Table 4.9 shows a shift of the confidence interval towards higher values of the temperature fluctuations of the order of 10%. In Table 4.10 the cosmic variance is computed using expression (2.91) of Chapter 2 and approximate window functions. The sample variance is obtained from the simulations. Computing σ_{sam} using the expression (2.92) of Chapter 2 we obtain a reasonable agreement (see Table 4.11). From Table 4.11 we conclude that the simulations give a smaller value of σ_{sam}^2 as compared to the approximate expression; with a maximum discrepancy of $\sim$ percent. From Table 4.10 considering the adiabatic models, we have for COBE a cosmic variance of the order of 19% and sample variance 21 %; for Tenerife a cosmic variance of the order of 5% and sample variance 53%; for South-Pole, Saskatoon and MAX a cosmic variance of the order of 1%, 1% and 0.6% respectively and sample variance 41%, 32% and 56% respectively.

In Fig. 4.8 we plot the ensemble average value of the temperature fluctuations, given

experiment	*model*	
	$h_0 = 0.5$ $\Omega_b = 0.03$ ad	$h_0 = 0.5$ $\Omega_b = 0.1$ ad
	68% conf. interval ($\times 10^5$)	
South-Pole, FWHM=1.5° L=90°, N=512	(1.205,1.818)	(1.359,2.077)
Saskatoon, FWHM=1.5° L=90°, N=512	(1.270,1.927)	(1.458,2.207)
MAX, FWHM=0.5° L=45°, N=512	(2.045,3.635)	(2.429,4.338)

Table 4.9: Theoretical uncertainties (cosmic and sample variances) in terms of 68% confidence intervals for BE models where ad stands for adiabatic, iso for isocurvature, as derived using FFT method. The displayed values of $(\Delta T/T)_{rms}$ are the averaged values obtained over 500 simulations. The simulations considered patches of the sky of size L^2 and a grid of N^2 points. (COBE normalization).

in Table 4.3 and the 68% c.i. of $(\Delta T/T)_{rms}$ displayed in Table 4.8, for the 2nd year COBE normalization. These plots show the results as obtained using the approximate window functions and the spherical harmonics representation for the simulations. In Fig. 4.9 we plot the $\langle(\Delta T/T)_{rms}\rangle_{ens}$ tabulated in Table 4.4 and the 68% c.i. of $(\Delta T/T)_{rms}$ displayed in Table 4.9, for the 2nd year COBE normalization. This Figure shows the results as obtained using the exact window functions and the Fourier expansion for the simulations. These Figures exhibit in particular the differences observed in the South-Pole experiment due to the use of the approximate and exact window function. In Fig 4.10 we plot the experimental results as tabulated in the last column of Table 4.5, except for the case of COBE where the excess rms noise as displayed in the first column of Table 4.5 is used instead. These observations are shown against the predictions and 68% c.i. for the models with σ_8 normalization. There is a slight displacement of the data points with respect to the theoretical ones for the sake of clarity. For the same reason the several scans of MAX experiment are plotted in different angular scales although all of them correspond to the same scale of the corresponding predicted fluctuation. We used here the σ_8 normalization to emphasize the importance of the normalization of the power spectrum considered and to show in particular the specific signature of the isocurvature fluctuations at large angular scales. As seen from the plots this model gives rise to larger temperature fluctuations for the large scales, this indicates that in order to have the COBE normalization this model needs a large value of the bias. This plot shows also the importance of the theoretical uncertainties when compared with the error bars affecting the detections. It also poses the question of to what extent the data analysis recovers completely these theoretical uncertainties.

The Bayesian approach using the likelihood function as described in Chapter 2 attempts to take into account random errors, cosmic and sample uncertainties. In order to investigate the information contained in the error bars obtained via a Bayesian approach

experiment	*model*			
	$h_0 = 0.75$ $\Omega_b = 0.03$ ad	$h_0 = 0.5$ $\Omega_b = 0.03$ ad	$h_0 = 0.5$ $\Omega_b = 0.1$ ad	$h_0 = 0.75$ $\Omega_b = 0.03$ iso
	$C(0,\sigma)$, $C_{s,d}(0)$ *and* σ_{cos}, σ_{sam} $(\times 10^{12})$			
COBE, FWHM=10°				
$C(0,\sigma)$	52	121	156	6496
σ_{cos}	10.1	23.7	30.6	1293.1
σ_{sam}	10.9	25.4	32.8	1356.7
Tenerife, FWHM=5.1°, $\beta = 8.1°$, triple beam				
$C_d(0,\sigma,\beta)$	35	74	100	3844
σ_{cos}	1.6	3.4	4.7	177.5
σ_{sam}	18.4	38.8	54.4	2023.6
South-Pole, FWHM=1.5°, $\beta = 2.1°$, double beam				
$C_s(0,\sigma,\beta)$	85	169	289	3795
σ_{cos}	1.1	2.0	3.3	70.7
σ_{sam}	34.6	68.3	115.4	1574.8
Saskatoon, FWHM=1.5°, $\beta = 2.45°$, triple beam				
$C_d(0,\sigma,\beta)$	62	121	196	2209
σ_{cos}	0.8	1.5	2.5	34.2
σ_{sam}	19.6	37.8	64.6	734.6
MAX, FWHM=0.5°, $\beta = 1.0°$, double beam				
$C_s(0,\sigma,\beta)$	174	441	784	3025
σ_{cos}	0.97	2.5	4.3	24.6
σ_{sam}	99.3	249.3	447.2	1881.2

Table 4.10: The autocorrelation function and σ_{cos}, σ_{sam} for BE models where ad stands for adiabatic, iso for isocurvature (σ_8 normalization).

Table 4.11: Comparison of the sample variance as obtained from simulations with the approximate expression (2.92) of Chapter 2, displayed via the the ratio between the sample and cosmic variances, $r = \sigma_{sam}/\sigma_{cos}$ as obtained from Table 4.10, for the adiabatic model with Ω_b=0.03 and $h_0 = 0.5$, and the factor $a = \sqrt{4\pi/A}$ of expression (2.92).

experiment	r	a
COBE	1.07	1.23
Tenerife	11.4	12.2
South-Pole	34.2	37.8
Saskatoon	25.2	30.4
MAX	100.0	118.2

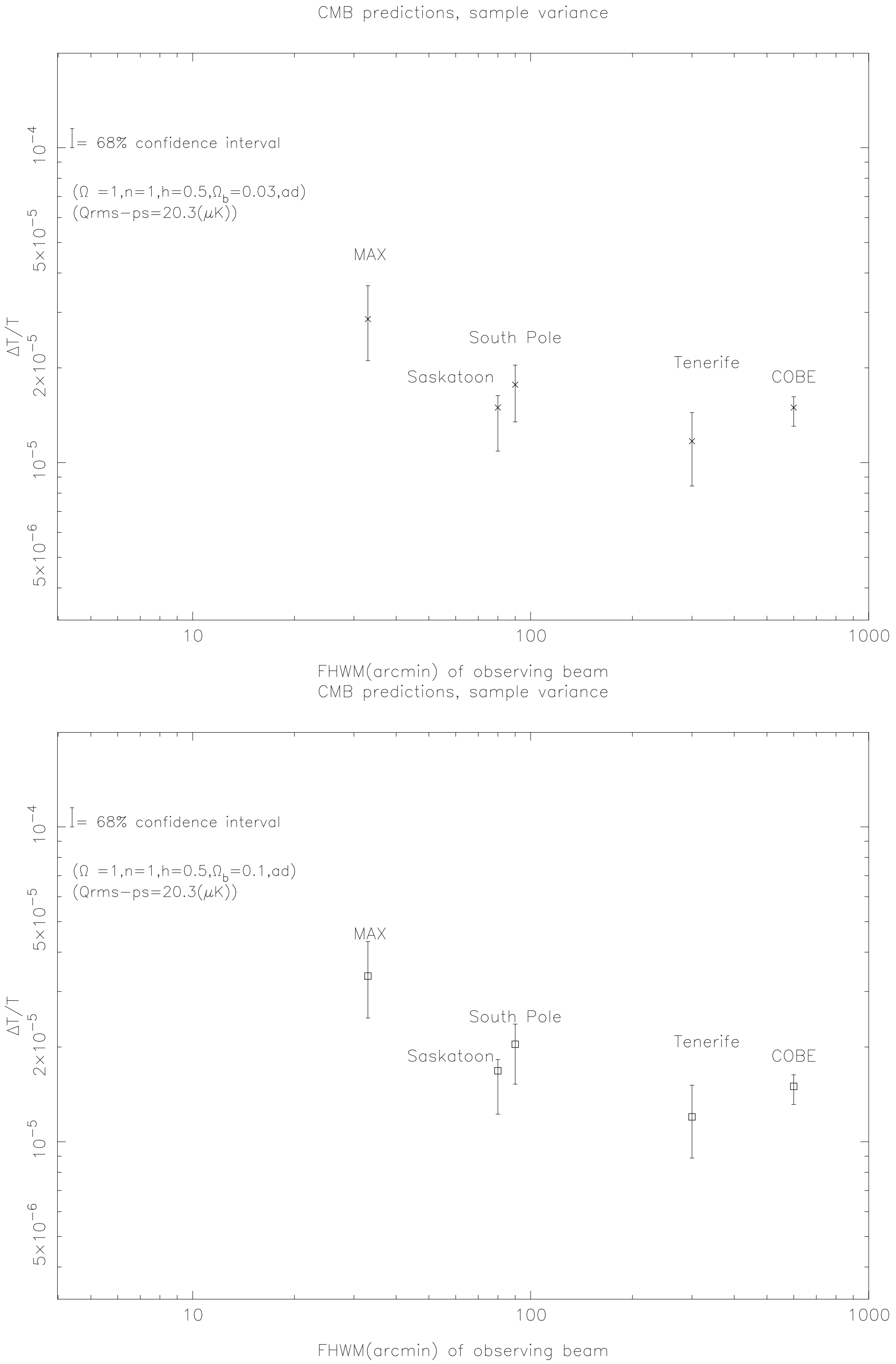

Figure 4.8: Plots of the predicted $\Delta T/T$ vs FWHM of the observing beam given in Table 4.3 (2nd year COBE normalized) and the theoretical uncertainties (68% c.i's) tabulated in Table 4.8. The model parameters are given at the top left of each panel. These results were obtained using the spherical harmonics expansion for the simulations and the approximate window functions for the predictions. The three first plots correspond to adiabatic models while the last one corresponds to an isocurvature model.

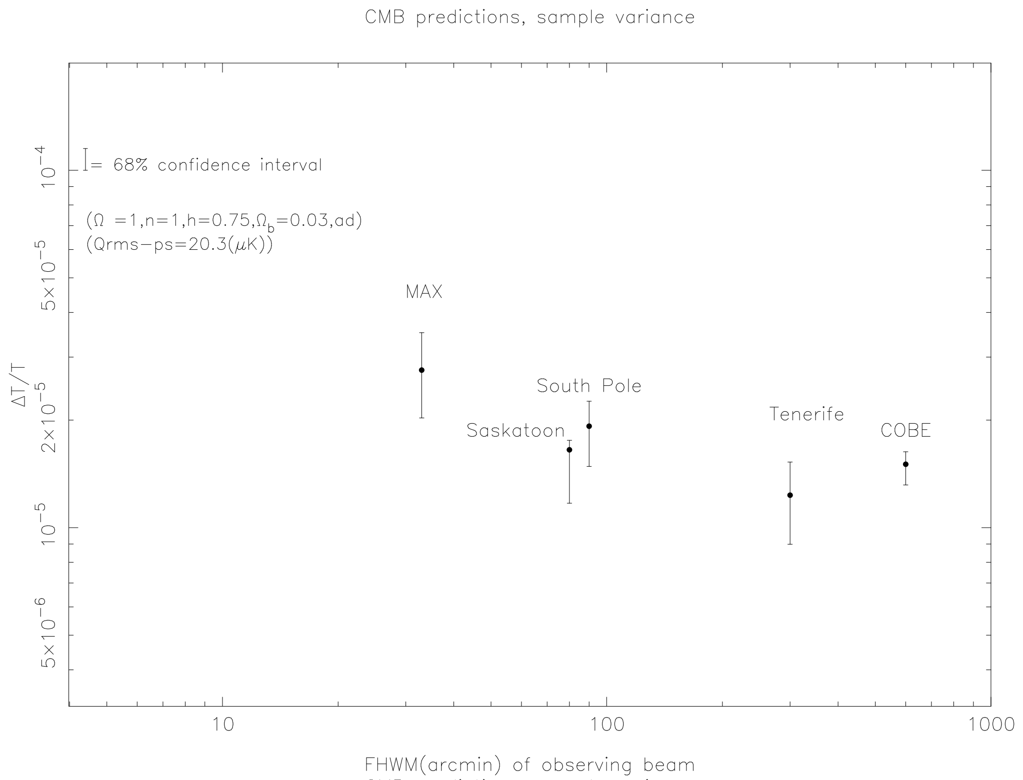

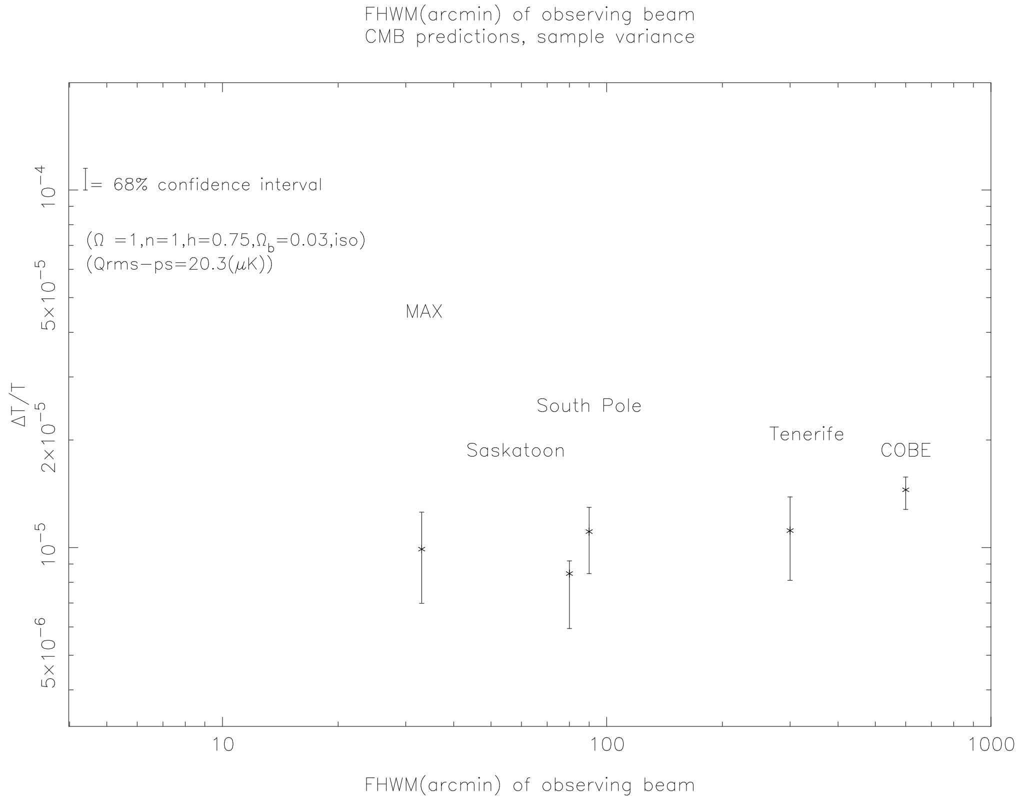

Figure 4.8: continued

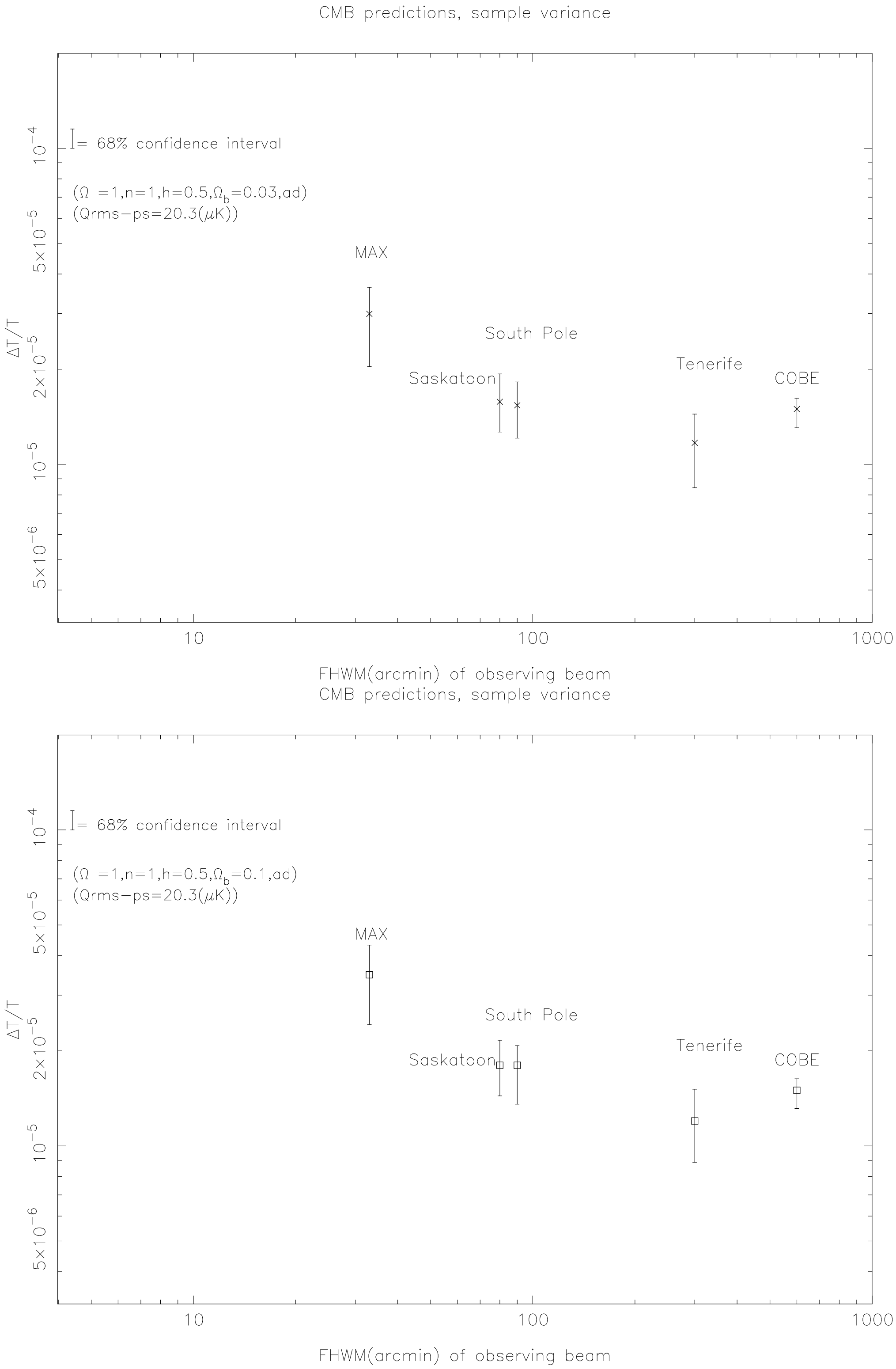

Figure 4.9: Plots of the predicted $\Delta T/T$ vs FWHM of the observing beam given in Table 4.4 (2nd year COBE normalized) and the theoretical uncertainties (68% c.i's) tabulated in Table 4.9. The model parameters are given at the top left of each panel. These results were obtained using FFT simulations for MAX, Saskatoon and South-pole, and the exact window functions for the predictions. The three first plots correspond to adiabatic models while the last one corresponds to an isocurvature model.

we considered the Tenerife experiment and compared the Bayesian probability distribution with that obtained from direct Monte Carlo simulations of the data. We applied the likelihood analysis to the simulated data with some noise contribution and obtained the corresponding Bayesian probability distribution. Using the frequentist approach we simulated a large number of Tenerife data scans and obtained the probability distribution directly. We found that the Bayesian probability distribution was broader then the frequentist one tending to it as the noise contribution was made to tend to zero. The Bayesian and frequentist approaches are found to be consistent for the Tenerife data and to a good approximation the likelihood function is also seen to be an unbiased estimator of the model parameters. This implies that the Bayesian error bars should include both uncertainties. Assuming that Likelihood analysis of data gives all the information, both about the instrumental and theoretical uncertainties, we use for comparison of models and experiments, Fig. 4.2. Following the discussion given in Section 4.2 we conclude from these plots, that isocurvature models are excluded and the best adiabatic candidate seems to be the model with $\mathrm{H}_0 = 50\,\mathrm{km\,s^{-1}\,Mpc^{-1}}$ and $\Omega_b = 0.03$.

4.4.1 5GHz interferometer

Simulating experiments helps also to estimate specific quantities prior to any observation. For instance in the case of the Jodrell Bank 5GHz interferometer we used the simulations in order to estimate the factor of smoothing of the intrinsic anisotropy amplitude due to convolution with the corresponding beam. The 5GHz interferometer is characterized by a primary beam of the order $\sigma_{env} = 3.5°$ and synthesized beam $\sigma_{fringe} = 1.83°$. We simulated a box of size $L = 64°$ for a grid of $N = 128$ points and convolved the resulting map with the interferometer scan strategy. Fig. 4.11 shows one simulated scan as observed by the interferometer, for a CDM model with $\Omega_b = 0.03$ and $\mathrm{H}_0 = 50\,\mathrm{km\,s^{-1}\,Mpc^{-1}}$, σ_8 normalized. For 1000 simulations we found a decrease by a factor of 10 of the amplitude of the temperature fluctuations, caused by the smoothing. The estimation of the CMB fluctuation amplitude expected to be observed by the experiment is particularly useful for the comparison with the expected amplitude contribution from foregrounds, in particular with the predicted Galactic emission.

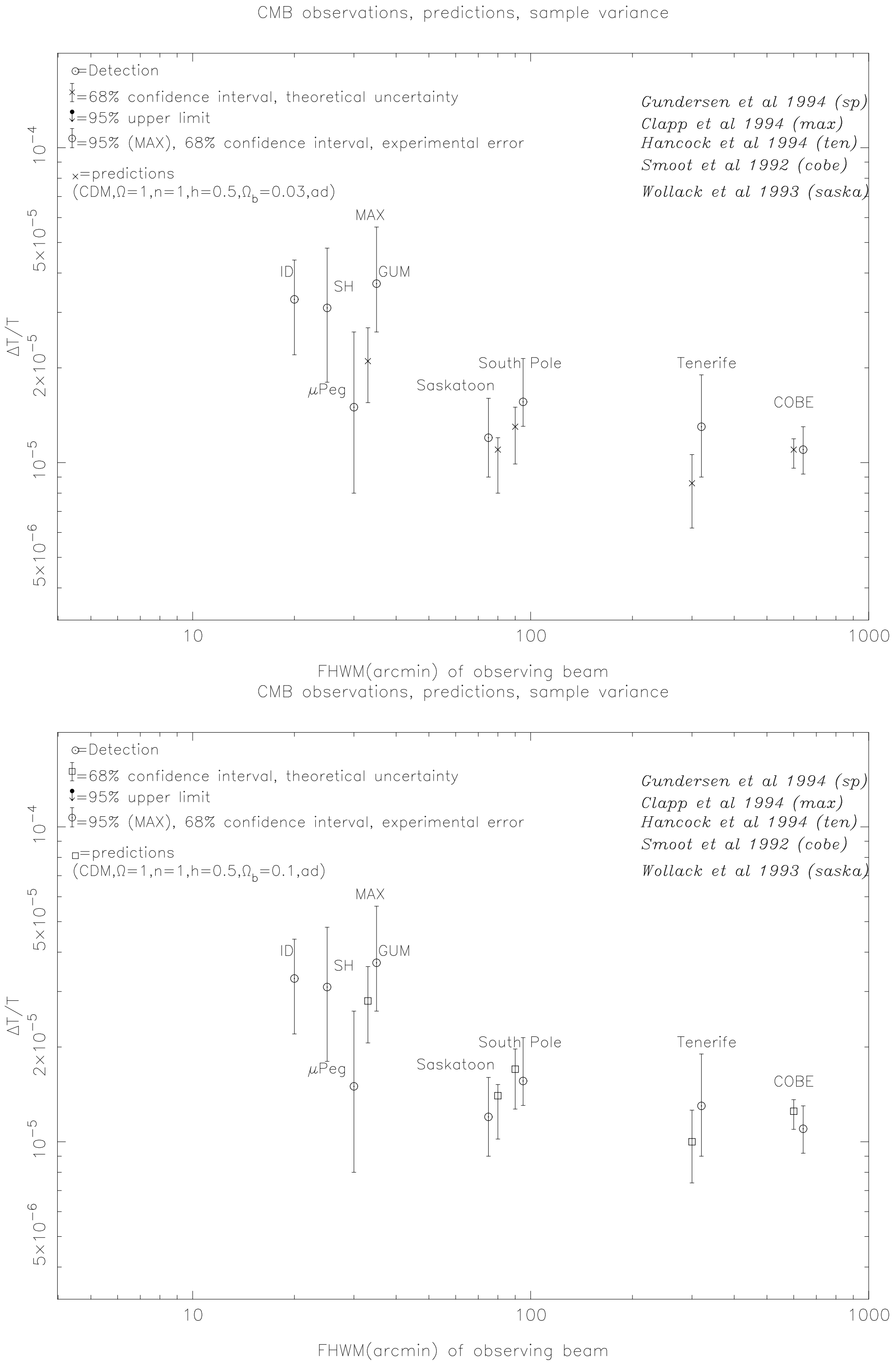

Figure 4.10: Plots of the predicted $\Delta T/T$ vs FWHM of the observing beam given in Table 4.3 and the corresponding 68% c.i. as tabulated in Table 4.8, both converted to σ_8 normalization. Also plotted are the observations displayed in the last column of the Table 4.5 for all experiments, except for COBE, for which the values displayed in the first column are used instead. The experimental error bars represent 95% c.i. for MAX, 90% for MSAM and 68% for the other experiments, while the OVRO data point represents a 95% upper limit. The model parameters are given at the top left of each panel. The three first plots correspond to adiabatic fluctuations while the fourth plot refers to an isocurvature model.

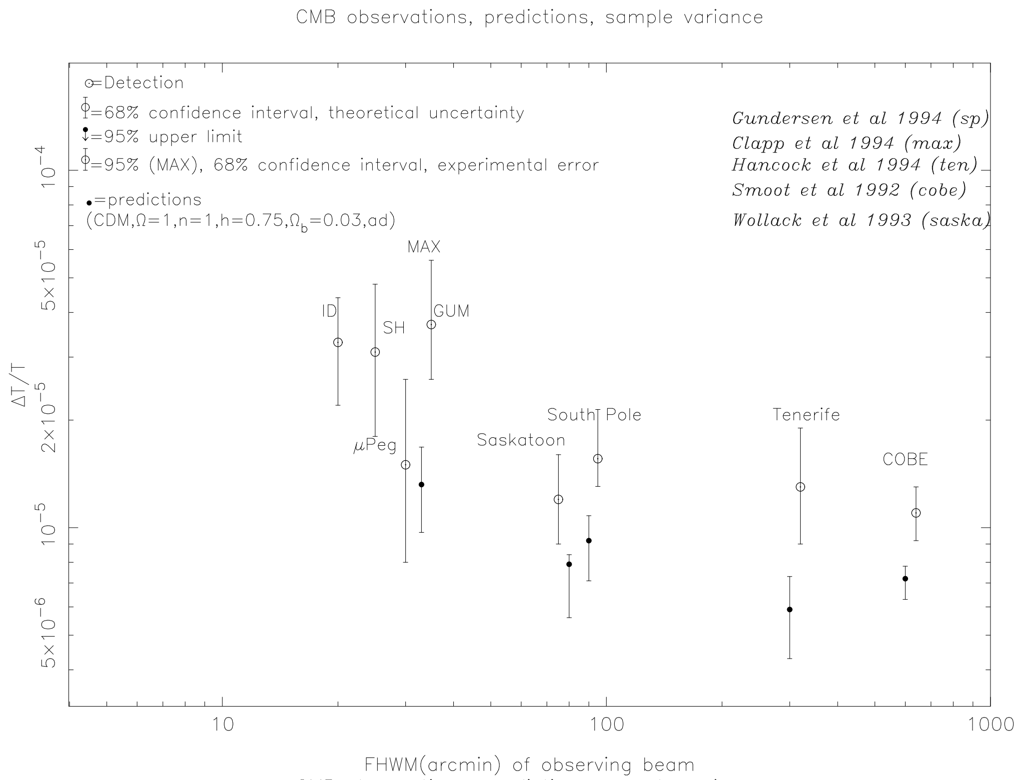

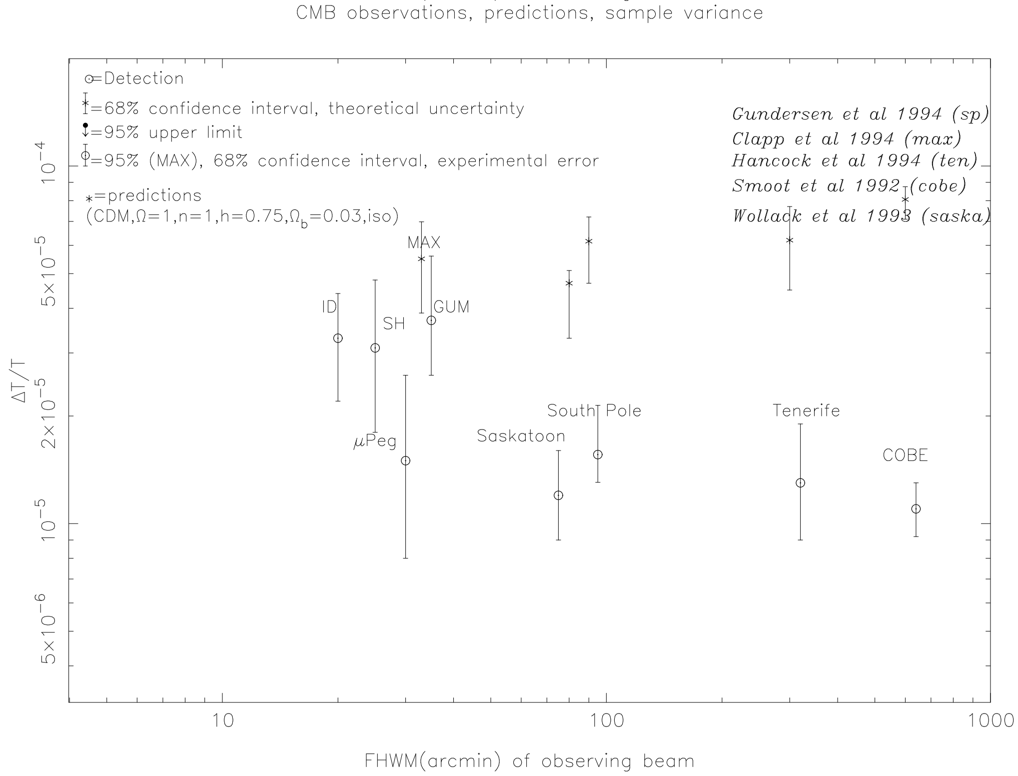

Figure 4.10: continued

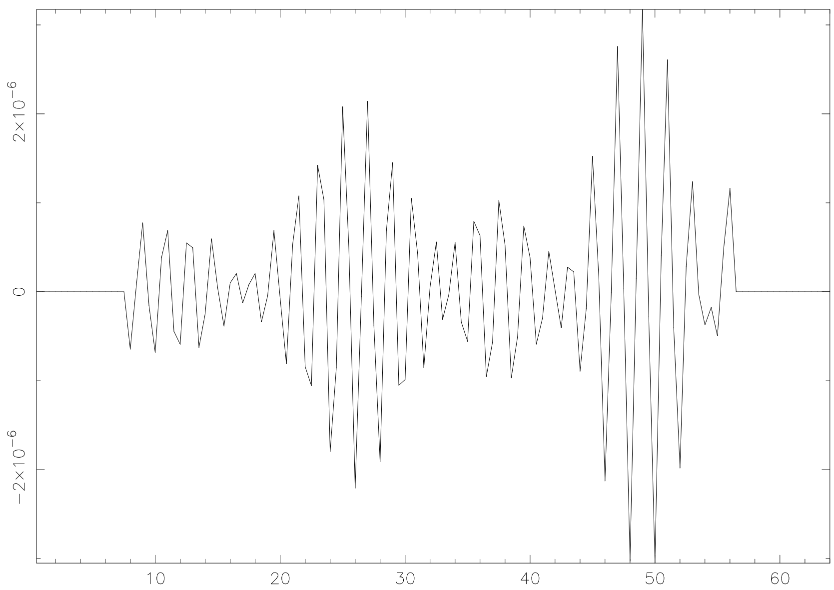

Figure 4.11: A 5Ghz interferometer simulated scan, for a standard CDM model with $\Omega_b = 0.03$ and $\mathrm{H}_0 = 50\,\mathrm{km\,s^{-1}\,Mpc^{-1}}$ (σ_8 normalized).

Chapter 5

The Tenerife experiment

5.1 Introduction

We here discuss the analysis and interpretation of results obtained on relatively large angular scales of $\sim 5^\circ$ by the Tenerife experiment. Observations of fluctuations in the Cosmic Microwave Background (CMB) have been widely recognized to be of fundamental significance to cosmology, offering a unique insight into the physical conditions in the early Universe. As we have seen the amplitudes and distribution of such fluctuations provide critical tests of the origin of the initial perturbations from which the structures seen today have formed. On scales $\gtrsim$ few degrees, CMB observations probe scales of 1000's of Mpc, inaccessible to conventional astronomy. At these large angles, the structures form part of an intrinsic spectrum of fluctuations generated through topological defects or inflation. In this linear growth regime, observations of the scalar CMB fluctuations provide a clean measure of the normalisation of the intrinsic fluctuation power spectrum. This normalisation has been established by a number of independent CMB observations [144, 62, 75]. In many theories, tensor CMB fluctuations from a background of gravitational waves are also expected to be significant on these large scales, and measuring the slope of the power spectrum offers the potential to constrain this contribution to the CMB anisotropy [75, 146, 37]. A comparison of the large-scale anisotropy results with those on medium scales can also be used to separate the scalar and tensor components under the assumption of a specific cosmological model.

The Tenerife CMB experiments were initiated in 1984, with the installation of the first 10 GHz switched-beam radiometer system at the Teide Observatory on Tenerife Island. A subsequent programme of development has led to the present trio of independent instruments working at 10, 15 and 33 GHz. The ultimate objective is to obtain three fully sampled sky maps covering some ~ 5000 square degrees of the sky at each frequency and attaining a sensitivity of ~ 50 μK at 10 GHz, and ~ 20 μK in the two highest frequency channels. Drift scan observations have been conducted over a number of years covering the sky area between Dec=$+30^\circ$ and $+45^\circ$. The deepest integrations have been conducted in the Dec=$+40^\circ$ region and resulted in strong evidence for the presence of individual CMB features (Hancock *et al.* 1994 [75]).

Davies *et al.* 1995 [43] (hereafter Paper I) described the performance of the experiments and gave an assessment of the atmospheric and foreground contributions to our data at

Dec=+40°; here we analyse in detail the results and cosmological implications of such observations. Section 2.4 describes the observational strategy and presents the stacked scans at each frequency. In Section 2.5 we use several statistical methods to calculate the level of the detected signals and their origin. A statistical comparison with the results of the COBE DMR two-year data conducted by Hancock S. and Tegmark M. is mentioned in Section 5.4 and used to place limits on the spectral index of the primordial fluctuations. In Section 5.5 we describe the new maximum entropy based method to reconstruct the intrinsic sky fluctuations as developed in Jones *et al.* [84].

5.2 The scans at Dec +40°

5.2.1 Observations

Observations were conducted at the three frequencies 10, 15 and 33 GHz by drift scanning in right ascension at a fixed declination of 40°. The measurements were made independently at each frequency, using separate dual-beam radiometer systems as described in Paper I. The three instruments are physically scaled so as to produce approximately the same beam pattern (FWHM$\sim 5°$) on the sky, thus allowing a direct comparison of structure between frequencies. A characteristic triple beam profile (switching angle 8.°1) is obtained by the combination of fast switching (63 Hz) of the horns between two independent receivers and secondary switching (0.125 Hz) provided by a wagging mirror. We make repeated observations of the sky, binning the data in 1° intervals in RA and stacking them together in order to reduce the noise as compared with individual measurements. As a consequence of using two independent channels, the receiver noise contribution to the final data scans is reduced by a factor $\sqrt{2}$ compared with single channel observations.

The data considered here are those presented in the preliminary report by Hancock *et al.* (1994) [75] and Hancock *et al.* (1996) [74]. We restrict our analysis to the RA range $161° - 230°$ corresponding to Galactic latitude $b > 56°$. At these high latitudes foreground emission from the Galaxy is expected to be at a minimum. This sky region has also been selected (see Paper I) to be free from discrete radio sources above the 1.5 Jy level at 10 GHz; assuming a flat spectrum this corresponds to an antenna temperature contribution of 48, 21 and 5 μK at 10, 15 and 33 GHz respectively in the Dec=+40° data. The actual contamination is reduced below these levels by using the Kühr catalogue [90] supplemented by the VLA calibrators list to subtract the discrete source contribution from each data scan. This amounts to making corrections to the *rms* signal level of 13, 8, and 3 μK at 10, 15 and 33 GHz respectively. The contribution of unresolved radio sources is expected to be $\Delta T/T \leq 5 \times 10^{-6}$ at 15 GHz and significantly smaller at 33 GHz [2, 59].

Fig. 5.1 presents our final stacked scans at 10, 15, 33 GHz and the weighted addition (named 15+33) of the data at the two higher frequencies. The standard error-bars of each point were calculated considering the presence of correlated atmospheric noise between the two channels of each receiver system as described in Paper I. This represents a mean enhancement of 3 % at 10 GHz, 4 % at 15 GHz, and 16 % at 33 GHz with respect to the estimation of the noise computed in Hancock *et al.* (1994) [75]. The revised sensitivities per beam-sized area are 61, 32, 25 and 20 μK at 10, 15, 33 and 15+33 respectively. A visual inspection reveals the presence of common features in the scans at the two higher frequencies; this is supported by a cross-correlation analysis in Section 5.3.2.

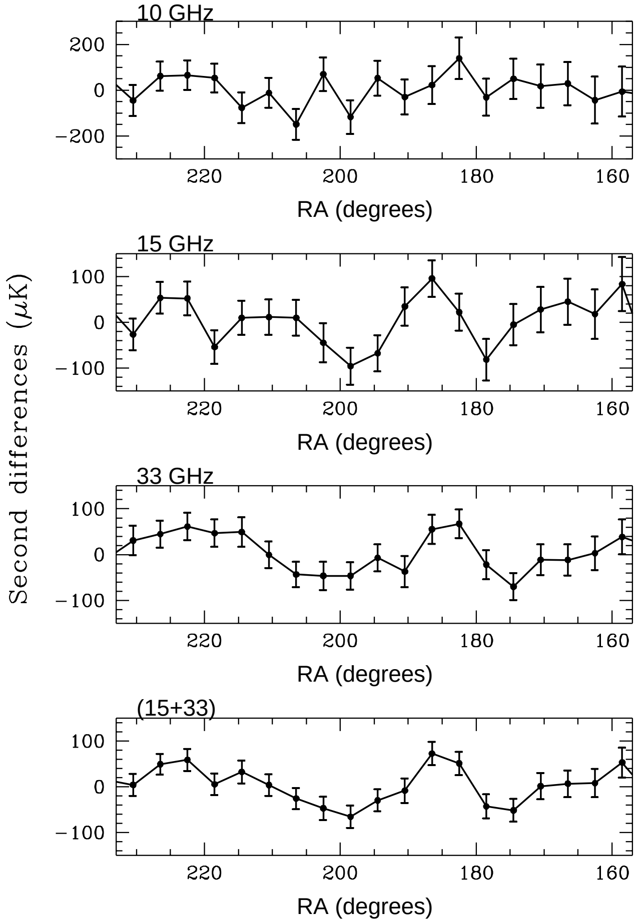

Figure 5.1: The stacked scans at Dec=+40°. The second differences in temperature are shown binned at 4° intervals in RA. The error bars are at 68 % confidence and take into account any atmospheric correlations between receiver channels. The scans labeled 15+33 represent the weighted addition of the data at 15 and 33 GHz.

5.2.2 Reliability of the detected signals

Determination of the amplitude of the CMB component of the structure requires one to consider the contributions of random noise and foreground signals to the observed data scans. The former has its origin in the thermal variations in the receivers and in the fluctuating component of the atmosphere, whilst the latter consists primarily of free-free and synchrotron emission in the Galaxy, plus emission from the Sun and Moon. Of these effects, only the Galactic emission remains constant from day to day at a given frequency. In Paper I it was estimated a maximum Galactic contribution of $\Delta T_{rms} = 4\mu$K in the results at 33 GHz. An improved separation between the Galactic and the cosmological signal at each frequency is under consideration and is partially mentioned in Section 5.5. The effects of the Sun and Moon were removed to better than 50 dB in each daily scan, and stacking n days of observations with the Sun and Moon in different positions will reduce any residual contribution to an insignificant level.

The thermal noise contribution from the receivers conforms to a random Gaussian distribution and integrates down accordingly. In each instrument, the channel 1 receiver is fully independent of the channel 2 receiver and hence there is no correlation between the receiver noise in the data recorded for the two channels. Atmospheric emission varies randomly over days and thus at each frequency, stacking together n days of observations reduces the atmospheric signals in a given day by $\sqrt{n}$. Additionally, the Tenerife observing strategy is such that the *independent* 10, 15 and 33 GHz instruments observe *different* declination strips on any given day so that the atmospheric contribution to data taken at each frequency is uncorrelated. This offers a key advantage over experiments such as Saskatoon [174], where the data in all of the frequency channels are highly correlated thus introducing an element of uncertainty due to the need to account for this. In our individual measurements the atmospheric contribution to each channel is correlated, since the timescale of the receiver switching is short compared with that for typical atmospheric fluctuations. In previous papers [41, 162, 75, 73] this effect was not considered. The presence of a correlated atmospheric component affects the estimation of the astronomical signal based on the difference of the $(A+B)/2$ and $(A-B)/2$ data sets (A and B being separate subsets of the data). In particular if A and B each correspond to one channel, $(A+B)/2$ contains the contribution of the astronomical signal, and the atmospheric and instrumental noise, whilst $(A-B)/2$ only contains the instrumental noise. This is the case for the analysis of the 33 GHz data presented in Hancock *et al.* (1994) [75] and therefore the signal level obtained from the difference in variance between the $(A+B)/2$ and $(A-B)/2$ scans contains a contribution from the atmosphere as well as the astronomy. Note that at 15 GHz the data were subdivided according to the observing epoch and consequently the contribution of the atmosphere to the derived signal was largely reduced.

Here we present a new split of the 33 GHz data into two subsets X and Y such that both channels of a given scan are included in the same data subset. Considering the non-repeatiblity of the atmosphere from day to day common atmospheric signals are not expected to occur in both subsets. Also, considering the large number of independent observations (more than 50 for each channel) we expect that the net effect of the atmospheric signals will be just an increase of the variance in the final stacked scans of each subset, this increase in variance being approximately the same in both. For these reasons, when X and Y are combined to form the $(X+Y)/2$ and the $(X-Y)/2$ scans we expect to have approximately the same atmospheric signals in the sum and in the difference. Fig. 5.2 shows the stacked data scans for the X and Y subsets and their sum and difference. We see a general agreement between the results of splits X and Y, and the presence of common features in both. An analysis similar to that presented in Hancock *et al.* (1994) [75] gives an astronomical signal ($\sigma_s^2 = \sigma^2_{(X+Y)/2} - \sigma^2_{(X-Y)/2}$) with an amplitude $\sigma_s = 43 \pm 12\ \mu$K. The value of the signal quoted in Hancock *et al.* [75] was $\sigma_{old} = 49 \pm 10\ \mu$K; the difference with our improved estimation is certainly due to the subtraction of the atmospheric signal. The difference between both estimates ($\sigma = (\sigma^2_{old} - \sigma^2_s)^{1/2}$) is $\sim 23\ \mu$K which is our best assessment of the atmospheric contamination in the analysis based on the addition and difference of the 33 GHz data; this value is in good agreement with estimates obtained using other methods.

5.3 Statistical analysis

The estimates of the astronomical signals made in the previous section can be improved on using a detailed statistical analysis. Here we use a likelihood analysis and take into account the contribution of the correlated atmospheric noise by enlarging the error bars on the scans as shown in Fig. 5.1. These modified scans are also used to study the presence of common features at 15 and 33 GHz by the calculation of the cross-correlation function.

5.3.1 Likelihood analysis

This analysis takes into account all the relevant parameters of the observations: experimental configuration, sampling, binning, etc. (see Chapter 2). The combination of the atmospheric and instrumental noise can be modeled by a Gaussian distribution uncorrelated from point to point, (see previous section), which implies that the noise only contributes to the diagonal terms of the covariance matrix. We also assume that the astronomical signal is described by a Gaussian random field and therefore our results correspond to a superposition of Gaussian fields in which all their statistical properties are specified by the covariance matrix, which takes into account the full correlation between the data points. The likelihood analysis procedure is to vary the parameters of the model to obtain different values of $C_{int}(\theta)$ and then to calculate the likelihood of observing the data set ΔT. Then the most probable model parameters are determined and a detection of fluctuations will show itself as a peak in likelihood away from zero (see Chapter 2).

For historical reasons we include here the results obtained from the likelihood analysis as applied to an older data set (data I), for a strip at declination 40° at the two lower frequencies, using data covering a period roughly a year longer than that considered in Watson et al. (1992) [162] which is considered in Rocha G. (1993) [126]. At the time these preliminar results already indicated the presence of a good candidate for a real fluctuation in the CMB and also confirmed the suspicion of galactic contamination of the 10GHz data [126].

Fluctuations with a Gaussian auto-correlation function (GACF)

We have analyzed our results for two hypothetical sky models, the first of which corresponds to a signal described by a Gaussian auto-correlation function (ACF) with amplitude $\sqrt{C_0}$ and width θ_c (see Chapter 2). This is not a realistic physical scenario but has been used widely in the past [41, 123, 162] because it provides for an easy comparison between the results of experiments with different configurations. The intrinsic ACF for these models is given by

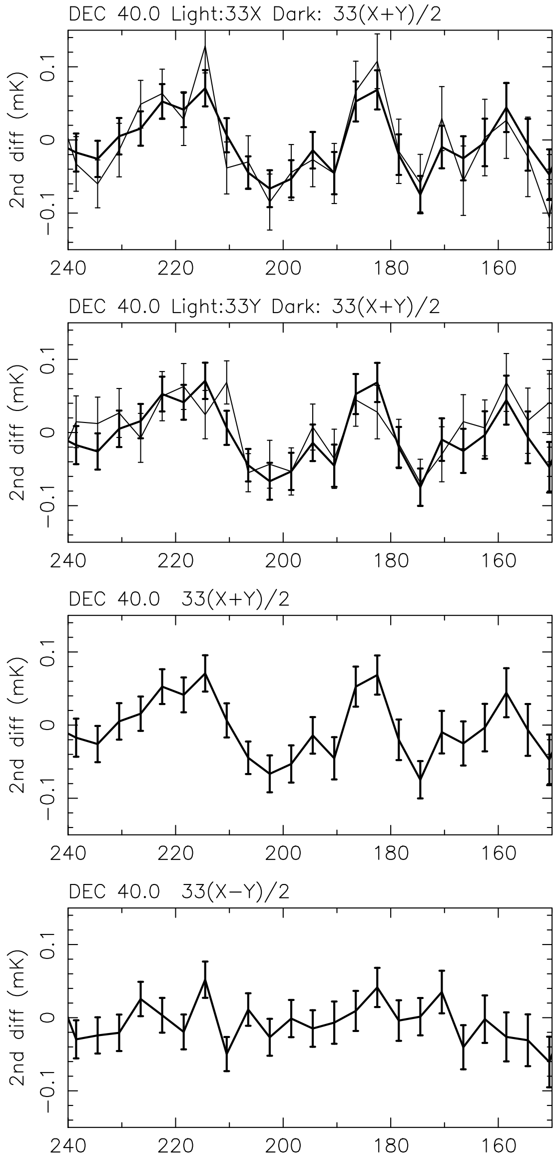

Figure 5.2: The data scans obtained from the analysis of two subsets of the 33 GHz data. In a) and b) are shown the subsets denoted X and Y which are constructed such that the atmospheric contributions to each are independent: see main text for details. The differences in the $(X+Y)/2$ (panel c)) and $(X-Y)/2$ (panel d)) scans should therefore be due only to astronomical signals.

$$C(\theta) = C_0 \exp(-\frac{\theta^2}{2\theta_c^2}). \tag{5.1}$$

which is modified accordingly by our triple beam filtering ([162], see Chapter 2). Our instrument is sensitive over a range of coherence angles $1^\circ \lesssim \theta_c \lesssim 10^\circ$, attaining peak sensitivity for a coherence angle of 4°.

As mentioned above we have applied this analysis to an older data set (data I) described in the introduction of this Section. We analysed two separate ranges of data after correction for known radio sources: RA 161° to 230°, and RA 161° to 250° excluding 181° to 200° (no 181° to 200°). In Fig. 5.3, the upper plot (figure1) represents the contours of equal probability in the (C_0,θ_c) plane. For the 15GHz data is clear that in the data with no 181°-200° the detection is weaker and has moved to a larger angular scale. At these large scales there exist a smearing due to the switching pattern of the experiment, and this in turn drives the likelihood to amplify the true sky level to match. A reasonable conclusion seems to be that a significant detection comes from the region at RA 181° to 200° indicating a strong candidate for a real fluctuation in the CMB. The feature at RA 187° is not predicted from lower frequency galactic maps or known radio sources. With respect to data at 10GHz the indication of detection exists for both regions; one notices that the values of θ_c are large being 10° and 8°, i.e. the analysis has moved to larger angular scales. It is possible that data contaminated by galactic emission could be responsible by the dissimilarity of these results with respect to those for 15GHz data but also the 10GHz data is intrinsically less sensitive.

We have applied this analysis to the latest data at declination 40° described in Section 2.4. We have analyzed the X and Y subsets for 15 and 33 GHz, the total stacked scans at these two frequencies, and our best scan 15+33. The results for $\theta_c = 4^\circ$ are presented in the third column of Table 5.1. The amplitude of the intrinsic signal corresponding to the maximum likelihood is given, along with the one-sigma confidence bounds calculated in a Bayesian sense with uniform prior. All results look consistent with clear detections at the two to three sigma level, and mean values of the signal slightly smaller than those presented in Hancock *et al.* [75], due to the improved estimate of the error bars in the stacked scans (see Section 2.4 and Paper I). Fig. 5.4 presents the contours of equal probability for the 15+33 scan. We see a well defined point of maximum likelihood at $\theta_c \sim 4^\circ$ and $\sqrt{C_0} \sim 50\ \mu$K.

Fluctuations with a power law spectrum

The second model considered here is more interesting from a cosmological viewpoint. It corresponds to the prediction of the power law form ($P(k) \propto k^n$) for the spectrum of the primordial fluctuations (see Chapter 2). Considering only the Sachs-Wolfe part of the spectrum of the fluctuations the intrinsic ACF can be expressed as

$$\begin{aligned} C(\theta) &= \frac{{Q_{rms-ps}}^2}{5} \sum_l (2l+1) C_l^{(S)} P_l(\cos\theta) \qquad (5.2) \\ C_l^{(S)} &= C_2^{(S)} \frac{\Gamma[l+(n-1)/2]\ \Gamma[(9-n)/2]}{\Gamma[l+(5-n)/2]\ \Gamma[(3+n)/2]} \end{aligned}$$

where the sum is extended to the multipoles $l \lesssim 60$ which corresponds to the range of angular sensitivity of our experiments. For $l \gtrsim 20$, standard models predict additional contributions to the CMB anisotropy, as one moves into the low l tail of the CMB Doppler peak. Hence fitting for the Sachs-Wolfe term alone (Equation 5.2) to CMB data on these scales can lead to the derived values for n being increased by as much as 10% over the true primordial value. This point should be borne in mind when comparing the limits on n from the Sachs-Wolfe term (Section 5.4) to those from a fit to a full CDM type functional form as in Chapter 7. For a given value of the spectral index n, the intrinsic ACF is a function only of Q_{rms-ps} .

We have applied this analysis to the older data set (data I) mentioned previously. In Fig. 5.3, the bottom plot (figure 2) represents the likelihood contours in the (Q_{rms-ps} ,n) plane, for the older data set [126]. For the 15GHz data one verifies that when removing the data from 181°-200° the spectral index n changes from 1 to 0.5, and the region of significant detection gives rise to $n = 1$, scale invariant spectrum, as expected from inflationary scenarios. The results for the 10GHz data are in agreement with the considerations drawn for the GACF case. The concern over residual Galactic emission at this lower frequency led us to exclude the 10GHz data from the weighted combination of the data scans.

The same analysis was applied to the recent data described in Section 2.4. Fig. 5.5 shows the likelihood surface as a function of Q_{rms-ps} and n for the 15+33 scan. The peak likelihood forms a ridge displaced from zero in Q_{rms-ps} and corresponds to a $3-4$ sigma detection of structure for each value of n considered. The shape of the surface implies that all values of n in this range are equally likely. This is predominantly a consequence of our observing technique which samples only a small angular range of the spectrum of fluctuations. Thus whilst our observations provide a good measure of the fluctuation power on $\sim 4°$ scales, they do not in themselves contain sufficient information about the distribution of power with angular scale to allow a useful determination of the spectral slope: for this one must compare with experiments on other angular scales (see Section 5.4 and Chapters 6 and 7). For the specific case of a Harrison-Zel'dovich spectrum ($n = 1$) the results of the likelihood analysis are given in column two of Table 5.1. The normalisation Q_{rms-ps} corresponds to the maximum of the likelihood function and the confidence intervals are at 68 %, calculated in the standard Bayesian manner using uniform prior. We see that in general the results are consistent and agree with a global normalization of the quadrupole $Q_{rms-ps} \sim 20-25\ \mu$K. Our best estimate for Q_{rms-ps} of $22^{+10}_{-6}\mu$K from the 15+33 scan is reduced over the value of $26 \pm 6\mu$K previously reported due to our now having properly accounted for the correlated atmospheric noise.

5.3.2 Cross-correlation analysis

We have investigated the presence of common features in our 15+33 scans at Dec=+40° by evaluating the cross-correlation function,

$$C(\theta) = \frac{\sum_{i,j} \Delta T_i \Delta T'_j w_i w'_j}{\sum_{i,j} w_i w'_j} \qquad (5.3)$$

where ΔT and $\Delta T'$ denote the second differences in the stacked scans at 15 and 33 GHz respectively. The sum is extended over all points subtending a mutual angle θ in RA, with weights $w_i = 1/\sigma_i^2$ and $w'_j = 1/\sigma_j'^2$ respectively. The data points in Fig. 5.6 represent the mean and 68 % confidence intervals of $C(\theta)$. The observed profile is characteristic of the triple beam sampling and it is clear that for angles $\theta \lesssim 20°$ the results are consistent with the presence of common signals in the two independent data sets. Because of the non-independence of the data points in the cross-correlation function, the statistical significance

Figure 5.3: Contour levels of equal likelihood for the older data set, data I. Figure 1: fluctuations with a Gaussian auto-covariance; Figure 2: fluctuations with a power law spectrum.

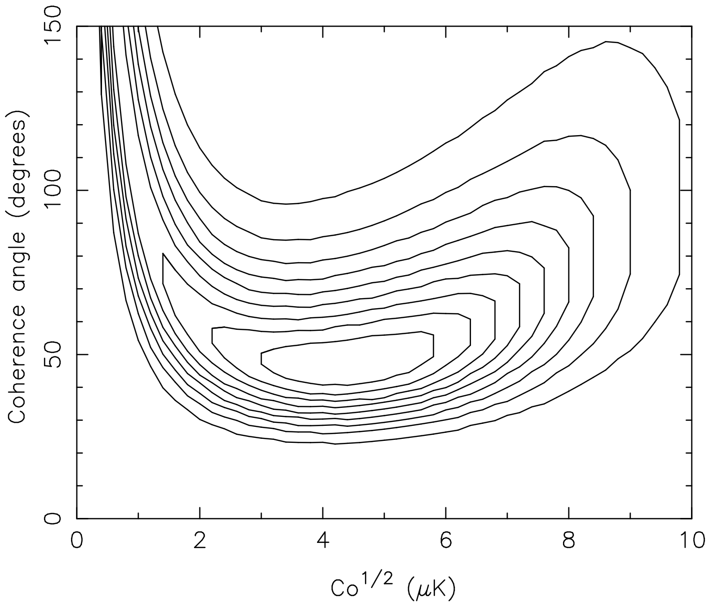

Figure 5.4: Contour levels of equal likelihood for the 15+33 scan in the case of a Gaussian shaped ACF. The contours correspond to 10, 20, 30 ... 90 % of the total probability distribution. The Tenerife configuration obtains maximum sensitivity for coherence angles in the range $2^\circ \lesssim \theta \lesssim 6^\circ$; structure is clearly detected at $\sim 50\mu$K over this angular scale range.

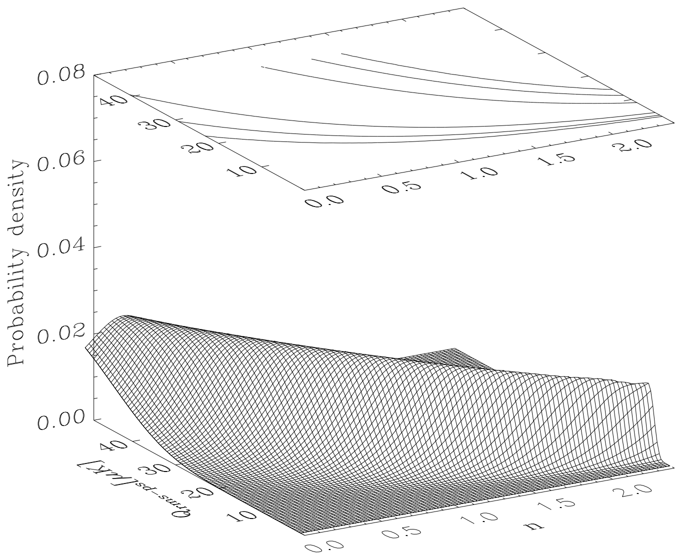

Figure 5.5: The two-dimensional normalised likelihood surface as a function of the spectral index n and the normalisation Q_{rms-ps} for the Tenerife data. The projected contours are at 68 %, 95 % and 99 % confidence.

Table 5.1: Results of the likelihood analysis for a Harrison-Zel'dovich spectrum of fluctuations (second column) and for a Gaussian ACF (third column).

ν (GHz)	Q_{rms-ps} (μK)	$\sqrt{C_0}$ (μK)
15A	27^{+16}_{-16}	54^{+37}_{-30}
15B	17^{+9}_{-17}	24^{+21}_{-24}
15	21^{+12}_{-9}	44^{+26}_{-19}
33A	22^{+14}_{-10}	45^{+32}_{-24}
33B	28^{+12}_{-9}	57^{+28}_{-25}
33	24^{+11}_{-8}	49^{+27}_{-17}
15+33	22^{+10}_{-6}	48^{+21}_{-15}

is difficult to evaluate, requiring the computation of the covariance matrix of the correlation function (see *e.g.* Ganga *et al.* 1993 [62]). However, considering only the correlation at zero lag, the observed value of $C(\theta) = 1100^{+680}_{-720}$ μK^2 is found to be inconsistent with noise at the 95 % level. This value for the amplitude of the component of the signal common to the 15 and 33 GHz data is in agreement with the equivalent estimates of the variance of the signals present in each data scan separately, demonstrating that common signals can account for all of the structure seen in the separate scans. This is contrary to what one expects for structure of Galactic origin, which in the case of synchrotron and free-free emission would exhibit a change in amplitude by a factor 9 and 5 respectively on moving from 15 GHz to the higher frequency of 33 GHz. This result taken in conjuction with the limits on the Galactic contamination of the 33 GHz scan (see above) and the successful comparison of the features seen in the 15 and 33 GHz scans with the higher frequency COBE data [105], leads us to assign a cosmological origin to the majority of the signal present in the 15 GHz data.

We have explicitly tested the consistency of the common signals with fluctuations originating in inflationary type models which predict an approximately scale invariant $n \simeq 1$ spectrum of fluctuations. Using the normalisation of $Q_{rms-ps} = 22\mu$K as derived from the likelihood analysis of the 15+33 scan we simulated 5000 realisations of a sky conforming to a Harrison-Zel'dovich spectrum and repeated the Tenerife sampling strategy. The mean value (solid line) and one-sigma confidence intervals (dashed lines) of the auto-correlation function obtained from these realisations are plotted in Fig. 5.6. There is clearly a good level of agreement in the amplitude and shape of the experimental results and the theoretical model. Statistically the Tenerife observations have the properties expected for primordial fluctuations generated from inflation, and although these results do not prove inflationary theory, this does offer a plausible explanation for the existence of structure on scales greater than the horizon volume at recombination. In this case, the clearly defined structures visible in the scans in Fig. 5.1 represent the seed perturbations generated in the inflationary era at $t < 10^{-34}$s. In the following section we investigate the potential to prove or disprove inflation by measuring the slope n of this primordial spectrum of fluctuations using large scale CMB anisotropy measurements.

5.4 Statistical comparison with COBE DMR

A comparison between the results of different CMB experiments offers the opportunity to check independent measurements, to extend the range in frequency and angular scale, to constrain cosmological models and, if the sensitivity of the experiments is sufficient, to compare features. There are several experiments operating on angular scales of a few degrees: MIT [62], COBE [144, 13]), RELIKT [149], ARGO [44] and Tenerife. The first comparison between independent CMB observations was made by Ganga *et al.* (1993) [62] who found a clear correlation between the results of the first year of COBE DMR observations and those of the MIT experiment. De Bernardis *et al.* (1994b) [45] have also made a statistical comparison between the amplitude of the signal reported for ARGO and that of the COBE DMR first year results, from which they constrain the spectral index to be $0.5 \leq n \leq 1.2$ in the absence of any gravity wave background. In the preliminary report (Hancock *et al.* 1994 [75]) the amplitude of the signal detected on $\sim 5°$ scales in our Dec=+40° data was compared with that on $\sim 7°$ scales for the first year of COBE data. In this comparison we estimated the predicted Tenerife triple beam variance necessary for

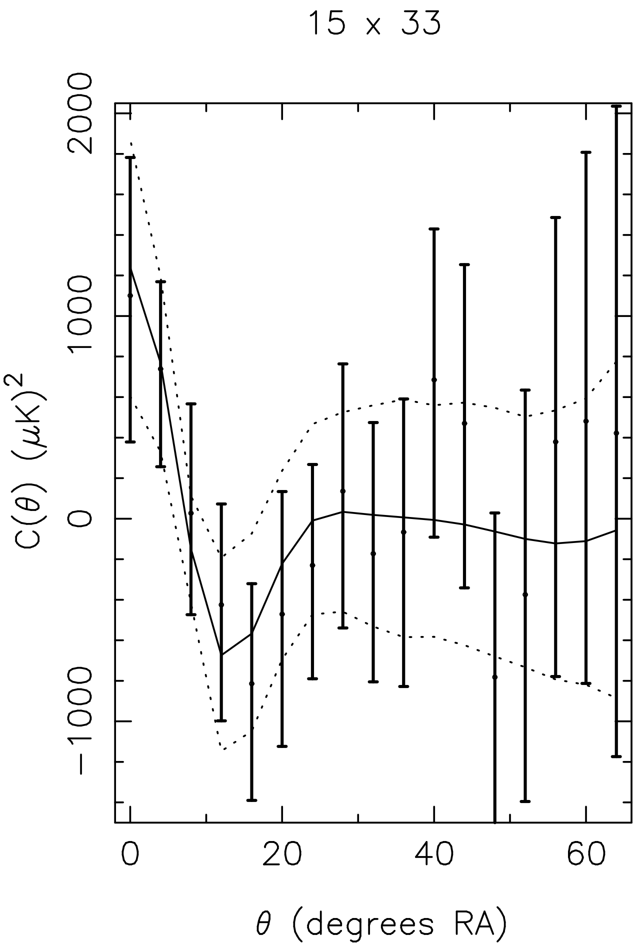

Figure 5.6: The cross-correlation function $C(\theta)$ for the 15 GHz and 33 GHz data over RA=161°−230° showing the data points and the one sigma error-bars. The solid line corresponds to the prediction of a Harrison-Zel'dovich spectrum of fluctuations with a normalization of $Q_{rms-ps} = 22\ \mu$K. The dashed lines are the 1σ confidence bounds arising from cosmic variance and sample variance.

agreement with the COBE results. On the COBE and Tenerife angular scales the main source of perturbations on the CMB is the Sachs-Wolfe effect and their spectrum reflects that of the initial seed fluctuations (see Chapter 2). Thus one can use the power-law representation for the power spectrum to scale the COBE detection level to the Tenerife angular scales. We estimated $(\Delta T/T)_{rms}$ for the Tenerife experiment using Equation 2.65 and 2.67 of Chapter 2, and the Sachs-Wolfe expression for the angular power spectrum given by Equation 2.99 and 2.95 of Chapter 2 or Equation 5.2. We normalized the angular power spectrum to the first year COBE detection of $Q_{rms-ps} = 16.3 \pm 4.6$ μK at $n = 1.15$ and scaled as function of n as described in Fig 3 of ref. [163]. In order to consider the uncertainty introduced by the cosmic variance and sample variance (Chapter 2) we used Monte Carlo simulations to produce a large number (5000) of realizations of skies described by a power-law power spectrum as normalized to the COBE first year detection. For each of these realizations we then mimic the Tenerife sampling strategy and predicted the variance and its confidence bounds for the range of n considered. Fig. 5.7 compares the Tenerife detection level in a triple beam as obtained in Hancock *et al.* 1994 [75] with that of the COBE observations. We found that both results were consistent with inflationary models ($n \gtrsim 0.9$) but with a favoured spectral index of $n = 1.6$ (this value decreases if we use in the comparison the new astronomical signal corrected for the atmospheric contamination). Lineweaver *et al.* (1995) [105] have presented the first direct comparison of CMB features between the two-year COBE DMR data and the Tenerife Dec=+40° observations, confirming the agreement in the level of the normalization of both experiments and providing clear evidence for the presence of common hot and cold spots in both data sets.

Here we give a brief account of a new comparison carried out by S. Hancock and M. Tegmark [74]. We include this method here due to the importance of the results obtained and also for comparison with the results obtained from COBE and Tenerife separately. This comparison is different to that conducted in Hancock *et al.* (1994) [75] in that they use a more rigorous comparison technique that utilises the likelihood function to incorporate fully the effects of cosmic and sample variance, random noise and the interdependence of the model parameters. In addition to the improvements from this revised analysis, the new results also reflect the increased sensitivity of the COBE data after two years of observing, along with the more accurate estimate of the cosmological signal in the Tenerife data.

5.4.1 Properties of the two data sets

The instrumental profile of the COBE data is described approximately by a Gaussian beam with FWHM$\sim 7°$. As can be seen in Fig. 1 of Watson *et al.* (1992) there is a range of angular scales to which the COBE DMR and Tenerife experiments are both sensitive. Measurements taken by COBE cover the full sky, but to determine the CMB fluctuations the region of the Galactic plane has been excluded ($|b| \leq 20°$) thereby introducing a degree of uncertainty in estimating the properties of the global field; this effect is commonly termed sample variance [135] (Chapter 2). The uncertainties in the COBE two year results are dominated by the effect of cosmic variance *i.e.* the fact that our stochastic theory describes the Universe as a particular realisation of a random field (Chapter 2). Together the cosmic and sample uncertainties form an intrinsic limitation of the COBE experiment since unlike random errors they are not reduced by increased integration time. The two year COBE data have been analysed independently by a number of authors (*e.g.* [8, 13, 65, 175]). All find evidence for statistically significant structure at an amplitude

Figure 5.7: Constraints on the spectral index n of fluctuations from a comparison of the Tenerife detection level with that of the COBE results. The variance in a Tenerife triple beam necessary for agreement with the COBE results is plotted as the solid curve, bounded by the one standard deviation confidence limits (dotted curves). Comparison of the observed value, $\sigma_{s,old} = 24 \pm 9$ μK according to Hancock *et al.* (1994), (horizontal lines) defines the shaded region of n space allowed by the combined observations.

consistent with that of 30 ± 5 μK *rms* on a $10°$ scale announced by Smoot *et al.* (1992) for the first year data. The best fit values for n and Q_{rms-ps} depend on the precise analysis techniques employed, but are generally consistent with the values of $n = 1.10 \pm 0.29$, $Q_{rms-ps} = 20.3 \pm 4.6$ μK found by Tegmark and Bunn (1995) [153] for the combined 53 and 90 GHz data with the quadrupole included. In the case of the Tenerife experiment the double-switching scheme removes the contribution of low order multipoles decreasing the cosmic variance of the signal on these large scales; the major source of uncertainty is produced by the partial sky coverage (sample variance) and the instrumental noise. The region observed by the Tenerife experiments covers ~ 5000 square degrees but here we have limited our analysis to our region of deepest integration at high Galactic latitude which constitutes a sample ~ 500 square degrees. For such a region the uncertainties due to the partial sky coverage dominate over the intrinsic variance by a factor ~ 10 [135] (see Chapter 4) and the combined uncertainty is approximately of the order of that introduced by the instrumental noise in the 15+33 scan.

In previous work (Hancock *et al.* 1994 [75]) the effects of cosmic and sample variance were taken explicitly into account by using Monte Carlo simulations. This was necessary because the simple excess variance statistic used in the comparison incorporated only the uncertainty due to random noise. The comparison by necessity assigned equal probability to all values of n for the COBE data, since the COBE first year results were only published in the form of a best fit n versus Q_{rms-ps} relation rather than a full two dimensional probability distribution. What is required is a data analysis technique that allows the joint probability of any combination of the model parameters to be calculated and which implicitly takes into account random errors and cosmic and sample uncertainties. The Bayesian approach using the likelihood function as described in Section 3 attempts to do precisely this. The likelihood function peaks at the most likely parameters (the best estimate of the true values if the likelihood function is unbiased) and has some distribution which through Bayes theorem is representative of the combined effects of the cosmic, sample and random uncertainties. The issue of how well this distribution reflects the true uncertainties is addressed by comparison of the Bayesian probability distribution with that obtained from direct Monte Carlo simulations of the data (see Chapter 4). The Bayesian and frequentist approaches are found to be consistent for the Tenerife data and to a good approximation the likelihood function is also seen to be an unbiased estimator of the model parameters. Consequently the likelihood surface for the joint Tenerife and COBE data set provides the definitive means of comparison of the observations under some assumed sky model.

5.4.2 The Tenerife-COBE likelihood function

S. Hancock and M. Tegmark applied the likelihood analysis to the COBE two year data and the Tenerife 15+33 scan, assuming a power law model with free parameters n and Q_{rms-ps}. The COBE Galaxy-cut two-year map consists of 4038 pixels, whilst the Tenerife Galaxy cut (RA $161° - 230°$) scan contains 70 pixels, requiring a 4108×4108 covariance matrix for a joint likelihood analysis of the data. For details about the implementation of the joint Tenerife-COBE likelihood function see Hancock *et al.* 1996 [74]. The covariance matrix consists of three parts: a 70×70 block with the covariance between the Tenerife pixels, a 4038×4038 block with the covariance between the COBE pixels, and off-diagonal 4038×70 blocks containing the covariance between the Tenerife and COBE pixels. Simply multiplying the likelihood curves resulting from two separate analyses of the COBE and

Tenerife data sets would correspond to neglecting the off-diagonal blocks, and this is clearly only a good approximation if the two data sets are almost uncorrelated. We find that the inclusion of the cross-terms makes a non-negligible difference, which is not surprising in view of the fact that the two experiments probe comparable angular scales and have observed a common region of the sky.

For our Tenerife data, the best estimate of the cosmological signal is obtained from the 15+33 combined scan after correction of the error bars for the correlated atmospheric noise term. The possible contribution of Galactic signals has been estimated from the 10 GHz data to be less than 4 μK at 33 GHz and has not been considered in the current comparison. The normalised likelihood function for this scan, as plotted in Fig. 5.8, represents the joint probability of obtaining a given combination of n and Q_{rms-ps}. On its own, the Tenerife configuration provides less leverage on the slope of the spectrum than the COBE satellite. This is because the Tenerife experiment is insensitive to the largest angular scales, and because the one-dimensional shape of the dec+40° strip makes it difficult to separate the power contributions from different scales. In other words, a narrow strip corresponds to wide window functions in ℓ-space, with considerable aliasing of small-scale power onto larger scales (just as the case is with one-dimensional "pencil beam" galaxy surveys). As a result, the Tenerife data can be equally well fit by a range of n and Q_{rms-ps} values, resulting in a likelihood ridge in (n, Q_{rms-ps})-space with minimal discriminatory power for the parameter n. In contrast, the COBE observations are sensitive to the slope to the extent that the likelihood surface is peaked in the n-dimension. Combining the COBE information with the Tenerife data improves the situation in two ways: it extends the lever arm on the spectral slope from the COBE scales down to the 4° scale of Tenerife, and in addition eliminates the above-mentioned aliasing problem, since the joint data set is no longer one-dimensional.

Fig. 5.8 shows the confidence contours obtained from Bayesian integration under the combined COBE and Tenerife likelihood surface assuming a uniform prior. The 68% joint confidence region in (n, Q_{rms-ps})-space encloses a region from 0.90 to 1.73 in n for Q_{rms-ps} in the range from 12.1 to 22.9 μK, with the peak at $n = 1.37$, $Q_{rms-ps} = 16.1\mu$K. Marginalizing over Q_{rms-ps} with a uniform prior, one obtains the probability distribution for n as given in Fig. 5.9, corresponding to $n = 1.33 \pm 0.30$ at 68% confidence. The resulting limits on the normalization, conditioned on $n = 1$ as is customary, are $Q_{rms-ps} = 21.0 \pm 1.6$. The corresponding results in Tegmark and Bunn (1995) [153], hereafter "TB95" using just the COBE data, and including the weak correlated noise term [105], were $n = 1.10 \pm 0.29$ and $Q_{rms-ps} = 20.3 \pm 1.5$, with the peak likelihood located at $n = 1.15$, $Q_{rms-ps} = 18.2\mu$K. In other words, although the total normalization has risen by a mere 3%, the slope estimate has risen by 12% and the peak likelihood has been shifted to higher n and lower Q_{rms-ps}. This indicates that the higher angular resolution data from the Tenerife experiment contains slightly more power on small scales. As explained in Section 2.5, this is not unexpected, since the presence of a Doppler peak would cause a rise in the power spectrum at higher l.

The large angular scale CMB observations from Tenerife and COBE probe fluctuations that have yet to go non-linear and the shape of the power spectrum is thus insensitive to the exact abundance of the baryonic mass (Ω_b) and to the value of $h = \mathrm{H}_0/100\,\mathrm{km\,s^{-1}\,Mpc^{-1}}$. However, together the Tenerife and COBE observations provide a direct measure of the CMB power spectrum normalisation, against which one can compare intermediate scale observations and hence discriminate between competing cosmological models. Here we stress the importance in the agreement between the derived normalisation for the inde-

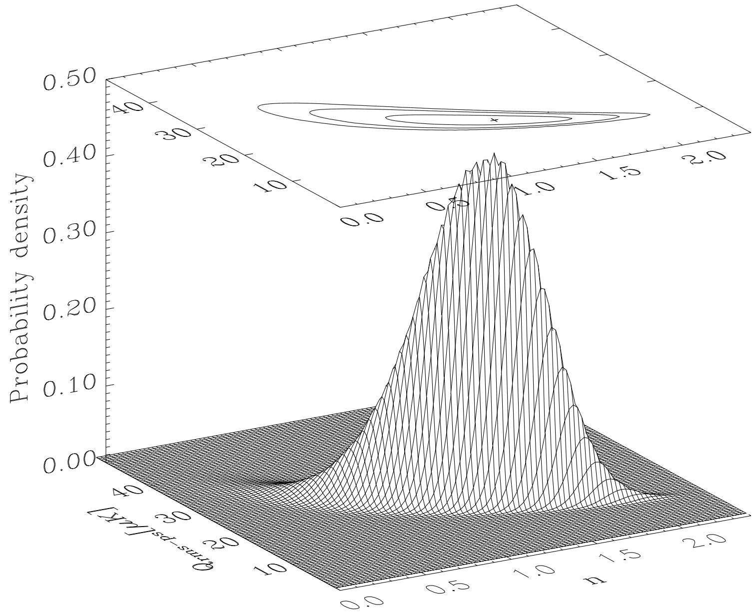

Figure 5.8: Constraints on the quadrupole Q_{rms-ps} and on the spectral index n of fluctuations obtained from a joint likelihood analysis of the Tenerife data and COBE DMR two-year data. The contour levels represent 68 %, 95 % and 99 % of the region of joint probability. The peak of the distribution lies at $n = 1.37$, $Q_{rms-ps} = 16.1\mu$K and is identified by the cross.

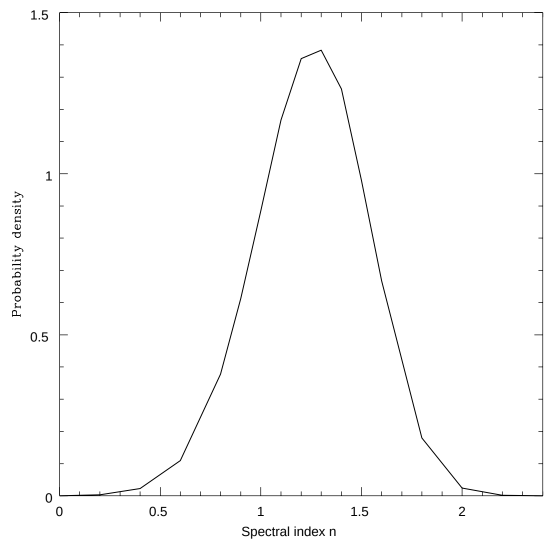

Figure 5.9: The marginal likelihood for the spectral index n as obtained from the joint analysis of the Tenerife and COBE data. The spectral index is seen to lie in the range $1.02 \leq n \leq 1.62$ at 68% confidence, with a best fit value of $n = 1.33$.

pendent Tenerife and COBE experiments, which are subject to different systematic errors and different foreground contamination. The accuracy to which we know the normalisation of the power spectrum clearly becomes an issue when comparing with smaller scale observations to determine cosmological parameters. This is a particular concern if, as has been suggested [37, 146, 1], a component of the large scale anisotropy may be due to tensor metric perturbations produced from a background of gravitational waves. These can arise naturally in inflationary scenarios and would contribute a component $C_l^{(T)} = < |a_{lm}^T|^2 >$ to the observed CMB angular power spectrum (cf Equation 5.2). The ratio of the tensor modes $C_l^{(T)}$ to the scalar modes $C_l^{(S)}$ (primordial density fluctuations) is highly suppressed for fluctuations contained within the horizon volume at recombination and hence their contribution is only significant on scales $\gtrsim 2^\circ$. Consequently the existence of a tensor contribution has implications when comparing the large scale anisotropy level with that on smaller scales and with large scale structure observations in order to test cosmological models. The anisotropy measurements from Tenerife and COBE fix the sum of $C_l^{(T)}$ and $C_l^{(S)}$, but the separation of the two terms requires a comparison with smaller scale observations under the assumption that a given cosmological model is correct [37, 146]. In the case of power law inflation a relation exists between the tensor to scalar ratio $C_2^{(T)}/C_2^{(S)}$ and the slope of the primordial power spectrum [37, 146]:

$$C_2^{(T)}/C_2^{(S)} \approx 7(1-n) \tag{5.4}$$

from which we see that the two contributions are comparable at $n = 0.85$ with $C_l^{(T)}$ decreasing relative to $C_l^{(S)}$ for higher values of n. Thus the limit of $n \geq 1.0$ obtained from the analysis of the combined Tenerife and COBE data in Section 5.4.2 implies that it is unlikely that the tensor component will be dominant in such models. This is investigated in more detail by comparing with medium-scale anisotropy results.

The work required to place the existing medium scale anisotropy results into a common statistical framework and then to compare them with the predictions of cosmological models, is carried out in Chapters 6 and 7.

5.5 Maximum Entropy deconvolution

A new maximum entropy based method to deconvolve CMB data has been developed and is described in Jones *et al.* [84]. In this procedure a positive/negative algorithm is used in order to produce two-dimensional maps of the intrinsic fluctuations. This technique enables to reconstruct data containing negative peaks. This procedure was applied to the original (FWHM$\simeq 8^\circ$) Tenerife twin horn radiometer experiments (Davies *et al.* 1992 [42]), covering a set of declinations ranging from -15° to $+45^\circ$, in order to produce 2D maps of intrinsic fluctuations and simultaneously produce scans free from atmospheric baseline variations. The separation between astronomical signal and long term atmospheric baseline drifts is achieved by using the time invariance and spatial continuity of the astronomical sky. Known discrete sources and Galactic features were identified in the deconvolved map and limits on the high Galactic latitude emission were obtained from the statistical analysis of the data scans. Since 10.4 GHz data is sensitive to CMB and discrete radio sources but also to synchroton and free-free emission these maps can be used to put constraints on the contamination of the high frequency data by using the different spectral signature of the CMB signal and the foregrounds. For the description of the data and the particular instrumental configuration as the implementation of the maximum entropy method (MEM) algorithm see Jones *et al.* [84]. The performance of this technique was tested using simulations of a CDM sky with some noise added as described in Section 5.5.4. This method showed no bias towards positive or negative reconstruction or towards any model, being only biased towards the smoothness premise. From these simulations we concluded that the algorithm succeed in recovering the shape, size, position and amplitude of structures in both the reconvolved scans and the two-dimensional deconvolved sky maps. The MEM approach permits to compare and combine data from different observational strategies, since each data set is considered as a separate constraint on a single reconstructed sky. This new method is particularly useful in reconstructing intrinsic sky fluctuations maps free of Galactic contamination since it allows the combined use of the data from different experiments and at different frequencies.

5.5.1 The problem

In general the data from a CMB experiment consists in the true sky convolved with the instrumental response matrix with any baseline variations or noise terms added on. We assume that the observations obtained from a particular experiment have been integrated into discrete bins. For the i-th row and the j-th column the data, $y_i^{(j)}$, recorded by the instrument can be expressed as the instrumental response matrix $R_i^{(j)}(i',j')$ acting on the true sky $x(i',j')$:

$$y_i^{(j)} = \sum_{(i',j')} R_i^{(j)}(i',j')x(i',j') + \epsilon_i^{(j)}, \tag{5.5}$$

where i' and j' label the true sky row and column position respectively. The $\epsilon_i^{(j)}$ term represents a noise term, assumed to be random Gaussian noise.

It is clear from Equation 5.5 that the inversion of the data $y_i^{(j)}$ to obtain the two-dimensional sky distribution $x(i', j')$, is singular. The inverse R^{-1} of the instrumental response function does not exist, unless the telescope samples all of the modes on the sky and consequently there is a set of signals, comprising the annihilator of R, which when convolved with R gives zero. Furthermore, the presence of the noise term ϵ will effectively enlarge the annihilator of R allowing small changes in the data to produce large changes in the estimated sky signal. It is therefore necessary to use a technique that will approximate this inversion.

One method proposed is Wiener filtering [27] of the data set, which allows the inversion to be performed under the assumption of a specific model for the power spectrum of the sky; the best sky for the data is not necessarily found. We are interested in an inversion process that does not assume an initial spectrum for the sky fluctuations; this can be achieved using maximum entropy method.

5.5.2 Bayes theorem and the entropic prior

We wish to find the best sky solution with minimal assumptions about the true sky to avoid bias towards any particular model. By considering the problem from a purely Bayesian viewpoint, we wish to find the most probable sky distribution given our data set and some prior information. Given a hypothesis H, data D and background information I, then Bayes theorem states that the posterior probability distribution $\Pr(H|DI)$ is the product of the prior probability $\Pr(H|I)$ and the likelihood $\Pr(D|HI)$, with some overall normalising factor called the evidence $\Pr(D|I)$:

$$\Pr(H|DI) = \frac{\Pr(H|I)\Pr(D|HI)}{\Pr(D|I)}. \tag{5.6}$$

The likelihood $\Pr(D|HI)$ is fully defined by our data, but we have freedom to choose the prior $\Pr(H|I)$. We will consider here random Gaussian fluctuations. The most conservative prior assumption in this case is to simply take the sky to be smooth at some level. We therefore wish to find the sky that contains the least amount of information, the one closest to being smooth, that is still consistent with our data set. This forms the basis of the so called "maximum entropy methods" (MEM) [70, 71] used in the reconstruction of images. If we restrict ourselves to the class of sky models with this property then this leads us to find a prior of form [142],

$$\Pr(H|I) \propto \exp(\alpha S(f, m)) \tag{5.7}$$

for an image $f(\xi)$ and prior information $m(\xi)$, where ξ is the position on the sky. The regularising parameter, α, is a dimensional constant that depends on the scaling of the problem and $S(f, m)$ is the cross entropy. For a positive, additive distribution, the cross entropy is given by [141]:

$$S(f, m) = \int d\xi \left[f(\xi) - m(\xi) - f(\xi) \ln\left(\frac{f(\xi)}{m(\xi)}\right)\right], \tag{5.8}$$

where $m(\xi)$ can also be considered a constraint on $f(\xi)$ such that when the entropic prior dominates, the aposteriori sky map $f(\xi)$ does not deviate significantly from $m(\xi)$.

This form is chosen for the entropy to ensure that the global maximum of the entropy at $f(\xi) = m(\xi)$ is zero and it is the only form of entropy consistent with coordinate and system invariance [141] which does not introduce any biases away from a smooth model.

5.5.3 Positive/negative data reconstruction

Due to the log entropy, this standard form is inapplicable in the more general case of an image $x(\xi)$ that can take both positive and negative values. Various methods in the past have been tried to reconstruct data containing negative peaks [99, 172]. It was shown that these processes posed some problems [84]. Jones *et al.* [84] proposed a new method to overcome such problems.

We consider the image to be the difference between two positive, additive distributions:

$$x(\xi) = u(\xi) - v(\xi),$$

so that the expression for the cross entropy becomes:

$$\begin{aligned} S(u,v,m) = & \int d\xi \left[u(\xi) - m_u(\xi) - u(\xi) \ln \left(\frac{u(\xi)}{m_u(\xi)} \right) \right] \\ & + \int d\xi \left[v(\xi) - m_v(\xi) - v(\xi) \ln \left(\frac{v(\xi)}{m_v(\xi)} \right) \right]. \end{aligned} \tag{5.9}$$

With the prior thus defined, we can calculate the probability of obtaining our reconstructed sky x (the hypothesis H) given y (the data D):

$$\Pr(x|y) \propto \Pr(x) \Pr(y|x), \tag{5.10}$$

and we can maximise $\Pr(x|y)$ to obtain the most likely 2-D image of the microwave sky.

5.5.4 Test of the algorithm

Before applying the MEM algorithm to the real data, we carried out simulations to test its performance. Two-dimensional sky maps were simulated using a standard cold, dark matter model ($H_o = 50 \mathrm{km\,s^{-1}}$, $\Omega_b = 0.1$) with an *rms* signal of 22μK per pixel (normalised to COBE second year data, $Q_{rms-PS} = 20.3\mu$K, see Tegmark & Bunn 1995 [153]). Observations from the sky maps were then simulated by convolving them with the Tenerife beam (see Chapter 4). With no noise added the positive/negative algorithm was tested by analysing the data and then changing the sign of the data and reanalysing again. In both cases, the same, but inverted, reconstruction was found for the MEM output and so we conclude that our method of two positive channels introduces no biases towards being positive or negative. Various noise levels were then added to the scans before reconstruction with MEM. The two noise levels considered here are 100μK and 25μK on the data scans, which represent the two extrema of the data that we expect from the various Tenerife configurations (100μK for the 10GHz, FWHM=8° data and 25μK for the 15 and 33 GHz, FWHM=5° data). Figure 5.10 shows the reconstructed intrinsic sky from two of the simulations after 60 iterations of the MEM algorithm as compared with the real sky simulations convolved in an 8° Gaussian beam. Various common features are seen in the three scans like the maxima at RA 150°, minima at RA 170° and the partial ring feature between RA 200° and 260° with central minima at RA 230°, Dec. +35°. All features

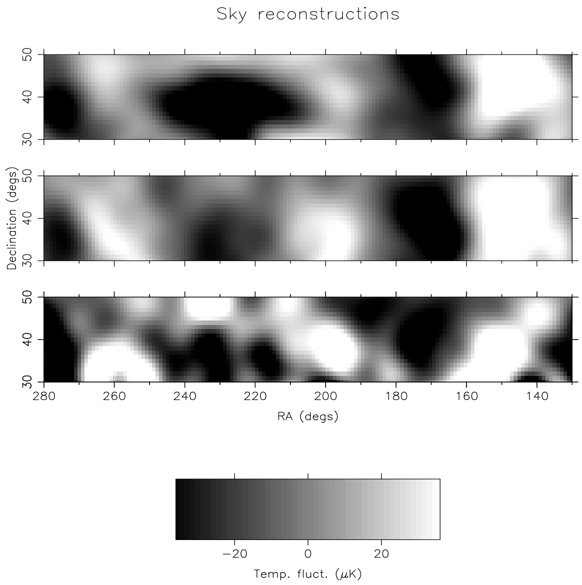

Figure 5.10: The top figure is the simulated sky convolved with an 8° Gaussian beam. Simulations of the Tenerife experiment were made and passed through MEM. They are all convolved with a final Gaussian of the same size. The middle and bottom figures are the reconstructed skies from that simulation after scans with 25μK and 100μK noise levels respectively.

larger than the rms are reconstructed in both the 25μK and 100μK noise simulations. The *rms* signal for the reconstructed map from the 25μK noise simulation was $50 \pm 32\mu$K and that for the 100μK noise simulation was $150 \pm 140\mu$K. Both of these represent a higher signal to noise than the original scans and are on the intrinsic sky fluctuations. It is seen that the noise level on the two maps is comparable to the *rms* signal. Since we are reconstructing features from constraints due to several points in the scans, the noise is no longer independent over features in the map. These tests, using simulated skies, show that this method is very successful and it has now been applied to real cases as the Tenerife experiment and to simulations for the COBRAS/SAMBA satellite.

5.6 Discussion and Conclusions

We have presented a detailed analysis of the measurements taken at Dec=+40° by the Tenerife experiments at 10, 15 and 33 GHz. After accounting for both local atmospheric and discrete radio source foregrounds, the 15 and 33 GHz data at high Galactic latitude are seen to contain statistically significant signals which have their origin in common hot and cold features. The cross-correlation function between the data at these two frequencies demonstrates that the amplitudes and shapes of the structures detected at 15 and 33 GHz are similar. This, combined with our measurements at the lower frequency of 10 GHz, implies that the CMB signal dominates over the Galactic contribution at 15 GHz, and that the maximum possible Galactic contribution at 33 GHz is smaller than 10 % of the detected signal. Our best estimate of the cosmological signal is $Q_{rms-ps} = 22^{+10}_{-6}\mu$K for an $n = 1$ inflationary spectrum. This amplitude is reduced by 4μK over that previously reported for the same data set and results from an improved separation of signal from atmospheric noise. Comparison of the Tenerife and COBE two year anisotropy detections by means of the likelihood function allows a detailed investigation of the allowed parameter space for a power law model of the fluctuation spectrum. The best fit values of n and Q_{rms-ps} are 1.37 and 16μK, and marginalising over Q_{rms-ps} we find both data sets consistent with n in the range $1.0 \leq n \leq 1.6$. These results support inflationary models, which predict $n \simeq 1$ and future improvements in the Tenerife data and use of the 4 year COBE data will narrow the range of allowed n. Improvements of this kind are important to determine the power spectrum normalisation, since *only* on these large angular scales is it possible to place limits on the tensor to scalar ratio independent of the precise details of the cosmological model. In Chapter 7 improved limits have been placed on n, by combining the large scale anisotropy measurements from Tenerife and COBE with observations of medium scale anisotropy measurements, but at the expense of assuming an underlying cosmological model (in our case CDM). We have also presented a new maximum entropy based method to deconvolve the CMB data. Via simulations we concluded that the algorithm performance is good recovering the morphology, position and amplitude of structures in both the reconvolved scans and the two-dimensional deconvolved sky maps. The MEM approach allows the combination of data from different experiments, since each data set acts as a separate constraint on a single reconstructed sky. This new method provides a powerful means of reconstructing intrinsic sky fluctuations maps free of Galactic contamination by combining data from different experiments and at different frequencies.

Chapter 6

Constraints on the Cosmological Parameters using current CMB observations-I

6.1 Introduction

Observations of the Cosmic Microwave Background (CMB) radiation provide information about epochs and physical scales that are inaccessible to conventional astronomy. In contrast to traditional methods of determining cosmological parameters, which rely on the combination of results from local observations [116], CMB observations provide direct measurements [23, 170] over cosmological scales, thereby avoiding the systematic uncertainties and biases associated with conventional techniques. As mentioned in Chapter 2 the principal cosmological information is contained in the acoustic peaks [81, 136] in the power spectrum, which are generated during acoustic oscillations of the photon-baryon fluid at recombination [56]. The main acoustic peak, known as the 'Doppler peak', is a strong prediction of contemporary cosmological models with adiabatic fluctuations and is expected to occur on an angular scale $\sim 1°$ (see Chapter 2); its observation is a major goal of observational cosmology. In the case that this peak was not observed, this would imply either that medium-scale primordial CMB fluctuations had been wiped out by reionization [56] or that there is a fundamental flaw in our theory. On the contrary, a conclusive observation of the first peak would provide strong support for current theoretical models and the determination of its angular position would constitute a direct probe of the large scale geometry of the Universe. The angular scale l_p of the main peak reflects the size of the horizon at last scattering of the CMB photons and thus depends almost entirely [81, 87] on the total density of the Universe according to $l_p \propto 1/\sqrt{\Omega}$. In conventional inflationary theory [72], one expects the Universe to be flat with $\Omega = 1.0$, which can be achieved if the total mass density is equivalent to the critical density or if there is a contribution from a cosmological constant Λ. The height of the peak provides additional cosmological information since it is directly proportional to the fractional mass in baryons Ω_b and also varies according to the expansion rate of the Universe as specified by the Hubble constant H_0; in general [81] for baryon fractions $\Omega_b \lesssim 0.05$, increasing H_0 reduces the peak height whilst the converse is true at higher baryon densities. Furthermore, by measuring the amplitude of the intermediate scale CMB fluctuations relative to those on large scales it is possible to place tight limits on the spectral slope n of the initial primordial spectrum of fluctuations. The latter is predicted by inflationary theory to be approximately scale invariant, in which case $n \simeq 1.0$, although the presence of a background of primordial gravity waves [37, 146] would generally lead to lower values of n. Thus, in summary, by comparing large and intermediate scale CMB observations and tracing out the Doppler peak, it is possible to directly estimate Ω, Ω_b and H_0 and to probe inflationary theory and the existence of primordial gravity waves. Recent improvements in the quality of CMB data, in particular on the angular scales probed by the CAT and Saskatoon experiments, now make this exercise of great interest. In Section 6.2 we describe the method applied for the intercomparison of experiments and models. In Section 6.3 we proceed to the discussion of the results obtained.

6.2 Method

Clear detections of CMB anisotropy have now been reported by a number of different groups, including the COBE satellite [144, 14]; ground-based switching experiments such as Tenerife [74, 75], Python [128], South Pole [69] and Saskatoon [114]; balloon mounted instruments such as ARGO [44], MAX [152], and MSAM [30, 31] and more recently the ground-based interferometer CAT [137] (see Chapter 3). Given the difficulties inherent in observing CMB anisotropy, it is possible that some of these results are contaminated by foreground effects and it is clear that determining the form of the CMB power spectrum in order to trace out the Doppler peak requires a careful, in-depth consideration of the CMB measurements from the different experiments within a common framework. We consider all of the latest CMB measurements, including new results from COBE, Tenerife, MAX, Saskatoon and CAT, with the exception of the MSAM results (see below) and the MAX detection in the Mu Pegasi region which is contaminated by dust emission [57].

The competing models for the origin and evolution of structure predict [23, 81], the shape and amplitude of the CMB power spectrum and its Fourier equivalent, the auto-correlation function $C(\theta) =< \Delta T(\mathbf{n_1})\Delta T(\mathbf{n_2}) >$ where $\mathbf{n_1} \cdot \mathbf{n_2} = \cos\theta$. According to Chapter 2 expanding the intrinsic angular correlation function $C(\theta)$ in terms of spherical harmonics one obtains

$$C(\theta) = \sum_{l\geq 2}^{\infty}(2l+1)C_l P_l(\cos\theta)/4\pi, \tag{6.1}$$

where low order multipoles l correspond to large angular scales θ and large l-modes are equivalent to small angles on the sky. The C_l's are predicted by the cosmological theories and contain all of the relevant statistical information for models described by Gaussian random fields [23]. As mentioned in Chapter 2 the different experiments sample different angular scales according to their *window functions* W_l [169, 168]. The window function W_l specifies the relative sensitivity of an experiment to a given l-mode, and the observed power in CMB fluctuations as seen through a window W_l is given by

$$C_{obs}(0) = \left(\frac{\Delta T_{obs}}{T}\right)^2 = \sum_{l\geq 2}^{\infty}(2l+1)C_l W_l/4\pi. \tag{6.2}$$

Given W_l, then for the C_l's corresponding to the theoretical model under consideration it is possible to obtain the value of ΔT_{obs} one would expect to observe using the chosen

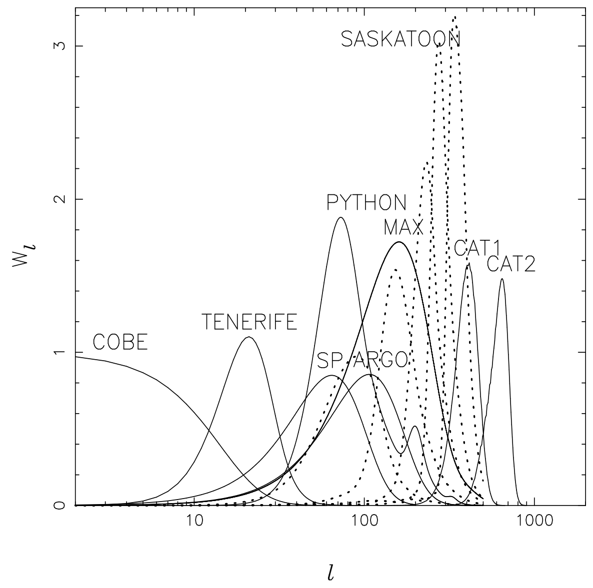

Figure 6.1: The window functions for the experiments listed in Table 6.1

experiment (see also Chapter 2). This value can then be compared to the value actually observed to test the cosmological model. Shown in Fig. 6.1 are the window functions for the various configurations of the experiments considered.

On the largest scales corresponding to small l, new COBE [14] and Tenerife [74] results improve the power spectrum normalisation, whilst significant gains in knowledge at high l are provided by new results from the Saskatoon and CAT experiments. The full data set spans a range of 2 to $\sim$ 700 in l, sufficient to test for the main Doppler peak out to $\Omega = 0.1$. We take the reported CMB detections and convert them to a common framework of flat bandpower results [19, 20] as given in Table 6.1. This is carried out as follows.

The CMB anisotropy measurements are converted to bandpower estimates $\Delta T_l \pm \sigma$ assuming in each case a flat spectrum of C_l centred on the effective multipole l_e (see below) of the window function. l_l and l_u represent the lower and upper points at which the window of each configuration reaches half of its peak value. In order to use the observed anisotropy levels to place constraints on the CMB power spectrum one must in general know the form of the C_l under test. However, in most cases the form of C_l can be represented by a flat spectrum $C_l \propto C_2/(l(l+1))$ over the width of a given experimental window, so that the bandpower is $\Delta T_l/T = \sqrt{C_{obs}(0)/I(W_l)}$, where we define $I(W_l)$ according to Bond [19, 20] as $I(W_l) = \sum_{l=2}^{\infty}(l+0.5)W_l/(l(l+1)$. This bandpower estimate is centred on the effective multipole $l_e = I(lW_l)/I(W_l)$. In many instances experimenters now report results directly for a flat spectrum and when this is not so we have converted the quoted power in fluctuations into the equivalent flat band estimate. Each group has obtained limits on the intrinsic anisotropy level using a likelihood analysis (see *e.g.* Hancock *et al.* [75]), which incorporates uncertainties due to random errors, sampling variance [135] and cosmic variance [132, 133] (see Chapter 2 and 4). The errors in ΔT_l quoted in column 3 of Table 6.1 are at 68 % confidence and have been obtained by averaging the difference in the reported 68% upper and lower limits and the best fit ΔT_l. Since the form of the likelihood function is in general only an approximation to a Gaussian distribution this averaging introduces a small bias into the results (see Chapter 7, [126]). Results from the MSAM experiment are not included here, because they do not provide an independent

Experiment	ΔT_l (μK)	σ (μK)	l_e	l_l	l_u	Reference
COBE	27.9	2.5	6	2	12	[14]
Tenerife	34.1	12.5	20	13	31	[74]
PYTHON	57.2	16.4	91	50	107	[128]
South Pole	39.5	11.4	57	31	106	[69]
ARGO	39.1	8.7	95	52	176	[44]
MAX GUM	54.5	13.6	145	78	263	[152]
MAX ID	46.3	17.7	145	78	263	"
MAX SH	49.1	19.1	145	78	263	"
MAX PH	51.8	15.0	145	78	263	"
MAX HR	32.7	9.5	145	78	263	"
Saskatoon1	49.0	6.5	86	53	132	[114]
Saskatoon2	69.0	6.5	166	119	206	"
Saskatoon3	85.0	8.9	236	190	274	"
Saskatoon4	86.0	11.0	285	243	320	"
Saskatoon5	69.0	23.5	348	304	401	"
CAT1	50.8	15.4	396	339	483	[137]
CAT2	49.0	16.9	608	546	722	"

Table 6.1: Details of data results used

measure of the power spectrum since their angular sensitivity and sky coverage are already incorporated within the Saskatoon measurements. Netterfield *et al.* [114] report good agreement between the MSAM double difference results and Saskatoon measurements, although the discrepancy with the MSAM single difference data is yet to be resolved.

The data points from Table 6.1 are plotted in Figure 6.2, in which the horizontal bars represent the range of l contributing to each data point. There is a noticeable rise in the observed power spectrum at $l \simeq 200$, followed by a fall at higher l, tracing out a clearly defined peak in the spectrum. In the past several groups [136, 88, 122] have attempted to determine the presence of a Doppler peak, but only now are the data sufficient to make a first detection and to put constraints on the closure parameter Ω. As a first step, we adopt a simple three parameter model of the power spectrum, which we find adequately accounts for the properties of the principal Doppler peak for both standard Cold Dark Matter (CDM) models [39, 56] and open Universe ($\Omega < 1$) models [88]. The functional form chosen is a modified version of that used in Scott, Silk & White [136] — we choose the following:

$$l(l+1)C_l = 6C_2\left(1+\frac{A_{peak}}{1+y(l)^2}\right) / \left(1+\frac{A_{peak}}{1+y(2)^2}\right) \tag{6.3}$$

where $y(l) = (\log_{10} l - log_{10}(220/\sqrt{\Omega}))/0.266$. In this representation C_2 specifies the power spectrum normalisation, whilst the first Doppler peak has height A_{peak} above C_2, width $\log_{10} l = 0.266$ and for $\Omega = 1.0$ is centred at $l \simeq 220$. By appropriately specifying the parameters C_2, A_{peak} and Ω it is possible to reproduce to a good approximation the C_l spectra corresponding to standard models of structure formation with different values of Ω, Ω_b and H_0. Such a form will not reproduce the structure of the *secondary* Doppler peaks, but we have checked the model against the overall form of the $\Omega = 1$ models of Efstathiou and the open models reported in Kamionkowsky *et al.* [88] and find that

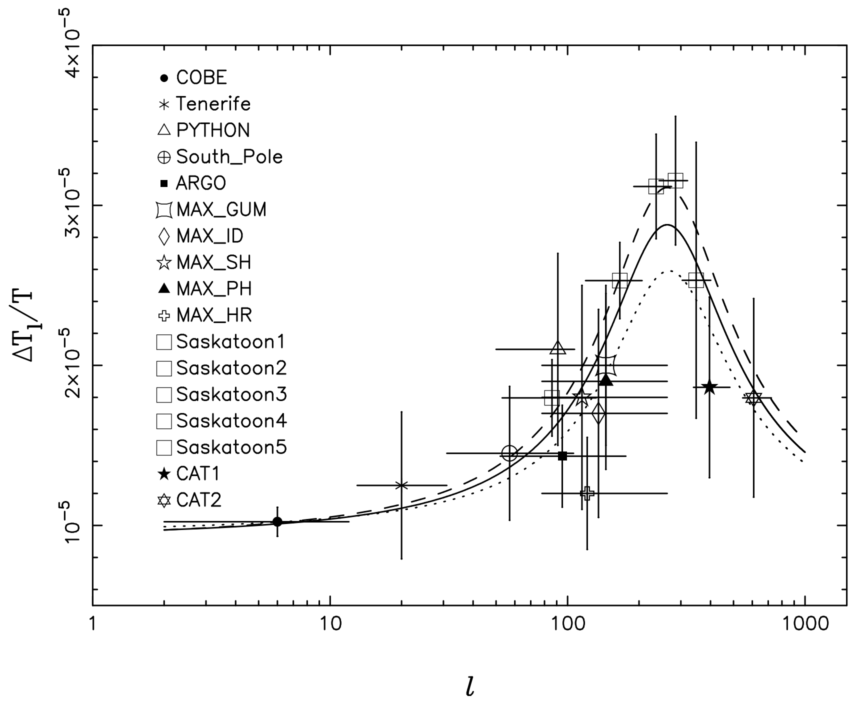

Figure 6.2: The data points from Table 6.1 are shown compared to the best fit analytical CDM model. The dotted and dashed lines show the best fit models which are obtained when the Saskatoon calibration is adjusted by $\pm14\%$. The data points from the MAX experiment are shown offset in l for clarity

this form adequately reflects the properties of the main peak. This satisfies our present considerations since the current CMB data are not yet up to the task of discriminating the secondary peaks. Varying the three model parameters in equation (6.3) we form C_l spectra corresponding to a range of cosmological models, which are then used in equation (6.2) to obtain a simulated observation for the ith experiment, before converting to the bandpower equivalent result $\Delta T_l[C_2, A_{peak}, \Omega](i)$. The chi-squared for this set of parameters is given by

$$\chi^2(C_2, A_{peak}, \Omega) = \sum_{i=1}^{nd} \frac{(\Delta T_l^{obs}(i) - \Delta T_l[C_2, A_{peak}, \Omega](i))^2}{\sigma_i^2},$$

for the nd data points in Table 6.1 and the relative likelihood function is formed according to $L(C_2, A_{peak}, \Omega) \propto \exp(-\chi^2(C_2, A_{peak}, \Omega)/2)$. We vary the power spectrum normalisation C_2 within the 95 % limits for the COBE 4-year data [14] and consider A_{peak} in the range 0 to 30 and values of the density parameter up to $\Omega = 5$. The data included in the fit are those from Table 6.1 1, which with the exception of Saskatoon include uncertainties in the overall calibration. There is a $\pm14\%$ calibration error in the Saskatoon data, but since the Saskatoon points are not independent this will apply equally to all five points [114]. The likelihood function is evaluated for three cases: (i) that the calibration is correct, (ii) the calibration is the lowest allowed value and (iii) the calibration is the maximum allowed value. In each case the likelihood function is marginalised over C_2 before calculating limits on the remaining two parameters according to Bayesian integration with a uniform prior.

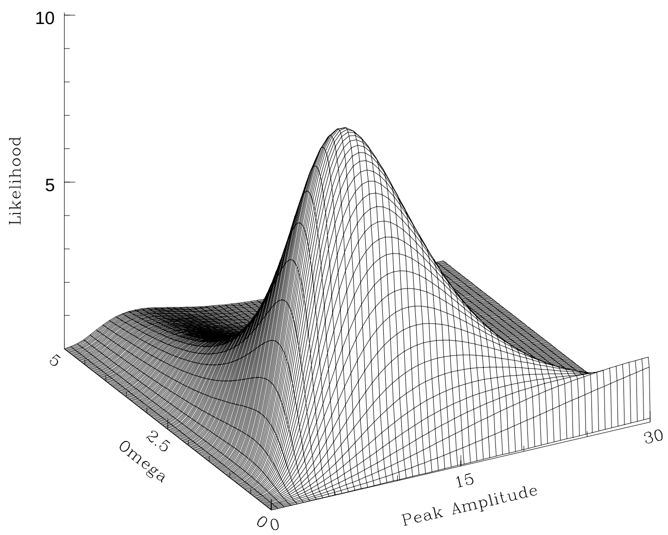

Figure 6.3: The likelihood surface for Ω and A_{peak}. (The nominal Saskatoon calibration is assumed.)

6.3 Results and Discussion

In Fig. 6.3 the likelihood function obtained from fitting the model C_l spectra to the data of Table 6.1 is shown plotted as a function of the amplitude and position (Ω) of the Doppler peak. The highly peaked nature of the likelihood function in Fig. 6.3 is good evidence for the presence of a Doppler peak localised in both position (Ω) and amplitude. In Fig. 6.4 we show the 1-D conditional likelihood curve for Ω, obtained by cutting through the surface shown in Fig. 6.3 at the best-fit value of A_{peak}. The best fit value of Ω is 0.7 with an allowed 68% range of $0.30 \leq \Omega \leq 1.73$.

In Figure 6.2 the best fit model, represented by the solid line, is shown compared to the data points, assuming no error in the calibration of the Saskatoon observations. The chi-squared per degree of freedom for this model is 0.9, implying a good fit to the data. The peak lies at $l = 263^{+139}_{-94}$ corresponding to a density parameter $\Omega = 0.70^{+1.0}_{-0.4}$; the height of the peak is $A_{peak} = 9.0^{+4.5}_{-2.5}$. The dashed and dotted lines show the best fit models ($\Omega = 0.70^{+0.92}_{-0.37}$, $A_{peak} = 11.0^{+5.0}_{-4.0}$ and $\Omega = 0.68^{+1.2}_{-0.4}$, $A_{peak} = 6.5^{+3.5}_{-2.0}$ respectively) assuming that the Saskatoon observations lie at the upper and lower end of the permitted range in calibration error.

These likelihood results using the analytic form for the C_l and the results from a chi-squared goodness of fit analysis using exact models (see below) imply that independent of calibration uncertainties in the data, current CMB data are inconsistent with cosmological models with $\Omega \lesssim 0.3$.

The analytic approximation to the true C_l such as we use here, is a useful general tool,

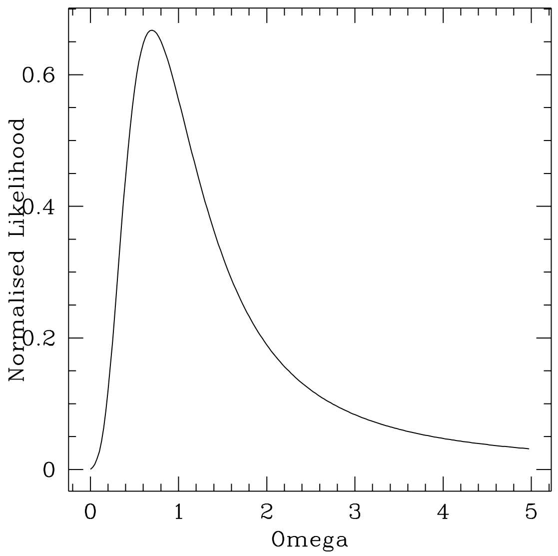

Figure 6.4: The 1-D conditional likelihood curve for Ω.

but as a detailed check we have also applied the chi-squared goodness of fit test to actual COBE normalised C_l models. In Fig. 6.5 the data are compared to exact forms of the C_l for a standard flat CDM model, an open CDM model, a Λ dominated model and a cosmic string model [109]. Allowing the model normalisation to vary within the two sigma COBE limit we find that the standard CDM model, non-zero Λ model and the string model all offer acceptable ($P(\chi^2) \geq 0.05$) chi-squared fits, whilst the probability of the open model fitting is $P(\chi^2) < 0.01$. A detailed comparison of the CMB data with these models is considered in Chapter 7. Considering a range of CDM models with varying Ω, in order to find the lowest Ω compatible with the observations, we have considered exact models with $\mathrm{H}_0 = 50\,\mathrm{km\,s^{-1}\,Mpc^{-1}}$ and $\Omega_b = 0.03$ for $\Omega = 0.1 - 0.5$ [88]. We find that $\Omega = 0.5$ is allowed, $\Omega = 0.3$ and below are completely ruled out (95% confidence) and $\Omega = 0.4$ is excluded unless all the Saskatoon points have the minimum allowed calibration. This result is confirmed in Chapter 7 for a more complet set of open models.

6.4 Conclusions

Our current results provide good evidence for the Doppler peak, verifying a crucial prediction of cosmological models and providing an interesting new measurement of fundamental cosmological parameters. This first estimate of the angular position of the Doppler peak is used to place a new direct limit on the curvature of the Universe, corresponding to a density of $\Omega = 0.7^{+1.0}_{-0.4}$, consistent with a flat Universe. Very low density 'open' Universe models are inconsistent with this limit unless there is a significant contribution from a cosmological constant. In Chapter 7 a detailed comparison of the CMB data is made with the theoretical power spectra predicted by a range of flat, tilted, open models and models with non-zero cosmological constant.

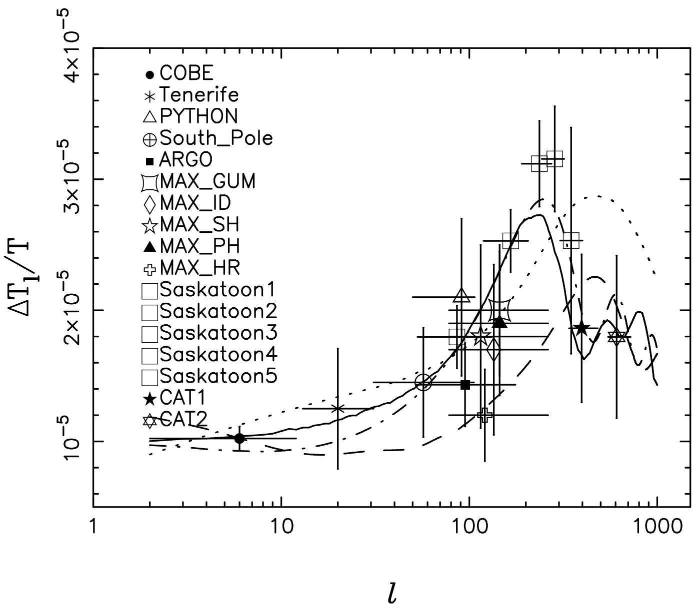

Figure 6.5: The data points from Table 6.1 compared to the exact forms of the C_l for an $\Omega = 1$, $\Omega_b = 0.10$, $\mathrm{H}_0 = 45\,\mathrm{km\,s^{-1}\,Mpc^{-1}}$ standard CDM model (bold line), an $\Omega = 0.3$, $\Omega_b = 0.03$, $\mathrm{H}_0 = 50\,\mathrm{km\,s^{-1}\,Mpc^{-1}}$ open model (dashed line), a flat $\Omega = 0.3$, $\Omega_\Lambda = 0.7$, $\Omega_b = 0.05$, $\mathrm{H}_0 = 50\,\mathrm{km\,s^{-1}\,Mpc^{-1}}$ model (dot-dash line) and an example cosmic string model (dotted line) [109]

Chapter 7

Constraints on the Cosmological Parameters using current CMB observations-II

7.1 Introduction

In this Chapter we give a detailed comparison of the CMB data with the theoretical power spectra predicted by a range of flat, tilted, open models and models with non-zero cosmological constant. In this analysis we only consider scalar fluctuations and we do not include reionization. This is an extension of the work carried out in Chapter 6 in which we used an analytic approximation of current CMB models. Here we consider some of the exact fourth-year COBE normalized angular power spectrum with fourth-year COBE normalization. The precise form of the Doppler peaks depend on the nature of the dark matter, and the values of Ω, Ω_b, and H_0 . Thus in order to use the medium-scale anisotropy results e.g. to provide additional leverage on the spectral index determination, it is necessary to adopt a given cosmological model. Recalling Chapter 6, the height of the peak depends on H_0 and Ω_b such that for a fixed value of H_0 the height of the peak increases with Ω_b while for a fixed value of $\Omega_b \geq 0.05$ it increases with H_0 but the converse is true for $\Omega_b < 0.05$ where it decreases with an increase of H_0 [82]. The angular scale l_p of the main Doppler peak depends almost entirely [81, 87] on the total density of the Universe according to $l_p \propto 1/\sqrt{\Omega}$. Each Section gives the results for each set of models of structure formation used in this intercomparison of data and models.

7.2 Data

We apply a fit procedure to two sets of CMB data first: the CMB data given in Table 6.1 of Chapter 6, where the COBE data consists in one multipole for COBE (namely C_2, obtained from the value of the Q_{rms-ps} =18 μK for the 4-year COBE data [14]) which we refer to as case (a); and the data as displayed in Table 7.1 which is the same as the data of Table 6.1 apart from COBE where we consider 4 of the 8 multipole bands of the angular power spectrum extracted from the 4-year COBE data [154], which we refer to as case

Table 7.1: Details of data results used

Experiment	ΔT_l (μK)	σ (μK)	l_e	l_l	l_u	Ref
COBE2	25.4	8.1	3	3	5	[154]
COBE4	28.1	3.9	5	5	8	[154]
COBE6	22.3	4.2	11	10	15	[154]
COBE8	31.9	24.3	25	22	30	[154]
Tenerife	34.1	12.5	20	13	31	[74]
PYTHON	57.2	16.4	91	50	107	[128]
South Pole	39.5	11.4	57	31	106	[69]
ARGO	39.1	8.7	95	52	176	[44]
MAX GUM	54.5	13.6	145	78	263	[152]
MAX ID	46.3	17.7	145	78	263	[152]
MAX SH	49.1	19.1	145	78	263	[152]
MAX PH	51.8	15.0	145	78	263	[152]
MAX HR	32.7	9.5	145	78	263	[152]
Saskatoon1	49.0	6.5	86	53	132	[114]
Saskatoon2	69.0	6.5	166	119	206	[114]
Saskatoon3	85.0	8.9	236	190	274	[114]
Saskatoon4	86.0	11.0	285	243	320	[114]
Saskatoon5	69.0	23.5	348	304	401	[114]
CAT1	50.8	15.4	396	339	483	[137]
CAT2	49.0	16.9	608	546	722	[137]

(b). In order to avoid eventual correlations between these data points we have applied the fitting analysis to the 4 even or 4 odd multipole bands in conjuntion with the remaining data points. The results are similar whether we use the even or the odd multipoles. The use of 4 instead of 1 multipole is particularly useful in discriminating the value of the spectral index n.

As already mentioned in Chapter 6 the different experiments sample different angular scales according to their window functions, W_l, [169, 168] as shown in Fig 7.1. The window functions for 4 of the 8 multipoles of the COBE experiment are shown, in conjunction with the window functions of the other experiments. The 4 window functions corresponding to the COBE experiment were obtained considering Gaussian functions centered in $\langle l \rangle$ with dispersion $(\Delta l)^2$, where the parameters are given in Tegmark 1996 [154].

The conversion of data to a common framework in terms of flat bandpower estimates [19, 20] follows the same procedure as in Chapter 6. In Table 7.1 we display these band-power estimates $\Delta T_l \pm \sigma$ where as before l_l and l_u represent the lower and upper points at which the window function for each configuration reaches half of its peak value. As in Chapter 6, the errors in ΔT_l quoted in column 3 are 68% confidence limits and have been obtained by averaging the difference in the reported 68% upper and lower limits and the best fit ΔT_l.

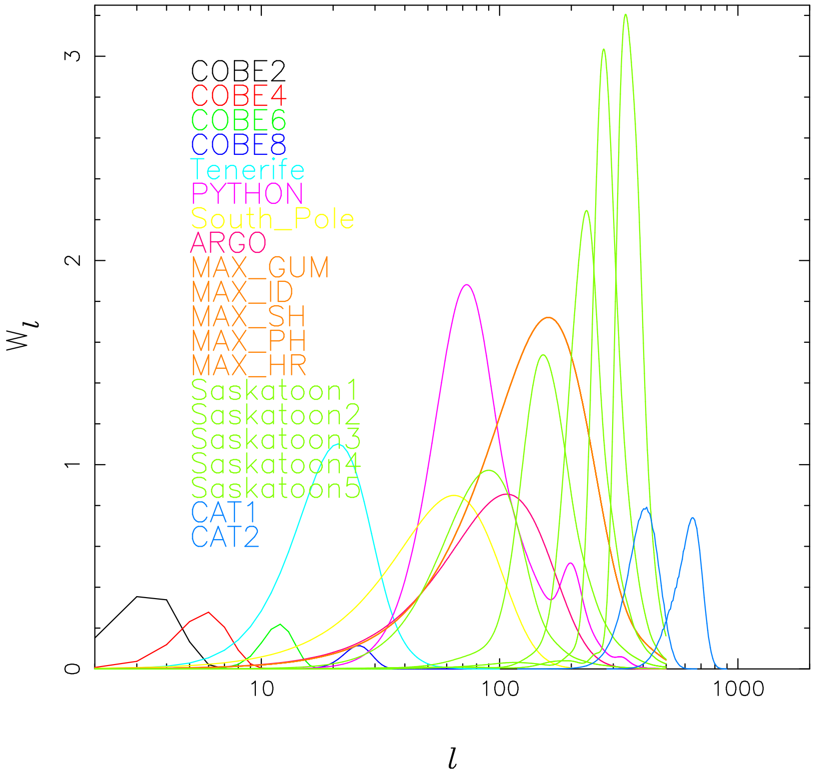

Figure 7.1: The window functions for the experiments listed in Table 7.1

7.3 Method

We pursued the same method as described in Chapter 6. Here we recall the main steps of the analysis, for details see Chapter 6. For a given theoretical model it is possible to compute the value of ΔT_{obs} one would expect to observe using the angular power spectrum C_l's as predicted by the model and the window function corresponding to the experimental configuration W_l. We convert this to the bandpower equivalent result ΔT_l and compare with ΔT_l^{obs}. We then compute the chi-squared for this set of C_l's for the nd data points in Table 6.1 of Chapter 6 and of Table 7.1, and the relative likelihood function is formed according to: $L \propto exp(-\chi^2/2)$ (for details see Chapter 6 and Hancock *et al.* [74]). The process by which the error bars quoted in Table 7.1 are computed introduces a small bias into the results since the likelihood function is in general only an approximation to a Gaussian distribution. In order to assess the significance of this we applied the fitting analysis to an alternative set of data which consisted of the mean value of the data and corresponding error bars. We find no significant difference in the results obtained. We also vary the power spectrum normalization within the 95% limits for the COBE 4-year data [14]. The data included in the fit are those from Table 6.1 of Chapter 6 and from Table 7.1, which, with the exception of Saskatoon, include uncertainties in the overall calibration. There is a $\pm 14\%$ calibration error in the Saskatoon data, but since the Saskatoon points are not independent this will apply equally to all five points [114]. Recalling Chapter 6, the likelihood function is evaluated for three cases: (i) that the calibration is correct, (ii) the calibration is the lowest allowed value and (iii) the calibration is the maximum allowed value. We consider that a given model offers an acceptable chi-squared fit when $P(\chi^2) \geq 0.05$. We increase the resolution of the parameters grid via interpolation procedures and compute the χ^2 and corresponding $P(\chi^2)$ for each model. Then we compute the best fit model and obtain the conditional and marginal probability distribution functions for each parameter.

7.4 Scale invariant flat CDM models

This work was initially applied to scale invariant ($n = 1$), flat ($\Omega = 1$) CDM models with Ω_b=0.01-0.3 and H_0=30-100 km s^{-1} Mpc^{-1} (kindly provided by G. Efstathiou). We considered these models normalised to the 4-year COBE value of Q_{rms-ps} =18 μK and applied the analysis to the data tabulated in Table 6.1 of Chapter 6 (i.e. case (a)). In Fig. 7.2 we have considered these COBE normalised CDM models. A dot is placed in the appropriate place in the parameter space if the exact power spectrum corresponding to these parameters gives a fit to the data in Table 6.1 of Chapter 6 with an acceptable χ^2 value ($P(\chi^2) \geq 0.05$). A blank is left at that position if not. Overlying these power spectrum constraints is the limit $0.009 \leq \Omega_b h^2 \leq 0.02$ provided by nucleosynthesis of the light elements [35]. As shown, the models offering an acceptable chi-squared fit ($P(\chi^2) \geq 0.05$) to the CMB power spectrum whilst simultaneously satisfying nucleosynthesis constraints [35], are those with $0.05 \leq \Omega_b \leq 0.2$, $30\,\mathrm{km\,s^{-1}\,Mpc^{-1}} \leq \mathrm{H_0} \leq 50\,\mathrm{km\,s^{-1}\,Mpc^{-1}}$. Considering the highest Saskatoon data calibration the constraints become $0.1 \leq \Omega_b \leq 0.2$, $30\,\mathrm{km\,s^{-1}\,Mpc^{-1}} \leq \mathrm{H_0} \leq 35\,\mathrm{km\,s^{-1}\,Mpc^{-1}}$ as shown in Fig. 7.3. Allowing for the lowest Saskatoon data calibration relaxes the constraints up to $\mathrm{H_0} = 70\,\mathrm{km\,s^{-1}\,Mpc^{-1}}$ and $0.02 \leq \Omega_b \leq 0.2$ as shown in Fig 7.3. In general, recent optical and Sunyaev-Zel'dovich observations of the Hubble constant [121, 60, 89, 96] imply $\mathrm{H_0}$ in the range $50-80\,\mathrm{km\,s^{-1}\,Mpc^{-1}}$.

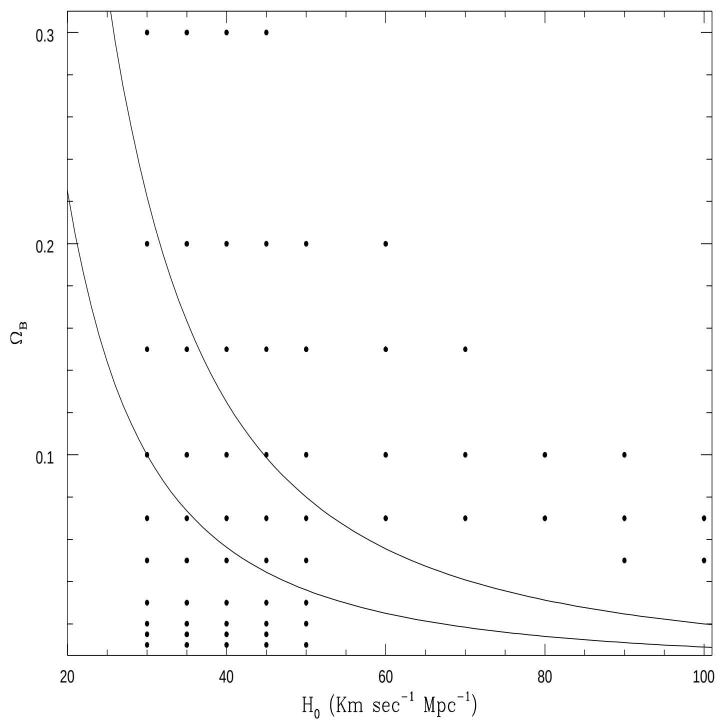

Figure 7.2: The COBE normalised CDM models with acceptable chi-squared fits to the CMB data (for case (i) calibration) are plotted as dots in the $\Omega_b - H_0$ space. Overlayed are the constraints on $\Omega_b h^2$ imposed by nucleosynthesis.

	H_0	Ω_b	Q_{rms-ps}
Best Model	30	0.02	17.64
Conditional(68 %)	30-50	0.02-0.15	16.02-19.44
(95%)	30-70	0.02-0.22	14.94-20.52
Marginal(68%)	30-60	0.04-0.16	14.94-18.36

Table 7.2: Results of the fitting analysis considering: one multipole for COBE experiment, that Saskatoon calibration is correct and without BBN constraints for scale invariant flat CDM models.

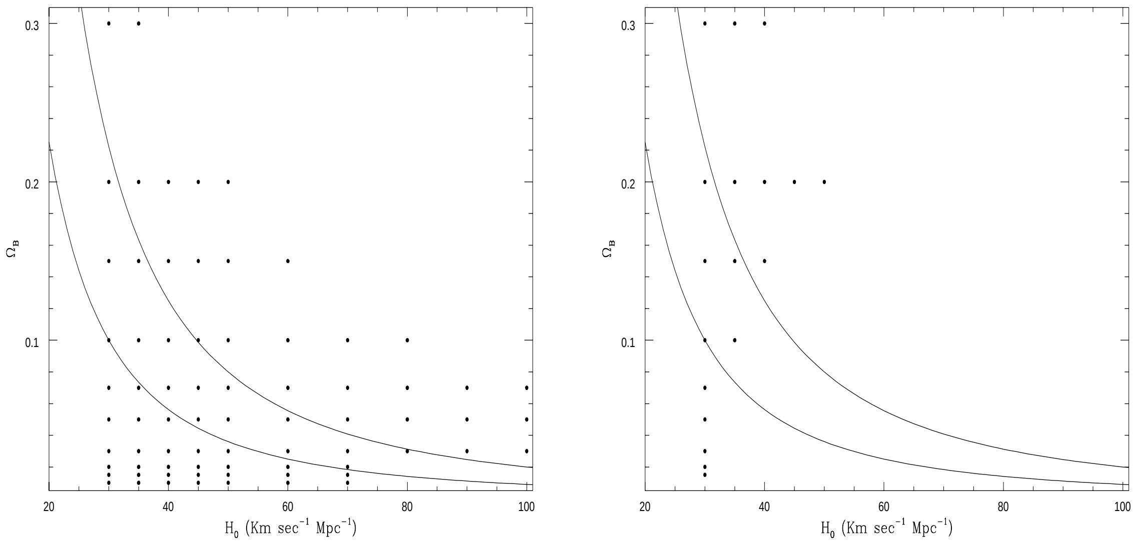

Figure 7.3: The COBE normalised CDM models with acceptable chi-squared fits to the CMB data (for case (ii) calibration on the left hand side and for case (iii) calibration on the right hand side) are plotted as dots in the $\Omega_b - H_0$ space. Overlayed are the constraints on $\Omega_b h^2$ imposed by nucleosynthesis.

	H_0	Ω_b	Q_{rms-ps}
Best Model	30	0.1	16.38
Conditional(68 %)	30-40	0.1-0.19	14.94-17.82
(95%)	30-40	0.1-0.22	14.94-19.8
Marginal(68%)	30-50	0.04-0.15	16.2-19.98

Table 7.3: Results of the fitting analysis considering: one multipole for COBE experiment, that Saskatoon calibration is correct and with BBN constraints for scale invariant flat CDM models.

Alternatively we generated the angular power spectrum, $C_l^{(S)}$, for these models using a CMB code kindly provided by U. Seljak and M. Zaldarriaga. The grid considered has Hubble constant, H_0, values in the range $\mathrm{H}_0 = 30 - 80\,\mathrm{km\,s^{-1}\,Mpc^{-1}}$in steps of 5 $\mathrm{km\,s^{-1}\,Mpc^{-1}}$, baryon density, Ω_b, values in the range $\Omega_b = 0.02 - 0.22$ in steps of 0.01 and $\Omega_0 = 1$. These models were checked against the models provided by G. Efstathiou. Including the 95% COBE normalization uncertainty and increasing the resolution of the parameter grid using interpolation procedures, we computed the best-fit model, its chi-squared value, the corresponding probability and the likelihood function. For each parameter both the conditional and marginal distributions were obtained as corresponding confidence intervals. We applied the same analysis to these models considering the data set referred to previously as (a) (ie one multipole for the COBE experiment), assuming that the Saskatoon calibration is correct (i)and with (1) no inclusion, (2) inclusion of BBN constraints. This analysis applied to case (b) (4 multipole bands for COBE) is under progress. The results are displayed in Table 7.2, for case (1) and in Table 7.3 for case (2). In order to set constraints on the parameters of these set of models we consider the 68% c.i. for the marginalized distribution of each parameter constrained to the BBN limits, these encompass $30\,\mathrm{km\,s^{-1}\,Mpc^{-1}} \leq \mathrm{H}_0 \leq 50\,\mathrm{km\,s^{-1}\,Mpc^{-1}}$, $0.04 \leq \Omega_b \leq 0.15$ and $16.2\ \mu\mathrm{K} \leq Q_{rms-ps} \leq 19.98\ \mu\mathrm{K}$. It should be stressed that these results were obtained considering only the case (i) for the Saskatoon calibration. This analysis confirms the previous results obtained using a cruder method.

7.5 Tilted flat CDM models

Initially we considered some of the best candidates for flat CDM models: (1) $h_0 = 0.3$, $\Omega_b = 0.2$, (2) $h_0 = 0.45$, $\Omega_b = 0.1$ and (3) $h_0 = 0.5$, $\Omega_b = 0.07$ and allowed for the tilting of the power spectrum to vary within $n = 0.7 - 1.4$. The fitting for the spectral index n of the primordial fluctuations was done considering the two sets of data mentioned above while at the same time allowing for the 2σ COBE normalization uncertainty. The results are displayed in Table 7.4. The third and fourth column display the uncertainties obtained considering the three calibration cases and taking extreme limits. Comparing e.g. first and second column we conclude that in general the effect of using 4 multipoles for COBE data produces an increase of n. In particular fixing $H_0 = 50\,\mathrm{km\,s^{-1}\,Mpc^{-1}}$ we find $n = 1.1 \pm 0.1$ (68 % confidence interval) allowing for the three calibration cases and taking extreme limits. This tight limit rules out a significant contribution from a gravity wave background for these models, in the case of power law inflation, but is consistent with the prediction of $n \simeq 1.0$ for scalar fluctuations generated by inflation.

In Fig. 7.5 on the top plot we present the model (3) and its 68 % confidence interval assuming the case (i) for the calibration. On the bottom plot is displayed the likelihood function for the parameter n for model (3) which peaks at $n = 1.1$ showing a significant estimate of the spectral index parameter based on the actual CMB data. In the previous analysis we used as normalization of the models, as first approximation, the quadrupole for the 4-year COBE data Q_{rms-ps} =18 μK and corresponding 95 % uncertainty. In order to normalize correctly we need to know the values of the Q_{rms-ps} for each value of the tilt. We have proceeded with a likelihood analysis of the COBE 4-year data in order to get for each n the corresponding Q_{rms-ps} and 95% confidence intervals. These values of Q_{rms-ps} (n) and c.i. are displayed in Table 7.5. We then considered the 4-year COBE normalized tilted flat CDM models. We generated the angular power spectrum, $C_l^{(S)}$,

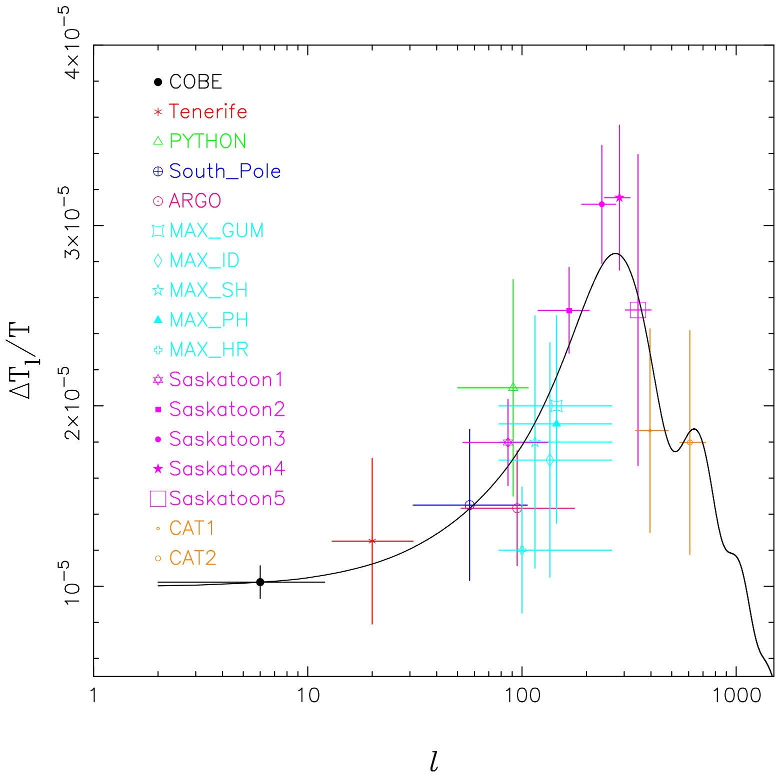

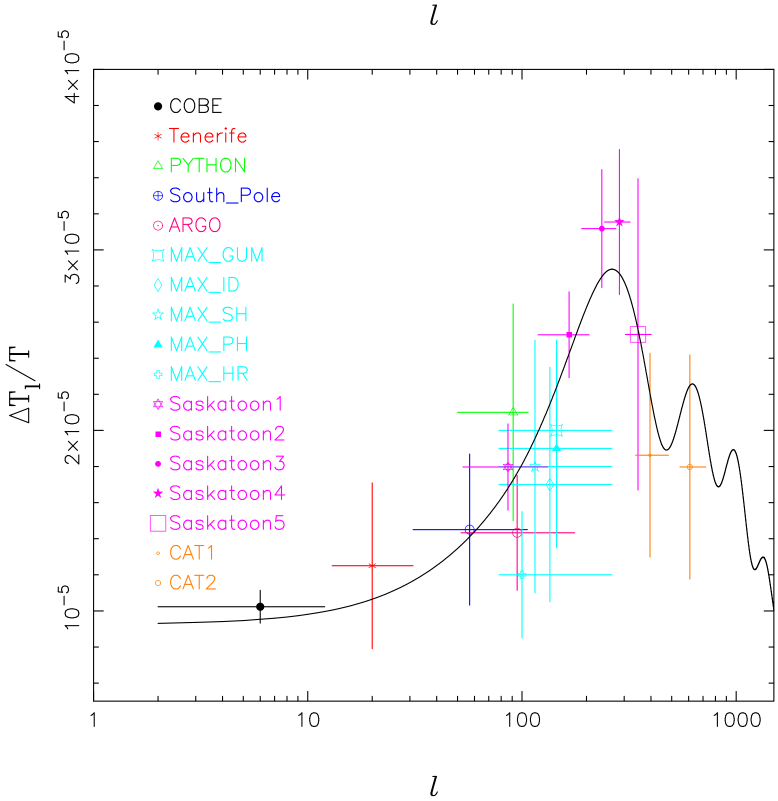

Figure 7.4: Top Figure: best-fit model for scale invariant flat CDM models not including BBN constraints with $H_0 = 30\,\mathrm{km\,s^{-1}\,Mpc^{-1}}$, $\Omega_b = 0.02$, Q_{rms-ps} =17.64 μK; Bottom Figure: including BBN constraints with $H_0 = 30\,\mathrm{km\,s^{-1}\,Mpc^{-1}}$, $\Omega_b =$ 0.1, Q_{rms-ps} =16.38 μK.

model	n (68% conf. interval)			
	(a),(i)	(b),(i)	(a),(i,ii,iii)	(b),(i,ii,iii)
$h_0 = 0.3$ $\Omega_b = 0.2$	0.94 ± 0.06	0.99 ± 0.07	0.94 ± 0.1	$0.99^{+0.11}_{-0.13}$
$h_0 = 0.45$ $\Omega_b = 0.1$	1.03 ± 0.07	1.08 ± 0.07	1.03 ± 0.1	1.08 ± 0.1
$h_0 = 0.5$ $\Omega_b = 0.07$	1.08 ± 0.07	1.11 ± 0.07	$1.08^{+0.09}_{-0.12}$	$1.11^{+0.09}_{-0.11}$

Table 7.4: Results of the fitting analysis for tilted flat models for: (a) data with 1 COBE multipole, (b) data with 4 COBE multipoles; (i) Saskatoon calibration is correct and (ii) lowest (iii) higher Saskatoon calibration.

n	Q_{rms-ps} (μK)	${Q_{rms-ps}}^l$(μK)	${Q_{rms-ps}}^u$(μK)
0.	39.0	30.0	60.0
0.20	34.0	26.0	46.0
0.40	30.0	22.0	42.0
0.60	26.0	18.0	38.0
0.80	22.0	16.0	26.0
0.90	20.0	15.0	25.0
1.0	19.0	14.0	24.0
1.1	18.0	13.0	23.0
1.2	16.0	12.0	22.0
1.3	15.0	11.0	21.0
1.4	14.0	10.0	20.0
1.5	13.0	9.0	19.0
1.6	12.0	9.0	19.0
1.8	11.0	8.0	16.0
2.0	9.0	6.0	14.0
2.2	8.0	4.0	12.0
2.4	7.0	2.0	10.0

Table 7.5: Q_{rms-ps} of 4-year COBE experiment according to each value of the power spectral index n; ${Q_{rms-ps}}^l$ stands for lower limit while ${Q_{rms-ps}}^u$ stands for upper limit (95% confidence).

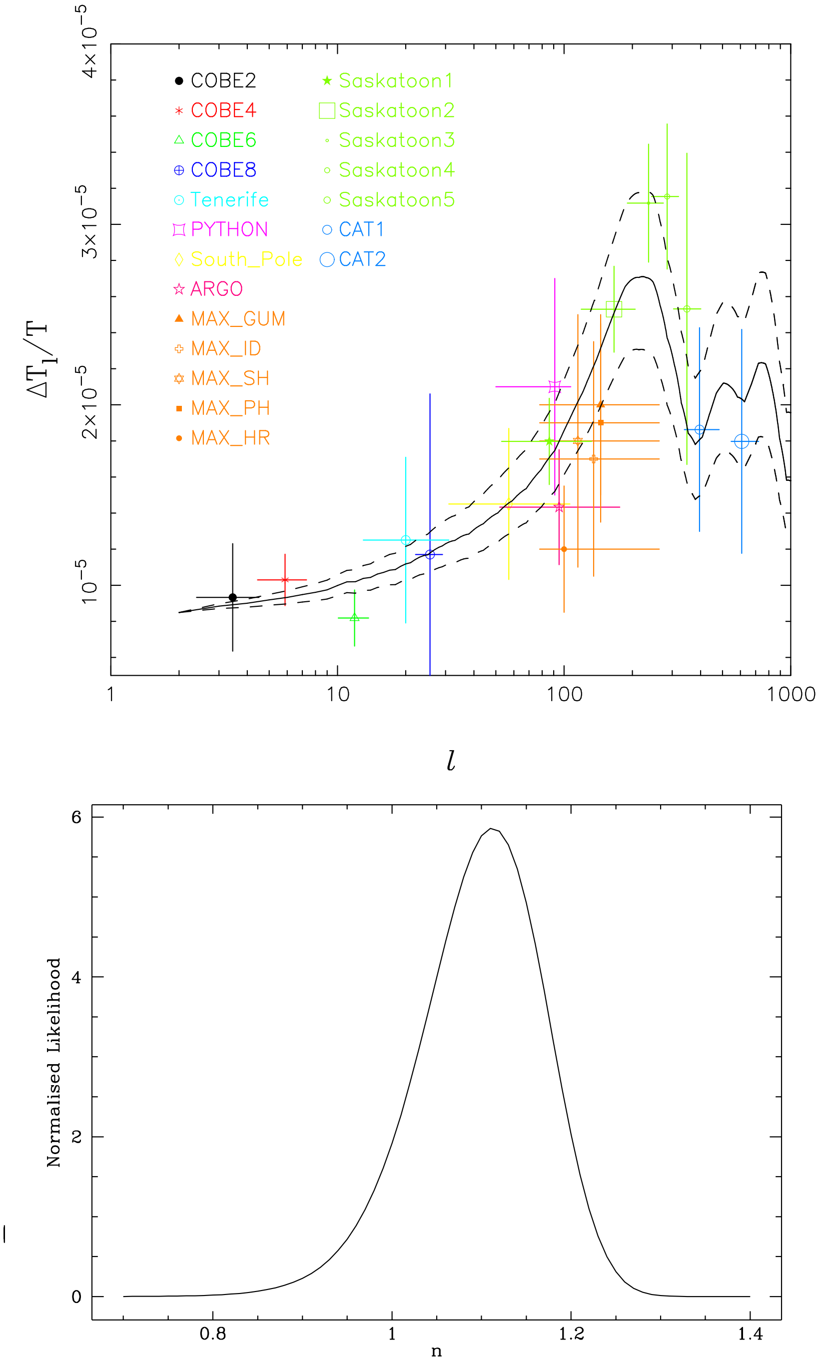

Figure 7.5: Tilted model with $h_0 = 0.5$, $\Omega_b = 0.07$, $n = 1.1$ and its 68 % confidence interval (Top Figure), likelihood function for the parameter n (Bottom Figure).

	H_0	Ω_b	n	Q_{rms-ps}
Best Model	30	0.22	0.92	17.95
Conditional(68 %)	30-55	0.10-0.22	0.81-1.0	16.18-20.12
(95%)	30-70	0.03-0.22	0.73-1.09	14.79-21.69
Marginal(68%)	30-70		0.78-1.12	

Table 7.6: Results of the fitting analysis considering: one multipole for COBE experiment, that Saskatoon calibration is correct and without BBN constraints for tilted flat CDM models.

	H_0	Ω_b	n	Q_{rms-ps}
Best Model	30	0.22	0.92	17.95
Conditional(68 %)	30-30	0.13-0.22	0.81-1.0	16.18-20.12
(95%)	30-30	0.10-0.22	0.73-1.09	14.79-21.69
Marginal(68%)	30-55	0.03-0.17	0.85-1.18	

Table 7.7: Results of the fitting analysis considering: one multipole for COBE experiment, that Saskatoon calibration is correct and with BBN constraints for tilted flat CDM models.

using a CMB code kindly provided by U. Seljak and M. Zaldarriaga. These models were checked against the scale invariant flat CDM models kindly provided by G. Efstathiou. The grid considered has H_0 values in the range $\mathrm{H}_0 = 30 - 80$ $\mathrm{km\,s^{-1}\,Mpc^{-1}}$ in steps of 5 $\mathrm{km\,s^{-1}\,Mpc^{-1}}$, Ω_b values in the range $\Omega_b = 0.02 - 0.22$ in steps of 0.01 and tilt in the range $n = 0.6 - 1.4$ in steps of 0.1 for $\Omega = 1$. Including the 95% COBE normalization uncertainty and increasing the resolution of the parameter's grid using interpolation procedures, we computed the best-fit model, its chi-squared value, corresponding probability and the likelihood function. For each parameter both the conditional and marginal distributions were obtained as corresponding confidence intervals.

We applied the analysis with the tilt in the range $n = 0.6 - 1.4$ but in steps of 0.01 for the case (i) of Saskatoon calibration. The results for case (a) are displayed in Table 7.6 and Table 7.7 without (2) and with (1) superimposed BBN constraints, respectively. Considering the BBN constraints we obtain for the marginalized distribution of the tilt a 68% c.i. of $0.85 \leq n \leq 1.18$ while not including this constraint implies an n in the range 0.78-1.12 (68 %). Both results are consistent with the prediction of $n \simeq 1.0$ for scalar fluctuations generated by inflation.

Fixing $\mathrm{H}_0 = 50\,\mathrm{km\,s^{-1}\,Mpc^{-1}}$ the results obtained are tabulated in Tables 7.8, 7.9, 7.10. Comparing Table 7.8 and Table 7.9 we observe that the effect of including the BBN constraints is to decrease the best fit value of Ω_b from $\Omega_b = 0.22$ to $\Omega_b = 0.08$. As H_0 is fixed at the value $50\,\mathrm{km\,s^{-1}\,Mpc^{-1}}$ decreasing Ω_b has the effect of decreasing the height of the main Doppler peak. The best fit to the CMB data is given by $\Omega_b = 0.22$. In order to obtain a satisfying fit for $\Omega_b = 0.08$ one needs to enhance the height of the peak for this value of Ω_b by, e.g., increasing the tilt. This is exactly what Table 7.8 and Table 7.9 give with the best fit value for $\Omega_b = 0.22$ of $n = 0.91\pm^{0.09}_{0.1}$ (68% c.i.) and for

	Ω_b	n	Q_{rms-ps}
Best Model	0.22	0.91	17.68
Conditional(68 %)	0.15-0.22	0.81-1.0	15.89-19.66
(95%)	0.07-0.22	0.71-1.08	14.89-21.45
Marginal(68%)		0.84-1.16	

Table 7.8: Results of the fitting analysis for $H_0 = 50\,\mathrm{km\,s^{-1}\,Mpc^{-1}}$ for case (a) and case (i) calibration without BBN constraints for tilted flat CDM models.

	Ω_b	n	Q_{rms-ps}
Best Model	0.08	1.07	16.79
Conditional(68 %)	0.05-0.08	0.98-1.18	15.14-18.82
(95%)	0.04-0.08	0.86-1.26	13.30-20.29
Marginal(68%)	0.04-0.07	0.93-1.21	

Table 7.9: Results of the fitting analysis for $H_0 = 50\,\mathrm{km\,s^{-1}\,Mpc^{-1}}$ for case (a) and case (i) calibration with BBN constraints for tilted flat CDM models.

$\Omega_b = 0.08$ of $n = 1.07\pm^{0.11}_{0.09}$ (68%). Note however that this variation of the tilt is affected by the permitted variation of the Q_{rms-ps} within the 2σ limits of the COBE uncertainty. We observe a decrease of the best fit value of Q_{rms-ps} when Ω_b decreases. The 68% c.i. for the marginalized distribution of the tilt suffers a shift towards higher values of n when we include the BBN constraints from 0.84-1.16 to 0.93-1.21. This is expected to be so because the BBN limits will not allow the higher values of Ω_b which seem to fit better the data.

In order to constrain H_0 for tilted CDM models consider Table 7.6 and Table 7.7. The inclusion of BBN constraints reduces the 68% c.i. for the marginalized distribution of the tilt from $30\,\mathrm{km\,s^{-1}\,Mpc^{-1}} - 70\,\mathrm{km\,s^{-1}\,Mpc^{-1}}$ to $30\,\mathrm{km\,s^{-1}\,Mpc^{-1}} - 55\,\mathrm{km\,s^{-1}\,Mpc^{-1}}$ assuming that Saskatoon calibration is correct. Fixing $n = 1$ reduces the upper limit of the H_0 c.i. in both situations. The marginalized distribution of the Hubble constant when considered in conjunction with BBN limits gives H_0 in the range $30\,\mathrm{km\,s^{-1}\,Mpc^{-1}} - 55\,\mathrm{km\,s^{-1}\,Mpc^{-1}}$ for case (i) calibration. The comparison of Table 7.6 and Table 7.8 permits one to comment on the variation of the best fit tilt with H_0 for a fixed value of Ω_b. Varying H_0 from $30\,\mathrm{km\,s^{-1}\,Mpc^{-1}}$ to $50\,\mathrm{km\,s^{-1}\,Mpc^{-1}}$ produces a slight decrease of the best fit value of the tilt from $n = 0.92$ to $n = 0.91$ while simultaneously the best fit Q_{rms-ps} decreases from Q_{rms-ps} =17.95 μK to Q_{rms-ps} =17.68 μK. This is an expected outcome because for $\Omega_b \geq 0.05$ an increase of H_0 will increase the height of the peak, as the value of $H_0 = 30\,\mathrm{km\,s^{-1}\,Mpc^{-1}}$ for $\Omega_b = 0.22$ seems to be the best fit to the CMB data; we need to decrease the height of the peak for the higher value of $H_0 = 50\,\mathrm{km\,s^{-1}\,Mpc^{-1}}$. This is achieved by decreasing the tilt and the value of Q_{rms-ps} . The decrease of the value of the tilt would be larger if we kept fixed the Q_{rms-ps} value. This tendency is not shown in the marginalized distribution of the tilt, because in Table 7.6 the marginalization is considered over all the available values of H_0 while in Table 7.8 the value of H_0 is fixed and equal to $50\,\mathrm{km\,s^{-1}\,Mpc^{-1}}$. Neverthless this variation is very small and it leads us to

	Ω_b	n	Q_{rms-ps}
Best Model	0.08	1.15	14.20
Conditional(68 %)	0.05-0.08	1.03-1.26	12.67-15.73
(95%)	0.04-0.08	0.90-1.35	12.50-17.59
Marginal(68%)	0.04-0.08	0.93-1.24	

Table 7.10: Results of the fitting analysis for $\mathrm{H}_0 = 50\,\mathrm{km\,s^{-1}\,Mpc^{-1}}$ for case (b) and case (i) calibration with BBN constraints for tilted flat CDM models.

conclude that in this case the large value of Ω_b is the determinant factor.

In Table 7.10 we display the results obtained for 4 multipole bands for COBE data (b), assuming that Saskatoon calibration is correct and including the BBN constraints. The best fit value of n is $n = 1.15^{+0.11}_{-0.12}$ (68 % c.i.) while the marginalized distribution gives n in the range 0.93-1.24 with 68 % confidence. For the value of $\mathrm{H}_0 = 50\,\mathrm{km\,s^{-1}\,Mpc^{-1}}$ considering the 4 multipoles instead of multipole C_2 produces an increase of the tilt and decrease of the value of Q_{rms-ps} with an unchanged best fit value of Ω_b. This is trying to account for the discretization of the total range of multipoles covered by the COBE experiment. The information contained in these 4 multipole bands seems to point for the existence of more power in the smaller scales probed by COBE and for the decrease of the normalization at low l. The marginal distribution suffers an insignificant variation with an interval 0.93-1.21 for case (a) and 0.93-1.24 for case (b). These results are consistent with the inflationary prediction of $n \simeq 1$. The presence of a gravity wave component in our models would require even larger values of n than those derived above. Considering Equation 5.4 of Chapter 5 this reaffirms our conclusion that a significant gravity wave contribution is unlikely.

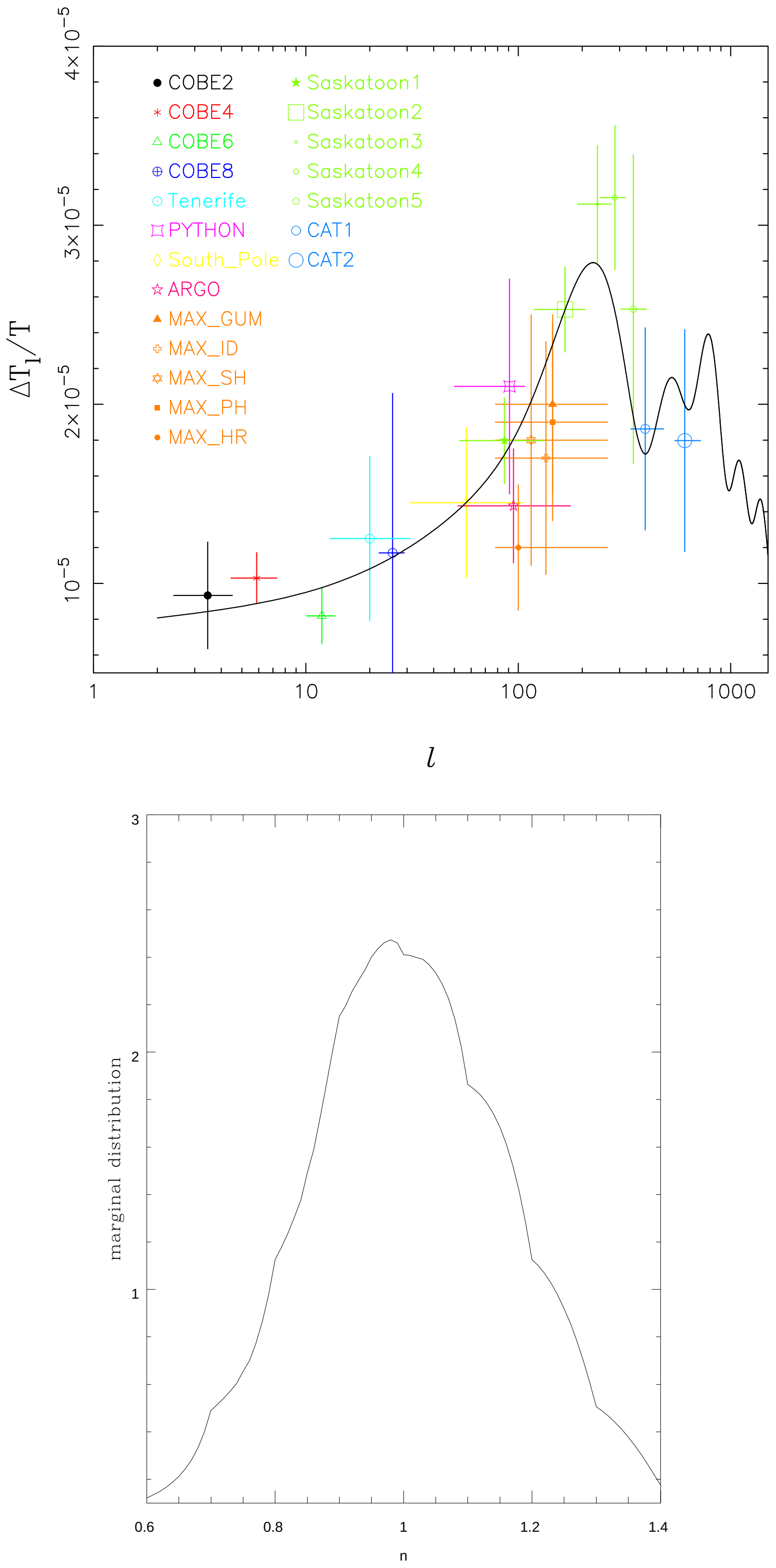

Figure 7.6: Tilted model with $h_0 = 0.5$, $\Omega_b = 0.08$, $n = 1.15$ and Q_{rms-ps} =14.20μK (top figure); marginal distribution for the parameter n as marginalized over H_0 , Ω_b and Q_{rms-ps} , as tabulated in Table 7.7 (Bottom figure).

	Ω	H_0	Ω_b	Q_{rms-ps}
Best Model	0.7	50	0.096	15.24 (15.01)
Conditional(68 %)	0.5-1.0	50-80	0.05-0.096	13.67-16.48
(95%)	0.4-1.0	30-80	0.01-0.096	12.66-17.07
Marginal(68%)	0.5-1.0	30-70		12.40-16.9

Table 7.11: Results of the fitting analysis for case (a) and case (i) calibration without BBN constraints for open and flat models.

7.6 Open models

We initially had access to the open models ($\Omega < 1$) with values for (Ω,h_0) (where $h_0 = H_0/(100\,\mathrm{km\,s^{-1}\,Mpc^{-1}})$) of (0.1,0.75), (0.2,0.7), (0.3,0.65), (0.4,0.65), (0.5,0.6) kindly provided by N. Sugiyama. Applying the analysis for case (b) ie 4 multipole bands for the COBE experiment, we conclude that $\Omega \leq 0.3$ is not compatible with the data, while the value of $\Omega = 0.4$ is only allowed for the lower Saskatoon calibration data. A value of $\Omega = 0.5$ offers an acceptable chi-squared fitting for both case (i) and (ii) calibrations. This confirms the results obtained using the approximate formula of Chapter 6 reassuring us that the generalized parametrized formula previously used constitutes a good approximation given the uncertainties in the data. We have also considered a more complete set of open models: the grid considered has h values of 0.3, 0.5, 0.6, 0.7 and 0.8 (where $h = \mathrm{H}_0/(100\,\mathrm{km\,s^{-1}\,Mpc^{-1}})$), and baryon density Ω_b values of 0.01, 0.03, 0.06, together with $\Omega_b = 0.0125h^{-2}$ and $0.024h^{-2}$ for each of the above values of h. The Ω range considered is 0.1 to 1.0 in steps of 0.1. (These models were kindly provided by N. Sugiyama). The unavaiability of exact models for $\Omega > 1$ limits some of the statistical conclusions we can draw here, but the results are still of interest. Assuming case (i) for the calibration and allowing the model normalisation to vary within the two sigma COBE limit we find that the best fit model has $\Omega = 0.7$, $\mathrm{H}_0 = 50\,\mathrm{km\,s^{-1}\,Mpc^{-1}}$ and $\Omega_b = 0.096$. This best fit value of Ω gives good agreement with the results obtained using the analytic approximation. Marginalizing over the other parameters, we obtain an allowed 68% range for Ω of $0.5 \leq \Omega \leq 1.0$. (The upper limit of 1 is due to the cutoff in the range of models considered.) The results are presented in table 7.11, assuming a similar amplitude for the the 95% uncertainty normalization as for the flat models. Fig. 7.7 shows the best fit open model for the fitting analysis applied to case (a) ie one multipole for COBE experiment and assuming that Saskatoon calibration is correct (i) (top plot); and the marginal distribution for the parameter Ω (bottom plot).

7.7 Tilted flat Λ models

We considered, in the first instance, some of the cosmological constant, Λ, models with no reionization, using the Berkeley CMB code. The initially used model parameters were (Λ,h_0,Ω_b) of (0.6,0.5,0.05), (0.6,0.5,0.03), (0.6,0.8,0.06), (0.7,0.5,0.05), (0.2,0.5,0.05). These models seem to be consistent with the data, with large values of Λ providing the best fit. Λ models compared with a flat CDM model with $h_0 = 0.45$ and $\Omega_b = 0.1$ assuming case (i) calibration. We then considered a more complete set of flat models with a

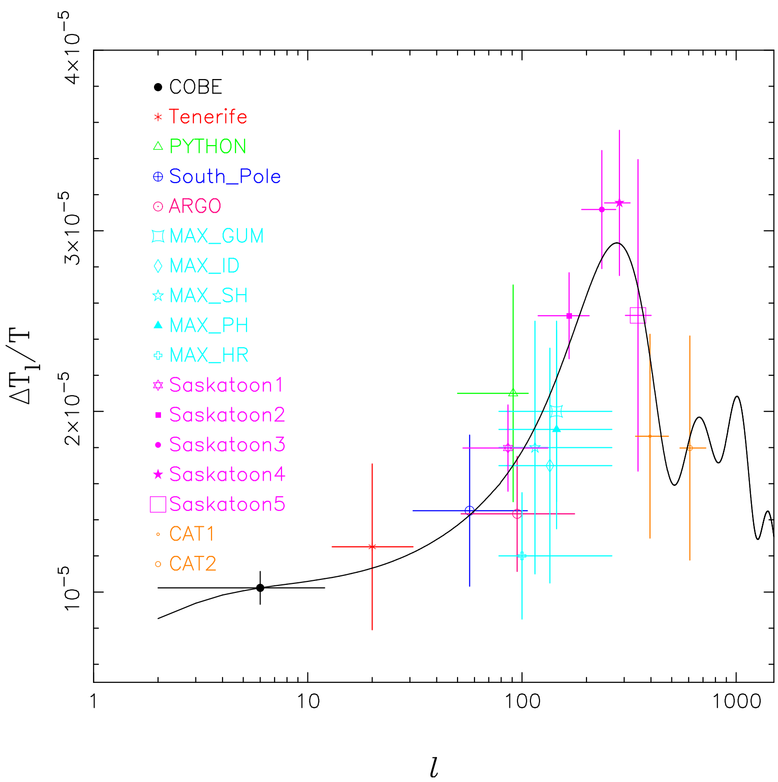

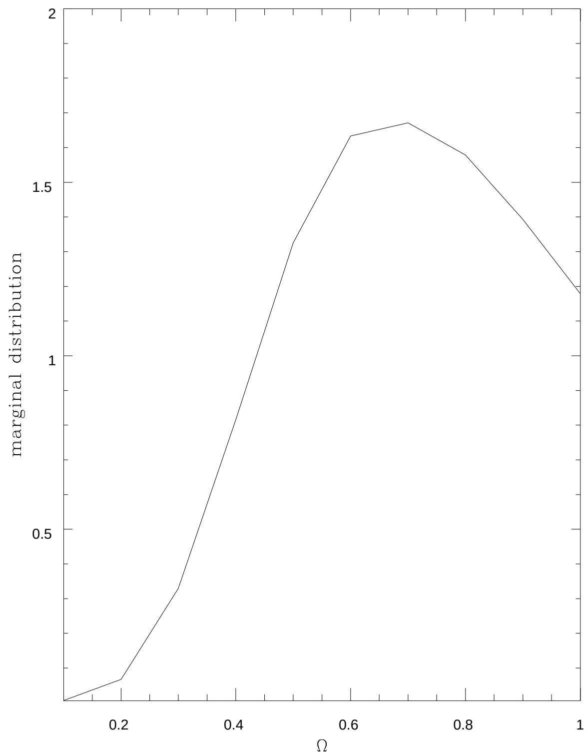

Figure 7.7: Best-fit open model with $\Omega = 0.7$, $\mathrm{H}_0 = 50$, $\Omega_b = 0.096$ and Q_{rms-ps} $=15.24$ μK(Top figure); marginal distribution for the parameter Ω (Bottom figure).

	Ω_Λ	H_0	Ω_b
Best Model	0.7	55	0.03
Conditional(68 %)	0.4-0.7	55-75	0.03-0.06
(95%)	0.3-0.7	55-80	0.03-0.06
Marginal(68%)	0.3-0.6	40-65	0.03-0.09

Table 7.12: Results of the fitting analysis for $n = 1$ considering case (a) and case (i) calibration with BBN constraints for a fixed value of the COBE normalization (Q_{rms-ps} =18 μK) for tilted flat Λ models.

	Ω_Λ	H_0	Ω_b	$Q_{rms-ps}/Qcobe$
Best Model	0.4	40	0.06	0.91
Conditional(68 %)	0.3-0.7	40-55	0.06-0.11	0.84-1.0
(95%)	0.3-0.7	40-55	0.06-0.12	0.83-1.1
Marginal(68%)	0.3-0.6	30-60	0.03-0.10	0.83-1.01

Table 7.13: Results of the fitting analysis for $n = 1$ considering case (a) and case (i) calibration with BBN constraints for tilted flat Λ models.

contribution from a cosmological constant, Λ, on the top of which we add some tilt. These models angular power spectra were generated using the CMB code provided by U.Seljac and M.Zaldarriaga. The grid considered has cosmological constant Λ density Ω_Λ in the range 0.3-0.7 in steps of 0.1, Hubble constant H_0 in the range 30-80 $\mathrm{km\,s^{-1}\,Mpc^{-1}}$ in steps of 5 $\mathrm{km\,s^{-1}\,Mpc^{-1}}$, baryon density Ω_b in the range 0.02-0.22 in steps of 0.01 and tilt n in the range 0.6-1.4 in steps of 0.1. Not having access to the value of the Q_{rms-ps} corresponding to each value of Λ for the 4-year COBE data we decided to use as first approximation the value of Q_{rms-ps} for the scale invariant flat CDM models instead of using the $(\Delta T/T)_{rms}$. We proceeded with the fitting incorporating the 95% COBE normalization uncertainty and increasing the resolution of the parameter's grid using an interpolation procedure as mentioned above. The fitting analysis was applied to case (a) for the COBE experiment, case (i) calibration and case (2) for the BBN constraints. Initially we considered only a scale invariant model and did not consider the 95% normalization uncertainty, the results are diplayed in Table 7.12. Incorporating this uncertainty the results are altered as shown in Table 7.13. Then we proceeded to include the effect of tilt; the results obtained are presented in Table 7.14, with n varying from 0.6 to 1.4 in steps of 0.01.

Only fixing $n = 1$ and the COBE normalization we reobtain that larger values of Λ provide the best fit. The opposite is true if we include the COBE normalization uncertainty and allow the tilt to vary. In the former case the 68% confidence interval for the marginal distribution places Λ in the range 0.3-0.6, H_0 in the range 40-65 $\mathrm{km\,s^{-1}\,Mpc^{-1}}$ while in the last case we get Λ in the range 0.4-0.7, H_0 in the range 30-55 $\mathrm{km\,s^{-1}\,Mpc^{-1}}$, tilt in the range 0.8-1.1. The conditional distribution is not particularly discriminatory for the Λ parameter and most of the models seem to offer good fit to the data. One must stress that the models considered only contemplate values of H_0 and Ω_b satisfying BBN constraints.

	Ω_Λ	H_0	Ω_b	n	$Q_{rms-ps}/Qcobe$
Best Model	0.3	35	0.16	0.9	1.0
Conditional(68 %)	0.3-0.7	30-35	0.11-0.16	0.8-1.0	0.91-1.1
(95%)	0.3-0.7	30-35	0.08-0.16	0.8-1.1	0.85-1.16
Marginal(68%)	0.4-0.7	30-55	0.03-0.13	0.8-1.1	0.88-1.11

Table 7.14: Results of the fitting analysis considering case (a) and case (i) calibration with BBN constraints for tilted flat Λ models.

Fig. 7.7 shows the best fit Λ models for scale invariant Λ model (top plot), and for tilted Λ models (bottom plot). Fig. 7.9 shows the conitional (top) and the marginal distribution (bottom) of the Λ parameter.

7.8 Topological defect models

We considered a string model (J. Magueijo, priv. comm.) and texture models with (Ω,h_0,Ω_b)=(1,0.5,0.05), (1,0.7,0.05) (N. Turok, priv. comm.). Models in which structure formation is initiated by cosmic strings [109] are consistent with the data, but are excluded for the higher calibration Saskatoon data. Texture models are also only allowed if one considers the lower calibration for the Saskatoon data. In Fig. 7.10 we present the data points of Table 7.1 compared with a cosmic string model, the best candidate of the texture models (with $\Omega = 1$, $h_0 = 0.5$ and $\Omega_b = 0.05$) and a flat CDM model with $h_0 = 0.45$ and $\Omega_b = 0.1$. On the top plot we present the same data points compared now with candidates of both the open and Λ models and with the same flat CDM model. As shown in Fig. 7.10 the peak of the amplitude of the angular power spectrum for these models shifts towards higher multipole l (i.e. towards smaller angular scales) with respect to the standard CDM model. Topological defect models fit better the CMB data than open models with low Ω, this seems to be related with the details of the shape of the power spectrum in the region of low and intermediate $l's$ as the comparison of these models with the open model on the top plot of Fig. 7.10 might reveal. The position of the first Doppler peak for Λ models is $\sim$ that of the standard CDM model as mentioned in chapter 2.

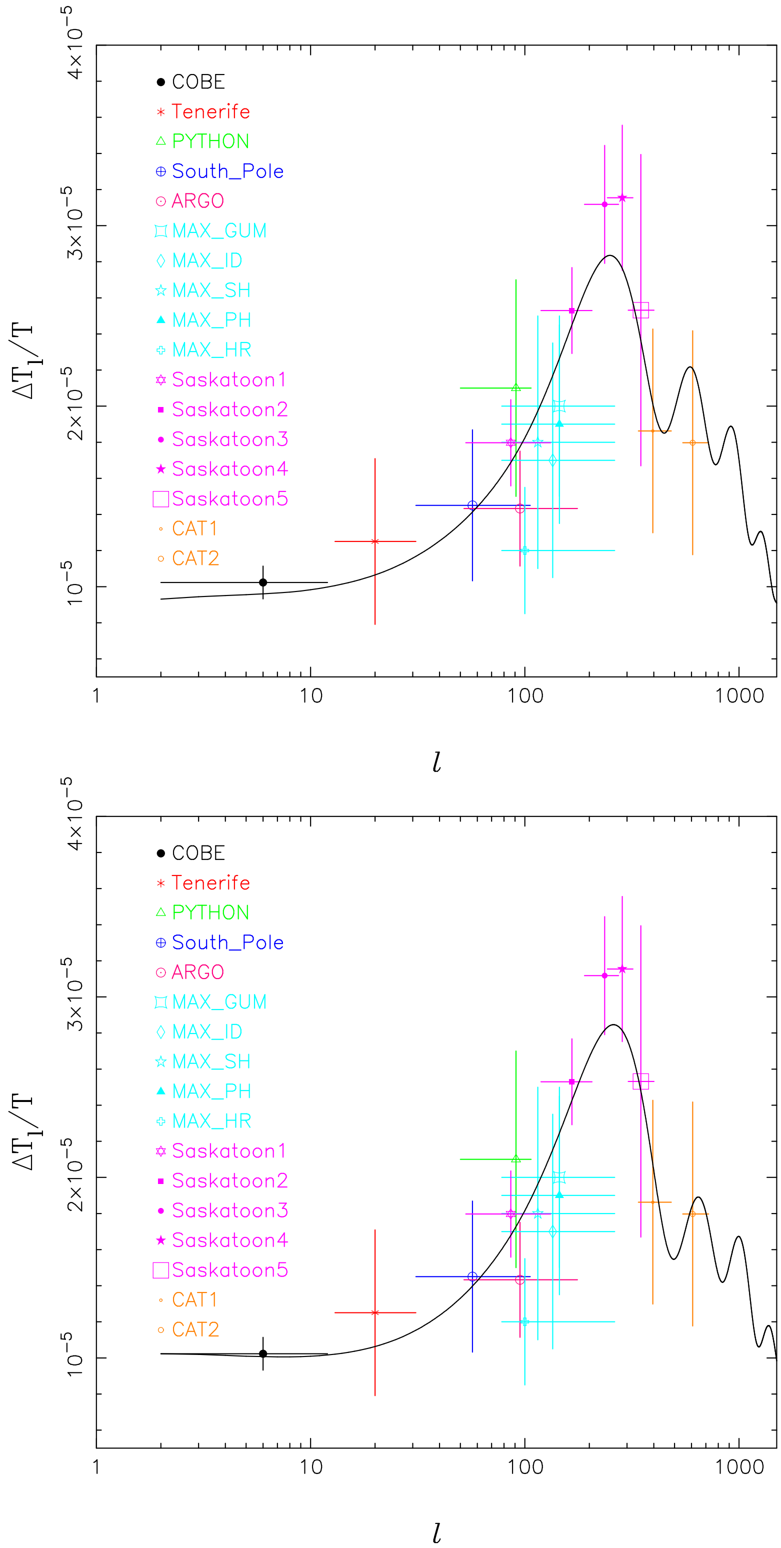

Figure 7.8: Top Figure: best-fit model for scale invariant Λ model with Λ=0.4, H_0 =40 km s^{-1} Mpc^{-1}, Ω_b=0.06 and Q_{rms-ps} =16.38μK; Bottom Figure: best-fit model for tilted Λ model with $n = 0.9$, Λ=0.3, H_0 =35 km s^{-1} Mpc^{-1}, Ω_b=0.16 and Q_{rms-ps} =18.0 μK; both results constrained to BBN limits.

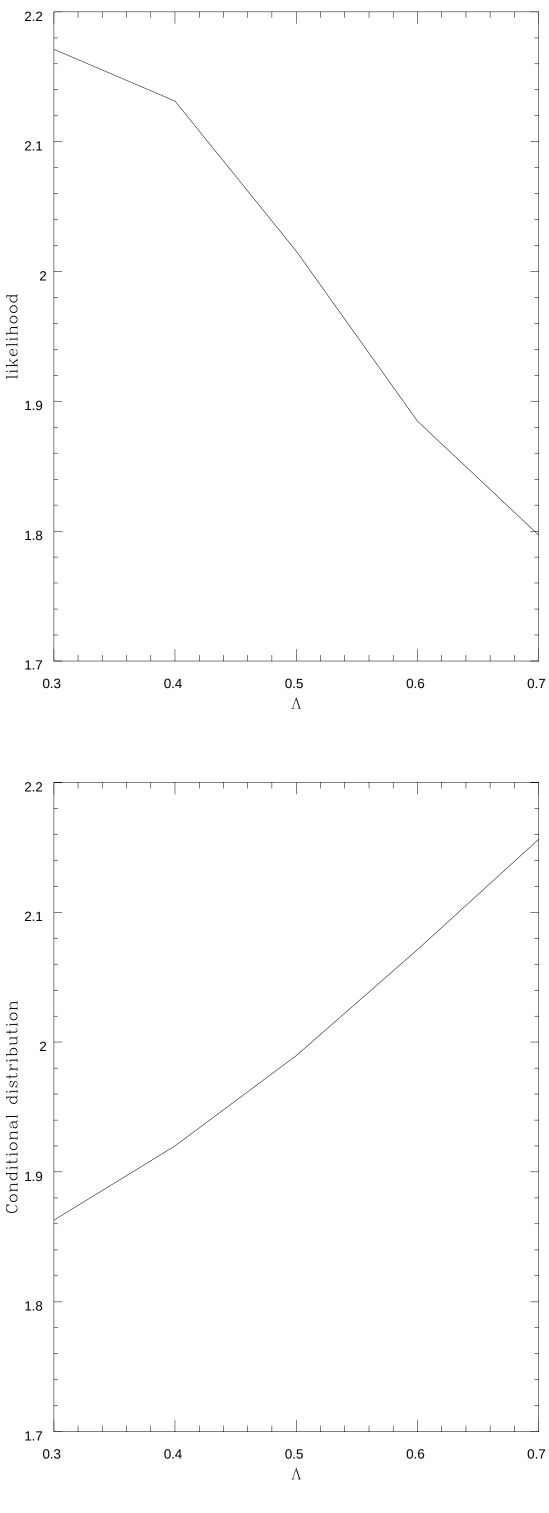

Figure 7.9: Top plot shows the likelihood for the parameter Λ conditional to the other parameters for the best fit model. Bottom plot shows the marginal distribution for the Λ parameter.

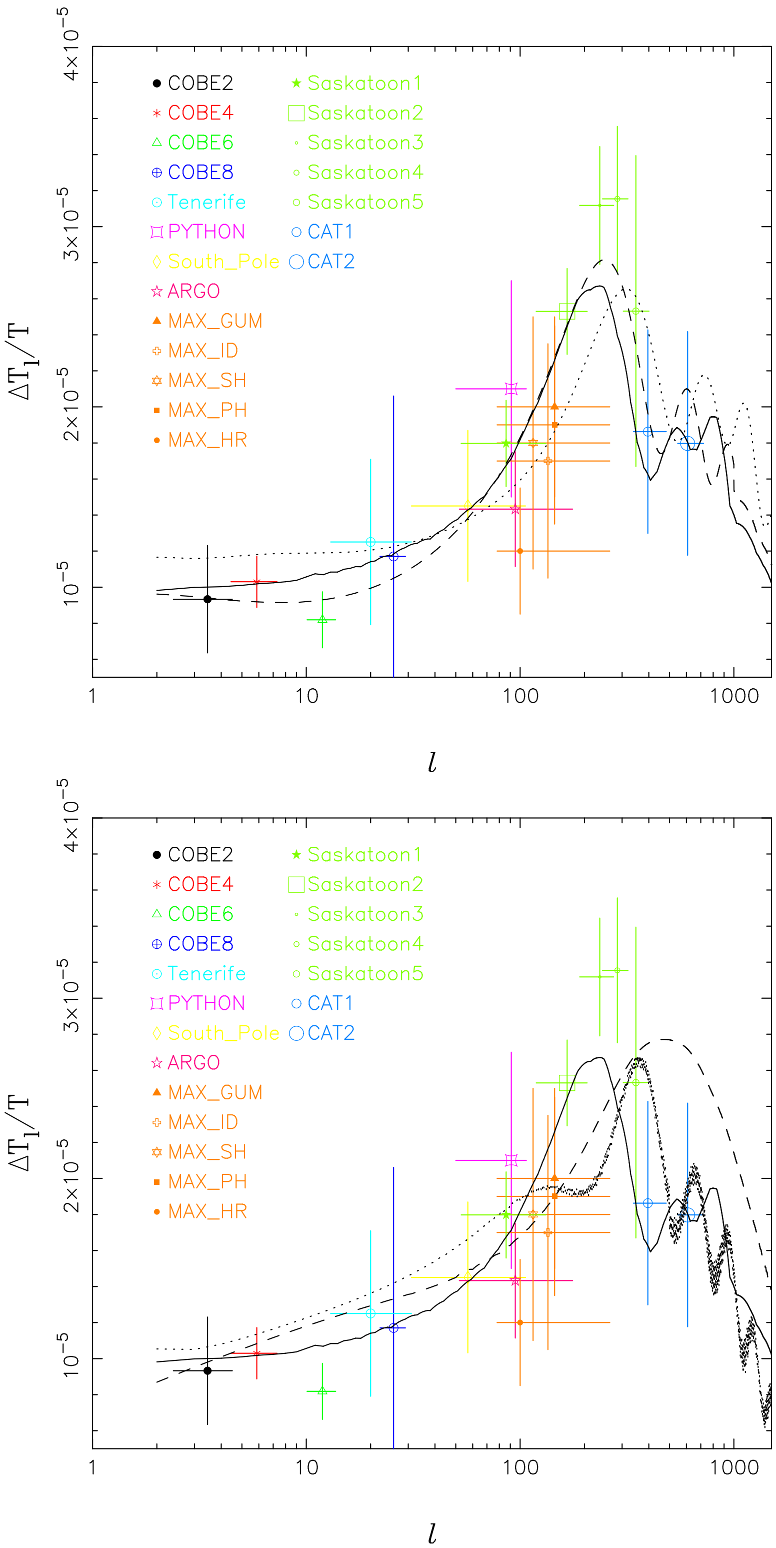

Figure 7.10: The data points from table 7.1 compared to the exact forms of the C_l for on the top figure: an $\Omega = 1$, $h_0 = 0.45$ and $\Omega_b = 0.1$ standard CDM model (bold line), an $\Omega = 0.5$, $h_0 = 0.6$ open model (dot line) and a flat $\Omega_\Lambda = 0.7$, $h_0 = 0.5$ and $\Omega_b = 0.05$ model (dashed line). For on the bottom figure: the same standard CDM model compared with a cosmic string model (dashed line) and an $\Omega = 1$, $h_0 = 0.5$ and $\Omega_b = 0.05$ texture model (dot line).

7.9 Conclusions

We have presented an intercomparison of the CMB data and the theoretical fourth-year COBE normalised power spectra predicted by several models. For flat, scale invariant, Cold Dark Matter dominated Universe, we used our results in conjunction with Big Bang nucleosynthesis constraints to determine the value of the Hubble constant as $\mathrm{H}_0 = 30 - 70\,\mathrm{km\,s^{-1}\,Mpc^{-1}}$ for baryon fraction $\Omega_b = 0.02$ to 0.2. We also considered a more detailed analysis of the fitting via calculation of the probability distribution function of the parameters. We obtained for the marginalized distribution of the parameters constrained to the BBN limits, considering that Saskatoon calibration is correct, a 68% c.i. of $30\,\mathrm{km\,s^{-1}\,Mpc^{-1}} \leq \mathrm{H}_0 \leq 50\,\mathrm{km\,s^{-1}\,Mpc^{-1}}$, $0.04 \leq \Omega_b \leq 0.15$ and 16.2 μK$\leq Q_{rms-ps} \leq$ 19.98 μK, confirming previous results. Tilting the initial fluctuations away from scale invariant and fitting to the ΔT_l we can delimit, n, using the two data sets: one COBE multipole (a) and four COBE multipole bands (b) for the same range in l. Assuming e.g. a CDM model without gravity waves with $\mathrm{H}_0 = 50\,\mathrm{km\,s^{-1}\,Mpc^{-1}}$ and $\Omega_b = 0.07$ we find the primordial spectral index of the fluctuations to be $n = 1.1 \pm 0.1$ (68% c.i.), with best fit values of Q_{rms-ps} =15 μK for $n = 1.1$ (allowing for the three calibration cases). This COBE normalised tilted model predicts a bias of the order $b \simeq 0.7$. So although this model fits well the CMB data alone it may not give a realistic scenario when we consider jointly the CMB data and the observed galaxy clustering. Aplying a more precise method to models with $\mathrm{H}_0 = 50\,\mathrm{km\,s^{-1}\,Mpc^{-1}}$, we found for the marginalized distribution of n a 68% c.i. of $0.93 \leq n \leq 1.21$ for case (a) and $0.93 \leq n \leq 1.24$ for case (b), assuming that Saskatoon calibration is correct. Including all our set of H_0 values we get for the marginalized distribution of the tilt a 68% c.i. $0.85 \leq n \leq 1.18$. These results are consistent with those from large scales alone given in Chapter 5, and are in close agreement with the inflationary prediction of $n \simeq 1.0$. They also state that a significant gravity wave contribution is unlikely.

Including open models in our analysis we obtain results consistent with those of Chapter 6 considering both cases (a) and (b). The best fit model has $\Omega = 0.7$, $\mathrm{H}_0 = 50\,\mathrm{km\,s^{-1}\,Mpc^{-1}}$, $\Omega_b = 0.096$ and Q_{rms-ps} =15.24 μK. Marginalizing over the other parameters we obtain a 68% c.i. for Ω of $0.5 \leq \Omega \leq 1.0$, where the upper limit of 1 is due to the range of models considered. For tilted models with non zero cosmological constant we obtain that lower values of Λ provide the best fit. The best fit has Λ=0.3, $\mathrm{H}_0 = 35\,\mathrm{km\,s^{-1}\,Mpc^{-1}}$, $n = 0.9$ and Q_{rms-ps} =18 μK. The marginal distribution places Λ in the range $0.4 \leq \Lambda \leq 0.7$ (68%) and the tilt in the range $0.8 \leq 1.1$. Models in which the fluctuations originate from cosmic strings appear to be consistent with the observations while the texture models are only allowed for the lower Saskatoon calibration case. Work is under progress in order to include all the situations for both the COBE data and the BBN constraints. The Saskatoon calibration cases will be incorporated in the analysis as a parameter over which the distribution function is marginalized in order to get a more definite information about the parameters of the models considered.

Chapter 8

Conclusions

This thesis has presented an intercomparison of CMB anisotropy experiments and models of structure formation. This comparison involves an accurate inclusion of theoretical uncertainties affecting theoretical predictions. If Bayesian analysis includes properly both instrumental and theoretical uncertainties then this should be evident when compared with the frequentist approach. Following the later approach we produced Monte Carlo simulations for several experiments and compared both methods with the Tenerife experiment. On large angular scales the CMB fluctuations may probe the initial power spectrum of the fluctuations, and in particular may be used to constrain the normalization and the spectral index of an initial power-law power spectrum. Results for both parameters were obtained for the Tenerife experiment, and an improved result achieved from the combined analysis of COBE and Tenerife data. These experiments in conjunction with medium angular scale experiments covers angular scales ranging from $10°$ to $0.25°$, probing the shape of the CMB 'angular power spectrum' all way up to $l \sim 700$, offering an unique opportunity of constraining model parameters. We carried out with a full comparison of these recent detections *as* CMB anisotropies in order to constrain e.g. Ω_0, H_0, Ω_b, n, Λ etc. A summary of the results from each of these areas is now given.

A theoretical intrinsic limitation follows from both the cosmic and sample variances due to the statistical nature of our theories. We calculated these theoretical uncertainties using a frequentist approach via Monte Carlo simulations of several experiments. Using these simulations we tested a 'maximum entropy method based' to reconstruct the intrinsic CMB sky for the Tenerife experiment, tested the consistency of underlying models with the observations, and computed the factor of smoothing of the intrinsic anisotropy amplitude with the corresponding beam, for the Jodrell Bank 5GHz interferometer. An initial intercomparison of some CDM models with 'old' CMB data (available at the time the work was carried out) ruled out isocurvature models.

A detailed analysis of the cosmic microwave background structure in the Tenerife Dec=$+40°$ data have been presented. The effect of local atmospheric contributions on the derived fluctuation amplitude is considered, resulting in an improved separation of the intrinsic CMB signal from noise. Our analysis demonstrates the existence of common structure in independent data scans at 15 and 33 GHz. For the case of fluctuations described by a Gaussian auto-correlation function, a likelihood analysis of our combined results at 15 and 33 GHz implies an intrinsic *rms* fluctuation level of 48^{+21}_{-15} μK on a coherence scale of 4°; the equivalent analysis for a Harrison-Zel'dovich model gives a power spectrum normalisation of $Q_{rms-ps} = 22^{+10}_{-6}$ μK. The fluctuation amplitude is seen to be consistent at the 68 % confidence level with that reported for the COBE two-year data for primordial fluctuations described by a power law model with a spectral index in the range $1.0 \leq n \leq 1.6$. This limit favours the large scale CMB anisotropy being dominated by scalar fluctuations rather than tensor modes from a gravitational wave background, if power law inflation is right. The large scale Tenerife and COBE results are considered in conjunction with observational results from medium scale experiments in order to place improved limits on the fluctuation spectral index; we find $n = 1.10 \pm 0.10$ assuming standard CDM with $\mathrm{H}_0 = 50\,\mathrm{km\,s^{-1}\,Mpc^{-1}}$. For an improved grid of the parameters in conjunction with Big Bang nucleosynthesis constraints, we find $0.85 \leq n \leq 1.18$ after marginalizing the distribution function over H_0 , Ω_b, and Q_{rms-ps} . This constraint on the spectral index is in close agreement with the inflationary prediction of $n \simeq 1.0$.

A key prediction of cosmological theories for the origin and evolution of structure in the Universe is the existence of a 'Doppler peak' in the angular power spectrum of cosmic microwave background (CMB) fluctuations. We presented new results from a study of recent CMB observations which provide the first strong evidence for the existence of a 'Doppler Peak' localised in both angular scale and amplitude. This first estimate of the angular position of the peak is used to place a new direct limit on the curvature of the Universe, corresponding to a density of $\Omega = 0.7^{+1.0}_{-0.4}$, consistent with a flat Universe, making use of an analytic approximate expression to describe these models. This was further confirmed by the analysis conducted for the exact form of the angular power spectrum. Very low density 'open' Universe models are inconsistent with this limit unless there is a significant contribution from a cosmological constant. Although the best fit Λ model has a small Λ content. For a flat standard Cold Dark Matter dominated Universe we use our results in conjunction with Big Bang nucleosynthesis constraints to determine the value of the Hubble constant as $\mathrm{H}_0 = 30 - 70\,\mathrm{km\,s^{-1}\,Mpc^{-1}}$ for baryon fractions $\Omega_b = 0.02$ to 0.2. Models in which the fluctuations originate from cosmic strings appear to be consistent with the observations.

Our attempts to place increasingly more accurate limits on fundamental cosmological parameters will undoubtedly place increasing demands on observers for ever improved accuracy until the point where the intrinsic cosmic variance becomes the dominant form of error. Confidence in the results to this tolerance level will probably require close co-operation between observers and the combination of results from space-based, balloon-based and ground-based telescopes working over a range of frequencies. Potentially the most powerful observations will result from mapping overlapping/ interlocking CMB fields with independent multi-frequency instruments. In contrast to the statistical results currently being reported, this method builds in the necessary redundancy to reduce systematic errors. As an example observations are currently in progress with the Tenerife instruments, which in conjunction with the COBE 4 year data should provide a high signal to noise map of the last scattering surface thus providing a two dimensional representation of the seed structures as compared to the simple 1-D scans reported here. Being on scales greater than the horizon size at recombination the form of such a map would reflect the structures generated in an inflationary driven phase in the very early universe.

The existence of the Doppler peak has important consequences for the future of CMB astronomy, implying that our basic theory is correct and that improving our constraints on cosmological parameters is simply a matter of improved instrumental sensitivity and ability to separate out foregrounds. New instruments such as VSA [96], MAP and the proposed COBRAS/SAMBA satellite [110] will provide this improved sensitivity and should delimit Ω and other parameters with unprecedented precision. It is difficult using the CMB data alone to disentangle the variation due to simultaneous changes of different cosmological parameters, until such high resolution and high sensitivity maps of the sky are available. We can however use the information from other areas of astrophysics, for example the measurements of Large-Scale Structure (LSS). The CMB observations and the LSS measurements provide information about the power spectrum from complementary regions, with some overlap, at different cosmological times. Since these two fields provide a larger coverage of the power spectrum, it is expected that their combined use will result in more severe constraints on the cosmological parameters [136]. The combination of CMB data with LSS observations is already in progress. In order to include overlapping sky fields and correlated data points an improvement over the analysis presented here is required. A χ^2 analysis is no longer suitable and this must be substituted by a correlation function. However this will require the use of supercomputers since matrix sizes in the Likelihood analysis will be large. Additionally further improvements are required in order to marginalize properly over all parameters. All of these points will be addressed in a future project.

REFERENCES

[1] Abbott, L.F., Wise, M., 1984, Nucl. Phys. B244, 541

[2] Aizu, K., Inoue, M., Tabara, H., Kato, T., 1987, in Proc. IAU symp. 124, "Observational Cosmology", Reidel, p. 565,

[3] Alcock C., *et al.*, 1993, Nature, 365, 621

[4] Alsop D.C., *et al.*, 1992, ApJ, 395, 317

[5] Banday A.J., Wolfendale A.W., 1990, MNRAS, 245, 182

[6] Banday A.J., Wolfendale A.W., 1991, MNRAS, 252, 462

[7] Banday A.J., Wolfendale A.W., 1991, MNRAS, 248, 705

[8] Banday, A.J. *et al.*, 1994, ApJ, 436, L99

[9] Banday, A.J., *et al.*, 1996a, ApJ, submitted

[10] Banday, A.J., *et al.*, 1996b, ApJ, submitted

[11] Bardeen, J.M., Bond, J.R., Kaiser, N., Szalay, A.S., 1986, ApJ., 304, 15

[12] Bennett, C.L., *et al.*, 1992, ApJ, 396, L7

[13] Bennett, C.L., *et al.*, 1994, ApJ, 436, 423

[14] Bennett, C.L., *et al.*, 1996, ApJ, 464, L1

[15] Berger, J.O., "Statistical Decision Theory and Bayesian Analysis', Springer Series in Statistics, Springer-Verlag

[16] Berkhuijsen, E.M., *et al.*, 1977, A&AS, 5, 263

[17] Blumenthal, G.R., Faber, S.M., Primack, J.R., Rees, M.J., 1984, Nature, 311, 517

[18] Bond, J.R., Efstathiou, G., Silk, J., 1980, Phys. Rev. Lett., 45, 1980

[19] Bond, J.R., 1995, in Schaeffer, R., ed., "Cosmology and Large Scale Structure", Proc. Les Houches School, Session LX, August 1993, Elsevier Science Publishers, Netherlands

[20] Bond, J.R., Astrophys. Lett. and Comm., in press

[21] Bond, J.R., 1995, Phys. Rev. Lett., 74, 4369

[22] Bond, J.R., Efstathiou, G.P., 1984, ApJ, 285, L45

[23] Bond, J.R., Efstathiou, G.P., 1987, MNRAS, 226, 655

[24] Bond, J.R., Szalay, A.S., 1983, ApJ, 274, 443

[25] Branenberger, R.H., 1990, in Peacock, J.A., Heavens, A.E., Davies, A.T., eds, Physics of the Early Universe, Adam Hilger, New York, p. 281

[26] Bunn, E.F., Sugiyama, N., 1995, ApJ, 446, 49

[27] Bunn, E.F., Hoffman, Y., Silk, J., 1996, ApJ, 464, 1

[28] Cayón, L., Martinez-González, E., Sanz, J.L., 1991, MNRAS, 253, 599

[29] Carr, B.J., 1990, Comments in Astrophys., 14, 257

[30] Cheng, E.S., *et al.*, 1994, ApJ, 422, L37

[31] Cheng, E.S., *et al.*, 1996, ApJ, 456, L71

[32] Church, S.E., *et al.*, 1995, ApJ, 440, L33

[33] Clapp, A.C. *et al.*, 1994, ApJ, 433, L57

[34] Coles, P., Lucchin, F. 1995, Cosmology: The Origin and Evolution of Cosmic Structure, Wiley, Chichester

[35] Copi, C.J., Schramm, D.N., Turner, M.S., 1995, Science, 267, 192

[36] Coulson, D., Ferreira, P., Graham, P., Turok, N., Nature, 1994, 368, 27

[37] Crittenden, R., Bond, J.R., Davis, R.L., Efstathiou, G., Steinhardt, P.J., 1993, Phys. Rev. Lett., 71, 324

[38] Crittenden, R., Bond, J.R., Davis, R.L., Efstathiou, G., Steinhardt, P.J., 1993, Phys. Rev. Lett., 69, 1856

[39] Davis, M., Efstathiou, G., Frenk, C.S., White, S.D.M, 1992, Nature, 356, 489

[40] Davis, M., Efstathiou, G., Frenk, C.S., White, S.D.M, 1985, ApJ, 292, 371

[41] Davies, R.D., *et al.*, 1987, Nature, 326, 462

[42] Davies, R.D., *et al.*, 1992, MNRAS, 258, 605

[43] Davies, R.D., *et al.*, 1996, MNRAS, 278, 883

[44] De Bernardis, P., *et al.*, 1994a, ApJ, 422, L33

[45] De Bernardis, P., De Gasparis, G., Masi, S., Vittorio, N., 1994b, ApJ, 433, L1

[46] Devlin, M.J., 1994, ApJ, 430, L1

[47] Devlin, M.J., *et al.*, 1993, Ann. N.Y. Acad. Sci., 688, 809

[48] Devlin, M.J., *et al.*, 1993, Proc. of the Nat. Acad. of Sciences of the USA., 90(11), 4774

[49] Dicke, R.H., Peebles, P.J.E., Roll, P.G., Wilkinson, D.T., 1965, ApJ, 142, 414

[50] Dodelson, S., Stebbins, A., 1994, ApJ, 433, 440

[51] Dodelson, S., Gates, E., Stebbins, A., 1996, ApJ, 467, 10

[52] Doroshkevich, A.G., Zel'dovich, Ya B., Sunyaev, R.A., 1978, Sov. Astron., 22, 523

[53] Doroshkevich, A.G., *et al.*, 1980, Sov. Astron. Lett., 6, 457

[54] Dragovan, M., *et al.*, 1994, ApJ, 427, L67

[55] Efstathiou, G., Bond, J.R., 1986, MNRAS, 218, 103

[56] Efstathiou, G.P., 1990, in Peacock, J.A., Heavens, A.E., Davies, A.T., eds, Physics of the Early Universe, Adam Hilger, New York

[57] Fischer, M.L., *et al.*, 1995, ApJ, 444, 226

[58] Fomalont, E.B., Partridge, R.B., Lowenthal, J.D., Windhorst, R.A., 1993, ApJ, 404, 8

[59] Franceschini, A., Toffolatti, L., Danese, L., De Zotti, G., 1989, ApJ, 344, 35

[60] Freedman, W.L., *et al.*, 1994, Nature, 371, 757

[61] Frenk, C.S., White, S.D.M., Efstathiou, G., Davis, M., 1990, ApJ, 351, 10

[62] Ganga, K., Cheng, E., Meyer, S., Page, L., 1993, ApJ, 410, L57

[63] Gaier, E.S., *et al.*, 1992, ApJ, 398, L1

[64] Górsky, K.M., Stompor, R., Juszkiewicz, R., 1993, ApJ, 410, L1

[65] Gorski, K.M., *et al.*, 1994, ApJ, 430, L89

[66] Gorski, K.M., Ratra, B., Sugiyama, N., Banday, A.J., 1995, ApJ, 444, L65

[67] Gorski, K.M., *et al.*, 1996, ApJ, 464, L11

[68] Gundersen, J.O., *et al.*, 1993, ApJ, 413, L1

[69] Gundersen, J.O, *et al.*, 1995, ApJ, 443 L57

[70] Gull, S.F., 1989, Maximum Entropy and Bayesian Methods, 53, ed. J. Skilling

[71] Gull, S.F., Skilling, J., 1984, Proc. IEEE, 131(F), 646

[72] Guth, A.H., 1981, Phys. Rev. D, 23, 347

[73] Gutierrez de la Cruz, C.M., Davies, R.D., Rebolo, R., Watson, R.A., Hancock, S., Lasenby, A.N., 1995, ApJ, 442, 10

[74] Hancock, S., *et al.*, 1997, MNRAS, in press

[75] Hancock, S., Davies, R.S., Lasenby, A.N., Gutiérrez de la Cruz, C.M., Watson, R.A., Rebolo, R., Beckman, J.E., 1994, Nature, 367, 333

[76] Harrison, E.R., 1970, Phys. Rev. D., 1, 2726

[77] Haslam, C.G.T., Salter C.J., Stoffel H., Wilson W.E., 1982, A&AS, 47, 1

[78] Hinshaw, G., *et al.*, 1996a, ApJ, 464, L17

[79] Hinshaw, G., *et al.*, 1996b, ApJ, 464, L25

[80] Holtzmann, J.A., 1989, ApJS, 71, 1

[81] Hu, W., Sugiyama, N., 1995, ApJ, 444, 489

[82] Hu, W., Sugiyama, N., 1995, Nature, submitted

[83] Hubble, E., 1927, Proc. Nat. Acad. Sci., 15, 168

[84] Jones, A.W., Hancock, S., Lasenby, A.N., Davies, R.D., Gutiérrez, C.M., Rocha, G., Watson, R.A., Rebolo, R., 1997, MNRAS, submitted

[85] Kaiser, N., 1983, MNRAS, 202, 1169

[86] Kaiser, N. 1984, ApJ, 284, L9

[87] Kamionkowsky, M., *et al.*, 1994a, ApJ, 426, L57

[88] Kamionkowsky, M., *et al.*, 1994b, ApJ, 434, L1

[89] Kennicutt, R.C., Freedman, W.L., Mould, J.R., 1995, ApJ, 110, 1476

[90] Kühr, H., Witzel, A., Pauliny-Toth, I.I.K., Nauber, U., 1981, A&AS, 45, 367

[91] Kogut, A., *et al.*, 1992, ApJ, 401, 1

[92] Kogut, A., *et al.*, 1996a, ApJ, 464, L5

[93] Kogut, A., *et al.*, 1996b, ApJ, 464, L29

[94] Kogut, A., *et al.*, 1996c, ApJ, 470, 653

[95] Kolb, & Turner, 1990, ... ********

[96] Lasenby, A.N., Hancock, S., 1995, in Sanchez, N., Zichichi, A., eds, Proc. of "Current Topics in Astrofundamental Physics: The Early Universe", Kluwer, Dordrecht, p. 327

[97] Lasenby, A.N., Hancock, S., Gutierrez de la Cruz, C.M., Davies, R.D., Watson, R.A., Rebolo, R., 1994, Astrophysical letters and Communications, in press

[98] Lasenby A.N., 1994, in Sanchez, N., Zichichi, A. eds, 2nd Erice course on Topics in Astrofundamental Physics, World Scientific, p. 209

[99] Laue, E., Skilling, J., Staunton, J., 1985, J. Mag. Res, 63, 418

[100] Lawson, K.D., Mayer, J.L, Osborne, J.L., Parkinson, M.L., 1987, MNRAS, 225, 307

[101] Liddle, A.R., Lyth, D.H., 1992, Phys. Letters, B291, 391

[102] Liddle, A.R., Lyth, D.H., Viana, P.T.P, White, M., 1996, MNRAS, submitted

[103] Lifschitz, E.M., 1946, J. Phys. USSR, 10, 16

[104] Linde, A.D., 1982, Phys. Lett., 1982, 108B, 389

[105] Lineweaver, C.H., *et al.*, 1995, ApJ, 448, 482

[106] Lyubimov, V.A., *et al.*, 1980, Phys. Lett., B94, 266

[107] Ma, C.P., Bertschinger, E., 1995, ApJ, 455, 7

[108] Maddox, S.J., Efstathiou, W.J., Sutherland G., Loveday J., 1990, MNRAS, 242, 43P

[109] Magueijo, J., Albrecht, A., Coulson, D., Ferreira, P., Phys. Rev. Lett., 1996, in press

[110] Mandolesi, N., *et al.*, 1995, Planetary and Space Science, 43, 1459

[111] Mather, J.C., *et al.*, 1994, ApJ, 420, 439

[112] Meyer, S.S., Cheng, E.S., Page, L., 1991, ApJ, 371, L7

[113] Myers, S.T., Readhead, A.C.S., Lawrence, C.R., 1993, ApJ, 405, 8

[114] Netterfield, C.B., *et al.*, ApJ, 1997, 474, 47

[115] O'Sullivan, C., *et al.*, 1995, MNRAS, 274, 861

[116] Ostriker, J.P., Steinhardt, P.J., 1995, Nature, 377, 600

[117] Peebles, P.J.E., 1987, ApJ, 315, L73

[118] Peebles, P.J.E., Yu, J.T., 1970, ApJ, 162, 815

[119] Peebles, P.J.E., 1982a, ApJ, 258, 415

[120] Penzias, A.A., Wilson, R.W., 1965, ApJ, 124, 419

[121] Pierce, M.J., *et al.*, 1994, Nature, 371, 385

[122] Ratra, B., *et al.*, 1997, ApJ, submitted

[123] Readhead, A.C.S., 1989, ApJ, 346, 566

[124] Reich, P., Reich, W., 1988, A&AS, 74, 7

[125] Robson, R., *et al.*, 1993, A&A, 277, 314

[126] Rocha, G., 1993, in Proc. of the Yamada Conference XXXVII, "Evolution of the Universe and its Observational Quest"

[127] Rocha, G., Hancock, S., Lasenby, A.N., Gutierrez, C.M., 1997, in preparation

[128] Ruhl, J.E., *et al.*, 1995, ApJ, 453, L1

[129] Sachs, R.K., Wolfe, A.M., 1967, ApJ, 147, 73

[130] Saunders, W., *et al.*, 1991, Nature, 349, 32

[131] Scaramela, R., Vittorio, N., 1988, ApJ, 331, L53

[132] Scaramela, N., Vittorio, N., 1990, ApJ, 353, 372

[133] Scaramela, N., Vittorio, N., 1993, ApJ, 411, 1

[134] Schuster, J., *et al.*, 1993, ApJ, 412, L47

[135] Scott, D., Srednicki, M., White M., 1994, ApJ, 241, L5

[136] Scott, D., Silk, J., White, M., 1995, Science, 268, 829

[137] Scott, P.F., *et al.*, 1996, ApJ, 461, L1

[138] Seljac, U., Zaldarriaga, M., 1996, ApJ, 469, 437

[139] Silk, J., 1967, Nature, 215, 1155

[140] Silk, J., 1968, ApJ, 151, 459

[141] Skilling, J., 1988, Maximum Entropy and Bayesian Methods in Science and Engineering, Volume 1, ed. G.J. Erickson and C.R. Smith, p. 173

[142] Skilling, J., 1989, Maximum Entropy and Bayesian Methods, 45, ed. J. Skilling

[143] Smoot, G.F., *et al.*, 1990, ApJ, 360, 685

[144] Smoot, G.F., *et al.*, 1992, ApJ, 396, L1

[145] Srednicky, M., 1993, Phys. Rev. Lett., 71, 23, 3747

[146] Steinhardt, P., 1993, in Proc. of the Yamada Conference XXXVII, "Evolution of the Universe and its Observational Quest", p. 159

[147] Steigman, G., 1993, Nucl. Phys. B Proc. Suppl., 31, 343

[148] Stompor, R., 1994, A&A, 287, 693

[149] Strukov, I.A., Brukhanov, A.A., Skulachev, D.P., Sazhin, M.V., 1993, Phys. Lett., B, 315, 198

[150] Sugiyama, N., 1995, ApJS, 100, 281

[151] Sugiyama, N., Gouda, N., 1992, Prog. Theo. Phys., 88, 803

[152] Tanaka, S.T., *et al.*, 1996, ApJ, 468, L81

[153] Tegmark, M., Bunn, E.F., 1995, ApJ, 455, 1

[154] Tegmark, M., 1996, ApJ, 464, L35

[155] Turner, M.S., 1991, Physica Scripta, T36, 167

[156] Turok, N., 1991, Physica Scripta, T36, 135

[157] Uson, J.M., Wilkinson, D.T., 1984, ApJ, 277, L1

[158] Uson, J.M., Wilkinson, D.T., 1984, Nature, 312, 427

[159] Uson, J.M., Wilkinson, D.T., 1984, ApJ, 283, 471

[160] Vittorio, N., Silk, J., 1984, ApJ, 285, L39

[161] Vogeley, M.S., Park C., Geller, M.J., Huchra, J.P., 1992, ApJ, 391, L5

[162] Watson, R.A., *et al.*, 1992, Nature, 357, 660

[163] Watson, R.A., Gutierrez de la Cruz, C.M., 1993, ApJ, 419, L5

[164] Wilson, M.L., Silk J., 1981, ApJ, 243, 14

[165] White, S.D.M., 1990, in Peacock, J.A., Heavens, A.E., Davies, A.T., eds, Physics of the Early Universe, Adam Hilger, New York, p. 1

[166] White, S.D.M., Frenk, C.S., Davis, M., 1983, ApJ, 274, L1

[167] White, S.D.M., Davis, M., Frenk, C.S., 1984, MNRAS, 209, 27P

[168] White, M., Srednicki, M., 1995, ApJ, 443, 6

[169] White, M., Krauss, L.M., Silk, J., 1993, ApJ, 418, 535

[170] White, M., Scott, D., Silk, J., 1994, ARA&A, 32, 319

[171] White, M., Scott, D., 1996, ApJ, 459, 415

[172] White, M., Bunn, E., 1995, ApJ, 443, L53

[173] Wilson, M.L., Silk, J., 1981, ApJ, 243, 14

[174] Wollack, E.J., *et al.*, 1993, ApJ, 419, L49

[175] Wright, E.L., *et al.*, 1994, ApJ, 436, 452

[176] Wright, E.L., *et al.*, 1996, ApJ, 464, L21

[177] Zel'dovich, Ya. B., 1972, MNRAS, 160, 1P